

# **Extensions and Applications of the Tail Pairwise Dependence Matrix**

**Matthew Pawley**

A thesis submitted for the degree of Doctor of Philosophy

**University of Bath**

Department of Mathematical Sciences

**December 2024**

# **Copyright**

Attention is drawn to the fact that copyright of this thesis rests with the author. A copy of this thesis has been supplied on the condition that anyone who consults it is understood to recognise that its copyright rests with the author and that they must not copy it or use material from it except as permitted by law or with the consent of the author.

This thesis may be made available for consultation within the University Library and may be photocopied or lent to other libraries for the purposes of consultation.

# **Declaration**

## **Declaration of any previous submission of the work**

The material presented here for examination for the award of a degree by research has not been incorporated into a submission for another degree.

**Candidate's signature:** .....

## **Declaration of authorship**

I am the author of this thesis, and the work described therein was carried out by myself personally, with the exception of:

- The article contained in Chapter 5, which was carried out in collaboration (equal contribution) with Henry Elsom (University of Bath).
- The pre-processed Red Sea data (Chapter 3) was kindly provided Dr Daniela Castro-Camilo (University of Glasgow).

**Candidate's signature:** .....

# Abstract

The aim of this thesis is to present novel statistical methods for analysing extremal dependence using the tail pairwise dependence matrix (TPDM). In multivariate extreme value theory (MEVT), extremal dependence relates to the joint stochastic behaviour of extreme, rare events involving several random variables, which is critical for risk assessment in a range of application areas, such as climatology and finance. The TPDM has proved a useful tool for analysing extremal dependence in high-dimensional settings, where the number of variables is large. Similar to the covariance matrix in non-extreme statistics, it provides a compact summary of the (potentially rather complicated) dependence structure and underpins a range of existing statistical methods. This thesis provides a new set of TPDM-based tools that may be used to validate key modelling assumptions and aid efficient statistical inference for rare events.

Our first contribution is to devise a formal procedure to test for changes in extremal dependence over time. In MEVT, it is typically assumed that extreme observations are identically distributed over time, despite the fact that climate change is known to induce non-stationary behaviour in extremes. Our test provides a simple way to validate this assumption. We devise a time-dependent extension to the TPDM and test for deviations in its empirical estimator. Since our procedure is rooted in the TPDM, it is applicable in high dimensions and is much less computationally intensive than existing methods.

Next, we explore connections between MEVT and the statistical discipline of compositional data analysis (CoDA). We discuss the common themes of these fields before providing concrete examples where CoDA methods may enhance inference for extremes: principal components analysis and classification. Empirically, we find that CoDA yields more efficient dimension reduction and reduced classification error.

A toolbox of TPDM-related methods for deriving data-driven predictions of environmental extremes is presented, resulting from participation in the EVA (2023) Data Challenge. The techniques used include completely positive factorisations of the TPDM, max-linear models, clustering, and sparse simplex projections.

Finally, we address a deficiency of the empirical TPDM estimator, whereby weak pairwise dependencies tend to be overestimated. We utilise regularisation techniques, including thresholding and Ledoit-Wolf linear shrinkage, to construct a broad class of flexible estimators that counteract the bias. A data-driven tuning procedure for selecting the Ledoit-Wolf regularisation parameter is proposed.

Software to apply our methods (or reproduce the results of our simulation studies and real-world examples) is freely available in a GitHub repository <https://github.com/pawleymatthew/Extensions-And-Applications-of-TPDM>.

# Acknowledgements

Write acknowledgements here (in `frontmatter.tex`).

# Table of contents

<b>Preface</b>	<b>1</b>
<b>1. Introduction</b>	<b>2</b>
1.1. Motivation . . . . .	2
1.2. Thesis aims and outline . . . . .	4
1.3. Notation . . . . .	6
<b>2. Background &amp; literature review</b>	<b>7</b>
2.1. Univariate extreme value theory . . . . .	7
2.1.1. Block maxima and the generalised extreme value (GEV) distribution	8
2.1.2. Threshold exceedances and the generalised Pareto distribution (GPD)	9
2.1.3. Non-stationary extremes . . . . .	10
2.2. Multivariate extreme value theory . . . . .	10
2.2.1. Componentwise maxima . . . . .	11
2.2.2. Copulae and marginal standardisation . . . . .	12
2.2.3. The exponent measure and angular measure . . . . .	13
2.2.4. Parametric multivariate extreme value models . . . . .	14
2.2.5. Multivariate regular variation . . . . .	20
2.2.6. Extremal dependence measures . . . . .	24
2.3. Inference . . . . .	29
2.3.1. Framework and notation . . . . .	29
2.3.2. Selecting the radial threshold or the number of exceedances . . . . .	30
2.3.3. The empirical angular measure . . . . .	31

---

2.3.4. Non-parametric estimators . . . . .	32
2.4. Tail pairwise dependence matrix (TPDM) . . . . .	33
2.4.1. Definition and examples . . . . .	33
2.4.2. Interpretation of the TPDM entries . . . . .	37
2.4.3. Decompositions of the TPDM . . . . .	39
2.4.4. The empirical TPDM . . . . .	41
2.5. Existing applications and extensions of the TPDM . . . . .	44
2.5.1. Principal component analysis (PCA) for extremes . . . . .	45
2.5.2. Inference for the max-linear model . . . . .	50
2.6. Bias in the empirical TPDM in weak-dependence scenarios . . . . .	52
2.6.1. Bias in the TPDM and threshold-based estimators . . . . .	52
2.6.2. Existing bias-correction approaches for the TPDM . . . . .	54
<b>3. Testing for time-varying extremal dependence</b>	<b>56</b>
3.1. Introduction . . . . .	56
3.2. Framework . . . . .	57
3.3. The local TPDM and integrated TPDM . . . . .	58
3.4. Inference . . . . .	62
3.4.1. The empirical local TPDM . . . . .	62
3.4.2. The empirical integrated TPDM . . . . .	63
3.4.3. Asymptotic properties of $\hat{\Sigma}(t)$ and $\hat{\Psi}(t)$ . . . . .	64
3.5. Test statistics and critical values . . . . .	68
3.6. Simulation experiments . . . . .	70
3.6.1. Data generating processes . . . . .	70
3.6.2. Large sample performance . . . . .	71
3.6.3. Small sample performance . . . . .	73
3.6.4. Computation time . . . . .	76
3.7. Loss of power under TPDM-invariant dependence changes . . . . .	77
3.8. Application: Extreme Red Sea surface temperatures . . . . .	81
3.9. Conclusion and outlook . . . . .	83

<b>4. A compositional perspective on multivariate extremes</b>	<b>86</b>
4.1. Motivation . . . . .	86
4.2. Compositional data analysis . . . . .	87
4.2.1. Compositions and the Aitchison geometry . . . . .	87
4.2.2. Connections between CoDA and multivariate extremes . . . . .	89
4.2.3. Comparison of the Euclidean and Aitchison distances . . . . .	89
4.3. Compositional PCA for extremes . . . . .	90
4.3.1. Motivation . . . . .	90
4.3.2. Methodology . . . . .	91
4.3.3. Simulation experiments . . . . .	95
4.4. Compositional classification for extremes . . . . .	105
4.4.1. Motivation and framework . . . . .	105
4.4.2. Compositional classifiers and the $\alpha$ -metric . . . . .	106
4.4.3. Simulation experiments . . . . .	108
4.5. Discussion and outlook . . . . .	111
<b>5. EVA (2023) Data Challenge</b>	<b>114</b>
5.1. Preliminaries . . . . .	114
5.2. Abstract . . . . .	117
5.3. Introduction . . . . .	117
5.4. Univariate Challenges . . . . .	118
5.4.1. Data . . . . .	120
5.4.2. Challenge 1 . . . . .	120
5.4.3. Challenge 2 . . . . .	124
5.5. Multivariate Challenges . . . . .	129
5.5.1. Background . . . . .	130
5.5.2. Challenge 3 . . . . .	137
5.5.3. Challenge 4 . . . . .	140
5.6. Conclusion . . . . .	146
5.7. Data availability . . . . .	147

5.8. Acknowledgements . . . . .	148
5.9. Funding . . . . .	148
<b>6. Bias-corrected estimation of the TPDM</b>	<b>149</b>
6.1. Introduction and motivation . . . . .	149
6.2. Regularised TPDM estimators . . . . .	150
6.2.1. Thresholded TPDM estimators . . . . .	150
6.2.2. The Ledoit-Wolf TPDM estimator . . . . .	154
6.3. Selecting the regularisation parameter . . . . .	156
6.3.1. Frobenius risk minimisation . . . . .	156
6.3.2. The optimal Ledoit-Wolf shrinkage intensity . . . . .	158
6.3.3. Practical and statistical considerations . . . . .	160
6.4. Simulation experiments . . . . .	161
6.4.1. Symmetric logistic . . . . .	161
6.4.2. EVA (2023) Data Challenge 4 . . . . .	164
6.4.3. Extremal SAR model . . . . .	166
6.5. Conclusions and outlook . . . . .	169
<b>7. Conclusion</b>	<b>171</b>
7.1. Summary . . . . .	171
7.2. Future research ideas . . . . .	173
7.2.1. Change-point detection . . . . .	173
7.2.2. Incorporating covariate information . . . . .	174
7.2.3. TPDM based on sparse simplex projections . . . . .	175
<b>Appendices</b>	<b>178</b>
<b>A. Supplementary Material for Chapter 2</b>	<b>178</b>
A.1. Properties of the TPDM . . . . .	178
A.1.1. Equivalence of TPDM definitions . . . . .	178
A.1.2. Formula for the asymptotic variance $\nu_{ij}^2$ . . . . .	181

A.1.3. Proof of Proposition 2.6 . . . . .	181
A.1.4. Derivation of $V$ under the max-linear model . . . . .	182
A.2. PCA in general finite-dimensional Hilbert spaces . . . . .	183
A.3. Literature review: clustering with the TPDM . . . . .	186
<b>B. Supplementary Material for Chapter 3</b>	<b>189</b>
B.1. Overview of Drees (2023) . . . . .	189
B.2. Additional figures . . . . .	190
B.3. Effect of the bias of the empirical TPDM . . . . .	190
<b>C. Supplementary Material for Chapter 4</b>	<b>194</b>
<b>References</b>	<b>197</b>

# List of Figures

2.1.	Empirical estimates $\hat{\chi}_{12}(u)$ for bivariate symmetric logistic data. . . . .	27
2.2.	Dependence $\chi$ and $\sigma$ for symmetric logistic and Hüsler-Reiss models. . . . .	36
2.3.	Max-linear parameter matrix $A$ and the associated $\Sigma$ and $V$ . . . . .	45
2.4.	Empirical verification of asymptotic normality of $\hat{\sigma}$ . . . . .	46
2.5.	Bias of $\hat{\sigma}$ for symmetric logistic and Hüsler-Reiss models. . . . .	53
3.1.	$\Sigma(t)$ and $\Psi(t)$ for symmetric logistic model under two scenarios. . . . .	61
3.2.	Large sample Q-Q plots for the KS/CM p-values and test statistics. . . . .	72
3.3.	Empirical power against the dependence parameter $\vartheta_1$ . . . . .	75
3.4.	Empirical power against the sample size $n$ . . . . .	77
3.5.	Computation times as a function of $n$ , $k_{\text{total}}$ and $d$ . . . . .	78
3.6.	Max-linear parameter matrices with common $\Sigma$ and $V$ . . . . .	79
3.7.	Diagnostics: our test under a TPDM-invariant dependence change. . . . .	80
3.8.	Diagnostics: Drees' test under a TPDM-invariant dependence change. . . .	81
3.9.	Locations in the north/south sub-regions of the Red Sea. . . . .	82
3.10.	Empirical distribution of p-values for Red Sea data. . . . .	84
4.1.	The Euclidean/Aitchison distance between points on the simplex. . . . .	91
4.2.	Max-linear parameter matrices with compositionally colinear columns. . . .	96
4.3.	CoDA- and DS-PCA applied to trivariate max-linear data. . . . .	97
4.4.	PCA performance metrics for trivariate max-linear data ( $n = 5,000$ ). . . . .	99
4.5.	PCA performance metrics for 10-dimensional max-linear data. . . . .	100
4.6.	Dependence structure of the Hüsler-Reiss model parametrised by $\Lambda_4$ . . . . .	102

---

4.7.	CoDA- and DS-PCA applied to trivariate Hüsler-Reiss data. . . . .	102
4.8.	Aitchison reconstruction errors for the trivariate Hüsler-Reiss models. . . . .	103
4.9.	Estimates of $p_{\min}$ for the Hüsler-Reiss models. . . . .	104
4.10.	Labelled extremal angles from logistic-type models. . . . .	109
4.11.	Asymptotic classification risk $\mathcal{L}_\infty$ against the transformation parameter $\alpha$ . .	110
4.12.	KDE of the sampling distribution of $\hat{\alpha}$ . . . . .	112
5.1.	Challenge 1: elbow plot to select the number of clusters. . . . .	121
5.2.	Challenge 2: loss function for assessing quantile estimates. . . . .	124
5.3.	Challenge 2: GPD model survival curve and posterior estimates. . . . .	126
5.4.	Challenge 2: histogram of residuals of GPD scale and shape. . . . .	127
5.5.	Challenge 2: return level sample before and after shifting. . . . .	128
5.6.	Challenge 3: ternary plots of the empirical (sparse) extremal angles. . . . .	139
5.7.	Challenge 3: visual representations of $\hat{A}$ and $\hat{A}^*$ . . . . .	139
5.8.	Challenge 3: probability estimates against $k$ . . . . .	140
5.9.	Challenge 4: empirical TPDMs for the first and second clusters. . . . .	144
5.10.	Challenge 4: cluster/overall joint exceedance probability estimates. . . . .	145
6.1.	Popular thresholding operators $s_\lambda(x)$ with $\lambda = 0.1$ . . . . .	152
6.2.	Regularised TPDM estimates corresponding to the Red Sea data. . . . .	154
6.3.	Hard-thresholded TPDM eigenvalues corresponding to the Red Sea data. .	155
6.4.	Exploratory plots for the Ledoit-Wolf TPDM and symmetric logistic data. .	163
6.5.	Optimal/estimated Ledoit-Wolf shrinkage for symmetric logistic data. . .	164
6.6.	Shrinkage parameters $\hat{\Sigma}$ and $\tilde{\Sigma}$ for the EVA (2023) Data Challenge data. .	165
6.7.	$\hat{\lambda}^{(1)}, \dots, \hat{\lambda}^{(5)}$ for the EVA (2023) Data Challenge data. . . . .	166
6.8.	Comparison of probability estimates for the EVA (2023) Data Challenge. .	167
6.9.	Results: TPDM estimation for fitting extremal SAR models. . . . .	168
B.1.	Empirical power against the dependence parameter $\vartheta_1$ for selected $b$ and $k$ . .	190
B.2.	Diagnostics: our test with five northerly/southerly sites in the Red Sea. . .	192
B.3.	Diagnostics: our test with symmetric logistic data. . . . .	193

C.1. PCA performance metrics for trivariate max-linear data ( $n = 50,000$ ). . . . .	194
C.2. Estimates of $p_{\max}$ for the Hüsler-Reiss models. . . . .	195
C.3. Comparison of the empirical and asymptotic classification risks. . . . .	196

# List of Tables

3.1.	Asymptotic critical values for selected dimensions and significance levels. . .	69
3.2.	Empirical Type I error rates (%). All tests have nominal size 5% . . . . .	74
5.1.	EVA (2023) Data Challenge sub-challenge rankings and overall points. . .	115
5.2.	Summary statistics for the Challenge 4 clusters' empirical TPDMs. . . . .	144

# **Preface**

Draft thesis of Matthew Pawley, created on December 15, 2024.

# 1. Introduction

## 1.1. Motivation

Across many fields, decision makers face the problem of assessing and mitigating the risk associated with rare, extreme events. For instance, institutions seek accurate models of financial losses to design strategies to reduce their exposure, while an understanding of rare environmental phenomena, such as floods or hurricanes, guides the development of resilient defence infrastructure and public safety measures. Extreme value theory (EVT) provides a rigorous probabilistic framework for analysing the stochastic behaviour of such events. In particular, EVT is underpinned by asymptotic arguments that allow the probability law to be extrapolated beyond the maxima of the observed data. In principle, one can estimate the risk of unprecedented occurrences (i.e. events of a magnitude that has not been observed previously). Naively assuming that such events are impossible, as one might conclude from an empirical approach, could have catastrophic consequences. Equally, overestimating the probability of such events leads to an inefficient allocation of resources. Effective risk management therefore involves evaluating the trade-off between events' impacts and their probabilities. The latter aspect falls under the remit of EVT and, by extension, this thesis.

The concept of extremal dependence is central to assessing the risk of joint extreme events involving several different variables or interacting systems. In many practical scenarios, extreme events do not occur in isolation but are fundamentally interconnected. Simultaneous extreme rainfall across multiple regions can lead to compounded flood risks; the co-occurrence of extreme market crashes in different sectors can exacerbate market instability. Accounting for these associations is a critical element of risk modelling. For example,

suppose a fund manager oversees a portfolio of  $d$  stocks and let  $X_i$  denote the daily negative log-return of the  $i$ th stock for  $i = 1, \dots, d$ . The Value-at-Risk (VaR) is a popular tool for assessing the portfolio risk in terms of total losses over a one-day horizon, defined as the  $100(1 - \alpha)\%$  quantile of  $L = \sum_{i=1}^d w_i X_i$ , where  $w_i \in (0, 1]$  represents the relative weight of stock  $i$  in the portfolio and  $\alpha \in (0, 1)$  is a prescribed confidence level (Yuen and Stoev 2014b). If one assumes that extreme losses behave independently then the VaR figure might appear reassuringly small. However, financial crises or sudden macroeconomic shocks often cause simultaneous and correlated extreme losses across multiple stocks due to shared exposure to systemic risk factors and herd behaviour among investors. The dependence structure of  $(X_1, \dots, X_d)$  influences the quantile behaviour of  $L$  and consequently the Value-at-Risk. Portfolio diversification aims to alleviate this risk by balancing exposure across different asset classes and markets that are deemed to be less correlated.

Modelling extremal dependence becomes especially challenging when the number of variables under consideration is large. High-dimensional extremal dependence arises in applications such as environmental science, where a climatic variable is studied across multiple sites in a spatial domain. In such settings, the curse of dimensionality, the complexity of the dependence structure, and the inherent scarcity of relevant data points all impede efforts to model the probabilistic structure of the joint tail. Advancing methods to analyse extremal dependence in high dimensions is critical for addressing real-world, large-scale problems. This is the overarching goal of this thesis.

One particularly useful tool for understanding high-dimensional extremal dependence is the tail pairwise dependence matrix (TPDM) developed by Cooley and Thibaud (2019). The TPDM provides a compact summary of extremal dependence among pairs of variables by quantifying their joint tail behaviour, similar to a covariance/correlation matrix in non-extreme statistics. This facilitates exploratory analyses of dependence patterns and underpins a whole host of modern techniques for analysing multivariate extremes, including dimension reduction methods (Cooley and Thibaud 2019; Drees and Sabourin 2021; Fomichev and Ivanovs 2023; Richards et al. 2024) and inference for parametric models (Fix et al. 2021; Kiriliouk and Zhou 2022). By leveraging the TPDM, it becomes possible to develop efficient and scalable methods for modelling extremal dependence, thereby addressing the challenges posed by high-dimensional settings while maintaining computational feasibility.

This thesis proposes new applications of this matrix, growing the toolbox of TPDM-based techniques for analysing multivariate extremes.

## 1.2. Thesis aims and outline

The primary aim of this thesis is to develop novel statistical applications of the TPDM. Our strategy for identifying new applications is two-fold. First, we observe that the TPDM is useful for overcoming the curse of dimensionality and compactly summarising the dependence structure. Thus, we seek out opportunities where these properties might be exploited. Second, we draw on the fact that the TPDM may be cast as an analogue to the correlation/covariance matrix in non-extremes settings. The covariance matrix is ubiquitous in multivariate statistics, underpinning many powerful methods, such as principal components analysis and linear discriminant analysis. Thus, whenever one finds an application of the covariance matrix, one can consider whether an analogous method might make sense for the TPDM and extremes. The rest of this section outlines the structure of the thesis and summarises its key contributions.

Chapter 2 provides a detailed overview of univariate and multivariate extreme value statistics, before introducing the main protagonist of the thesis: the TPDM. We provide an overview of its mathematical properties, which will be called upon throughout the later chapters of the thesis. Next, we survey the TPDM-related literature, detailing its existing applications with a focus on principal components analysis and max-linear models. By acquainting the reader with these methods, we can build upon them in later chapters and highlight gaps they fail to address. Finally, we illustrate a known deficiency of the standard TPDM estimator, whereby it overestimates the dependence between weakly correlated variables. While the bias issue is not of direct interest until Chapter 6, issues stemming from it will be pointed out throughout the thesis.

Chapter 3 presents a statistical procedure to test for temporal non-stationarity in the extremal dependence structure of a (potentially high-dimensional) random vector indexed by time. This is motivated by the need to validate the ubiquitous assumption that extreme observations are identically distributed over time. We define a time-dependent extension of the TPDM and establish its basic properties. Next, we derive the asymptotic null

distribution of functionals of this object, which we use to test for deviations over time. In contrast to existing methods, our test scales to high dimensions and has a much lower computational overhead because it is rooted in the TPDM. The performance of the test across a range of scenarios is illustrated using simulation experiments. An application to Red Sea surface temperature data corroborates the theory that the region is undergoing changes driven by climate change.

Chapter 4 explores connections between multivariate extremes and compositional data analysis (CoDA). Observing that both disciplines boil down to analysing distributions on the simplex, we argue that off-the-shelf CoDA tools are an underutilised resource among the extremes community. Our simulation experiments show how compositional PCA may yield more efficient and interpretable dimension reduction compared to the TPDM-based method of Drees and Sabourin (2021). We also investigate the use of CoDA techniques for binary classification of extreme events (Jalalzai et al. 2018). Our results show that accounting for the geometry of the sample space (i.e. the simplex) can enhance predictive performance significantly.

Chapter 5 summarises the techniques employed by team ‘Uniofbathtopia’ as part of the data competition organised for the 13th International Conference on Extreme Value Analysis (EVA2023). The competition comprised four sub-challenges focussing on a multitude of aspects from univariate and multivariate EVT. Additional information and context are provided in Section 5.1 and in the editorial (Rohrbeck et al. 2023). Section 5.2 onwards are taken from the paper *Extreme value statistics for analysing simulated environmental extremes*, which I co-authored with H. Elsom and which details our methods for each sub-challenge. Section 5.4, researched and written by H. Elsom, pertains to the univariate sub-challenges (Challenges 1 and 2). Section 5.5 concerns the multivariate tasks (Challenges 3 and 4) and was researched and written by myself. In Challenge 3 (Section 5.5.2), we combine sparse simplex projections with a flexible parametric model to obtain probability estimates for joint extreme events involving different combinations of variables. Our methodology exhibits state-of-the-art performance, topping the rankings for this sub-challenge. For Challenge 4 (Section 5.5.3) we combine clustering and completely positive factorisations of the TPDM (Kiriliouk and Zhou 2022) to estimate exceedingly rare events in high dimensions. Our post-hoc analysis reveals that unreliable TPDM estimation hin-

dered our performance, prompting us to address this issue in the following chapter.

In Chapter 6 we consider ways of addressing a well-known bias of the empirical TPDM, whereby it tends to overestimate the dependence between weakly correlated variables. We employ regularisation methods such as thresholding and linear shrinkage to generate classes of flexible estimators. We devise the first data-driven method for selecting the regularisation parameter. Our estimator is illustrated using a series of simulated examples and may be readily incorporated into existing/future modelling frameworks.

The thesis concludes with a summary and discussion of future research directions in Chapter 7.

The code required to reproduce all the results contained in this thesis (including figures and tables) has been made available in a GitHub repository at <https://github.com/pawleymatthew/Extensions-And-Applications-of-TPDM>.

### 1.3. Notation

*E.g. vector raised to a power, vector of ones, zero vector, matrix ones, probability space.*

## 2. Background & literature review

This section provides a general overview of the key mathematical concepts and techniques underpinning the research in subsequent chapters. Section 2.1 presents a brief overview of univariate extreme value theory (EVT), describing how the distributional tail of a random variable can be extrapolated from large observations. Section 2.2 extends these concepts to the multivariate setting. We formally introduce the notion of extremal dependence and describe the framework of multivariate regular variation, in which all our work is set (Section 2.2.5). The remaining sections explore how the angular measure – a measure that characterises the extremal dependence structure (Section 2.2.3) – can be modelled parametrically (Section 2.2.4) or non-parametrically (Section 2.3.3). Finally, we introduce the key protagonist of this thesis, the tail pairwise dependence matrix (TPDM). Section 2.4 reviews its main theoretical properties; Section 2.5 is a survey of selected applications in the literature; Section 2.6 contains simulation experiments illustrating a deficiency of the standard TPDM estimator that is prevalent throughout the later chapters.

### 2.1. Univariate extreme value theory

This section introduces the fundamentals of EVT for univariate random variables. Although this thesis primarily focuses on multivariate EVT – the notion of extremal dependence is inherently multivariate – it is necessary to introduce some prerequisites from the univariate setting. Moreover, in multivariate analyses, univariate EVT is often utilised during pre-processing (Section 2.2.2). The theory presented herein largely follows Coles (2001); the reader is referred there for a more detailed treatment of this wide ranging topic.

### 2.1.1. Block maxima and the generalised extreme value (GEV) distribution

Let  $X_1, X_2, \dots$  be a sequence of independent, identically distributed, continuous random variables with distribution function  $F$ . For  $n \geq 1$ , define the random variable

$$M_n := \max(X_1, \dots, X_n) = \bigvee_{i=1}^n X_i. \quad (2.1)$$

The exact distribution of  $M_n$  is given by

$$\mathbb{P}(M_n \leq x) = \mathbb{P}(X_1 \leq x, \dots, X_n \leq x) = \prod_{i=1}^n \mathbb{P}(X_i \leq x) = F^n(x), \quad (x \in \mathbb{R}).$$

From a practical modelling perspective, this result is not particularly useful because  $F$  is typically unknown. Instead, we study the limiting behaviour of  $F^n$  as  $n \rightarrow \infty$ . Clearly the asymptotic distribution of  $M_n$  is degenerate, since  $M_n \xrightarrow{p} x_F := \sup\{x : F(x) < 1\}$ , the (possibly infinite) upper end-point of  $F$ . However, the Extremal Types Theorem states that, with suitable rescaling, there are three classes of non-degenerate asymptotic distribution (Coles 2001, Theorem 3.1).

**Theorem 2.1.** *Suppose there exist real sequences  $\{a_n > 0\}$  and  $\{b_n \in \mathbb{R}\}$  and a non-degenerate distribution function  $G$  such that*

$$\mathbb{P}\left(\frac{M_n - b_n}{a_n} \leq x\right) \rightarrow G(x), \quad (n \rightarrow \infty). \quad (2.2)$$

*Then  $G$  belongs to one of three parametric families: Gumbel, Fréchet or negative Weibull.*

When (2.2) holds, we say that  $F$  lies in the maximum domain of attraction (MDA) of  $G$ . The three families are unified by the Generalised Extreme Value (GEV) distribution with distribution function

$$G(x) = \exp\left\{-\left[1 + \xi \left(\frac{x - \mu}{\sigma}\right)\right]_+^{-1/\xi}\right\}, \quad (2.3)$$

where  $[x]_+ := \max(0, x)$  denotes the positive part of  $x$ . The parameters  $\mu \in \mathbb{R}$ ,  $\sigma > 0$  and  $\xi \in \mathbb{R}$  are called the location, scale, and shape, respectively. The sign of the shape parameter determines the sub-class that  $G$  belongs to:  $\xi > 0$  corresponds to the heavy-tailed Fréchet class,  $\xi = 0$  (with (2.2) interpreted as  $\xi \rightarrow 0$ ) corresponds the exponential-

tailed Gumbel class, and  $\xi < 0$  is the negative Weibull class, which has a finite upper limit.

The GEV distribution is used to model the upper tail of the distribution of  $X$  via the block maxima approach (Coles 2001, Section 3.3). Let  $x_1, \dots, x_n$  denote independent realisations of  $X_1, \dots, X_n$  and suppose these are partitioned into finite blocks of size  $m$ . Provided  $m$  is sufficiently large, Theorem 2.1 gives that the maximum observation in each block is approximately GEV distributed. Once the block-wise maxima have been extracted, estimates of the GEV parameters may be obtained, e.g. by maximum likelihood inference. The performance of the fitted model is sensitive to the choice of block size. Selection of the tuning parameter  $m$  requires managing a bias-variance trade-off. If the blocks are too small, then the underlying asymptotic approximation may not be valid and the maxima may not be representative of ‘extreme’ events, biasing the estimates. Taking larger blocks reduces the amount of data available for inference, resulting in a higher variance of the GEV parameter estimates.

### 2.1.2. Threshold exceedances and the generalised Pareto distribution (GPD)

The block maxima procedure is considered inefficient, because it fails to exploit all the available information. Each block is summarised by a (single) maximum value, even if it contains other ‘extreme’ events that might be informative for the tail. The intimately related peaks-over-threshold method makes better use of the available data (Coles 2001, Sections 4.2 and 4.3). If  $X$  is in the maximum domain of attraction of a  $\text{GEV}(\mu, \sigma, \xi)$  distribution, then

$$\lim_{u \rightarrow \infty} \mathbb{P}(X - u > x \mid X > u) = \left[ 1 + \frac{\xi x}{\tilde{\sigma}} \right]_+^{-1/\xi}, \quad (x > 0), \quad (2.4)$$

where  $\tilde{\sigma} = \sigma + \xi(u - \mu)$ . This limiting conditional distribution is called the generalised Pareto distribution (GPD), which describes the distribution of excesses over a high threshold. Given observations  $x_1, \dots, x_n$ , the peaks-over-threshold method assumes that exceedances of some pre-specified high threshold  $u > 0$  are approximately GPD distributed. Maximum likelihood or Bayesian inference procedures may be used to estimate the GPD parameters  $\tilde{\sigma}, \xi$ . Threshold selection is subject to similar considerations as for the block

size. Picking a low threshold risks model misspecification, causing bias in the fitted model. Choosing a high threshold directly reduces the number of threshold exceedances, increasing the uncertainty in the parameter estimates. Various diagnostics and procedures have been proposed to aid with this choice. Early approaches rely on inspecting diagnostic plots, such as mean residual life plots and parameter stability plots (Davison and Smith 1990). Automated selection procedures aim to remove subjectivity by optimising with respect to some criterion. These include change-point methods (Wadsworth 2016), cross-validation in a Bayesian framework (Northrop et al. 2017), and minimising expected quantile discrepancies (Murphy et al. 2024).

### 2.1.3. Non-stationary extremes

The block-maxima and peaks-over-threshold methods as presented above assume that the data are stationary over the observation period. In environmental applications, climate change threatens the validity of this assumption, with changes in the frequency and intensity of extreme weather events (Calvin et al. 2023). Non-stationary models accommodate such changes by allowing parameters to vary over time or in relation to covariates. For example, Vanem (2015) incorporates trends into the GEV location and scale parameters by specifying

$$\mu(t) = \mu_0 + \mu_1 t, \quad \sigma(t) = \exp(\sigma_0 + \sigma_1 t). \quad (2.5)$$

If the parameters  $\mu_1$  and/or  $\sigma_1$  are significantly different from zero, it suggests the data exhibit non-stationarity. In principle the shape parameter  $\xi$  may be extended analogously, but it is often assumed to be constant because it is notoriously difficult to estimate accurately and results (quantiles, return periods, etc.) are very sensitive to changes in its sign. The evGAM framework by Youngman (2019) provides a flexible extension to (2.5) using generative additive models (GAMs).

## 2.2. Multivariate extreme value theory

Multivariate extreme value theory (MEVT) generalises the study of extreme events from univariate to multivariate settings. Understanding the joint tail behaviour of several vari-

ables is critical in various fields. In environmental science, practitioners are tasked with assessing the risk of compound extreme events involving several variables. For example, the impact of drought – defined by the IPCC as a prolonged period of low precipitation (Calvin et al. 2023, p. 123) – is exacerbated by high temperatures. Similarly, extreme rainfall occurring simultaneously across multiple locations may lead to a widespread flood event. In finance, investors seek to diversify their portfolio to mitigate against the risk of simultaneous extreme losses across multiple assets. Each of these examples calls for an analysis of the joint tail distribution of a random vector.

### 2.2.1. Componentwise maxima

Consider a  $d$ -dimensional random vector  $\mathbf{X} = (X_1, \dots, X_d)$  with unknown joint distribution function  $F$ , meaning

$$F(\mathbf{x}) := \mathbb{P}(X_1 \leq x_1, \dots, X_d \leq x_d),$$

for any  $\mathbf{x} = (x_1, \dots, x_d) \in \mathbb{R}^d$ . Let  $\mathbf{X}_1, \mathbf{X}_2, \dots$  be a sequence of independent copies of  $\mathbf{X}$ . The notion of ‘extremes’ or a ‘maximum’ becomes subjective in the multivariate setting, because  $\mathbb{R}^d$  is not an ordered set. One possibility is to define the maximum in componentwise fashion as

$$\mathbf{M}_n := \left( \bigvee_{i=1}^n X_{i1}, \dots, \bigvee_{i=1}^n X_{id} \right).$$

We say that  $F$  lies in the multivariate MDA of a non-degenerate distribution  $G$  if there exist  $\mathbb{R}^d$ -valued sequences  $\{\mathbf{a}_n > \mathbf{0}\}$  and  $\{\mathbf{b}_n \in \mathbb{R}^d\}$  such that

$$\mathbb{P} \left( \frac{\mathbf{M}_n - \mathbf{b}_n}{\mathbf{a}_n} \leq \mathbf{x} \right) \xrightarrow{d} G(\mathbf{x}), \quad (n \rightarrow \infty). \quad (2.6)$$

Application of Theorem 2.1 to the marginal components implies that the margins of  $G$  follow a univariate GEV distribution. The crucial difference to the univariate setting is that now the limit (joint) distribution  $G$  sadly no longer admits a parametric representation. The problem of estimating/modelling  $G$  is usually split into two steps that are performed sequentially. First, one models the margins to describe the extreme behaviour of each

variable individually using univariate techniques. Then, one standardises to common margins and models the extremal dependence structure, i.e. the inter-relationships between extremes across multiple variables. Copula theory provides a rigorous justification for this two-step procedure.

### 2.2.2. Copulae and marginal standardisation

In multivariate statistics, Sklar's theorem (Sklar 1959) allows for the separation of the marginal distributions of variables from their joint dependence structure through the use of a copula. It states that any multivariate distribution can be expressed in terms of the individual marginal distributions and a copula that captures the dependence between them.

**Theorem 2.2.** *Suppose  $\mathbf{X} = (X_1, \dots, X_d)$  has joint distribution function  $F$  and continuous marginal distributions  $X_i \sim F_i$  for  $i = 1, \dots, d$ . Then there exists a unique copula  $C : [0, 1]^d \rightarrow [0, 1]$  such that*

$$F(x_1, \dots, x_d) = C(F_1(x_1), \dots, F_d(x_d)). \quad (2.7)$$

The copula  $C$  characterises the dependence structure of the variables, and represents the distribution function of  $\mathbf{X}$  after transforming to standard uniform margins. Uniform margins are a standard choice in multivariate statistics, but copulae may be defined with alternative marginal distributions. In MEVT, it is common to use Fréchet, exponential or Gumbel margins. The different choices accentuate particular features of the extreme values. For example, heavy-tailed Fréchet margins serve to highlight the most extreme values, while Gumbel or exponential margins are often favoured for conditional extremes modelling (Heffernan and Tawn 2004). Although the marginal distribution is an important modelling choice, ultimately all choices are valid/equivalent in the sense that monotonic transformations of the univariate marginals do not change the nature of tail dependence (Resnick 2007).

There are broadly two ways of performing the preliminary marginal standardisation. If the functions  $F_1, \dots, F_d$  are known, then the marginal distributions can be transformed to

some common target distribution  $F_\star$  via the probability integral transform:

$$X_i \mapsto F_\star^{-1}(F_i(X_i)) \sim F_\star, \quad (i = 1, \dots, d). \quad (2.8)$$

If the marginal distributions are unknown, as is usually the case, then  $F_1, \dots, F_d$  are replaced with estimates  $\hat{F}_1, \dots, \hat{F}_d$  in (2.8). A standard choice for  $\hat{F}_i$  is the empirical cumulative distribution function (non-parametric), perhaps with GPD tails above a high threshold (semi-parametric). Examples of these two approaches can be found in Russell and Hogan (2018) and Rohrbeck and Cooley (2023), respectively. Throughout this thesis, uncertainty arising from estimation of the marginal distributions shall be neglected. Relaxing this assumption, as in Clémenton et al. (2023), represents an avenue for future work.

### 2.2.3. The exponent measure and angular measure

Suppose  $\mathbf{X}$  is on unit Fréchet margins, that is

$$\mathbb{P}(X_i < x) = \exp(-1/x), \quad (x > 0), \quad (2.9)$$

for  $i = 1, \dots, d$ . This corresponds to a GEV distribution with  $\mu = \sigma = \xi = 1$ . The joint distribution  $G$  in (2.6) may be rewritten in the form

$$G(\mathbf{x}) = \exp(-V(\mathbf{x})), \quad (2.10)$$

where  $\mathbf{x} = (x_1, \dots, x_d)$  and  $x_i > 0$  for  $i = 1, \dots, d$ . The exponent measure  $V$  is a function of the form

$$V(\mathbf{x}) = d \int_{\mathbb{S}_{+(1)}^{d-1}} \bigvee_{i=1}^d \left( \frac{\theta_i}{x_i} \right) dH(\boldsymbol{\theta}), \quad (2.11)$$

where

$$\mathbb{S}_{+(p)}^{d-1} := \{\mathbf{x} \in \mathbb{R}_+^d : \|\mathbf{x}\|_p = 1\} \quad (2.12)$$

denotes the  $L_p$ -simplex in the non-negative orthant

$$\mathbb{R}_+^d := \{\mathbf{x} \in \mathbb{R}^d : x_1, \dots, x_d \geq 0\}$$

of  $\mathbb{R}^d$  and the angular measure  $H$  is a probability measure on  $\mathbb{S}_{+(1)}^{d-1}$  satisfying the moment constraints

$$\int_{\mathbb{S}_{+(1)}^{d-1}} \theta_i dH(\boldsymbol{\theta}) = 1/d, \quad i = 1, \dots, d. \quad (2.13)$$

Our notation for the simplex is borrowed from Fix et al. (2021). The exponent  $d - 1$  highlights the fact that the simplex is a  $(d - 1)$ -dimensional set embedded in the  $d$ -dimensional space  $\mathbb{R}^d$ . The + and  $(p)$  in the subscript convey that the set is restricted to the non-negative orthant and is with respect to the  $L_p$ -norm. The constraints on  $H$  arise due to tail equivalence of the margins. Functions  $G$  satisfying (2.10)-(2.13) are called multivariate extreme value distributions. If  $V$  is differentiable, then the density  $h$  of  $H$  exists in the interior and on the low-dimensional boundaries of the simplex. The relation between  $V$  and  $h$  is given by

$$h\left(\frac{\mathbf{x}}{\|\mathbf{x}\|_1}\right) = -\frac{\|\mathbf{x}\|_1^{d+1}}{d} \frac{\partial^d}{\partial x_1 \cdots \partial x_d} V(\mathbf{x}). \quad (2.14)$$

Models for  $G$  are typically specified in terms of  $V$  or  $H$ . Crucially, the extremal dependence structure of  $\mathbf{X}$  is completely characterised by  $H$ : the angular measure determines  $V$  via (2.11) and subsequently  $G$  via (2.10). Modelling the angular measure now becomes our primary focus.

#### 2.2.4. Parametric multivariate extreme value models

The class of valid dependence structures is in direct correspondence to the infinite-dimensional class of valid measures  $H$ . The lack of a finite-dimensional representative class greatly hinders efforts to perform statistical inference: efficient estimation via likelihood inference, hypothesis testing, and inclusion of covariates all become unavailable.

Of course, we may revert to the parametric paradigm by postulating a suitable parametric sub-family. Ideally the chosen sub-family generates a wide class of valid dependence structures. A detailed review of popular models can be found in Gudendorf and Segers (2010). There are several drawbacks to this approach. First, working with a parametric model instead of the general class runs the risk of model misspecification. Second, generating valid models is a challenging endeavour due to the moment constraints, resulting in models that are either overly simplistic or have unwieldy distribution functions and parameter constraints. Third, striking a balance between flexibility and parsimony becomes especially

tricky in high dimensions (i.e. when  $d$  is large). For these reasons, parametric models are not a primary focus of this thesis. Nevertheless, we now review a small selection of models. These primarily feature as data-generating processes for our numerical experiments. The R package `mev` provides functionality for generating independent observations  $\mathbf{x}_1, \dots, \mathbf{x}_n$  of  $\mathbf{X}$  or  $\boldsymbol{\theta}_1, \dots, \boldsymbol{\theta}_n \sim H$  based on the sampling algorithms formulated in Dombry et al. (2016).

#### 2.2.4.1. Logistic-type models

One of the earliest and simplest multivariate extreme value models is the symmetric logistic distribution (Gumbel 1960).

**Definition 2.1.** The exponent measure of a random vector  $\mathbf{X} = (X_1, \dots, X_d)$  following the symmetric logistic distribution is

$$V(\mathbf{x}) = \left( \sum_{i=1}^d x_i^{-1/\gamma} \right)^\gamma, \quad \gamma \in (0, 1]. \quad (2.15)$$

The single dependence parameter  $\gamma \in (0, 1]$  characterises the strength of the association between all variables. Independence occurs when  $\gamma = 1$  and the variables approach complete dependence as  $\gamma \rightarrow 0$ . All variables are exchangeable, since the distribution function is invariant under coordinate permutation. A flexible extension is the asymmetric logistic model of Tawn (1990). Greater control over the dependence structure is achieved by increasing the number of parameters.

**Definition 2.2.** The exponent measure of a random vector  $\mathbf{X} = (X_1, \dots, X_d)$  following the asymmetric logistic distribution is

$$V(\mathbf{x}) = \sum_{\beta \in \mathcal{P}(\{1, \dots, d\}) \setminus \emptyset} \left[ \sum_{i \in \beta} \left( \frac{\theta_{i,\beta}}{x_i} \right)^{1/\gamma_\beta} \right]^{\gamma_\beta}, \quad \begin{cases} \gamma_\beta \in (0, 1], \\ \theta_{i,\beta} \in [0, 1], & \text{if } i \in \beta, \\ \theta_{i,\beta} = 0, & \text{if } i \notin \beta, \\ \sum_{\beta \in \mathcal{P}(\{1, \dots, d\}) \setminus \emptyset} \theta_{i,\beta} = 1, \end{cases} \quad (2.16)$$

where  $\mathcal{P}(\{1, \dots, d\}) \setminus \emptyset$  denotes the set of non-empty subsets of  $\{1, \dots, d\}$ .

The set of parameters  $\{\gamma_\beta : \beta \in \mathcal{P}(\{1, \dots, d\}) \setminus \emptyset\}$  controls the dependence strength among the corresponding variables  $\{X_i : i \in \beta\}$  in a similar way to the symmetric logistic model. The model's complexity arises from the set of asymmetry parameters  $\boldsymbol{\theta}_\beta = \{\theta_{i,\beta} : i \in \beta\}$ , which dictates the direction/composition of extreme events involving the variables  $\{X_i : i \in \beta\}$ . Related models are generated by inverting the logistic and asymmetric models, resulting in the negative symmetric logistic (Galambos 1975) and negative asymmetric logistic models (Joe 1990), respectively. Other logistic-type models include the bilogistic (Smith et al. 1990) and negative bilogistic (Coles and Tawn 1994) distributions.

#### 2.2.4.2. The Brown-Resnick process and Hüsler-Reiss distribution

The Brown-Resnick process of Brown and Resnick (1977) is a class of stochastic processes commonly used to model the extremal dependence structure of spatial phenomena, including rainfall (Davison et al. 2012), snow depths (Schellander and Hell 2018) and wind gusts (Oesting et al. 2017). It is naturally defined through a transformation of a Gaussian process – a formal construction can be found in Kabluchko et al. (2009). Let  $\Omega \subset \mathbb{R}^2$  be a spatial domain. Consider a Brown-Resnick process  $\{X(\mathbf{s}) : \mathbf{s} \in \Omega\}$  with semi-variogram

$$\gamma(\mathbf{s}, \mathbf{s}') = (\|\mathbf{s} - \mathbf{s}'\|_2 / \rho)^\kappa, \quad \rho > 0, \kappa \in (0, 2]. \quad (2.17)$$

Semi-variograms of this form are called fractal semi-variograms and the associated process  $\{X(\mathbf{s}) : \mathbf{s} \in \Omega\}$  is stationary and isotropic (Engelke et al. 2015). Stationarity and isotropy mean that the statistical properties of the spatial process are invariant under translation and rotation. Specifically, the dependence between two sites only depends on the distance between them, not the direction or their position within the spatial domain. The parameters  $\rho$  and  $\kappa$  in (2.17) are termed the range and smoothness, respectively. The range parameter determines how quickly the dependence strength decreases over distance, while the smoothness parameter governs the regularity of the process and affects its local behaviour.

Let  $\mathbf{s}_i, \mathbf{s}_j \in \Omega$  be a pair of spatial locations and define random variables  $X_i = X(\mathbf{s}_i)$  and

$X_j = X(\mathbf{s}_j)$ . The exponent measure of the bivariate random vector  $(X_i, X_j)$  is

$$V(x_i, x_j) = \frac{1}{x_i} \Phi \left( \frac{a_{ij}}{2} + \frac{1}{a_{ij}} \log \frac{x_j}{x_i} \right) + \frac{1}{x_j} \Phi \left( \frac{a_{ij}}{2} + \frac{1}{a_{ij}} \log \frac{x_i}{x_j} \right), \quad (2.18)$$

where  $a_{ij} = \sqrt{\gamma(\mathbf{s}_i, \mathbf{s}_j)}$  (Huser and Davison 2013). The stationary/isotropic nature of the underlying process is apparent because  $V$  depends on  $\mathbf{s}_i$  and  $\mathbf{s}_j$  only through  $\|\mathbf{s}_i - \mathbf{s}_j\|_2$ .

The Brown-Resnick process is intimately related to the Hüsler-Reiss distribution of Hüsler and Reiss (1989). The Hüsler-Reiss distribution is of fundamental importance in multivariate extremes, fulfilling “a similar role as Gaussian distributions in the non-extreme world” (Engelke and Hitz 2019). In  $d \geq 2$  dimensions the distribution is parametrised by a matrix  $\Lambda = (\lambda_{ij}^2)_{1 \leq i,j \leq d}$  belonging to the class of symmetric, strictly conditionally negative definite matrices

$$\mathcal{M}_{\text{SND}} := \left\{ M \in \mathbb{R}_+^{d \times d} : M = M^T, \text{diag}(M) = \mathbf{0}, \mathbf{x}^T M \mathbf{x} < 0 \forall \mathbf{x} \in \mathbb{R}^d \setminus \{\mathbf{0}\} \text{ such that } \sum_{j=1}^d x_j = 0 \right\}.$$

The class of Hüsler-Reiss distributions is closed in the sense that if  $\mathbf{X} = (X_1, \dots, X_d)$  follows a Hüsler-Reiss distribution with parameter matrix  $\Lambda$ , then any random sub-vector  $(X_i, X_j)$  is also Hüsler-Reiss distributed with parameter  $\lambda_{ij}^2$ . This permits very flexible control over the pairwise dependence structure. The dependence between any pair of variables  $X_i$  and  $X_j$  can be adjusted by modifying the corresponding parameter  $\lambda_{ij}$ , subject to the constraint  $\Lambda \in \mathcal{M}_{\text{SND}}$ . The finite-dimensional distribution of a Brown-Resnick process at locations  $\mathbf{s}_1, \dots, \mathbf{s}_d$  is precisely the Hüsler-Reiss distribution with  $\Lambda = (\gamma(\mathbf{s}_i, \mathbf{s}_j)/4)_{1 \leq i,j \leq d}$  (Engelke et al. 2015). Due to this link, the exponent measure of  $(X_i, X_j)$  is given by (2.18) with  $a_{ij}$  replaced by  $2\lambda_{ij}$ .

#### 2.2.4.3. The max-linear model

The final parametric model we consider is the max-linear (factor) model, a simple but flexible class possessing important theoretical properties (Einmahl et al. 2012; Fougères et al. 2013; Yuen and Stoev 2014a). Any discrete angular measure concentrating on finitely many points corresponds to a max-linear model (Yuen and Stoev 2014a). Due to its flexibility and theoretical properties, the max-linear model has enjoyed widespread use

across several areas of extremes, including clustering (Janßen and Wan 2020; Avella-Medina et al. 2024), graphical modelling for causal inference (Gissibl et al. 2020; Gissibl and Klüppelberg 2018; Tran et al. 2021) and tail event probability estimation (Kiriliouk and Zhou 2022). In future sections/chapters, the max-linear model will be applied in more general settings where the marginal distributions are Fréchet with shape parameter  $\alpha \geq 1$  and the angular measure is defined with respect to the  $L_\alpha$ -norm on  $\mathbb{R}^d$ . In anticipation of this, we define the max-linear model in this more general setting.

**Definition 2.3.** Let  $A = (\mathbf{a}_1, \dots, \mathbf{a}_q) \in \mathbb{R}_+^{d \times q}$  for some  $q \geq 1$ . Assume that  $\mathbf{a}_j \neq \mathbf{0}$  for all  $j = 1, \dots, q$  and each row has unit  $L_\alpha$ -norm, i.e.  $\sum_{j=1}^q a_{ij}^\alpha = 1$  for  $i = 1, \dots, d$ . A random vector  $\mathbf{X} = (X_1, \dots, X_d)$  with discrete probability angular measure

$$H(\cdot) = \frac{1}{\sum_{j=1}^q \|\mathbf{a}_j\|_\alpha^\alpha} \sum_{j=1}^q \|\mathbf{a}_j\|_\alpha^\alpha \delta_{\mathbf{a}_j / \|\mathbf{a}_j\|_\alpha}(\cdot) \quad (2.19)$$

is said to follow the max-linear model with parameter matrix  $A$ .

The row-wise unit-norm constraint on  $A$  ensures the marginal components are Fréchet distributed with unit scale and shape  $\alpha$ . Setting  $\alpha = 1$ , we see that (2.19) is a valid angular measure: for any  $i = 1, \dots, d$ ,

$$\int_{\mathbb{S}_{+(1)}^{d-1}} \theta_i dH(\boldsymbol{\theta}) = \frac{1}{\sum_{j=1}^q \|\mathbf{a}_j\|_1} \sum_{j=1}^q \int_{\mathbb{S}_{+(1)}^{d-1}} \theta_i \|\mathbf{a}_j\|_1 \delta_{\mathbf{a}_j / \|\mathbf{a}_j\|_1}(\boldsymbol{\theta}) d\boldsymbol{\theta} = \frac{\sum_{j=1}^q a_{ij}}{\sum_{i=1}^d \sum_{j=1}^q a_{ij}} = \frac{1}{d}.$$

The number of free parameters is  $d \times (q - 1)$  and the order of the columns of  $A$  is inconsequential. The factors  $\mathbf{a}_1, \dots, \mathbf{a}_q$  correspond to the possible directions that extremal observations may take, with the column norms  $\|\mathbf{a}_1\|_\alpha, \dots, \|\mathbf{a}_q\|_\alpha$  determining the respective weights assigned to these directions. There is a direct correspondence between the class of discrete angular measures placing mass on  $q < \infty$  points and the class of max-linear random vectors with  $q$  factors (Yuen and Stoev 2014a). Moreover, the class of angular measures (2.19) is dense in the class of valid angular measures (Fougères et al. 2013). In other words, any extremal dependence structure can be arbitrarily well-approximated by that of a max-linear model with sufficiently many factors. This makes max-linear modelling a versatile and powerful framework, despite its simplicity.

There are several ways to construct a random vector  $\mathbf{X} = (X_1, \dots, X_d)$  with angular

measure (2.19). This thesis employs two constructions. Letting  $Z_1, \dots, Z_q$  be independent Fréchet random variables with unit scale and shape parameter  $\alpha$  and  $\mathbf{Z} = (Z_1, \dots, Z_q)$ , these are

$$\mathbf{X} = A \times_{\max} \mathbf{Z} := \left( \bigvee_{j=1}^q a_{1j} Z_j, \dots, \bigvee_{j=1}^q a_{dj} Z_j \right) \quad (2.20)$$

and

$$\mathbf{X} = A \otimes \mathbf{Z} := \bigoplus_{j=1}^q (\mathbf{a}_j \odot Z_j). \quad (2.21)$$

Adopting the terminology of Cooley and Thibaud (2019), we refer to these as the max-stable and transformed-linear constructions, respectively. Under the max-stable construction, each component  $X_i$  is the maximum of linear combinations of the heavy-tailed latent variables  $Z_1, \dots, Z_q$ . The second construction is defined in terms of transformed-linear vector space operations  $\oplus$  and  $\odot$  defined by Cooley and Thibaud (2019). These operations will be defined explicitly and discussed later in Section 2.5.1. The difference between the two constructions manifests in their realisations, as illustrated in Figure 7 in the Supplementary Material of Cooley and Thibaud (2019). The directions of large realisations of the max-stable construction tend to correspond almost exactly to the points  $\mathbf{a}_1/\|\mathbf{a}_1\|_\alpha, \dots, \mathbf{a}_q/\|\mathbf{a}_q\|_\alpha$ . Under the transformed-linear construction, the directions of extreme events tend to lie in a neighbourhood of, but not exactly on, these discrete locations.

Computing joint tail event probabilities is straightforward under the max-linear model. Suppose  $\mathbf{X}$  is max-linear with parameter matrix  $A$ . Consider the extreme failure region

$$\mathcal{R}_f(x) := \{\mathbf{y} \in \mathbb{R}_+^d : f(\mathbf{y}) > x\}$$

for some function  $f : \mathbb{R}_+^d \rightarrow \mathbb{R}$ . Provided the failure region is sufficiently extreme (i.e. distant from the origin), then

$$\mathbb{P}(\mathbf{X} \in \mathcal{R}_f(x)) \approx \sum_{j=1}^q \frac{\|\mathbf{a}_j\|_\alpha^\alpha}{r_*(\mathbf{a}_j/\|\mathbf{a}_j\|_\alpha)^\alpha}, \quad (2.22)$$

where  $r_* = r_*(\boldsymbol{\theta})$  is such that  $f(r_* \boldsymbol{\theta}) = x$  (Cooley and Thibaud 2019; Kiriliouk and Zhou

2022). The formulae corresponding to some popular failure regions are listed below:

$$\begin{aligned} f(\mathbf{y}) &= \max \mathbf{y}, & \mathbb{P}(\max \mathbf{X} > x) &\approx \sum_{j=1}^q \max_{i=1,\dots,d} \left( \frac{a_{ij}}{x} \right)^\alpha \\ f(\mathbf{y}) &= \min \mathbf{y}, & \mathbb{P}(\min \mathbf{X} > x) &\approx \sum_{j=1}^q \min_{i=1,\dots,d} \left( \frac{a_{ij}}{x} \right)^\alpha \\ f(\mathbf{y}) &= \mathbf{v}^T \mathbf{y}, & \mathbb{P}(\mathbf{v}^T \mathbf{X} > x) &\approx \sum_{j=1}^q \left( \frac{\mathbf{v}^T \mathbf{a}_j}{x} \right). \end{aligned}$$

The first and second regions concern extreme events affecting at least one variable or all variables simultaneously, respectively. For the third region, the weight vector  $\mathbf{v}$  satisfies  $v_i \geq 0$  and  $v_1 + \dots + v_d = 1$ . Such regions are of interest for climate event attribution (Kiriliouk and Naveau 2020) or quantifying the Value-at-Risk of an asset portfolio (Yuen and Stoev 2014b). Each of these failure probabilities may be perceived as a measure of risk. Risk mitigation is the practice of taking action – bolstering flood defences or diversifying a portfolio – to ensure these probabilities are acceptably small.

### 2.2.5. Multivariate regular variation

Multivariate regular variation (MRV) provides an alternative framework for characterising the probabilistic structure of the joint tail of random vectors. By imposing a regularity structure on the joint tail, MRV facilitates the development of theoretically justified procedures for extrapolating the probability law from moderately large values to more extreme tail regions. We introduce the concept of regular variation in the univariate setting before extending to the multivariate case.

**Definition 2.4.** A function  $f : \mathbb{R}_+ \rightarrow \mathbb{R}_+$  is regularly varying with index  $\alpha \in \mathbb{R}$  if, for all  $x > 0$ ,

$$\lim_{t \rightarrow \infty} \frac{f(tx)}{f(t)} = x^\alpha. \quad (2.23)$$

If  $\alpha = 0$ , then  $f$  is called slowly-varying. Intuitively, a regularly varying function is one that behaves like a power function as the argument approaches infinity. This notion is generalised to random variables by taking the distributional tail as the function of interest.

**Definition 2.5.** A non-negative random variable  $X$  is regularly varying with tail index  $\alpha \geq 0$  if the right-tail of its distribution function is regularly varying with index  $-\alpha$ , i.e. for all  $x > 1$ ,

$$\lim_{t \rightarrow \infty} \mathbb{P}(X > tx \mid X > t) = x^{-\alpha}.$$

If  $X$  is regularly varying with index  $\alpha$ , then its survivor function is of the form

$$\mathbb{P}(X > x) = x^{-\alpha} L(x) \tag{2.24}$$

for some slowly-varying function  $L$  (Jessen and Mikosch 2006). Regularly varying random variables are those with power law tails. In fact, a random variable  $X$  is regularly varying if and only if it belongs to the Fréchet MDA (Mikosch and Wintenberger 2024, Section 3.2.4.4). Crucially, (2.24) reveals that regularly varying distributions possess asymptotic scale invariance, in the sense that for all  $\lambda > 0$ ,

$$\mathbb{P}(X > \lambda x) = (\lambda x)^{-\alpha} L(\lambda x) \sim \lambda^{-\alpha} \mathbb{P}(X > x).$$

The ubiquity of regular variation in extreme value statistics is due to this homogeneity property. Under regular variation, the probability law of  $X$  at some level  $\lambda x$  is identical to the probability law at level  $x$ , up to some constant factor. An analogous interpretation holds when regular variation is generalised to multivariate random vectors, where the joint tail distribution is represented by a homogeneous limit measure.

Although MRV can be formulated more generally – see Section 6.5.5 in Resnick (2007) – we exclusively focus on random vectors  $\mathbf{X}$  taking values on the positive orthant  $\mathbb{R}_+^d := [0, \infty)^d$ . This common assumption is not as restrictive as it might initially seem. In most applications, the risk being assessed is directional. For example, a climatologist might model the lows or the highs of precipitation records depending on whether they are analysing drought risk or flood risk. Without loss of generality and by means of a transformation if necessary, this direction of interest can be defined as ‘positive’. The two equivalent definitions below express the MRV property in terms of vague convergence to some limiting measure. Similar to univariate regular variation (Definition 2.5), the salient property of these limit measures is their power law behaviour.

**Definition 2.6.** A random vector  $\mathbf{X} = (X_1, \dots, X_d)$  is multivariate regularly varying with tail index  $\alpha > 0$ , denoted  $\mathbf{X} \in \mathcal{RV}_+^d(\alpha)$ , if it satisfies the following (equivalent) statements (Resnick 2007):

1. There exists a sequence  $b_n \rightarrow \infty$  and a non-negative Radon measure  $\nu$  on  $\mathbb{E}_0 := [0, \infty]^d \setminus \{\mathbf{0}\}$  such that

$$n\mathbb{P}(b_n^{-1}\mathbf{X} \in \cdot) \xrightarrow{\text{v}} \nu(\cdot), \quad (n \rightarrow \infty), \quad (2.25)$$

where  $\xrightarrow{\text{v}}$  denotes vague convergence in the space of non-negative Radon measures on  $\mathbb{E}_0$ . The exponent measure  $\nu$  is homogeneous of order  $-\alpha$ , that is, for any  $s > 0$ ,

$$\nu(s \cdot) = s^{-\alpha} \nu(\cdot). \quad (2.26)$$

2. Let  $\|\cdot\|$  be an arbitrary norm on  $\mathbb{R}^d$ . Denote the radial and angular components of  $\mathbf{X}$  by  $R := \|\mathbf{X}\|$  and  $\Theta := \mathbf{X}/\|\mathbf{X}\|$ . Then there exists a sequence  $b_n \rightarrow \infty$  and a finite measure  $H$  on the simplex

$$\mathbb{S}_+^{d-1} := \{\mathbf{x} \in \mathbb{R}_+^d : \|\mathbf{x}\| = 1\} \quad (2.27)$$

such that

$$n\mathbb{P}((b_n^{-1}R, \Theta) \in \cdot) \xrightarrow{\text{v}} \nu_\alpha \times H(\cdot), \quad (n \rightarrow \infty), \quad (2.28)$$

in the space of non-negative Radon measures on  $(0, \infty] \times \mathbb{S}_+^{d-1}$ , where  $\nu_\alpha((x, \infty)) = x^{-\alpha}$  for any  $x > 0$ .

The limit measures  $\nu$  and  $H$  in (2.25) and (2.28) are related via

$$\nu(\{\mathbf{x} \in \mathbb{E}_0 : \|\mathbf{x}\| > s, \mathbf{x}/\|\mathbf{x}\| \in \cdot\}) = s^{-\alpha} H(\cdot), \quad \nu(dr \times d\Theta) = \alpha r^{-\alpha-1} dr dH(\Theta). \quad (2.29)$$

The attractive feature of MRV is best represented by its pseudo-polar formulation (2.28). This states that the extremal behaviour of  $\mathbf{X}$  is fully characterised by two quantities: the tail index and the angular measure. The tail index  $\alpha$  represents the index of regular variation of the (univariate) radial component. It governs the heavy-tailedness of the size (norm) of  $\mathbf{X}$ . The angular measure  $H$  fully characterises the dependence structure.

Crucially, the right-hand side of (2.28) is a product measure, signifying that the radial and angular components are independent in the limit.

The MRV property implicitly requires that the marginal components  $X_1, \dots, X_d$  are heavy-tailed with a shared tail index. Standard practice is to standardise the margins prior to modelling the dependence structure (Section 2.2.2), so this is not restrictive. In this thesis, we will always choose Fréchet margins with unit scale and shape parameter  $\alpha > 0$ , that is

$$\mathbb{P}(X_i < x) = \exp(-x^{-\alpha}), \quad (x > 0). \quad (2.30)$$

An MRV random vector on  $\alpha$ -Fréchet margins (2.30) has tail index  $\alpha$ . Thus, as before, fixing the margins deals with the tail index and the angular measure becomes the object of interest.

The angular measure is unique only with respect to a pre-specified norm  $\|\cdot\|$  and lies on the corresponding unit simplex (2.27). As mentioned previously, we exclusively choose the  $L_p$ -norm

$$\|\cdot\|_p : \mathbb{R}^d \rightarrow \mathbb{R}, \quad \|\mathbf{x}\|_p = \left( \sum_{i=1}^d x_i^p \right)^{1/p} \quad (2.31)$$

with (2.12) the corresponding simplex. The mass of the angular measure is  $m := H(\mathbb{S}_+^{d-1}) \in (0, \infty)$ . The sequence  $\{b_n\}$  and the quantity  $m$  are jointly determined by (2.28). Replacing  $\{b_n\}$  by  $\{sb_n\}$  for some  $s > 0$  yields a new angular measure  $H' = s^{-\alpha}H$  whose mass is  $m' = s^{-\alpha}m$ . We are free to choose whether the scaling information is contained in  $\{b_n\}$  or  $m$ . Possible reasons for preferring one over the other are discussed in Fougères et al. (2013), but ultimately it is an arbitrary modelling choice. In previous sections,  $H$  was normalised to be a probability measure with  $m = 1$ . Henceforth, we will tend to specify  $\{b_n\}$  and push the scaling information onto  $H$ . With  $\mathbf{X}$  standardised to  $\alpha$ -Fréchet margins, the centre of mass of  $H$  must lie in the simplex interior:

$$\int_{\mathbb{S}_+^{d-1}} \theta_i dH(\boldsymbol{\theta}) = \mu > 0, \quad (i = 1, \dots, d). \quad (2.32)$$

Were this not the case it would imply that at least one variable can never be extreme, contradicting the assumption that all variables have equally heavy tails. The value of  $\mu$  depends on the choice of norm and the mass of  $H$ . If  $\|\cdot\| = \|\cdot\|_1$ , then  $\mu = m/d$  in

accordance with (2.13). If  $\|\cdot\| = \|\cdot\|_2$ , then  $m/d \leq \mu \leq m/\sqrt{d}$  according to Lemma 2.1 in Fomichov and Ivanovs (2023). The lower and upper bounds are attained when  $H$  places all its mass at the vertices of the simplex or at its centre, respectively. These can be understood as the limiting cases of extremal dependence, which is formalised in the next section.

## 2.2.6. Extremal dependence measures

The extremal dependence structure of a random vector  $\mathbf{X}$  can be quantified and classified using a plethora of summary measures (Coles et al. 1999). We focus on the tail dependence coefficient and the extremal dependence measure.

### 2.2.6.1. The tail dependence coefficient

Extremal dependence is analogous to, but separate from, the notion of statistical dependence in non-extreme statistics. In particular, two random processes might appear independent in the bulk of the distribution but exhibit dependence in their extremes, or vice versa. The extremal dependence structure may be very complex; angular measures form an infinite-dimensional class subject only to a set of moment constraints. For example, suppose  $X_i$  and  $X_j$  represent the recorded values of a meteorological variable measured at two spatial locations. The extremal dependence between  $X_i$  and  $X_j$  may depend on the spatial proximity of the sites, the topography of the spatial domain, the physics of the climatological process, and a multitude of other factors. The complexity grows as more variables are introduced, as higher-order dependencies come into play. Extremal dependence measures aim to provide summary information about particular aspects of the dependence structure. One such measure is the tail dependence coefficient.

**Definition 2.7.** Let  $\mathbf{X} = (X_1, \dots, X_d)$  with  $X_i \sim F_i$  for  $i = 1, \dots, d$ . Let  $\beta \subseteq \{1, \dots, d\}$  with  $|\beta| \geq 2$  and define  $\mathbf{X}_\beta := \{X_i : i \in \beta\}$ . The tail dependence coefficient associated with  $\beta$  is (Simpson et al. 2020)

$$\chi_\beta = \lim_{u \rightarrow 1} \chi_\beta(u) = \lim_{u \rightarrow 1} \frac{\mathbb{P}(F_i(X_i) > u : i \in \beta)}{1 - u}. \quad (2.33)$$

When  $\beta = \{i, j\}$  for  $i \neq j$ , we write  $\chi_\beta =: \chi_{ij}$ .

We say that  $X_i$  and  $X_j$  are asymptotically independent (AI) if and only if  $\chi_{ij} = 0$ . Asymptotic independence means that both variables cannot take extreme values simultaneously. If  $\chi_{ij} \in (0, 1]$ , then the variables are asymptotically dependent (AD) and may be simultaneously extreme. The interpretation of  $\chi_\beta$  for  $|\beta| > 2$  is more subtle. If  $\chi_\beta \in (0, 1]$ , then all components of  $\mathbf{X}_\beta$  may be simultaneously large. If  $\chi_\beta = 0$ , then the corresponding variables may not be concomitantly extreme, but this does not preclude the possibility that  $\chi_{\beta'} > 0$  for some  $\beta' \subset \beta$  with  $|\beta'| \geq 2$ .

Whether a particular tail dependence coefficient is zero or non-zero is determined by which subspaces of the simplex are charged with  $H$ -mass. Specifically,  $\chi_\beta > 0$  if and only if there exists  $\beta' \supseteq \beta$  such that

$$H(\{\boldsymbol{\theta} \in \mathbb{S}_+^{d-1} : \theta_i > 0 \iff i \in \beta'\}) > 0. \quad (2.34)$$

For example, consider the angular measures

$$H^{(1)} = \frac{m}{d} \sum_{i=1}^d \delta_{\mathbf{e}_i}, \quad H^{(2)} = m \delta_{\mathbf{1}_d / \|\mathbf{1}_d\|}, \quad (2.35)$$

where  $\mathbf{e}_1, \dots, \mathbf{e}_d$  denote the canonical basis vectors of  $\mathbb{R}^d$ . The measure  $H^{(1)}$  places all its mass on the vertices of the simplex. This corresponds to full asymptotic independence, since then  $\chi_\beta = 0$  for all  $\beta \subseteq \{1, \dots, d\}$  with cardinality at least equal to two. The angular measure  $H^{(2)}$  concentrates at a single point at the centre of the simplex. This implies that  $\chi_{\{1, \dots, d\}} > 0$  and consequently  $\chi_\beta > 0$  for all subsets  $\beta$ .

If the bivariate exponent measure  $V_{ij}$  of  $(X_i, X_j)$  is known, then the tail dependence coefficient  $\chi_{ij}$  may be computed using the relation  $\chi_{ij} = 2 - V_{ij}(1, 1)$  (Coles et al. 1999). The following examples illustrate this for selected parametric models.

**Example 2.1.** Let  $\mathbf{X} = (X_1, \dots, X_d)$  be symmetric logistic distributed with dependence parameter  $\gamma \in (0, 1]$ . For any  $i \neq j$ , let  $V_{ij}$  denote the bivariate exponent measure of  $(X_i, X_j)$ . Then

$$\chi_{ij} = 2 - V_{ij}(1, 1) = 2 - \left[ \left( x_i^{-1/\gamma} + x_j^{-1/\gamma} \right)^\gamma \right] = 2 - 2^\gamma.$$

Therefore  $X_i$  and  $X_j$  are asymptotically independent when  $\gamma = 1$  and approach complete asymptotic dependence as  $\gamma \rightarrow 0$ .

**Example 2.2.** Let  $\mathbf{X} = (X_1, \dots, X_d)$  be Hüsler-Reiss distributed with parameter matrix  $\Lambda = (\lambda_{ij}^2)$ . For any  $i \neq j$ , let  $V_{ij}$  denote the bivariate exponent measure of  $(X_i, X_j)$ . Then

$$\chi_{ij} = 2 - V_{ij}(1, 1) = 2 - 2\Phi\left(\lambda_{ij} + \frac{1}{2\lambda_{ij}} \log 1\right) = 2 - 2\Phi(\lambda_{ij}),$$

where  $\Phi$  is the standard normal distribution function. Variables  $X_i$  and  $X_j$  are asymptotically dependent for all  $\lambda_{ij} > 0$ , with asymptotic independence in the limit as  $\lambda_{ij} \rightarrow \infty$ .

**Example 2.3.** Suppose  $\mathbf{X} = (X_1, \dots, X_d)$  is max-linear with parameter matrix  $A \in \mathbb{R}_+^{d \times q}$ . Substituting (2.19) into (2.11) yields

$$\chi_{ij} = 2 - V_{12}(1, 1) = 2 - 2 \int_{\mathbb{S}_{+(1)}^1} (\theta_1 \vee \theta_2) dH(\boldsymbol{\theta}) = 2 - \sum_{l=1}^q (a_{il} \vee a_{jl}). \quad (2.36)$$

Consider two max-linear random vectors with discrete angular measures  $H^{(1)}$  and  $H^{(2)}$  as in (2.35). The parameter matrices are given by

$$A^{(1)} = I_d \in \mathbb{R}_+^{d \times d}, \quad A^{(2)} = \mathbf{1}_d \in \mathbb{R}_+^{d \times 1}.$$

The tail dependence coefficients under these models are

$$\chi_{ij}^{(1)} = 2 - \sum_{j=1}^2 \max(0, 1) = 0, \quad \chi_{ij}^{(2)} = 2 - \sum_{j=1}^1 \max(1, 1) = 1,$$

corresponding to complete dependence and asymptotic dependence, as expected.

Estimates of  $\chi_{ij}$  are obtained by estimating  $\hat{\chi}_{ij}(u)$  at a sequence of high quantiles  $u$  approaching one. The `taildep` function in the R package `extRemes` achieves this using the estimator given in (2.62) in Reiss and Thomas (2007) and produces a diagnostic plot as shown in Figure 2.1. For this example the data were generated from a symmetric logistic model with  $\gamma = 0.5$ . The horizontal dashed line indicates the true value  $\chi_{ij} = 2 - \sqrt{2} \approx 0.59$ , while the blue points represent the estimates  $\hat{\chi}_{ij}(u)$  over the range  $0.8 \leq u \leq 0.995$ . The shaded region depicts the 95% Wald confidence interval. We encounter a bias-variance

trade-off in relation to quantile/threshold, similar in nature to that described in Section 2.1 with respect to the selecting the block size/threshold.

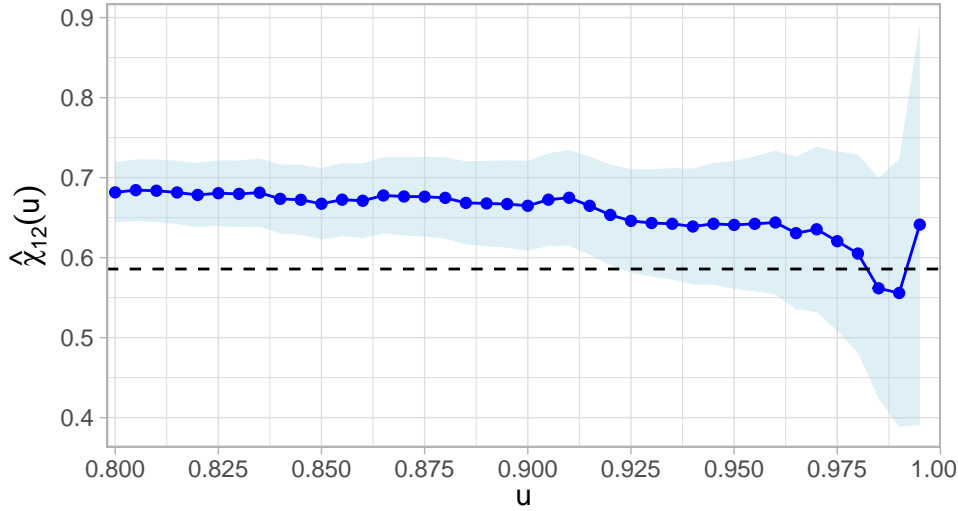


Figure 2.1.: Empirical estimates  $\hat{\chi}_{12}(u)$  of the tail dependence coefficient for bivariate symmetric logistic data with  $\gamma = 0.5$  and  $n = 5,000$  observations. The true coefficient  $\chi_{12} = 2 - 2^\gamma \approx 0.59$  is marked by the dashed line. The shaded region represents the 95% Wald confidence interval.

Estimation of  $\chi_\beta$  for  $|\beta| > 2$  is more complicated and is related to the task of determining the support of the angular measure (Goix et al. 2017; Meyer and Wintenberger 2023; Simpson et al. 2020). This thesis primarily concerns dependence at the pairwise level, so we direct the reader to the aforementioned papers and the review in Engelke and Ivanovs (2021) for further details.

Let  $\chi = (\chi_{ij})$  denote the Tail Dependence Matrix (TDM) of bivariate tail dependence coefficients with diagonal entries  $\chi_{ii} := 1$ . The TDM provides a high level summary of the extremal dependence structure. It has been applied for exploratory analysis (Huang et al. 2019) and considered as a tool for clustering (Fomichov and Ivanovs 2023). Shyamalkumar and Tao (2020) conjecture that the ‘realisation problem’ – determining whether a given matrix is a valid TDM – is NP-complete; this was recently proved by Janßen et al. (2023). By establishing a correspondence between the class of TDMs and a metric space, Janßen et al. (2023) also show that, in certain cases, higher order tail-dependence is fully determined by the bivariate TDM. Section 2.4 introduces a similar (and almost identically named) matrix, the Tail *Pairwise* Dependence Matrix (TPDM), which is the eponym of this thesis. Rather than the tail dependence coefficient  $\chi_{ij}$ , the TPDM is founded on an alternative

bivariate summary measure called the Extremal Dependence Measure (EDM).

### 2.2.6.2. Extremal dependence measure

The extremal dependence measure (EDM) is a pairwise summary measure similar to  $\chi_{ij}$ . It was originally proposed by Resnick (2004) and later generalised by Larsson and Resnick (2012).

**Definition 2.8.** Let  $\mathbf{X} \in \mathcal{RV}_+^d(\alpha)$  with angular measure  $H$ . The EDM between  $X_i$  and  $X_j$  is

$$\text{EDM}_{ij} := \int_{\mathbb{S}_+^{d-1}} \theta_i \theta_j dH(\boldsymbol{\theta}). \quad (2.37)$$

The EDM depends on the choice of norm via the angular measure, but Larsson and Resnick (2012) show that EDMs under different norms are equivalent in a certain sense. The EDM was originally defined by Resnick (2004) for bivariate random vectors  $\mathbf{X} = (X_1, X_2)$ . In their definition, the integrand is

$$\left(\frac{4}{\pi}\right)^2 \arctan\left(\frac{\theta_2}{\theta_1}\right) \left[\frac{\pi}{2} - \arctan\left(\frac{\theta_2}{\theta_1}\right)\right] \quad (2.38)$$

rather than  $\theta_1 \theta_2$ . The original and refined versions are also equivalent.

Being explicitly defined in terms of the angular measure, the EDM's interpretation in terms of AD/AI is straightforward. Recall from (2.34) that variables  $X_i$  and  $X_j$  are asymptotically independent if and only if  $H(\{\boldsymbol{\theta} : \theta_i, \theta_j > 0\}) = 0$ . Then

$$\chi_{ij} = 0 \iff \int_{\{\boldsymbol{\theta} \in \mathbb{S}_+^{d-1} : \theta_i, \theta_j > 0\}} \theta_i \theta_j dH(\boldsymbol{\theta}) = 0 \iff \text{EDM}_{ij} = 0.$$

The EDM is maximal when  $X_i$  and  $X_j$  are perfectly asymptotically dependent. The maximal value depends on the choice of norm and the mass of the angular measure. When  $d = 2$  and  $\|\cdot\| = \|\cdot\|_p$  we have  $\text{EDM}_{ij} \leq 2^{-2/p}m$  with equality if and only if  $H$  places all its mass at the simplex barycentre, that is  $H(\{(2^{-1/p}, 2^{-1/p})\}) = m$ . We return to the EDM in Section 2.4 when introducing the tail pairwise dependence matrix.

## 2.3. Inference

We now shift our attention to the topic of (non-parametric) inference in multivariate extremes. The general approach entails using the angular components of large observations to learn a model for  $H$ . This strategy is justified by the MRV assumption: (2.28) implies that

$$\Theta \mid (R > t) \xrightarrow{d} H(\cdot), \quad (t \rightarrow \infty). \quad (2.39)$$

The angular measure is the limiting distribution of the angles of exceedances of some radial threshold. By analogy to the peaks-over-threshold approach (Section 2.1.2), it suggests itself to base inference on the subset of data points whose norm exceeds some high, fixed threshold. Increasing the threshold reduces the number of observations that enter into the estimators, and vice versa. It is generally more convenient to specify the desired number of threshold exceedances, denoted  $k$ , and set the threshold accordingly. This approach is most conveniently described using order statistics.

### 2.3.1. Framework and notation

Consider a  $d$ -dimensional MRV random vector  $\mathbf{X} \in \mathcal{RV}_+^d(\alpha)$ . Let  $\mathbf{X}_1, \mathbf{X}_2, \dots$  denote a sequence of independent copies of  $\mathbf{X}$  and fix a norm  $\|\cdot\|$  on  $\mathbb{R}^d$ . For  $i \geq 1$ , denote by

$$R_i := \|\mathbf{X}_i\|, \quad \Theta_i := (\Theta_{i1}, \dots, \Theta_{id}) = \frac{\mathbf{X}_i}{\|\mathbf{X}_i\|}, \quad (2.40)$$

the radial and angular components of  $\mathbf{X}_i$  with respect to the chosen norm. Assume that the distribution of  $\|\mathbf{X}\|$  is continuous. Then for any  $n \geq 1$ , there exists a permutation  $\pi : \{1, \dots, n\} \rightarrow \{1, \dots, n\}$  such that

$$\|\mathbf{X}_{(1),n}\| > \|\mathbf{X}_{(2),n}\| > \dots > \|\mathbf{X}_{(n),n}\|,$$

where  $\mathbf{X}_{(i),n} := \mathbf{X}_{\pi(i)}$  for  $i = 1, \dots, n$ . The random variable  $\|\mathbf{X}_{(j),n}\|$  is called the  $j$ th (upper) order statistic of  $\{\|\mathbf{X}_i\| : i = 1, \dots, n\}$ . Henceforth, we suppress the dependence on  $n$  in our order statistic notation. Let the radial and angular components of  $\mathbf{X}_{(i)}$  be

denoted by

$$R_{(i)} = \|\mathbf{X}_{(i)}\|, \quad \Theta_{(i)} = (\Theta_{(i),1}, \dots, \Theta_{(i),d}) = \frac{\mathbf{X}_{(i)}}{\|\mathbf{X}_{(i)}\|}. \quad (2.41)$$

Performing inference based on the  $k = k(n)$  largest observations is equivalent to performing inference based on the set of observations whose norm exceeds the threshold  $t = R_{(k+1)}$ .

### 2.3.2. Selecting the radial threshold or the number of exceedances

All estimators will require us to choose the number of extreme observations  $k$  that enter into them. In theoretical analyses, it is customary to choose the sequence  $\{k(n) : n \geq 1\}$  such that

$$\lim_{n \rightarrow \infty} k(n) = \infty, \quad \lim_{n \rightarrow \infty} \frac{k(n)}{n} = 0. \quad (2.42)$$

These arise as sufficient conditions for proving various asymptotic properties (e.g. consistency, asymptotic normality) of estimators. The condition  $k \rightarrow \infty$  ensures that the number of extremes – the effective sample size – grows arbitrarily large. The second condition  $k/n \rightarrow 0$  requires that the proportion of threshold exceedances becomes vanishingly small, ensuring that inference is targeting the tail. In practice,  $n$  is fixed and selecting  $k$  requires striking a balance between these two aspects. Choosing  $k$  too small reduces the amount of available information and leads to unnecessarily high uncertainty. If  $k$  is too large, we risk using data that does not reflect the extremal dependence structure, leading to bias. An appropriate choice depends on both the sample size and the underlying distribution of  $\mathbf{X}$ . If the convergence in (2.39) is rapid, then a low threshold may be adequate. Several threshold selection procedures have been proposed in univariate extremes (Section 2.1), but the literature on radial threshold selection is comparatively scant. By combining two sub-tests regarding (i) independence of the radial and angular components and (ii) regular variation of the radial component, Einmahl et al. (2020) devise a formal procedure testing the validity of the MRV assumption. They suggest choosing the threshold by examining a plot of the sequence of p-values against  $k$ . The support-detection algorithm of Meyer and Wintenberger (2023) chooses  $k$  automatically via minimisation of a penalised log-likelihood. This procedure is specific to their setting and relies on additional technical assumptions. Most applied studies use a rule-of-thumb approach and/or produce a threshold stability plot checking the (in)sensitivity of some quantity to the choice of  $k$  – see Jiang et al. (2020),

Szemkus and Friederichs (2024) and Russell and Hogan (2018) for examples.

### 2.3.3. The empirical angular measure

Once the tuning parameter  $k$  has been chosen, attention turns towards the extremal angles  $\Theta_{(1)}, \dots, \Theta_{(k)}$ . In view of (2.39), the empirical distribution of  $\Theta_{(1)}, \dots, \Theta_{(k)}$  is the natural non-parametric estimator for the angular measure.

**Definition 2.9.** The empirical angular measure based on  $\mathbf{X}_1, \dots, \mathbf{X}_n$  is the random measure on  $\mathbb{S}_+^{d-1}$  defined as

$$\hat{H}(\cdot) := \frac{m}{k} \sum_{i=1}^n \delta_{\Theta_i}(\cdot) \mathbf{1}\{R_i > R_{(k+1)}\} = \frac{m}{k} \sum_{i=1}^k \delta_{\Theta_{(i)}}(\cdot). \quad (2.43)$$

Note that  $\hat{H}$  does not enforce the moment constraints (2.13), so is not necessarily a valid angular measure. Einmahl and Segers (2009) construct an alternative non-parametric estimator that does enforce these restrictions, but it is limited to the bivariate setting. Proposition 3.3 in Janßen and Wan (2020) establishes consistency  $\hat{H} \xrightarrow{p} H$  of the empirical angular measure provided the level  $k$  satisfies the rate conditions (2.42). Their result holds for general norms in arbitrary dimensions. Clémençon et al. (2023) conduct a non-asymptotic (i.e. finite sample) analysis of  $\hat{H}$ , establishing high-probability bounds on the worst-case estimation error  $\sup_{A \in \mathcal{A}} |H(A) - \hat{H}(A)|$  over classes  $\mathcal{A}$  of Borel subsets on  $\mathbb{S}_+^{d-1}$ . Their results hold with  $\|\cdot\| = \|\cdot\|_p$  for  $p \in [1, \infty]$ . Since  $\hat{H}$  is a discrete measure concentrating at  $k$  points, there exists a max-linear random vector  $\mathbf{X}$  with parameter matrix

$$\hat{A} := \left(\frac{m}{k}\right)^{1/\alpha} (\Theta_{(1)}, \dots, \Theta_{(k)}) \in \mathbb{R}_+^{d \times k}. \quad (2.44)$$

whose angular measure is  $\hat{H}$ . Estimates of tail event probabilities under the empirical model  $\hat{H}$  may then be computed using the formula (2.22).

### 2.3.4. Non-parametric estimators

Larsson and Resnick (2012) remark that analysing extremal dependence often involves quantities of the form

$$\mathbb{E}_H[f(\boldsymbol{\Theta})] := \int_{\mathbb{S}^{d-1}_+} f(\boldsymbol{\theta}) dH(\boldsymbol{\theta}) = \mathbb{E}_{m^{-1}H}[mf(\boldsymbol{\Theta})], \quad (2.45)$$

where  $f : \mathbb{S}^{d-1}_+ \rightarrow \mathbb{R}$ . We have already seen an example of this in Definition 2.8: the EDM between  $X_i$  and  $X_j$  is defined as (2.45) with  $f(\boldsymbol{\theta}) = \theta_i \theta_j$ . We reiterate that in our notation, the expectation is with respect to a measure  $H$  that is not necessarily normalised. When manipulating expectations/variances, the following relations may be useful to bear in mind:

$$\begin{aligned} \mathbb{E}_H[f(\boldsymbol{\Theta})] &= \mathbb{E}_{m^{-1}H}[mf(\boldsymbol{\Theta})] = m\mathbb{E}_{m^{-1}H}[f(\boldsymbol{\Theta})] \\ \text{Var}_H[f(\boldsymbol{\Theta})] &= \mathbb{E}_{m^{-1}H}[m^2 f(\boldsymbol{\Theta})^2] - \mathbb{E}_{m^{-1}H}[mf(\boldsymbol{\Theta})]^2 = m^2 \text{Var}_{m^{-1}H}[f(\boldsymbol{\Theta})]. \end{aligned}$$

Klüppelberg and Krali (2021) opt to normalise  $H$  and absorb  $m$  into  $f$ . For example, the EDM would correspond to  $f(\boldsymbol{\theta}) = m\theta_i \theta_j$  in their notation. Suppressing the normalising constant arguably results in less cumbersome notation, but in any case the choice is purely stylistic.

To construct non-parametric estimators of quantities (2.45), Klüppelberg and Krali (2021) replace  $H$  with the empirical angular measure  $\hat{H}$ , yielding

$$\hat{\mathbb{E}}_H[f(\boldsymbol{\Theta})] := \mathbb{E}_{\hat{H}}[f(\boldsymbol{\Theta})] = \int_{\mathbb{S}^{d-1}_+} f(\boldsymbol{\theta}) d\hat{H}(\boldsymbol{\theta}) = \frac{m}{k} \sum_{i=1}^k f(\boldsymbol{\Theta}_{(i)}). \quad (2.46)$$

The authors further prove asymptotic normality of these estimators by generalising a result in Larsson and Resnick (2012).

**Theorem 2.3.** *Let  $f : \mathbb{S}^{d-1}_+ \rightarrow \mathbb{R}$  be continuous and assume  $k$  satisfies the rate conditions (2.42). Moreover, suppose that*

$$\lim_{n \rightarrow \infty} \sqrt{k} \left[ \frac{n}{k} \mathbb{E}[f(\boldsymbol{\Theta}_1) \mathbf{1}\{R_1 \geq b_{\lfloor n/k \rfloor} t^{-1/\alpha}\}] - \mathbb{E}_H[f(\boldsymbol{\Theta})] \frac{n}{k} \bar{F}_R(b_{\lfloor n/k \rfloor} t^{-1/\alpha}) \right] = 0 \quad (2.47)$$

holds locally uniformly for  $t \in [0, \infty)$ , where  $\bar{F}_R(\cdot) = \mathbb{P}(R > \cdot)$  denotes the survivor function of  $R$ . Finally, assume that

$$\nu^2 := \text{Var}_H(f(\Theta)) > 0. \quad (2.48)$$

Then

$$\sqrt{k} [\hat{\mathbb{E}}_H[f(\Theta)] - \mathbb{E}_H[f(\Theta)]] \rightarrow N(0, \nu^2), \quad (n \rightarrow \infty). \quad (2.49)$$

The rate condition (2.47) requires that the dependence between the radius and angle decays sufficiently quickly. This condition is non-observable and must be assumed.

**Example 2.4.** Let  $\mathbf{X}_1, \dots, \mathbf{X}_n$  be independent copies of  $\mathbf{X} \in \mathcal{RV}_+^d(\alpha)$ . The estimator for the EDM between  $X_i$  and  $X_j$  is

$$\widehat{\text{EDM}}_{ij} := \hat{\mathbb{E}}_H[\Theta_i \Theta_j] = \frac{m}{k} \sum_{l=1}^k \Theta_{(l),i} \Theta_{(l),j}.$$

Under the conditions of Theorem 2.3,

$$\sqrt{k} [\widehat{\text{EDM}}_{ij} - \text{EDM}_{ij}] \rightarrow N(0, \nu_{ij}^2), \quad \nu_{ij}^2 = \text{Var}_H(\Theta_i \Theta_j).$$

## 2.4. Tail pairwise dependence matrix (TPDM)

This section introduces the key protagonist of this thesis: the tail pairwise dependence matrix (TPDM). We define the TPDM and review its key properties. In doing so, we create a repository of results about the TPDM to exploit and refer back to throughout the thesis.

### 2.4.1. Definition and examples

Inspired by Larsson and Resnick (2012), Cooley and Thibaud (2019) leverage the EDM to form a matrix of pairwise dependence measures.

**Definition 2.10.** Let  $\mathbf{X} \in \mathcal{RV}_+^d(2)$  with normalising sequence  $b_n = n^{1/2}$ . Let  $H$  denote the angular measure with respect to  $\|\cdot\|_2$ . The TPDM of  $\mathbf{X}$  is the  $d \times d$  matrix

$$\Sigma = (\sigma_{ij}), \quad \sigma_{ij} = \int_{\mathbb{S}_{+(2)}^{d-1}} \theta_i \theta_j \, dH(\boldsymbol{\theta}) = \mathbb{E}_H[\Theta_i \Theta_j]. \quad (2.50)$$

The TPDM is essentially a matrix of EDMs subject to additional restrictions on the tail index, normalising sequence, and norm. Each off-diagonal entry  $\sigma_{ij}$  may be interpreted as summarising the dependence between  $X_i$  and  $X_j$ , with  $\sigma_{ij} = 0$  if and only if the corresponding variables are asymptotically independent. The original definition was later generalised by Kiriliouk and Zhou (2022) to permit general  $\alpha$ .

**Definition 2.11.** For  $\alpha \geq 1$ , let  $\mathbf{X} \in \mathcal{RV}_+^d(\alpha)$  with normalising sequence  $b_n = n^{1/\alpha}$ . Let  $H$  denote the angular measure with respect to  $\|\cdot\|_\alpha$ . The TPDM of  $\mathbf{X}$  is the  $d \times d$  matrix

$$\Sigma = (\sigma_{ij}), \quad \sigma_{ij} = \int_{\mathbb{S}_{+(\alpha)}^{d-1}} \theta_i^{\alpha/2} \theta_j^{\alpha/2} \, dH(\boldsymbol{\theta}) = \mathbb{E}_H[\Theta_i^{\alpha/2} \Theta_j^{\alpha/2}]. \quad (2.51)$$

The tail index of  $\mathbf{X}$  is now arbitrary, but the normalisation sequence and norm are still required to conform with this index. Kiriliouk and Zhou (2022) provide no direct rationale for why (2.51) is the natural generalisation of (2.50); in Section A.1.1 we present a series of results about this. After generalising a result in Fix et al. (2021) (Lemma A.1), we prove that the TPDM is invariant to the choice of  $\alpha$  (Proposition A.1), culminating in an expression for its entries given in terms of the  $L_1$  angular density (A.2). Now, using this formula and the angular densities in Semadeni (2020), we are able to compute the TPDM under the symmetric logistic and Hüsler-Reiss models. These will be especially useful in Chapter 6 for evaluating the performance of TPDM estimators.

**Example 2.5.** Suppose  $\mathbf{X} = (X_1, \dots, X_d) \in \mathcal{RV}_+^d(\alpha)$  follows the symmetric logistic distribution with dependence parameter  $\gamma \in (0, 1)$ . For any  $i \neq j$ ,

$$\sigma_{ij} = \frac{1-\gamma}{\gamma} \int_0^1 [u(1-u)]^{\frac{1}{\gamma}-\frac{3}{2}} [(1-u)^{1/\gamma} + u^{1/\gamma}]^{\gamma-2} \, du. \quad (2.52)$$

**Example 2.6.** Suppose  $\mathbf{X} = (X_1, \dots, X_d) \in \mathcal{RV}_+^d(\alpha)$  follows the Hüsler-Reiss distribution with parameter matrix  $\Lambda = (\lambda_{ij}^2)$ . For any  $i \neq j$ ,

$$\sigma_{ij} = \int_0^1 \frac{\exp(-\lambda_{ij}/4)}{2\lambda_{ij}u(1-u)} \phi\left(\frac{1}{2\lambda_{ij}} \log\left(\frac{u}{1-u}\right)\right) du. \quad (2.53)$$

The blue lines in Figure 2.2 plot (2.52) and (2.53) against the model parameter. For comparison, we also include the tail dependence coefficients (red lines) computed using Example 2.1 and Example 2.2. For both models, the strength of association is a decreasing function of the model parameter, with complete dependence (resp. asymptotic independence) as the parameter approaches zero (resp. its upper limit). For the Hüsler-Reiss distribution, dependence is very weak beyond  $\lambda \approx 3$ . We can check that this is correct by comparing with Figure 1 in the Supplementary Material of Cooley and Thibaud (2019). The figure reveals that for a Brown-Resnick process with semi-variogram (2.17) with range  $\rho = 2.4$  and smoothness  $\kappa = 1.8$ , dependence vanishes beyond a distance of approximately 12 units. Recall from Section 2.2.4.2 that the dependence between two sites  $h$  units apart under the Brown-Resnick model is equivalent to the dependence between two Hüsler-Reiss variables with dependence parameter  $\lambda_{ij} = \sqrt{2(h/\rho)^\kappa}/2$ . Setting  $h = 12$  gives  $\lambda_{ij} = \sqrt{2(12/2.4)^{1.8}}/2 \approx 3.01$ , corroborating the results of Figure 2.2. Further verification of our expressions are provided by the shaded regions in Figure 2.2. These represent the minimum/maximum values of 10 estimates of  $\chi_{ij}$  and  $\sigma_{ij}$  for a sequence of values of  $\gamma$  and  $\lambda$ . The estimates are obtained from large samples ( $n = 5 \times 10^5$ ) so it is reasonable to neglect the influence of estimation error. The empirical estimates agree with our calculations.

The angular measure of a max-linear random vector is discrete, so the angular density does not exist. Nevertheless, it is straightforward to compute the model TPDM directly from the definition (Cooley and Thibaud 2019; Kiriliouk and Zhou 2022). This connection between  $A$  and  $\Sigma$  will be exploited in various points throughout this thesis, e.g. Chapter 5 and Chapter 6.

**Example 2.7.** Suppose  $\mathbf{X} = (X_1, \dots, X_d) \in \mathcal{RV}_+^d(\alpha)$  is max-linear with parameter matrix

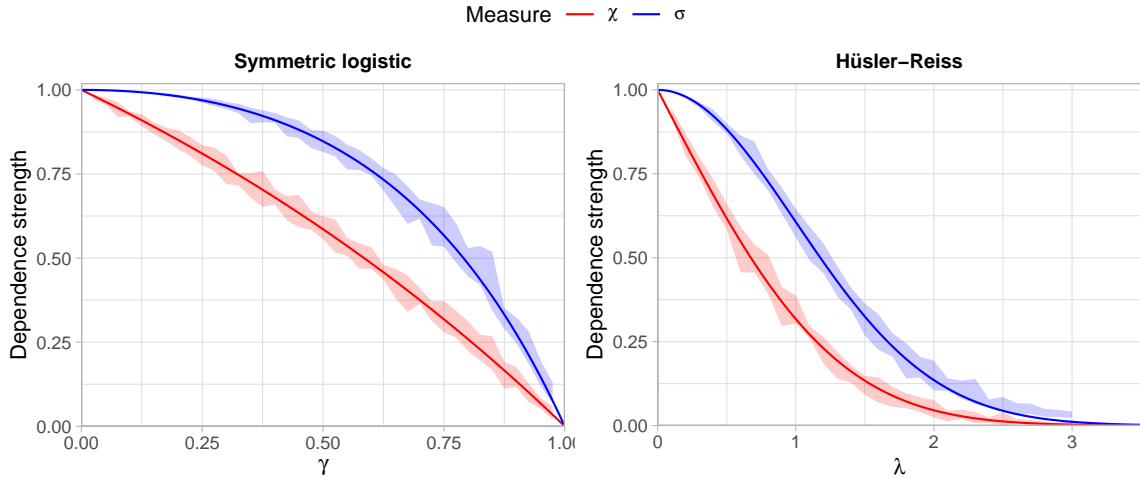


Figure 2.2.: True dependence strengths for the symmetric logistic (left) and Hüsler-Reiss (right) models, measured using the tail dependence coefficient (red line) and TPDM (blue line). The shaded regions represent the minimum/maximum values of empirical estimates over 10 repeated simulations using bivariate samples of size  $n = 5 \times 10^5$ .

A. Then for any  $i \neq j$ ,

$$\begin{aligned}\sigma_{ij} &= \int_{\mathbb{S}_{+(\alpha)}^{d-1}} \theta_i^{\alpha/2} \theta_j^{\alpha/2} dH(\boldsymbol{\theta}) \\ &= \sum_{l=1}^q \|\mathbf{a}_l\|_\alpha^\alpha \left( \frac{a_{li}}{\|\mathbf{a}_l\|_\alpha} \right)^{\alpha/2} \left( \frac{a_{lj}}{\|\mathbf{a}_l\|_\alpha} \right)^{\alpha/2} \\ &= \sum_{l=1}^q a_{il}^{\alpha/2} a_{jl}^{\alpha/2}.\end{aligned}$$

Therefore  $\Sigma = A^{\alpha/2}(A^{\alpha/2})^T$ . Taking  $A$  to be  $A^{(1)}$  and  $A^{(2)}$  as defined in Example 2.3, the corresponding TPDMs are

$$\Sigma^{(1)} = I_d I_d^T = I_d, \quad \Sigma^{(2)} = \mathbf{1}_d \mathbf{1}_d^T = J_d,$$

where  $J_d$  is the  $d \times d$  all-ones matrix. By construction, these represent the TPDMs under asymptotic dependence and complete dependence, respectively.

### 2.4.2. Interpretation of the TPDM entries

The definition of the TPDM

$$\Sigma = \mathbb{E}_H \left[ \Theta^{\alpha/2} (\Theta^{\alpha/2})^T \right], \quad (2.54)$$

bears a striking resemblance to the definition of a covariance matrix in the non-extreme setting. The covariance matrix represents the second-order (central) moment of a random vector. Its diagonal entries convey the scale (variance) of the components, while the off-diagonal entries summarise the strength of association (unnormalised correlation) between all pairs of variables. The TPDM entries offer analogous interpretations, except the notions of scale and association are adapted to refer to properties of the joint distributional tail.

**Definition 2.12.** Let  $\mathbf{X} \in \mathcal{RV}_+^d(\alpha)$  with normalisation sequence  $b_n$ . For  $i = 1, \dots, d$ , the scale of  $X_i$  is defined as (Klüppelberg and Krali 2021)

$$\text{scale}(X_i) = \left[ \int_{\mathbb{S}_{+}^{d-1}} \theta_i^\alpha dH(\boldsymbol{\theta}) \right]^{1/\alpha}.$$

As discussed earlier, a well-defined notion of scale must fix either the sequence  $b_n$  or the mass of the angular measure in advance. In the above definition, the normalisation sequence is fixed and scaling information is contained in  $H$ . The scale is so-called because it yields information about the scale of the marginal distributions. Using (2.29), one can show that

$$\begin{aligned} \lim_{n \rightarrow \infty} n\mathbb{P}(b_n^{-1} X_i > x) &= \int_{\mathbb{S}_{+}^{d-1}} \int_{x/\theta_i}^{\infty} \alpha r^{-\alpha-1} dr dH(\boldsymbol{\theta}) \\ &= \int_{\mathbb{S}_{+}^{d-1}} [r^{-\alpha}]_{\infty}^{x/\theta_i} dH(\boldsymbol{\theta}) \\ &= x^{-\alpha} [\text{scale}(X_i)]^\alpha, \end{aligned}$$

Moreover, it behaves like a measure of scale: for any  $c > 0$ ,

$$\begin{aligned}\text{scale}(cX_i) &= \left[ \frac{\lim_{n \rightarrow \infty} n\mathbb{P}(b_n^{-1}cX_i > x)}{x^{-\alpha}} \right]^{1/\alpha} \\ &= \left[ c^\alpha \frac{\lim_{n \rightarrow \infty} n\mathbb{P}(b_n^{-1}X_i > x/c)}{(x/c)^{-\alpha}} \right]^{1/\alpha} \\ &= c \cdot \text{scale}(X_i).\end{aligned}$$

Comparing Definition 2.12 against Definition 2.11, the diagonal entries of the TPDM are related to the marginal scales via  $\text{scale}(X_i) = \sigma_{ii}^{1/\alpha}$ . Consequently, if the marginal distributions are standardised to have unit scales, then all diagonal entries of the TPDM are equal to one. Moreover, when  $b_n = n^{1/\alpha}$  and  $\|\cdot\| = \|\cdot\|_\alpha$ , the mass of the angular measure relates to the marginal scales via

$$\sum_{i=1}^d \sigma_{ii} = \sum_{i=1}^d \int_{\mathbb{S}_{+(\alpha)}^{d-1}} \theta_i^\alpha dH(\boldsymbol{\theta}) = \int_{\mathbb{S}_{+(\alpha)}^{d-1}} \sum_{i=1}^d \theta_i^\alpha dH(\boldsymbol{\theta}) = \int_{\mathbb{S}_{+(\alpha)}^{d-1}} dH(\boldsymbol{\theta}) = m.$$

In this thesis, all random vectors will be pre-processed to be on  $\alpha$ -Fréchet margins and we take  $b_n = n^{1/\alpha}$ , so that

$$\begin{aligned}\sigma_{ii} &= \text{scale}(X_i)^\alpha \\ &= \frac{\lim_{n \rightarrow \infty} n\mathbb{P}(X_i > n^{1/\alpha}x)}{x^{-\alpha}} \\ &= \frac{\lim_{n \rightarrow \infty} n \left\{ 1 - \exp \left[ -(n^{1/\alpha}x)^{-\alpha} \right] \right\}}{x^{-\alpha}} \\ &= 1,\end{aligned}$$

and

$$m = \sum_{i=1}^d \sigma_{ii} = d.$$

Standardising the margins is akin to working with re-scaled variables with unit variance in the non-extremes setting. The appropriate analogue to the TPDM then becomes the correlation rather than covariance matrix.

As mentioned earlier, the TPDM's off-diagonal entries are simply pairwise EDMs. Thus the interpretation of  $\sigma_{ij}$  is inherited from the EDM:  $X_i$  and  $X_j$  are asymptotically independent

if and only if  $\sigma_{ij} = 0$ , and the magnitude of  $\sigma_{ij} > 0$  reveals the strength of tail dependence between  $X_i$  and  $X_j$ . Like a correlation matrix,  $\sigma_{ij}$  attains its maximal value ( $\sigma_{ij} = 1$ ) when  $X_i$  and  $X_j$  are completely dependent (Example 2.7).

### 2.4.3. Decompositions of the TPDM

The TPDM is useful as a summary statistic for quantifying pairwise dependencies, but what sets it apart from other pairwise dependence matrices (e.g. the TDM)? The TPDM admits two types of decomposition: eigendecomposition and the completely positive decomposition (Cooley and Thibaud 2019). These underpin the key statistical applications of the TPDM described in Section 2.5. The following results and proofs are reproduced from Kiriliouk and Zhou (2022).

**Proposition 2.1.** *The TPDM is symmetric and positive semi-definite.*

*Proof.* For any  $i, j = 1, \dots, d$ ,

$$\sigma_{ij} = \int_{\mathbb{S}_+^{d-1}} \theta_i^{\alpha/2} \theta_j^{\alpha/2} dH(\boldsymbol{\theta}) = \int_{\mathbb{S}_+^{d-1}} \theta_j^{\alpha/2} \theta_i^{\alpha/2} dH(\boldsymbol{\theta}) = \sigma_{ji}.$$

Hence  $\Sigma = \Sigma^T$ . For any  $\mathbf{y} \in \mathbb{R}^d \setminus \{\mathbf{0}\}$ ,

$$\mathbf{y}^T \Sigma \mathbf{y} = \mathbf{y}^T \mathbb{E}_H [\Theta^{\alpha/2} (\Theta^{\alpha/2})^T] \mathbf{y} = \mathbb{E}_H \left[ (\mathbf{y}^T \Theta^{\alpha/2})^2 \right] \geq 0. \quad \square$$

By standard linear algebra results, the TPDM can be decomposed as  $\Sigma = UDU^T$ , where  $D \in \mathbb{R}^{d \times d}$  is a diagonal matrix of eigenvalues  $\lambda_1 \geq \dots \geq \lambda_d \geq 0$  and  $U \in \mathbb{R}^{d \times d}$  is an orthogonal matrix whose columns are the corresponding eigenvectors  $\mathbf{u}_1, \dots, \mathbf{u}_d \in \mathbb{R}^d$ . The eigendecomposition potentially offers a low-rank representation of the TPDM expressed in terms of its eigenvalues and eigenvectors. In contrast, the completely positive decomposition represents the matrix as a product of a (potentially low-rank) non-negative matrix with its transpose.

**Definition 2.13.** A matrix  $M \in \mathbb{R}^{d \times d}$  is completely positive (CP) if there exists a matrix  $B \in \mathbb{R}_+^{d \times q}$  such that  $M = BB^T$ .

**Proposition 2.2.** *The TPDM is completely positive.*

*Proof.* Let  $\mathbf{X} \in \mathcal{RV}_+^d(\alpha)$  with angular measure  $H$  and TPDM  $\Sigma$ . By Proposition 5 in Fougères et al. (2013), there exists a sequence of matrices  $\{A_q \in \mathbb{R}_+^{d \times q} : q \geq 1\}$  such that  $H_q \xrightarrow{v} H$ , where  $H_q$  is the angular measure of the max-linear random vector  $\mathbf{X}_q \in \mathcal{RV}_+^d(\alpha)$  parametrised by  $A_q$ . The TPDM of  $\mathbf{X}_q$  is  $\Sigma_q = A_q^{\alpha/2}(A_q^{\alpha/2})^T$  by Example 2.7. Thus,  $\{\Sigma_q : q \geq 1\}$  is a sequence of completely positive matrices. The limit  $\lim_{q \rightarrow \infty} \Sigma_q = \Sigma$  must also be completely positive because the set of completely positive matrices is closed (Haufmann 2011, Theorem 2.1.9).  $\square$

In principle this provides a way to check whether a given matrix is a TPDM, but the membership problem for the completely positive cone is NP-hard (Dickinson and Gijben 2014). The following example illustrates how these two decompositions apply to the symmetric logistic model and hints towards their use for dimension reduction, to be formalised in Section 2.5.

**Example 2.8.** Suppose  $\mathbf{X} = (X_1, \dots, X_d) \in \mathcal{RV}_+^d(\alpha)$  is symmetric logistic with parameter  $\gamma \in (0, 1]$ . Then

$$\Sigma = (1 - \sigma)I_d + \sigma J_d,$$

where the constant  $\sigma$  depends on  $\gamma$  via the formula in Example 2.5. The eigenvalues of  $\Sigma$  are  $\lambda_1 = 1 + (d - 1)\sigma$  and  $\lambda_2 = \dots = \lambda_d = 1 - \sigma$ . The principal eigenvector is  $\mathbf{u}_1 = d^{-1/2}\mathbf{1}_d$  and the remaining eigenvectors  $\mathbf{u}_2, \dots, \mathbf{u}_d$  are orthogonal to  $\mathbf{u}_1$ . Rewriting the TPDM as

$$\Sigma = \sum_{i=1}^d (1 - \sigma) \mathbf{e}_i \mathbf{e}_i^T + \sigma \mathbf{1}_d \mathbf{1}_d^T,$$

and using Example 2.7, the TPDM of  $\mathbf{X}$  is identical to that of a max-linear random vector  $\mathbf{Y} = (Y_1, \dots, Y_d) \in \mathcal{RV}_+^d(\alpha)$  with parameter matrix

$$A = \begin{pmatrix} (1 - \sigma)^{1/\alpha} & 0 & 0 & \cdots & 0 & \sigma^{1/\alpha} \\ 0 & (1 - \sigma)^{1/\alpha} & 0 & \cdots & 0 & \sigma^{1/\alpha} \\ 0 & 0 & (1 - \sigma)^{1/\alpha} & \cdots & 0 & \sigma^{1/\alpha} \\ \vdots & \vdots & \vdots & \ddots & \vdots & \vdots \\ 0 & 0 & 0 & \cdots & (1 - \sigma)^{1/\alpha} & \sigma^{1/\alpha} \end{pmatrix}.$$

Consider the limiting case of complete dependence as  $\gamma \rightarrow 0$ , whereby the angular measure tends towards  $H^{(2)}$  in (2.35) in the limit. The eigenvalues are  $\lambda_1 \rightarrow d, \lambda_2, \dots, \lambda_d \rightarrow 0$ , indicating a single eigenvector  $\mathbf{u}_1$  is sufficient to fully ‘explain’ the dependence structure. We also have  $A \rightarrow (\mathbf{0}, \dots, \mathbf{0}, \mathbf{1}_d) = \mathbf{1}_d = A^{(2)}$ . (The first equality an abuse of notation; we simply mean that zero columns have no effect and may be omitted.) Both perspectives point towards a low-rank representation of the dependence structure involving the vector directed towards the centre of the simplex. Indeed, this perfectly describes  $H^{(2)} = d\delta_{\mathbf{1}_d/\|\mathbf{1}_d\|_\alpha}$ .

#### 2.4.4. The empirical TPDM

**Definition 2.14.** Let  $\mathbf{X} \in \mathcal{RV}_+^d(\alpha)$  on Fréchet margins (2.30) and let  $H$  be the angular measure with respect to  $\|\cdot\|_\alpha$  and normalising sequence  $b_n = n^{1/\alpha}$ . Let  $\mathbf{X}_1, \dots, \mathbf{X}_n$  be an iid sample of  $\mathbf{X}$ . The empirical TPDM estimator is the  $d \times d$  matrix

$$\hat{\Sigma} = (\hat{\sigma}_{ij}), \quad \hat{\sigma}_{ij} := \hat{E}_H[\Theta_i^{\alpha/2} \Theta_j^{\alpha/2}] = \frac{d}{k} \sum_{l=1}^k \Theta_{(l),i}^{\alpha/2} \Theta_{(l),j}^{\alpha/2}. \quad (2.55)$$

Note that the empirical TPDM implicitly depends on the customary tuning parameter  $k$  – or equivalently a radial threshold  $t > 0$  – via the empirical angular measure.

**Proposition 2.3.** *The empirical TPDM is completely positive.*

*Proof.* Let  $A = \hat{A}$ , the  $d \times k$  matrix with non-negative entries defined in (2.44). Then

$$\hat{A}^{\alpha/2} (\hat{A}^{\alpha/2})^T = \frac{d}{k} \sum_{i=1}^k \Theta_{(i)}^{\alpha/2} (\Theta_{(i)}^{\alpha/2})^T = \hat{\Sigma}. \quad \square$$

**Proposition 2.4.** *The empirical TPDM is symmetric and positive semi-definite.*

*Proof.* By complete positivity,  $\hat{\Sigma} = AA^T$  for some matrix  $A$ . For any  $\mathbf{y} \in \mathbb{R}^d \setminus \{\mathbf{0}\}$ ,

$$\mathbf{y}^T \hat{\Sigma} \mathbf{y} = \mathbf{y}^T AA^T \mathbf{y} = \|A^T \mathbf{y}\|_2^2 \geq 0. \quad (2.56)$$

Since  $\text{rank}(\hat{\Sigma}) = \text{rank}(AA^T) = \text{rank}(A)$ , the empirical TPDM is positive definite if and only if the columns of  $A$  are linearly independent.  $\square$

**Proposition 2.5.** *Under the conditions of Theorem 2.3, the entries of  $\hat{\Sigma}$  are consistent and asymptotically normal, that is, for any  $i, j = 1, \dots, d$ ,*

$$\sqrt{k}(\hat{\sigma}_{ij} - \sigma_{ij}) \rightarrow N(0, \nu_{ij}^2), \quad \nu_{ij}^2 := \text{Var}_H(\Theta_i^{\alpha/2}\Theta_j^{\alpha/2}). \quad (2.57)$$

*Proof.* See Example 2.4.  $\square$

If  $X_i$  and  $X_j$  are asymptotically independent ( $\sigma_{ij} = 0$ ), then  $\nu_{ij}^2 = 0$  and the limit distribution is degenerate. In this case, the above result only proves consistency, i.e.  $\hat{\sigma}_{ij} \rightarrow 0$ , and cannot be used to formally test for asymptotic independence (Lehtomaa and Resnick 2020).

Using asymptotic normality one may construct asymptotic confidence intervals

$$\lim_{n \rightarrow \infty} \mathbb{P} \left[ |\sigma_{ij} - \hat{\sigma}_{ij}| < z_{\beta/2} \sqrt{\nu_{ij}^2/k} \right] = 1 - \beta, \quad (2.58)$$

where  $z_{\beta/2} = \Phi^{-1}(1 - \beta/2)$ . If the angular measure is known the asymptotic variance  $\nu_{ij}^2$  may be computed using the formula derived in Section A.1.2.

**Example 2.9.** Suppose  $\mathbf{X} = (X_1, \dots, X_d) \in \mathcal{RV}_+^d(\alpha)$  is symmetric logistic with  $\gamma = 0.6$ . Using Example 2.5 and results in Section A.1,  $\sigma_{ij} \approx 0.760$  and  $\nu_{ij}^2 \approx 0.065$  for all  $i \neq j$ . For sufficiently large  $n$ ,

$$\mathbb{P} \left[ \hat{\sigma}_{ij} \in \left( 0.760 \pm 1.96 \sqrt{\frac{0.065}{k}} \right) \right] \approx 0.95.$$

For example, setting  $n = 10^4$  and  $k = \sqrt{n}$  yields  $\mathbb{P}(0.710 < \hat{\sigma}_{ij} < 0.810) \approx 0.95$ .

In practice, the asymptotic variance may be replaced with the plug-in estimator (Lee and Cooley 2023)

$$\hat{\nu}_{ij}^2 := \frac{1}{k-1} \sum_{l=1}^k \left( d\Theta_{(l),i}\Theta_{(l),j} - \hat{\sigma}_{ij} \right)^2. \quad (2.59)$$

The following result, proved by Krali (2018) for  $\alpha = 2$ , generalises asymptotic normality of the empirical TPDM to the entire matrix, rather than just individual entries. This is

most simply expressed in terms of upper-half vectorisations of  $\Sigma$  and  $\hat{\Sigma}$ , that is

$$\boldsymbol{\sigma} := \text{vecu}(\Sigma) := (\sigma_{12}, \sigma_{13}, \dots, \sigma_{1d}, \sigma_{23}, \dots, \sigma_{2d}, \dots, \sigma_{d-1,d}), \quad (2.60)$$

$$\hat{\boldsymbol{\sigma}} := \text{vecu}(\hat{\Sigma}) := (\hat{\sigma}_{12}, \hat{\sigma}_{13}, \dots, \hat{\sigma}_{1d}, \hat{\sigma}_{23}, \dots, \hat{\sigma}_{2d}, \dots, \hat{\sigma}_{d-1,d}). \quad (2.61)$$

Each vector contains

$$|\{(i, j) : 1 \leq i < j \leq d\}| = \binom{d}{2} = \frac{1}{2}d(d - 1)$$

entries. This is justified because the matrices are symmetric and their diagonal entries are irrelevant. Components are indexed according to the sub-indices of the corresponding matrix entry, e.g. the first entry of  $\boldsymbol{\sigma}$  is  $\sigma_{12}$  rather than  $\sigma_1$ .

**Proposition 2.6.** *Under the conditions of Theorem 2.3, the estimator  $\hat{\boldsymbol{\sigma}}$  is consistent and asymptotically normal, i.e.*

$$\sqrt{k}(\hat{\boldsymbol{\sigma}} - \boldsymbol{\sigma}) \rightarrow N(\mathbf{0}, V),$$

The diagonal and off-diagonal entries of the  $\binom{d}{2} \times \binom{d}{2}$  asymptotic covariance matrix  $V$  are given by

$$v_{ij,lm} := \lim_{n \rightarrow \infty} k\text{Cov}(\hat{\sigma}_{ij}, \hat{\sigma}_{lm}) = \begin{cases} \nu_{ij}^2, & (i, j) = (l, m), \\ \rho_{ij,lm} & \text{otherwise,} \end{cases}$$

where  $\nu_{ij}^2$  is as defined in Proposition 2.5 and

$$\rho_{ij,lm} := \frac{1}{2} \left[ \text{Var}_H(\Theta_i^{\alpha/2} \Theta_j^{\alpha/2} + \Theta_l^{\alpha/2} \Theta_m^{\alpha/2}) - \nu_{ij}^2 - \nu_{lm}^2 \right].$$

The proof can be found in Section A.1.3. It extends the proof of Theorem 5.23 in Krali (2018) to permit general  $\alpha$ . The following example illustrates an application of Proposition 2.6 to the max-linear model.

**Example 2.10.** Suppose  $\mathbf{X} = (X_1, \dots, X_4) \in \mathcal{RV}_+^4(1)$  is max-linear with (randomly generated) parameter matrix  $A \in \mathbb{R}_+^{4 \times 12}$  as shown in Figure 2.3 (top). The TPDM  $\Sigma = A^{1/2}(A^{1/2})^T$  is visualised in the bottom-left plot, with each cell's colour intensity representing the magnitude of the corresponding entry of  $\Sigma$ . All pairs of components exhibit strong dependence. The matrix in the bottom-right is the asymptotic covariance

matrix  $V$  of  $\hat{\sigma}$ , derived in Section A.1.4. It has  $\binom{4}{2} = 6$  rows and columns. We now run simulations verifying/illustrating Proposition 2.6 for this example. We generate  $n = 10^4$  independent observations  $\mathbf{x}_1, \dots, \mathbf{x}_n$  of  $\mathbf{X} = A \times_{\max} \mathbf{Z}$  (see (2.20)) and compute the empirical TPDM using  $k = \sqrt{n} = 100$  extremes. Repeating this process, we obtain 1,000 independent realisations of  $\hat{\Sigma}$ . After row-wise vectorisation, these estimates should be approximately  $N(\boldsymbol{\sigma}, k^{-1}V)$  distributed. Figure 2.4 examines whether this is the case. First consider the diagonal panels. These show that the density function of an  $N(\sigma_{ij}, \nu_{ij}^2/k)$  random variable (blue curve) provides a good fit for the empirical distribution of  $\hat{\sigma}_{ij}$  (red histogram). Now consider the scatter plots in the lower triangular portion of the plot. The grey points represent 1,000 realisations of  $(\hat{\sigma}_{ij}, \hat{\sigma}_{lm})$ . The blue ellipses are the true asymptotic 95% data ellipses centred at  $(\sigma_{ij}, \sigma_{lm})$  (blue crosses). Their orientation relates to the association  $\rho_{ij,lm}$  between  $\hat{\sigma}_{ij}$  and  $\hat{\sigma}_{lm}$ , while the lengths of the major and minor axes are dictated by the asymptotic variances  $\nu_{ij}^2, \nu_{lm}^2$ . The red ellipses and crosses are defined analogously but estimated from the data. They are generally in close agreement. The upper-triangular panels list the values of  $\rho_{ij,lm}$  (blue) alongside empirical estimates (red) based on the sample covariance between  $\hat{\sigma}_{ij}$  and  $\hat{\sigma}_{lm}$ .

In summary, our simulation results show how the asymptotic distribution of  $\hat{\Sigma}$  may be computed (for simple models) using Proposition 2.6 or estimated empirically from a sufficient number of extreme samples.

## 2.5. Existing applications and extensions of the TPDM

The general objective of this thesis is to develop novel statistical tools for analysing extremal dependence based on the TPDM. Before presenting these, we acquaint the reader with existing TPDM-based methods, selected according to their relevance to the thesis. Our survey divides the related literature into two main categories: principal components analysis (PCA) and inference for the max-linear model. Clustering features occasionally (e.g. in Chapter 5), but does not constitute an essential pillar of our research; a brief overview of TPDM-based clustering algorithms (Fomichov and Ivanovs 2023; Richards et al. 2024) is contained in Section A.3. Further interesting topics that are not covered include time series (Mhatre and Cooley 2024; Wixson and Cooley 2023) and graphical

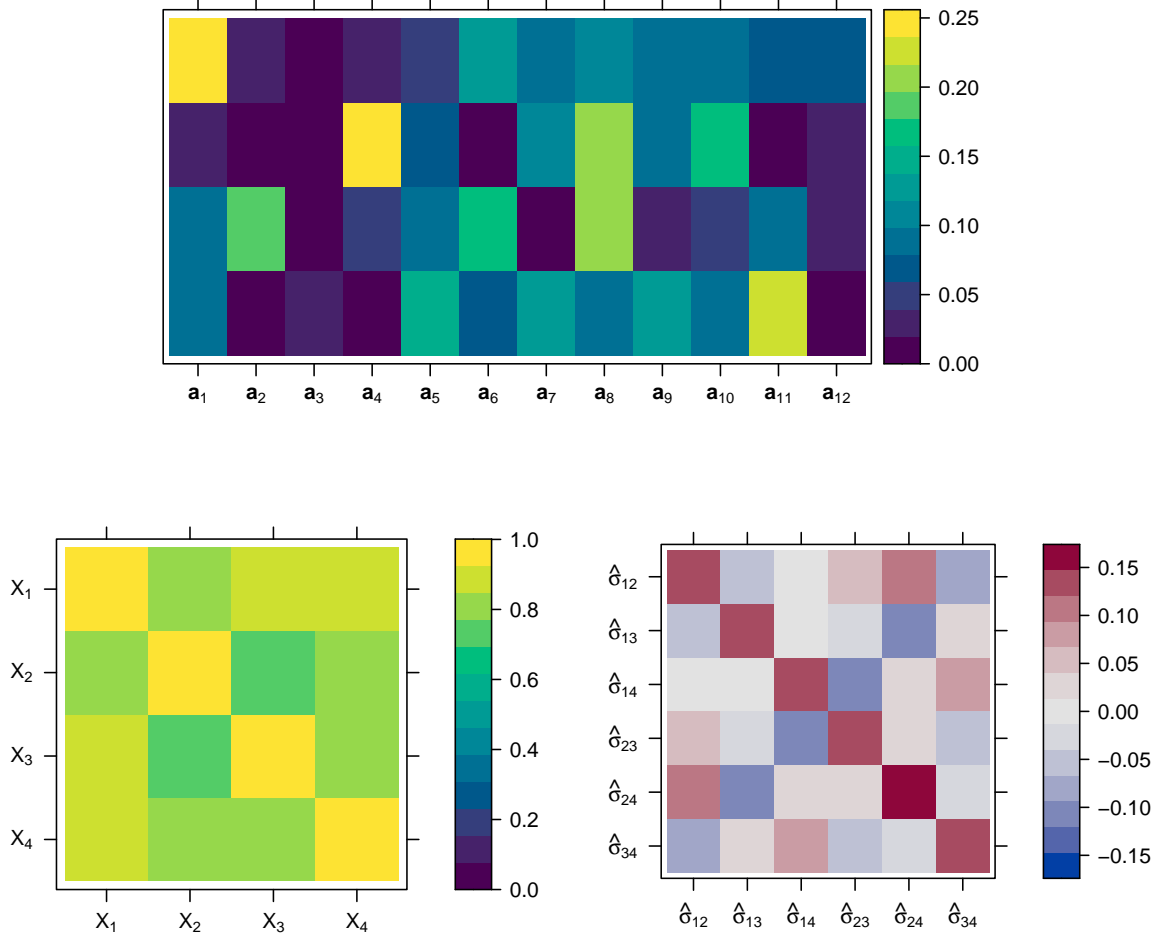


Figure 2.3.: Visual representation of the matrices discussed in Example 2.10. Top: a randomly generated max-linear parameter matrix  $A$  with  $d = 4$  and  $q = 12$ . Bottom left: the TPDM  $\Sigma$  of  $\mathbf{X} = A \times_{\max} \mathbf{Z}$ . Bottom right: the asymptotic covariance matrix  $V$  of  $\hat{\sigma}$ .

models (Gong et al. 2024; Lee and Cooley 2023). Throughout this section,  $\mathbf{X} \in \mathcal{RV}_+^d(\alpha)$  is a random vector on  $\alpha$ -Fréchet margins with angular measure  $H$  with respect to  $\|\cdot\| = \|\cdot\|_\alpha$  and  $b_n = n^{1/\alpha}$ , while  $\mathbf{X}_1, \dots, \mathbf{X}_n$  are independent copies of  $\mathbf{X}$ .

### 2.5.1. Principal component analysis (PCA) for extremes

In classical multivariate statistics, principal component analysis (PCA) is the flagship method for reducing the dimension of a random vector by finding linear subspaces that minimise the distance between the data and its low-dimensional projections (Blanchard et al. 2007; Jolliffe 2002). The central idea is to transform the original set of correlated variables into a new set of uncorrelated variables – the principal components – which are

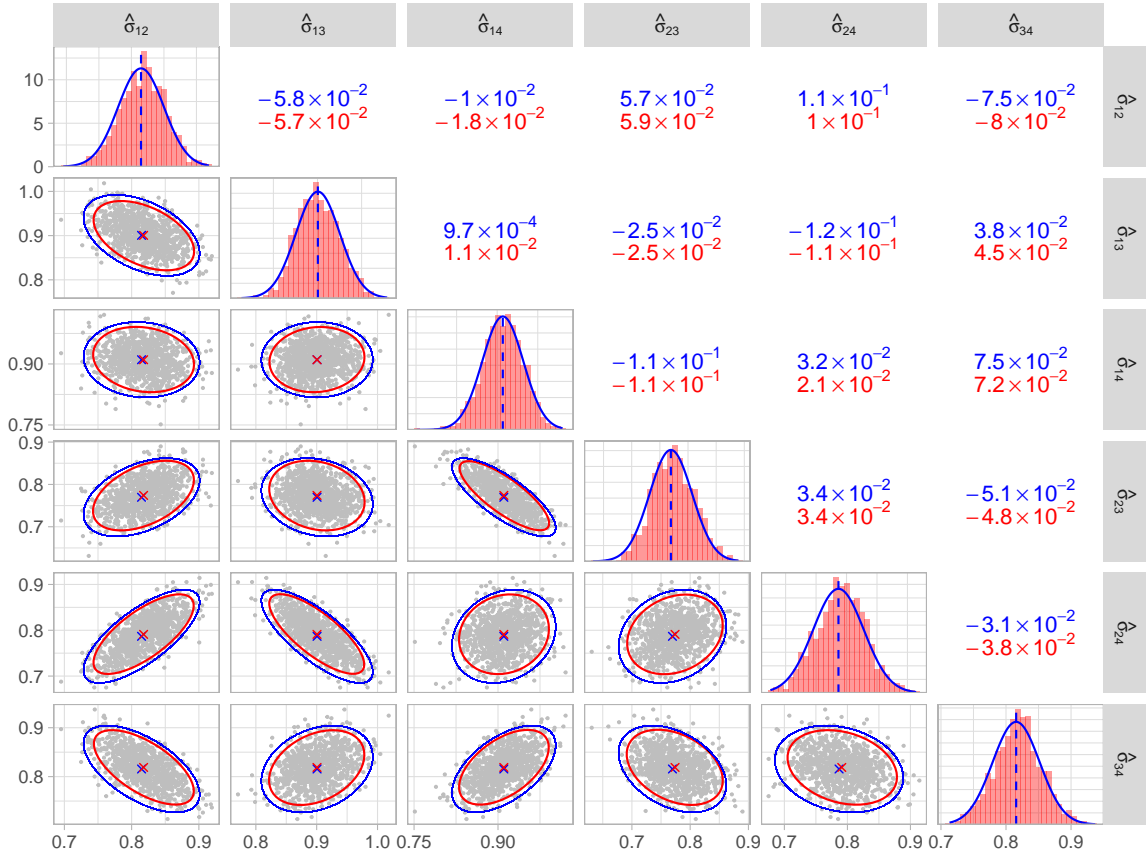


Figure 2.4.: Pairs plot illustrating asymptotic normality of the empirical TPDM – see Example 2.10 for details. All panels: red represents the empirical quantity based on the 1,000 repeated simulations; blue represents the theoretical quantity based on asymptotic normality. Diagonal panels: the distribution (histogram or density function) of  $\hat{\sigma}_{ij}$ . Lower triangular panels: pairwise scatter plots of  $(\hat{\sigma}_{ij}, \hat{\sigma}_{lm})$  (grey points) along with the mean (crosses) and the 95% data ellipse. Upper triangular panels: the entries  $v_{ij,lm}$  of  $V$ .

ordered so that the first few capture most of the variability in the data. Computing these variables boils down to computing the eigendecomposition of a symmetric, positive semi-definite matrix. A more detailed review of the theory of PCA is given in Section A.2.

In multivariate extremes, it is often assumed that the angular measure has a low-dimensional structure (Engelke and Ivanovs 2021). For example, weather extremes typically exhibit spatial patterns related to geographical or topographical drivers, e.g. north/south, coastal/inland, high-lying/low-lying (Bernard et al. 2013; Jiang et al. 2020). These patterns permit a description of a process' extremal behaviour in terms of a smaller number of variables. This is the key objective of PCA for extremes.

Classical (non-extreme) PCA is not appropriate for this task for several reasons. The

original variables  $X_1, \dots, X_d$  are usually heavy-tailed, so the requirement on the existence of second-order moments may be violated; the variance of an  $\alpha$ -regularly varying random variable is infinite if  $\alpha \leq 2$ . Standard PCA reveals relationships between variables in the centre rather than the tail of the joint distribution, because it arises from the covariance matrix. Moreover, it captures dependence in both directions around the origin/mean, whereas we focus on a particular direction of interest. Finally, standard PCA fails to capitalise on the probabilistic structure inherent to MRV random vectors. The heavy-tailed, univariate radial component accounts for most of the variability in the data, but it is (asymptotically) independent of the angular component that actually contains the relevant information about the association between the variables. This suggests performing dimension reduction on the (empirical) angular measure via eigendecomposition of the (empirical) TPDM (Cooley and Thibaud 2019; Drees and Sabourin 2021).

Drees and Sabourin (2021) adopt a risk minimisation perspective aiming to minimise the mean-squared reconstruction error of  $\Theta_{(1)}, \dots, \Theta_{(k)}$  with respect to the limit distribution  $H$ . They define the (asymptotic) risk of a subspace  $\mathcal{S} \subset \mathbb{R}^d$  as

$$R(\mathcal{S}) = \mathbb{E}_H[\|\Theta - \Pi_{\mathcal{S}}\Theta\|_2^2],$$

where  $\Pi_{\mathcal{S}}$  denotes orthogonal projection onto  $\mathcal{S}$ . The true risk cannot be minimised directly because  $H$  is unknown. Instead, the authors minimise the empirical risk

$$\hat{R}(\mathcal{S}) := \hat{\mathbb{E}}_H[\|\Theta - \Pi_{\mathcal{S}}\Theta\|_2^2] = \frac{d}{k} \sum_{i=1}^k \|\Theta_{(i)} - \Pi_{\mathcal{S}}\Theta_{(i)}\|_2^2.$$

This is justified because, above a sufficiently high threshold, the extremal angles will lie in a neighbourhood of the target subspace. Let  $\mathcal{V}_p$  denote the class of all linear subspaces of dimension  $1 \leq p \leq d$  in  $\mathbb{R}^d$ . Minimisers of  $\hat{R}$  are computed via eigendecomposition of the empirical TPDM. Let  $(\hat{\mathbf{u}}_j, \hat{\lambda}_j)$  denote the (ordered) eigenpairs of  $\hat{\Sigma}$  for  $j = 1, \dots, d$ . Then  $\hat{\mathcal{S}}_p := \text{span}\{\hat{\mathbf{u}}_1, \dots, \hat{\mathbf{u}}_p\}$  minimises  $R$  in  $\mathcal{V}_p$  and  $\hat{R}(\mathcal{S}_p) = \sum_{j>p} \hat{\lambda}_j$  (Drees and Sabourin 2021, Lemma 2.1). If the data exhibit a low-dimensional (linear) structure, then one can find  $p \ll d$  such that the risk is acceptably small. It is recommended to plot  $\hat{R}(\mathcal{S}_p)$  against  $p$  when choosing the number of principal components to retain. In terms of theoretical statistical guarantees, Theorem 2.4 in Drees and Sabourin (2021) proves that the learnt

subspace converges to the optimal one as the sample size increases to infinity. Suppose there exists  $p^* < d$  and a linear subspace  $\mathcal{S}^* \in \mathcal{V}_{p^*}$  such that  $R(\mathcal{S}^*) = 0$  and  $R(\mathcal{S}) > 0$  for any  $\mathcal{S} \in \cup_{p < p^*} \mathcal{V}_p$ . Then, provided  $k(n)$  satisfies the rate conditions (2.42),  $\hat{\mathcal{S}}_{p^*} \rightarrow \mathcal{S}^*$  in the sense that

$$\lim_{n \rightarrow \infty} \sup_{\boldsymbol{\theta} \in \mathbb{S}_{+(\alpha)}^{d-1}} \|\Pi_{\hat{\mathcal{S}}_{p^*}} \boldsymbol{\theta} - \Pi_{\mathcal{S}^*} \boldsymbol{\theta}\|_2 = 0.$$

Treating the angles  $\Theta_{(1)}, \dots, \Theta_{(k)}$  as points in  $\mathbb{R}^d$  rather than  $\mathbb{S}_{+(\alpha)}^{d-1}$  simplifies the derivation of theoretical guarantees but creates interpretability issues. The rank- $p$  reconstructions of the angles do not lie in the simplex, in general. Shifting/normalising the reconstructed vectors corrects this, but optimality properties will not be preserved. One may also question the appropriateness of the Euclidean norm as a measure for the angular reconstruction error. In the context of clustering, Janßen and Wan (2020) argue that angular distances (e.g. the cosine dissimilarity) are a more natural choice. On a similar note, their working hypothesis that the low-dimensional structure of  $H$  is linear in  $\mathbb{R}^d$  is restrictive. Avella-Medina et al. (2022) develop a kernel PCA method for extracting non-linear patterns. In Chapter 4, we propose our own PCA method, inspired by compositional PCA, that addresses all of these concerns: reconstructions are in  $\mathbb{S}_{+(\alpha)}^{d-1}$ , errors are defined using a simplicial metric, and non-linearity (curvature) in the data is captured.

Cooley and Thibaud (2019) propose an alternative approach based on the so-called transformed-linear inner product space on  $\mathbb{R}_+^d$ , the sample space of  $\mathbf{X}$ . It is grounded on the softplus transformation

$$\tau : \mathbb{R} \rightarrow \mathbb{R}_+, \quad \tau(x) = \log[1 + \exp(x)].$$

This transformation is bijective with inverse function  $\tau^{-1}(y) = \log[\exp(y)-1]$  and, crucially, it is tail-preserving, i.e.  $\lim_{x \rightarrow 1} \tau(x)/x = 1$ . The role of  $\tau$  is to provide a pathway between  $\mathbb{R}^d$  and  $\mathbb{R}_+^d$  that doesn't disturb the tails. The inner product space is constructed as follows. For any  $\mathbf{x}, \mathbf{y} \in \mathbb{R}_+^d$  and  $\alpha \in \mathbb{R}$ , they define operations

$$\mathbf{x} \oplus \mathbf{y} = \tau[\tau^{-1}(\mathbf{x}) + \tau^{-1}(\mathbf{y})], \quad \alpha \odot \mathbf{x} = \tau[a\tau^{-1}(\mathbf{x})].$$

and an inner product and norm

$$\langle \mathbf{x}, \mathbf{y} \rangle_{\tau} = \left\langle \tau^{-1}(\mathbf{x}), \tau^{-1}(\mathbf{y}) \right\rangle, \quad \|\mathbf{x}\|_{\tau} = \langle \mathbf{x}, \mathbf{x} \rangle_{\tau}^{1/2} = \|\tau^{-1}(\mathbf{x})\|_2.$$

The PCA procedure may then be formulated in the transformed-linear space  $\mathcal{H} = \mathbb{R}_+^d$  or in  $\mathbb{R}^d$  under the transform/back-transform approach (see Section A.2). As in Drees and Sabourin (2021), let  $(\hat{\mathbf{u}}_j, \hat{\lambda}_j)$  be the ordered eigenpairs (in  $\mathbb{R}^d$ ) of  $\hat{\Sigma}$ . Then  $\{\hat{\omega}_1, \dots, \hat{\omega}_d\} = \{\tau(\hat{\mathbf{u}}_1), \dots, \tau(\hat{\mathbf{u}}_d)\}$  forms an orthonormal basis of  $\mathbb{R}_+^d$ . In this new basis, the random vector  $\mathbf{X}$  may be decomposed as

$$\mathbf{X} = \bigoplus_{j=1}^d (\hat{V}_j \odot \hat{\omega}_j) = \tau \left( \sum_{j=1}^d \hat{V}_j \hat{\mathbf{u}}_j \right), \quad (2.62)$$

where  $\hat{V}_j = \langle \mathbf{X}, \hat{\omega}_j \rangle_{\tau}$  for  $j = 1, \dots, d$ . Truncating the expansion (2.62) yields low-rank reconstructions of  $\mathbf{X}$ . The random variables  $\hat{V}_1, \dots, \hat{V}_d$  are called the extremal principal components of  $\mathbf{X}$ . The MRV  $\mathbb{R}^d$ -valued random vector  $\hat{\mathbf{V}}$  has the same dimension as  $\mathbf{X}$ , but its components are ordered according to their contribution to the extremal behaviour of  $\mathbf{X}$  in the sense that (Cooley and Thibaud 2019, Proposition 6)

$$\text{scale}(|\hat{V}_i|) = \hat{\lambda}_i^{1/\alpha}, \quad (i = 1, \dots, d),$$

Thus, the  $i$ th eigenvector  $\hat{\omega}_i$  represents the direction of maximum scale after accounting for information contained in the previous eigenvectors  $\{\hat{\omega}_j : j < i\}$ .

Visualising/examining the TPDM eigenvectors provides a powerful tool for gaining insight into the extremal dependence structure. In a study of precipitation extremes in the United States, Jiang et al. (2020) relate the leading eigenvectors to the El-Niño Southern Oscillation (ENSO), a cyclical phenomenon that is known to be a key climatological driver. Low-rank reconstructions of Hurricane Floyd broadly capture the large-scale structure, but recreating localised features requires a large number of components. Russell and Hogan (2018) compare covariance matrix eigenvectors against TPDM eigenvectors to characterise performance differences between typical and elite-level National Football League (NFL) performers across a battery of physical tests. Szemkus and Friederichs (2024) apply PCA to the cross-TPDM, an extension to the TPDM that is analogous to the cross-covariance

matrix, to analyse the dynamics of compound extreme weather events. For event detection and attribution purposes, they devise indices quantifying whether particular patterns of interest – those signified by the cross-TPDM’s singular vectors – are highly pronounced. Rohrbeck and Cooley (2023) move beyond exploratory analysis and demonstrate how the framework can be used to generate synthetic extreme events, which may, for instance, be used in catastrophe modelling to assess exposure to extreme events. Their sampling algorithm exploits the fact that the leading components of  $\hat{\mathbf{V}}$  account for a significant proportion of the extremal behaviour of  $\mathbf{X}$ . Roughly speaking, dependence between  $\hat{V}_1, \dots, \hat{V}_p$  is captured with a flexible model and a simple model is used to account for the remaining, relatively unimportant components. They use this model to generate samples of  $\hat{\mathbf{V}}$ , from which samples of  $\mathbf{X}$  are produced via (2.62).

Results based on Cooley and Thibaud (2019) require accurate estimation of the TPDM so that the empirical eigenvectors reflect the true eigenvectors. However, in weak-dependence scenarios the empirical TPDM suffers from a positive bias (Section 2.6). This is problematic when the spatial extent of the study region is large relative to that of the modelled phenomenon. Jiang et al. (2020) ameliorate this using a ‘pairwise-thresholded’ estimator instead of (2.55), defined as

$$\hat{\Sigma}^{(p)} = (\hat{\sigma}_{ij}^{(p)}), \quad \hat{\sigma}_{ij}^{(p)} = \frac{2}{k} \sum_{l=1}^n \Theta_{li} \Theta_{lj} \mathbf{1}\{R_l^{ij} > R_{(k+1)}^{ij}\},$$

where  $R_l^{ij} = \|(X_{li}, X_{lj})\|$  and  $R_{(k+1)}^{ij}$  is the  $(k+1)$ th upper order statistic of  $\{R_l^{ij} : l = 1, \dots, n\}$ . However, the resulting estimator  $\hat{\Sigma}^{(p)}$  is not positive semi-definite. This may be resolved by projecting  $\hat{\Sigma}^{(p)}$  onto the space of correlation matrices (Higham 2002), but this ad-hoc step does not address the fundamental problem. Partly motivated by this, Chapter 6 proposes an improved estimator that is positive semi-definite.

### 2.5.2. Inference for the max-linear model

Estimating the parameter matrix  $A$  of the max-linear model is a challenging task. The lack of an angular density function precludes the use of standard maximum likelihood procedures. Einmahl et al. (2018) propose a procedure that minimises a weighted least-squares distance to some initial (non-parametric) estimator. Their procedure becomes

computationally intensive when  $q$  is large. Janßen and Wan (2020) and Avella-Medina et al. (2024) cluster the angles of extreme observations and identify the normalised columns of  $A$  with the  $q$  cluster centres. The minimum-distance and clustering approaches assume  $q$  is fixed; Kiriliouk (2020) present a hypothesis test to assist with choosing  $q$ .

Recently, the TPDM has emerged as a promising tool for inference for the max-linear model (Fix et al. 2021; Kiriliouk and Zhou 2022). Recall from Example 2.7 that the TPDM of a max-linear random vector  $\mathbf{X} \in \mathcal{RV}_+^d(\alpha)$  is  $\Sigma = \hat{A}^{\alpha/2}(\hat{A}^{\alpha/2})^T$ . Now consider Proposition 2.2, which says that the TPDM is completely positive (Definition 2.13). Based on this connection, originally observed by Cooley and Thibaud (2019), any matrix belonging to the set

$$\mathcal{CP}(\hat{\Sigma}) := \left\{ \hat{A} \in \mathbb{R}_+^{d \times q} : q \geq 1, \hat{\Sigma} = \hat{A}^{\alpha/2}(\hat{A}^{\alpha/2})^T \right\}.$$

may be considered a reasonable estimate for  $A$ , in the sense that the pairwise dependencies of the fitted model conform with those implied by  $\hat{\Sigma}$ . The set  $\mathcal{CP}(\hat{\Sigma})$  is in one-to-one correspondence with the set of completely positive (CP) factors of  $\hat{\Sigma}$ . We call  $\hat{A} \in \mathcal{CP}(\hat{\Sigma})$  a CP-estimate of  $A$ . In general, a completely positive matrix may have many CP factorisations (Shaked-Monderer 2021). Among these, the simplest CP-estimate is the empirical estimate  $\hat{A} \in \mathbb{R}_+^{d \times k}$  as defined in (2.44). Cooley and Thibaud (2019) describe the empirical estimate as ‘naive’ because it probably contains more columns than necessary. Kiriliouk and Zhou (2022) provide an algorithm for efficiently factorising  $\hat{\Sigma}$ ; the efficiency of their algorithm permits repeated application to obtain multiple estimates of  $A$ . The performance of their CP-estimation procedure is assessed in simulation studies by computing tail event probability estimates under the true and fitted models using (2.22). The fitted models capture the dependence structure reasonably well, except for certain classes of failure regions. This is partly attributed to estimation error in the TPDM.

Fix et al. (2021) analyse the effect of TPDM estimation error for max-linear model fitting in more detail. Focussing on spatial extremes, they define the extremal spatial autoregressive (SAR) model, a special case of the max-linear model where  $A = A(\rho)$  is determined by a single dependence parameter  $\rho \in (0, 1/4)$ . The model parameter  $\rho$  is estimated by minimising the discrepancy between  $\hat{\Sigma}$  and the theoretical TPDM  $\Sigma(\rho) := A(\rho)A(\rho)^T$

(assuming  $\alpha = 2$ ):

$$\hat{\rho} = \arg \min_{\rho \in (0,1/4)} \|\Sigma(\rho) - \hat{\Sigma}\|_F^2. \quad (2.63)$$

They find that  $\hat{\rho}$  has a positive bias when  $\rho$  is small (weak dependence). The proximate cause is that  $\hat{\Sigma}$  overestimates weak dependencies, biasing the fitted model. This fundamental problem, and their proposed remedy, is the subject of the following section.

## 2.6. Bias in the empirical TPDM in weak-dependence scenarios

The empirical TPDM is consistent and asymptotically unbiased (Proposition 2.6). This provides a guarantee that, with sufficient data, the empirical TPDM reflects the true pairwise dependence structure. The associated rate of convergence is  $\mathcal{O}(k^{-1/2})$ , where  $k = k(n)$  represents the number of extreme observations and satisfies the rate conditions (2.42). However, in real-world applications, data are limited and extreme observations are scarce. For example, commonly available climate records typically span approximately 50 years (Boulaguiem et al. 2022). A study of summer heatwaves might then be based on, say,  $n \approx 50 \times 100 = 5,000$  daily observations. The second condition in (2.42) requires that the effective sample size is some small fraction of  $n$ , resulting in a very limited number of extreme data points. Asymptotic guarantees are therefore of limited value for the sample sizes available in practice. This motivates an analysis of the empirical TPDM's finite-sample performance. As alluded to in the previous section, it will transpire that the TPDM is biased in scenarios where tail dependence is weak (Cooley and Thibaud 2019; Fix et al. 2021; Mhatre and Cooley 2024), herein referred to as the '(weak dependence) bias issue'. Chapter 6 proposes bias-corrected estimators with superior finite-sample performance, but the bias issue will arise at various points in the preceding chapters, so we choose to highlight it now.

### 2.6.1. Bias in the TPDM and threshold-based estimators

The bias issue is not exclusive to the empirical TPDM. In fact, it applies more generally to threshold-based estimators in multivariate extremes. For example, Huser et al. (2016) conduct simulation studies examining the finite-sample performance of estimators of  $\gamma$ ,

the dependence parameter of the symmetric logistic model. The results show that block-maxima based estimators have a small bias but very high variability. On the other hand, the estimator  $\hat{\gamma}$  based on threshold exceedances tends to overestimate the dependence strength, that is  $\text{Bias}(\hat{\gamma}) = \mathbb{E}[\hat{\gamma}] - \gamma < 0$ . This discrepancy increases as dependence weakens; see the second column of Figure 3 in Huser et al. (2016). Problems of a similar nature can be found across the multivariate extremes literature, for example in spatial modelling (Boulaguiem et al. 2022, Figure 6c) and lower-tail dependence modelling (Dobrić and Schmid 2005).

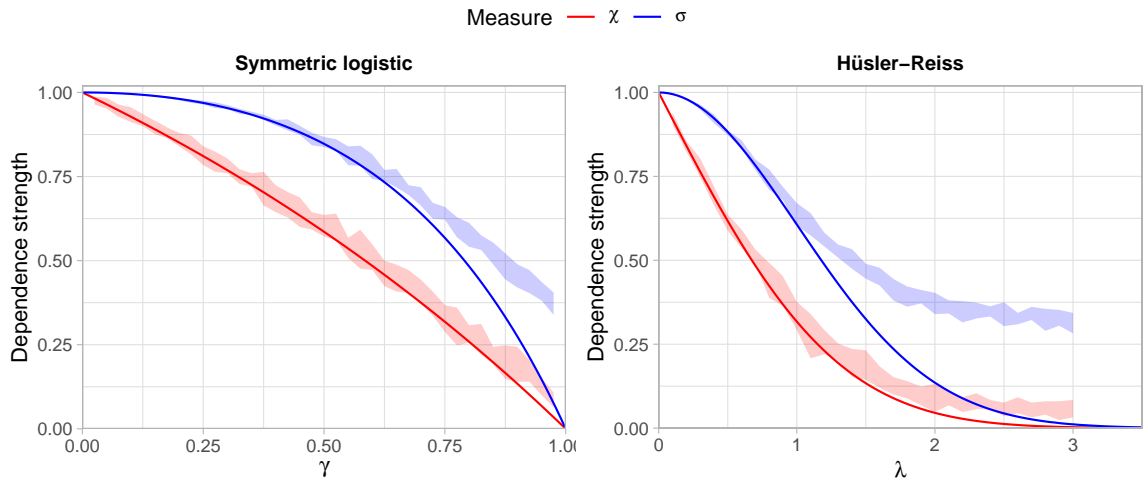


Figure 2.5.: True dependence strengths for the symmetric logistic (left) and Hüsler-Reiss (right) models, measured using the tail dependence coefficient (red line) and TPDM (blue line). The shaded regions represent the minimum/maximum values of empirical estimates over 10 repeated simulations using bivariate samples of size  $n = 5 \times 10^3$ .

The empirical TPDM suffers from the same issue when dependence is weak. This phenomenon is illustrated in Figure 2.5. Like in Figure 2.2, the blue lines represent the true dependence strength for a given model parameter and the shaded regions indicate the minimum/maximum over a set of ten empirical estimates. The only difference is that here the underlying sample size is  $n = 5 \times 10^3$ , whereas in Figure 2.2 it was  $n = 5 \times 10^5$ . In both plots, the tuning parameter was set as  $k = \sqrt{n}$ . The plot definitively shows that the empirical TPDM overestimates the dependence as  $\gamma$  and  $\lambda$  approach their upper limits, or, equivalently, as  $\sigma \rightarrow 0$ . This can be summarised as

$$\sigma_{ij} \ll 1 \implies \text{Bias}(\hat{\sigma}_{ij}) = \mathbb{E}[\hat{\sigma}_{ij}] - \sigma_{ij} > 0. \quad (2.64)$$

Note that overestimating the dependence strength corresponds to a positive bias in the

TPDM estimate, so the inequality is reversed when compared to  $\gamma$ .

Estimation error in the empirical TPDM was first studied by Cooley and Thibaud (2019). Figure 3 in their Supplementary Material assesses the accuracy of the eigenvalues/eigenvectors of the empirical TPDM based on data generated from a Brown-Resnick model. The leading eigenvalue is consistently overestimated ( $\hat{\lambda}_1 > \lambda_1$ ) and subsequent eigenvalues are underestimated ( $\hat{\lambda}_j < \lambda_j$  for  $j \geq 2$ ). The sample covariance matrix suffers a similar deficiency, especially when the sample size and dimension are comparable in magnitude (Mestre 2008). The magnitude of the bias depends on the sample size and the proportion  $k/n$ . Errors in the eigenvalues may influence the results of downstream PCA analysis, e.g. in deciding how many components are to be retained in the PCA.

### 2.6.2. Existing bias-correction approaches for the TPDM

The first strategy for tackling the bias issue is found in Mhatre and Cooley (2024). Working in a time series context, they study serial dependence in extremes using the tail pairwise dependence function (TPDF)  $\sigma(h)$ , which summarises the tail dependence between  $X_t$  and  $X_{t+h}$  for a tail stationary time series  $\{X_t : t = 1 \dots, n\}$ . Simulation experiments reveal that the empirical TPDF  $\hat{\sigma}(h)$  is biased at higher lags where the true dependence is close to zero. To counteract this, they subtract the mean from the time series in pre-processing. The rationale for this is described in terms of the position of extreme points in a lag plot (i.e. a scatter plot of  $(X_t, X_{t+h})$  for fixed  $h$ ). Subtracting the mean has negligible effect on the angles corresponding to joint extremes, but points near a coordinate axis are shifted even closer to the axis.

Fix et al. (2021) develop the first bias-corrected estimate of the TPDM. Recall from Section 2.5.2 the problem of estimating the spatial dependence parameter  $\rho$  of the extremal SAR model. When the study domain is large or the modelled phenomenon is highly localised, the pairwise dependence between distant sites is weak and the empirical TPDM is prone to overestimation in the corresponding entries. This bias carries over to  $\hat{\rho}$  defined in (2.63). Their bias-corrected estimate  $\tilde{\Sigma}$  reduces the entries of  $\hat{\Sigma}$  by element-wise application

of the soft-thresholding operator (Rothman et al. 2009), that is

$$\tilde{\Sigma} = (\tilde{\sigma}_{ij}), \quad \tilde{\sigma}_{ij} = \begin{cases} \hat{\sigma}_{ij}, & i = j, \\ (\hat{\sigma}_{ij} - \lambda)_+, & i \neq j. \end{cases} \quad (2.65)$$

The threshold  $\lambda \geq 0$  is selected by assuming that the pairwise tail dependence vanishes to zero as the distance between two sites increases. For  $i \neq j$ , let  $h_{ij}$  denote the (known) spatial distance between the sites corresponding to the variables  $X_i$  and  $X_j$ . Treating the empirical TPDM entries  $\{\hat{\sigma}_{ij} : i \neq j\}$  as functions of distance, they model tail dependence strength against spatial distance via

$$\hat{\sigma}(h) = \beta_0 \exp(-\beta_1 h) + \beta_2.$$

The parameters  $\beta_0, \beta_1, \beta_2$  are estimated from the data  $\{(\hat{\sigma}_{ij}, h_{ij}) : 1 \leq i < j \leq d\}$  by non-linear least squares estimation, e.g. using `nls()`. Since  $\hat{\sigma}(h) \rightarrow \beta_2$  as  $h \rightarrow \infty$ , the horizontal asymptote  $\hat{\beta}_2$  of the fitted model is used as a proxy for the bias at large distances. It suggests itself to choose  $\lambda = \hat{\beta}_2$ . Clearly this procedure is only viable in spatial contexts where a notion of proximity exists.

The contrasting strategies of Mhatre and Cooley (2024) and Fix et al. (2021) point towards two qualitatively different ways of improving tail dependence estimation. The first approach acts directly on the data by moving (some of) the extremal angles  $\boldsymbol{\theta}_{(1)}, \dots, \boldsymbol{\theta}_{(k)}$  closer to the boundary of the simplex in some principled way. In other words, improved inference may be achieved by perturbing the empirical angular measure. This outlook is central to Chapter 5, where we employ sparse simplex projections (Meyer and Wittenberger 2021) to fit max-linear models. Under the second approach, bias-correction is undertaken as a post-processing step. Chapter 6 pursues this idea in more detail. We propose a general class of shrinkage/thresholded TPDM estimators that includes (2.65). Unlike Fix et al. (2021), our tuning procedure for selecting the hyperparameter  $\lambda$  is purely data-driven and can be applied in general settings, not just spatial.

## 3. Testing for time-varying extremal dependence

### 3.1. Introduction

Multivariate extreme value models typically assume that the data represent independent realisations from some fixed distribution. This requires that both the marginal distributions and the extremal dependence structure are constant throughout the observation period. As explained in Section 2.1.3 with regards to univariate (marginal) modelling, this assumption is not always valid and non-stationary models are being developed to account for this. However, there is much less research on the topic of non-stationarity in the extremal dependence structure, even though the same problems apply. Anthropogenic climate change is driving changes in the spatial structure of climate extremes (Zhou et al. 2023) and regulatory changes can cause structural changes in the joint tail behaviour of financial asset prices (Poon et al. 2003). Thus, a crucial step in the modelling process is to determine whether it is reasonable to assume stationary dependence or not. In this chapter, we present a formal procedure for testing this assumption.

Before proceeding, we clarify an important distinction between *testing for* versus *modelling* non-stationary dependence. Both represent very challenging statistical problems: the underlying signal (e.g. climate change) may be very weak, perhaps only becoming apparent over very long observation periods. The latter task refers to the development of multivariate extreme value models that allow for temporal non-stationarity in the dependence structure. For example, the regression model of Castro-Camilo et al. (2018) and the spectral density ratio model of De Carvalho and Davison (2014) can incorporate covariate effects, including time. These models rely on parametric assumptions and are restricted to a small number

of dimensions. To the best of our knowledge, the only existing work on *testing* for changing dependence is Drees (2023). Roughly speaking, their procedure involves partitioning the observation period into temporal blocks and testing for deviations in the empirical angular measure  $\hat{H}$  between blocks. This is very computationally intensive and thus is restricted to  $d \leq 5$  in practice.

Our contribution is to devise a procedure that instead tests for changes in  $\hat{\Sigma}$ , the empirical TPDM. Considering pairwise dependencies instead of the full angular measure eases the computational burden significantly and enables testing even in high dimensions. Section 3.2 to Section 3.5 details our framework, which is then applied to simulated and Red Sea surface temperature data in Section 3.6 and Section 3.8, respectively. Our test achieves superior performance to Drees (2023) in many realistic scenarios, except when neglecting higher-order dependencies necessarily incurs a significant loss of information (Section 3.7).

## 3.2. Framework

Suppose  $\{\mathbf{X}(t) = (X_1(t), \dots, X_d(t)) : t \in [0, 1]\}$  is an  $\mathbb{R}_+^d$ -valued, continuous time stochastic process with no serial dependence. For  $t \in [0, 1]$ , assume that the random vector  $\mathbf{X}(t)$  is MRV (Definition 2.6) with constant index of regular variation  $\alpha(t) = \alpha$  and potentially time-varying angular measure  $H(\cdot; t)$  on  $\mathbb{S}_{+(\alpha)}^{d-1} := \{\mathbf{x} \in \mathbb{R}_+^d : \|\mathbf{x}\|_\alpha = 1\}$ . The underlying norm is  $\|\cdot\|_\alpha$  and the normalising sequence is  $b_n = n^{1/\alpha}$ , so that  $H(\mathbb{S}_{+(\alpha)}^{d-1}; t) = d$  for all  $t \in [0, 1]$ . Denote the radial and angular components of  $\mathbf{X}(t)$  by  $R(t) := \|\mathbf{X}(t)\|_\alpha$  and  $\Theta(t) := \mathbf{X}(t)/\|\mathbf{X}(t)\|_\alpha$ , respectively. In this time-dependent setting, the MRV property states that for all  $z > 0$  and Borel sets  $\mathcal{B} \subset \mathbb{S}_{+(\alpha)}^{d-1}$ ,

$$\lim_{u \rightarrow \infty} \frac{\mathbb{P}(R(t) > zu, \Theta(t) \in \mathcal{B})}{\mathbb{P}(R(t) > u)} = z^{-\alpha(t)} H(\mathcal{B}; t). \quad (3.1)$$

We assume  $\mathbf{X}(t)$  is on stationary  $\alpha$ -Fréchet margins, perhaps after a suitable marginal transformation. This pre-processing step may require removing marginal non-stationarity using the univariate techniques described in Section 2.1.3. Without loss of generality, we take  $\alpha = 2$  throughout.

Following Drees (2023), our working null and alternative hypotheses are

$$H_0 : \forall t \in [0, 1], H(\cdot; t) = H(\cdot; 1), \quad (3.2)$$

$$H_1 : \exists t, H(\cdot; t) \neq H(\cdot; 1). \quad (3.3)$$

Under the null hypothesis, the angular measure (extremal dependence structure) is constant/stationary. The alternative states that the angular measure is time-varying. The nature of the time-dependence is unspecified. This includes the possibility of instantaneous change-points, smooth gradual evolutions, or a mixture of both. Our goal is to devise a statistical procedure for testing (3.2) against (3.3) based on a discretised sample path of  $\{\mathbf{X}(t) : t \in [0, 1]\}$ . This will be achieved by testing for deviations in a time-dependent version of the TPDM. In particular, we will work with an integrated version of the TPDM. Since we work with an integrated quantity, the alternative hypothesis might be revised to instead say that there exists a set  $\mathcal{T} \in [0, 1]$  of non-zero measure such that  $H(\cdot; t) \neq H(\cdot; 1)$  for all  $t \in \mathcal{T}$ .

### 3.3. The local TPDM and integrated TPDM

Given non-stationary dependence as in (3.1), a time-dependent version of the TPDM is naturally defined by replacing  $H$  with the local angular measure  $H(\cdot; t)$  in Definition 2.10.

**Definition 3.1.** The local TPDM of  $\mathbf{X}(t)$  is the  $d \times d$  matrix

$$\Sigma(t) = (\sigma_{ij}(t)), \quad \sigma_{ij}(t) = \int_{\mathbb{S}_{+(2)}^{d-1}} \theta_i \theta_j \, dH(\boldsymbol{\theta}; t) = \mathbb{E}_{H(\cdot; t)}[\Theta_i \Theta_j]. \quad (3.4)$$

Since  $H(\cdot; t)$  is a valid angular measure, the local TPDM possesses all the usual properties of a TPDM (Section 2.4). Its entries summarise the tail dependence strength between pairs of components of  $\mathbf{X}(t)$ . While our principal objective is to detect changes in the local TPDM, Drees (2023) notes that it is common to devise statistical tests using integrated versions of the quantity of interest, and therefore ground their test statistics not on the

angular measure, but rather the integrated angular measure,

$$\text{IH}(\cdot; t) := \int_0^t H(\cdot; s) \, ds.$$

We define the integrated TDPM analogously.

**Definition 3.2.** The integrated TPDM of  $\{\mathbf{X}(t) : t \in [0, 1]\}$  at a fixed time  $t \in [0, 1]$  is the  $d \times d$  matrix given by

$$\Psi(t) = (\psi_{ij}(t)), \quad \psi_{ij}(t) = \int_0^t \sigma_{ij}(s) \, ds.$$

The integrated TPDM can be equivalently expressed in terms of the integrated angular measure, since

$$\begin{aligned} \psi_{ij}(t) &= \int_0^t \int_{\mathbb{S}_{+(2)}^{d-1}} \theta_i \theta_j \, dH(\boldsymbol{\theta}; s) \, ds \\ &= \int_{\mathbb{S}_{+(2)}^{d-1}} \theta_i \theta_j \int_0^t \, dH(\boldsymbol{\theta}; s) \, ds \\ &= \int_{\mathbb{S}_{+(2)}^{d-1}} \theta_i \theta_j \, d\text{IH}(\boldsymbol{\theta}; t). \end{aligned}$$

The following result lists some useful properties of  $\Psi(t)$ .

**Lemma 3.1.** *Let  $\Psi(t)$  be an integrated TPDM for some  $t \in [0, 1]$ . Then:*

1. *For any  $i \neq j$ , the entries of  $\Psi(t)$  satisfy  $\psi_{ii}(t) = t$  and  $\psi_{ij}(t) \in [0, t]$ .*
2. *The entry  $\psi_{ij}(t) = 0$  if and only if  $X_i(s)$  and  $X_j(s)$  are asymptotically independent for almost all  $s \in [0, t]$ .*
3.  *$\Psi(t)$  is symmetric, positive semi-definite.*

*Proof.* Recall that the local TPDM possesses the properties of the TPDM.

1. From Section 2.4.2, we know that  $\sigma_{ii}(s) = 1$  and  $\sigma_{ij}(s) \in [0, 1]$  for all  $s \in [0, 1]$ . It

immediately follows that

$$\begin{aligned}\psi_{ii}(t) &= \int_0^t \sigma_{ii}(s) \, ds = \int_0^t 1 \, ds = t, \\ \psi_{ij}(t) &= \int_0^t \sigma_{ij}(s) \, ds \leq \int_0^t 1 \, ds = t.\end{aligned}$$

2. For any (measurable) non-negative function  $f : \mathbb{R} \rightarrow \mathbb{R}_+$ , the condition

$$\int_a^b f(x) \, dx = 0$$

holds if and only if  $f(x) = 0$  for almost every  $x \in [a, b]$ . Applying this fact to  $f(t) = \sigma_{ij}(t)$  with  $a = 0$  and  $b = t$  yields the result.

3. Symmetry of  $\Psi(t)$  is inherited from symmetry of the local TPDM. For any  $\mathbf{y} \in \mathbb{R}^d \setminus \{\mathbf{0}\}$ , we have

$$\mathbf{y}^T \Psi(t) \mathbf{y} = \mathbf{y}^T \left( \int_0^t \Sigma(s) \, ds \right) \mathbf{y} = \int_0^t \mathbf{y}^T \Sigma(s) \mathbf{y} \, ds.$$

Positive semi-definiteness of  $\Sigma(t)$  guarantees the integrand is non-negative. Therefore  $\mathbf{y}^T \Psi(t) \mathbf{y} \geq 0$ .  $\square$

Due to properties in Lemma 3.1 we may focus on vectorised forms of  $\Sigma(t)$  and  $\Psi(t)$  defined analogously to  $\boldsymbol{\sigma}$  in (2.60), i.e. by row-wise flattening of the strictly upper-triangular elements of  $\Sigma(t)$  and  $\Psi(t)$ :

$$\boldsymbol{\sigma}(t) := \text{vecu}(\Sigma(t)) = (\sigma_{12}(t), \sigma_{13}(t), \dots, \sigma_{1d}(t), \sigma_{23}(t), \dots, \sigma_{2d}(t), \dots, \sigma_{d-1,d}(t)), \quad (3.5)$$

$$\boldsymbol{\psi}(t) := \text{vecu}(\Psi(t)) = (\psi_{12}(t), \psi_{13}(t), \dots, \psi_{1d}(t), \psi_{23}(t), \dots, \psi_{2d}(t), \dots, \psi_{d-1,d}(t)). \quad (3.6)$$

Each vector has dimension  $\mathcal{D} = \binom{d}{2}$ .

Using a simple example, we now sketch how the integrated TPDM will be used to test for non-stationary dependence. Suppose  $\mathbf{X}(t)$  follows a symmetric logistic distribution with dependence parameter  $\gamma(t)$ . Consider the following two scenarios:  $\gamma(t) = 0.7$  (constant dependence) and  $\gamma(t) = 0.5 + |t - 0.5|$  (changing dependence). These cases correspond to the left- and right-hand plots in Figure 3.1, respectively, with  $\gamma(t)$  represented by the

blue line. The red and green lines depict the local TPDM  $\sigma_{ij}(t)$  and integrated TPDM  $\psi_{ij}(t)$ , respectively, as functions of  $t$ . Under the symmetric logistic model all pairs are equivalent, so we may suppress the  $ij$  subscript. In the left-hand plot, constant dependence manifests as a horizontal line for  $\sigma(t)$  and a straight line for  $\psi(t)$ . In the right-hand plot, the dependence strength  $\sigma(t)$  is greatest near the centre of the time interval and  $\psi(t)$  is the time-integral of this non-linear function. Intuitively, our test works by quantifying whether (estimates of)  $\psi_{ij}(t)$  deviate from straight lines. Mathematically it will prove more convenient to instead consider deviations of (estimates of)  $\psi_{ij}(t) - t\psi_{ij}(1)$  from zero. The function  $\psi(t) - t\psi(1)$  is plotted in black. In the constant dependence case,  $\sigma(t) = \sigma$  for all  $t \in [0, 1]$ , so

$$\psi(t) - t\psi(1) = \int_0^t \sigma(s) ds - t \int_0^1 \sigma(s) ds = \sigma \left( \int_0^t ds - t \int_0^1 ds \right) = 0. \quad (3.7)$$

The following sections concern the main statistical challenges, namely (i) how to estimate  $\sigma(t)$  and  $\psi(t)$ , and (ii) the construction of test statistics quantifying whether an estimate of  $\{\psi(t) - t\psi(1) : t \in [0, 1]\}$  is sufficiently different from zero.

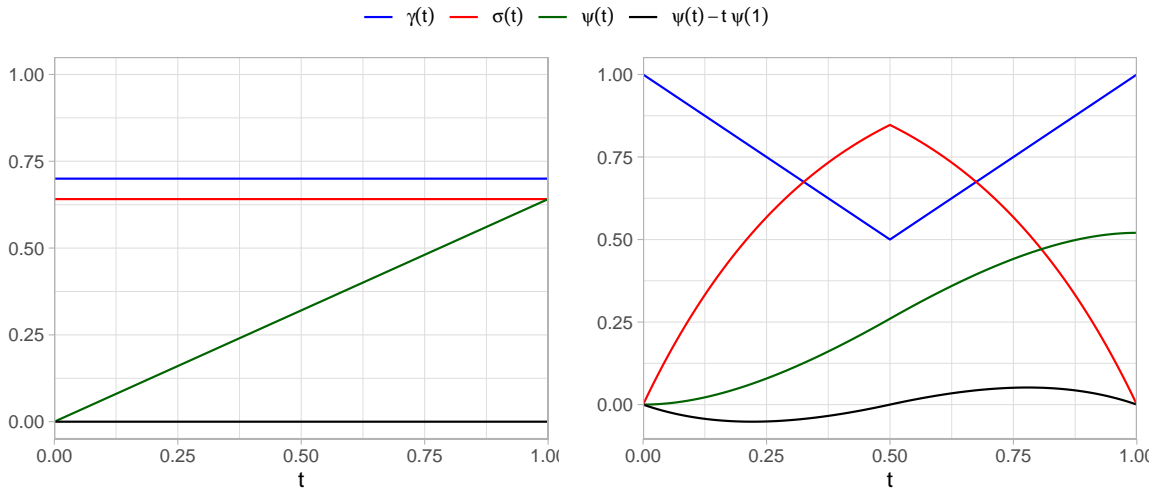


Figure 3.1.: The quantities  $\sigma_{ij}(t)$ ,  $\psi_{ij}(t)$ , and  $\psi_{ij}(t) - t\psi_{ij}(1)$  as functions of  $t$  when  $\mathbf{X}(t)$  is symmetric logistic with dependence parameter  $\gamma(t)$ . Left: constant dependence with  $\gamma(t) = 0.7$ . Right: time-varying dependence with  $\gamma(t) = 0.5 + |t - 0.5|$ .

### 3.4. Inference

Suppose we observe a sample path of  $\{\mathbf{X}(t) : t \in [0, 1]\}$  along  $n$  discrete time-points according to an equidistant sampling scheme, corresponding to realisations of the independent random vectors  $\{\mathbf{X}(i/n) : i = 1, \dots, n\}$ .

#### 3.4.1. The empirical local TPDM

Provided the tail distribution of  $\mathbf{X}(t)$  varies sufficiently smoothly with  $t$ , we may infer the local dependence structure at time  $t \in [0, 1]$  using the most extreme observations lying within a small neighbourhood of  $t$ . For some positive bandwidth  $h = h(n)$ , define by

$$\mathcal{I}(t) := \{i \in \{1, \dots, n\} : i/n \in (t - h, t + h]\}$$

the index set of observations in a  $h$ -neighbourhood of  $t$ . Among  $\{\mathbf{X}(i/n) : i \in \mathcal{I}(t)\}$ , only those whose norm exceeds some high radial threshold will enter into our estimator for  $\Sigma(t)$ . The threshold  $\hat{u}(t)$  is set as the  $(k+1)$ th upper order statistic of  $\{R(i/n) : i \in \mathcal{I}(t)\}$ , resulting in exactly  $k$  radial threshold exceedances. Drees (2023) use the same setup to define the empirical local angular measure, which forms the basis of our estimator for the local TPDM.

**Definition 3.3.** For any  $t \in [0, 1]$ , the empirical local angular measure is the random measure on  $\mathbb{S}_{+(2)}^{d-1}$  defined by

$$\hat{H}(\cdot; t) := \frac{d}{k} \sum_{l \in \mathcal{I}(t)} \mathbf{1}\{R(l/n) > \hat{u}(t), \Theta(l/n) \in \cdot\}. \quad (3.8)$$

**Definition 3.4.** For  $t \in [0, 1]$ , the empirical local TPDM estimator is the  $d \times d$  matrix  $\hat{\Sigma}(t) = (\hat{\sigma}_{ij}(t))$ , where

$$\hat{\sigma}_{ij}(t) := \int_{\mathbb{S}_{(2)+}^{d-1}} \theta_i \theta_j \, d\hat{H}(\theta; t) = \frac{d}{k} \sum_{l \in \mathcal{I}(t)} \Theta_i(l/n) \Theta_j(l/n) \mathbf{1}\{R(l/n) > \hat{u}(t)\}. \quad (3.9)$$

We recognise  $\hat{H}(\cdot; t)$  and  $\hat{\Sigma}(t)$  as simply time-localised versions of the empirical angular measure (Definition 2.9) and empirical TPDM (Definition 2.14). It is easy to see that the

empirical local TPDM possesses the same finite-sample properties as the empirical TPDM, such as positive semi-definiteness and complete positivity. Unlike the empirical TPDM, the performance of  $\hat{\Sigma}(t)$  depends not only on  $k$  but also on the additional tuning parameter  $h$ . Joint selection of  $k$  and  $h$  involves managing several trade-offs. A large effective sample size can be achieved by increasing  $k$  and/or  $h$ . As we know, increasing  $k$  risks bias due the inclusion of observations from the bulk. Increasing  $h$  introduces the possibility of another kind of bias due to the influence of non-local extreme observations, i.e. data that are not representative of the tail distribution at time  $t$ . These trade-offs will appear via modified rate conditions when describing the asymptotic properties of  $\hat{\Sigma}(t)$  in Section 3.4.3.

### 3.4.2. The empirical integrated TPDM

The best approach for estimating the integrated TPDM is slightly less obvious because  $\Psi(t)$  depends on the entire history  $\{\Sigma(s) : s \in [0, t]\}$ . For computational and mathematical reasons, we opt for a block-based approach that involves performing estimation in a piecewise constant fashion over disjoint time intervals of width  $2h$ . For any  $t \in [0, 1]$  and  $h > 0$ , by the additive property of the integral we have that

$$\begin{aligned}\psi_{ij}(t) &= \int_0^t \sigma_{ij}(s) ds \\ &= \int_0^{2h} \sigma_{ij}(s) ds + \int_{2h}^{4h} \sigma_{ij}(s) ds + \dots + \int_{2h\lfloor t/(2h) \rfloor}^t \sigma_{ij}(s) ds \\ &= \sum_{l=1}^{\lfloor t/(2h) \rfloor} \int_{2h(l-1)}^{2hl} \sigma_{ij}(s) ds + \int_{2h\lfloor t/(2h) \rfloor}^t \sigma_{ij}(s) ds.\end{aligned}$$

The first term corresponds to the  $\lfloor t/(2h) \rfloor$  whole blocks in  $[0, t]$ . The second term corresponds to the final partial block; this term vanishes if  $t$  is a multiple of  $2h$ . Our estimator for  $\psi_{ij}(t)$  assumes that  $\sigma_{ij}(s)$  is constant across each of the disjoint intervals and then estimates  $\sigma_{ij}(s)$  empirically at the interval centres using  $h$  as the bandwidth. Henceforth, assume for simplicity that the number of blocks  $1/(2h)$  is an integer.

**Definition 3.5.** For  $t \in [0, 1]$ , the empirical integrated TPDM estimator is the  $d \times d$  matrix

$\hat{\Psi}(t) = (\hat{\psi}_{ij}(t))$ , where

$$\begin{aligned}\hat{\psi}_{ij}(t) &:= \sum_{l=1}^{\lfloor t/(2h) \rfloor} \int_{2h(l-1)}^{2hl} \hat{\sigma}_{ij}((2l-1)h) ds + \int_{2h\lfloor t/(2h) \rfloor}^t \hat{\sigma}_{ij}((2\lfloor t/(2h) \rfloor + 1)h) ds \\ &= 2h \sum_{l=1}^{\lfloor t/(2h) \rfloor} \hat{\sigma}_{ij}((2l-1)h) + (t - 2h\lfloor t/(2h) \rfloor) \hat{\sigma}_{ij}((2\lfloor t/(2h) \rfloor + 1)h).\end{aligned}$$

This construction permits efficient computation of the entire process  $\{\hat{\Psi}(t) : t \in [0, 1]\}$ . Note that the partition of the time-interval  $[0, t]$  depends only on  $h$ , not on  $t$ . Hence, the estimates  $\hat{\Sigma}(s)$  at the time points  $s \in \{h, 3h, \dots, 1-h\}$  are sufficient to estimate  $\Psi(t)$  at any  $t \in [0, 1]$  via a simple weighted sum. The piecewise constant assumption on  $\Sigma(t)$  implies that  $\hat{\psi}_{ij}(t)$  is a piecewise linear function of  $t$ . Therefore, to compute the full path  $\{\hat{\Psi}(t) : t \in [0, 1]\}$  one need only compute  $\hat{\Psi}(s)$  at the interval endpoints  $s \in \{2h, 4h, \dots, 1\}$  and fill in the intermediate time points by linear interpolation.

Mathematically, the appeal of a block-based construction is that  $\hat{\Psi}(t)$  is a weighted sum of independent random matrices  $\hat{\Sigma}(h), \hat{\Sigma}(3h), \dots, \hat{\Sigma}(1-h)$ . Independence is due to the blocks being non-overlapping and choosing the bandwidth as half the block width, so that dependence within each block is estimated using only observations contained in it. This independence is crucial in the elicitation of the asymptotic results to follow.

### 3.4.3. Asymptotic properties of $\hat{\Sigma}(t)$ and $\hat{\Psi}(t)$

We now formulate the asymptotic properties of the estimators  $\hat{\sigma}(t) := \text{vecu}(\hat{\Sigma}(t))$  and  $\hat{\psi}(t) := \text{vecu}(\hat{\Psi}(t))$  of  $\sigma(t)$  and  $\psi(t)$  defined in (3.5) and (3.6). Our main result in Theorem 3.1 states that, under the null, suitably rescaled functionals of  $\hat{\Psi}(t)$  converge to a Brownian bridge. Fundamentally, this is due to asymptotic normality of the empirical local TPDM.

**Lemma 3.2.** *Assume  $k(n)$  and  $h(n)$  satisfy the rate conditions*

$$h(n) \rightarrow 0, \quad k(n) \rightarrow \infty, \quad nh(n) \rightarrow \infty, \quad \frac{k(n)}{nh(n)} \rightarrow 0 \tag{3.10}$$

as  $n \rightarrow \infty$  and the null hypothesis (3.2) is true. Then, for any  $t \in [0, 1]$ ,

$$\sqrt{k}(\hat{\boldsymbol{\sigma}}(t) - \boldsymbol{\sigma}(t)) \rightarrow N(\mathbf{0}, V(t)) \quad (3.11)$$

as  $n \rightarrow \infty$ . The  $\mathcal{D} \times \mathcal{D}$  asymptotic covariance matrix  $V(t)$  has entries given by

$$v_{ij,lm}(t) := \lim_{n \rightarrow \infty} k\text{Cov}(\hat{\sigma}_{ij}(t), \hat{\sigma}_{lm}(t)) = \begin{cases} \nu_{ij}^2(t), & (i, j) = (l, m), \\ \rho_{ij,lm}(t) & \text{otherwise,} \end{cases},$$

where

$$\begin{aligned} \nu_{ij}^2(t) &:= \text{Var}_{H(\cdot;t)}(\Theta_i \Theta_j) \\ \rho_{ij}(t) &:= \frac{1}{2} [\text{Var}_{H(\cdot;t)}(\Theta_i \Theta_j + \Theta_l \Theta_m) - \nu_{ij}^2(t) - \nu_{lm}^2(t)] \end{aligned}$$

*Proof.* Fix  $t \in [0, 1]$ . The random vectors  $\{\mathbf{X}(l/n) : l \in \mathcal{I}(t)\}$  are independent and identically distributed with distribution  $H(\cdot; t)$ . The modified rate conditions (3.10) ensure that the original rate conditions (2.42) are satisfied on the sub-interval  $(t-h, t+h]$ : the number of local observations  $2nh(n) \rightarrow \infty$  and the extreme sampling fraction  $k(n)/2nh(n) \rightarrow 0$  as  $n \rightarrow \infty$ . Thus, we may invoke asymptotic normality of the empirical TPDM (Lemma 3.2) and the result follows immediately.  $\square$

We will always assume that  $V(t)$  is invertible. (This would not be permissible if we had defined the vecu operator to include diagonal entries.) The above result means that, roughly speaking, the entries of  $\hat{\Sigma}(t)$  behave like (correlated) normal random variables when  $n$  is sufficiently large. The implication is that each entry  $\psi_{ij}(t)$  of  $\hat{\Psi}(t)$  is the weighted sum of independent, asymptotically normal random variables. With this intuition, we can apply a functional central limit theorem type argument to derive the asymptotic behaviour of the stochastic process  $\{\hat{\psi}(t) : t \in [0, 1]\}$ .

**Lemma 3.3.** *Under the conditions of Lemma 3.2, the  $\mathcal{D}$ -dimensional, continuous-time stochastic process*

$$\left\{ \sqrt{\frac{k}{2h}} (\hat{\psi}(t) - \psi(t)) : t \in [0, 1] \right\}, \quad (3.12)$$

converges to a  $\mathcal{D}$ -dimensional centred Gaussian process  $\{\mathbf{Y}(t) : t \in [0, 1]\}$  with covariance function

$$\text{Cov}(\mathbf{Y}(s), \mathbf{Y}(t)) = \min(s, t)V \quad (3.13)$$

*Proof.* Since dependence is constant, we may denote by  $\boldsymbol{\sigma}$  and  $V$  the true local TPDM and asymptotic covariance matrix for all  $t \in [0, 1]$ . Let  $B = 1/(2h)$  be the number of blocks. For  $i = 1, \dots, B$ , let

$$\mathbf{Y}_{i/B} := \sqrt{k}(\hat{\boldsymbol{\sigma}}((2i-1)h) - \boldsymbol{\sigma}).$$

Then  $\{\mathbf{Y}_{i/B} : i = 1, \dots, B\}$  are independent, asymptotically normal random vectors with  $\mathbf{Y}_{i/B} \rightarrow N(\mathbf{0}, V)$  as  $n \rightarrow \infty$ . (Note that  $B \rightarrow \infty$  as  $n \rightarrow \infty$  due to the rate conditions.) Donsker's invariance principle states that the empirical process

$$\{\mathbf{Y}_B(t) : t \in [0, 1]\}, \quad \mathbf{Y}_B(t) := \frac{1}{\sqrt{B}} \sum_{i=1}^{\lfloor Bt \rfloor} \mathbf{Y}_{i/B},$$

converges to the process  $\{\mathbf{Y}(t) : t \in [0, 1]\}$  defined in the statement of the lemma. To complete the proof, observe that

$$\begin{aligned} \mathbf{Y}_N(t) &= \sqrt{2h} \sum_{i=1}^{\lfloor t/(2h) \rfloor} \sqrt{k}(\hat{\boldsymbol{\sigma}}((2i-1)h) - \boldsymbol{\sigma}) \\ &= \sqrt{2kh} \left( \frac{\hat{\psi}(t)}{2h} - \frac{t\boldsymbol{\sigma}}{2h} \right) \\ &= \sqrt{\frac{k}{2h}} (\hat{\psi}(t) - \psi(t)). \end{aligned} \quad \square$$

The drift and diffusion coefficients associated with each univariate limiting process  $\{Y_{ij}(t) : t \in [0, 1]\}$  are controlled by  $\{\psi_{ij}(t) : t \in [0, 1]\}$  and  $\{\nu_{ij}^2(t) : t \in [0, 1]\}$ , respectively. Meanwhile, the cross-correlation between  $\{Y_{ij}(t) : t \in [0, 1]\}$  and  $\{Y_{lm}(t) : t \in [0, 1]\}$  is determined by  $\{\rho_{ij,lm}(t) : t \in [0, 1]\}$ .

**Theorem 3.1.** *Suppose the conditions of Lemma 3.2 hold. Define*

$$\hat{\mathbf{Z}}(t) := \sqrt{\frac{k}{2h}} V(t)^{-1/2} (\hat{\psi}(t) - t\hat{\psi}(1)). \quad (3.14)$$

Then  $\{\hat{\mathbf{Z}}(t) : t \in [0, 1]\}$  converges to  $\{\mathbf{B}(t) : t \in [0, 1]\}$ , a standard  $\mathcal{D}$ -dimensional Brownian bridge.

*Proof.* Using Lemma 3.3 and pre-multiplying the process (3.12) by  $V^{-1/2}$ , it follows that

$$\left\{ \sqrt{\frac{k}{2h}} V^{-1/2} (\hat{\psi}(t) - \psi(t)) : t \in [0, 1] \right\}$$

converges to a  $\mathcal{D}$ -dimensional centred Gaussian process  $\{\mathbf{Y}(t) : t \in [0, 1]\}$  with covariance function

$$\text{Cov}(\mathbf{Y}(s), \mathbf{Y}(t)) = \min(s, t), \quad (3.15)$$

i.e. a  $\mathcal{D}$ -dimensional standard Brownian motion. By (3.7),  $\psi(t) = t\psi(1)$  under the null and therefore

$$\begin{aligned} \hat{\mathbf{Z}}(t) &= \sqrt{\frac{k}{2h}} V^{-1/2} (\hat{\psi}(t) - t\hat{\psi}(1)) \\ &= \sqrt{\frac{k}{2h}} V^{-1/2} [\hat{\psi}(t) - \psi(t) - t(\hat{\psi}(1) - \psi(1))] \\ &= \sqrt{\frac{k}{2h}} V^{-1/2} (\hat{\psi}(t) - \psi(t)) - t \left[ \sqrt{\frac{k}{2h}} V^{-1/2} (\hat{\psi}(t) - \psi(1)) \right] \\ &\rightarrow \mathbf{W}(t) - t\mathbf{W}(1), \end{aligned}$$

which is equivalent to a  $\mathcal{D}$ -dimensional standard Brownian bridge.  $\square$

This main result provides the foundation for our test. The test statistics defined in the following section will quantify whether the realised sample path of (3.14) is consistent with a Brownian bridge. We are not the first to use Brownian bridges in hypothesis testing in extremes; Gadeikis and Paulauskas (2005) use the same principle to test for changes in the tail index.

### 3.5. Test statistics and critical values

From the test process (3.14) we define Kolmogorov-Smirnov (KS) and Cramér-von-Mises (CM) type test statistics by

$$T^{(KS)} := \sup_{t \in [0,1]} \|\hat{\mathbf{Z}}(t)\|_\infty = \sup_{\substack{t \in [0,1] \\ i < j}} |Z_{ij}(t)|, \quad (3.16)$$

$$T^{(CM)} := \sup_{1 \leq i < j \leq d} \|\hat{Z}_{ij}(t)\|_{L^2[0,1]}^2 = \sup_{i < j} \int_0^1 |\hat{Z}_{ij}(t)|^2 dt, \quad (3.17)$$

where  $\|\mathbf{x}\|_\infty := \max\{|x_i| : i = 1, \dots, \mathcal{D}\}$  denotes the sup-norm in  $\mathbb{R}^\mathcal{D}$ ,  $\mathcal{D} = \binom{d}{2}$  and  $\|Y(t)\|_{L^2[0,1]}^2 := \int_0^1 |Y(t)|^2 dt$  denotes the  $L^2$ -norm of a stochastic process on  $[0, 1]$ . Their asymptotic null distributions are given below.

**Proposition 3.1.** *Under the null hypothesis (3.2),*

$$T^{(KS)} \rightarrow \sup_{t \in [0,1]} \|\mathbf{B}(t)\|_\infty \stackrel{d}{=} \sup_{i < j} K_{ij}, \quad T^{(CM)} \rightarrow \sup_{i < j} \|B_{ij}(t)\|_{L^2[0,1]}^2, \quad (3.18)$$

where  $\mathbf{B}(t) = (B_{ij}(t) : i < j)$  denotes a standard  $\mathcal{D}$ -dimensional Brownian bridge and  $\{K_{ij} : i < j\}$  are independent Kolmogorov random variables with distribution function

$$\mathbb{P}(K_{ij} < x) = F_K(x) = \begin{cases} 1 + 2 \sum_{m=1}^{\infty} (-1)^m \exp(-2m^2 x^2), & x \geq 0, \\ 0, & x < 0. \end{cases}$$

*Proof.* The asymptotic null distributions follows directly from Theorem 3.1. It is well known that  $K_{ij} := \sup_{t \in [0,1]} |B_{ij}(t)|$  follows a Kolmogorov distribution (Henze 2024, p. 328).  $\square$

Each test statistic  $T^{(KS)}$  and  $T^{(CM)}$  may be used to define an asymptotic test for constant dependence. For the KS test, the decision rule that rejects the null when

$$\mathbf{1}\{T^{(KS)} > c_\alpha\}, \quad c_\alpha = F_K^{-1}((1 - \alpha)^{1/\mathcal{D}}), \quad (3.19)$$

constitutes an asymptotic level  $\alpha$  test. The critical value  $c_\alpha$  represents the value for which a set of  $\mathcal{D}$  independent one-dimensional Brownian bridges *all* remain in the region  $(-c_\alpha, c_\alpha)$

Table 3.1.: Asymptotic critical values for selected dimensions and significance levels.

$d$	$\mathcal{D}$	$\alpha = 0.01$		$\alpha = 0.05$		$\alpha = 0.10$	
		CM	KS	CM	KS	CM	KS
2	1	0.743	1.628	0.460	1.358	0.346	1.224
3	3	0.953	1.788	0.648	1.544	0.524	1.425
4	6	1.086	1.882	0.775	1.652	0.643	1.540
5	10	1.173	1.949	0.874	1.727	0.733	1.620
10	45	1.479	2.133	1.152	1.933	1.024	1.837
15	105	1.623	2.230	1.310	2.039	1.174	1.949
20	190	1.724	2.296	1.433	2.111	1.287	2.024
25	300	1.824	2.345	1.532	2.164	1.370	2.079

with probability  $1 - \alpha$ . Note that we avoid issues with multiple testing because the critical value implicitly accounts for the dimension  $d$ . Specifically, the critical value increases with  $d$ . This is intuitive because with a greater number of paths  $\mathcal{D} = \mathcal{O}(d^2)$  there is a higher chance that at least one of them will exit a fixed interval  $(-c, c)$ . A CM-type test is constructed analogously. The only material difference is that the distribution of the  $L^2$ -norm of a Brownian bridge is unknown, so the critical values must be obtained via simulation. To this end, we generate 50,000 Brownian bridge sample paths on a fine mesh and compute their  $L^2$ -norms by numerical integration. Quantiles of the empirical distribution of these values are used to obtain approximate critical values. Critical values for selected dimensions and significance levels are listed in Table 3.1.

It is only feasible to produce a table of critical values due to the inclusion of the ‘nuisance process’  $\{V(t) : t \in [0, 1]\}$  in (3.14). Its role is to standardise and remove cross-correlation in  $\hat{\mathbf{Z}}(t)$ , ensuring a convenient asymptotic null distribution for our test statistics. In contrast, when  $d \geq 3$ , the critical values in Drees (2023) depend on the class of sets  $\mathcal{A}$  under consideration, so one is forced to resort to (intensive) simulations. To deal with the nuisance process, we simply estimate it from the data under the assumption of stationarity. Under the null,  $\{V(t) : t \in [0, 1]\}$  reduces to a single matrix,  $V$ , which we estimate as the sample covariance matrix of  $\hat{\boldsymbol{\sigma}} = \hat{\boldsymbol{\sigma}}(t)$  based on the set of radial threshold exceedances over

all blocks. That is

$$\hat{v}_{ij,lm} := 2h \sum_{s=1}^{1/(2h)} \hat{v}_{ij,lm}((2s-1)h),$$

$$\hat{v}_{ij,lm}(t) := \frac{1}{k-1} \sum_{\tau \in \mathcal{I}(t)} \left[ d\Theta_i \left( \frac{\tau}{n} \right) \Theta_j \left( \frac{\tau}{n} \right) - \hat{\sigma}_{ij}(t) \right] \left[ d\Theta_l \left( \frac{\tau}{n} \right) \Theta_m \left( \frac{\tau}{n} \right) - \hat{\sigma}_{lm}(t) \right] \mathbf{1} \left\{ R \left( \frac{\tau}{n} \right) > \hat{u}(t) \right\}.$$

Provided the rank condition

$$k_{\text{total}} := k/(2h) > \mathcal{D} \quad (3.20)$$

is satisfied, the estimator  $\hat{V}$  is full-rank and therefore invertible. For a fixed sample size and choice of  $k$  and  $h$ , the rank condition imposes an upper limit on the dimension, roughly  $d < \sqrt{2k_{\text{total}}} = \sqrt{k/h}$ . The existence of this limit reflects the principle that reliable inference in high-dimensional settings requires commensurate data. For fixed  $n$ , we may increase the limit by increasing  $k$  and/or  $h$ , but these parameters are subject to their own particular trade-offs that will influence the performance of the test. Alternatively, one could substitute  $V^{-1}$  with the pseudoinverse to circumvent the issue of invertibility altogether. This avenue is not explored on the basis that it doesn't seem sensible to proceed when the rank condition indicates there is insufficient data for the task at hand.

## 3.6. Simulation experiments

In this section, we present a series of numerical experiments demonstrating our method's performance and, where applicable, providing comparisons against Drees (2023).

### 3.6.1. Data generating processes

Suppose the extremal dependence structure of  $\mathbf{X}(t) = (X_1(t), \dots, X_d(t))$  is parametrised by  $\vartheta(t) \in \Omega$ , where  $\Omega$  is a convex parameter space. Let  $\vartheta_0, \vartheta_1 \in \Omega$  denote arbitrary parameters. We consider three scenarios for how the dependence varies over time:

1. **Constant:** the parameter is fixed, i.e.  $\vartheta(t) = \vartheta_0$ .
2. **Jump:** the parameter changes (instantaneously) from  $\vartheta_0$  to  $\vartheta_1$  at a change point  $\tau \in (0, 1)$ , i.e.  $\vartheta(t) = \vartheta_0 \mathbf{1}\{t < \tau\} + \vartheta_1 \mathbf{1}\{t \geq \tau\}$ . In all experiments we set  $\tau = 0.5$ .

3. **Linear:** the parameter evolves linearly from  $\vartheta_0$  to  $\vartheta_1$ , i.e.  $\vartheta(t) = \vartheta_0 + t(\vartheta_1 - \vartheta_0)$ . Convexity of  $\Omega$  guarantees that  $\vartheta(t) \in \Omega$  for all  $t \in [0, 1]$ .

The parametric models we consider are as follows:

1. **Symmetric logistic (SL):** with  $\gamma(t) = 1/\vartheta(t)$  and  $\Omega = [1, \infty)$ . With this parametrisation, asymptotic independence occurs when  $\vartheta(t) = 1$  and complete asymptotic dependence as  $\vartheta(t) \rightarrow \infty$ .
2. **Hüsler-Reiss (HR):** with  $\Lambda(t) = \vartheta(t)\Lambda_0$  and  $\Omega = (0, \infty)$ , where  $\Lambda_0 \in \mathbb{R}_+^{d \times d}$  is a valid HR parameter matrix (see Section 2.2.4.2). The multiplicative scalar  $\vartheta(t)$  has the effect of increasing ( $0 < \vartheta(t) < 1$ ) or decreasing ( $\vartheta(t) > 1$ ) the strength of all pairwise dependencies relative to  $\Lambda_0$ . While not strictly necessary, we take  $\vartheta_0 = 1$  so that  $\Lambda(0) = \Lambda_0$ . For each dimension  $d$ , the initial matrix  $\Lambda_0$  is randomly generated using the procedure outlined in Appendix B1 in Fomichov and Ivanovs (2023).

The three dependence scenarios and two parametric distributions give six qualitatively different models. We refer to these as, e.g. SL-constant, HR-jump, and so on. When  $d = 2$ , the test of Drees (2023) is included as a comparator. Results pertaining to their test are based on our own implementation based on a family of Borel subsets  $\mathcal{A} = \{A_y : y = 0.01, 0.02, \dots, 0.99\}$ , where

$$A_y := \{\boldsymbol{\theta} \in \mathbb{S}_{+(2)}^1 : \theta_1 \leq y\} \subset \mathbb{S}_{+(2)}^1. \quad (3.21)$$

For further details about the meaning and role of  $\mathcal{A}$ , see Section B.1.

### 3.6.2. Large sample performance

In an idealised setting with infinite data, the null distribution of the test statistics is as described in Proposition 3.1. This may be empirically validated via large-sample simulations by checking whether the p-values are uniformly distributed.

We generate 350 samples of size  $n = 10^6$  from the SL-constant ( $\vartheta_0 = 2$ ) and HR-constant ( $\vartheta_0 = 1$ ) models in dimensions  $d \in \{2, 5\}$ . The bandwidth is  $h = 10^{-3}$  and the level is  $k = 50$ . This yields 500 blocks containing  $b := 2nh = 2,000$  observations, a tail sampling fraction of  $k/b = 2.5\%$ , and an overall effective sample size of  $k_{\text{total}} = 25,000$ .

Figure 3.2 depicts the empirical quantile functions of the p-values (upper plots) and test statistics (lower plots) against their theoretical counterparts. For the KS-type test (left), the theoretical quantiles in the QQ plots are computed using the Kolmogorov quantile function implemented in the CPAT package. The theoretical quantiles for the CM-type test (right) are estimated from the aforementioned simulated Brownian bridges. In each panel, the dimension and parametric distribution are represented by the line type and colour, respectively. In all cases, the p-values appear to be approximately uniformly distributed. This indicates that for all nominal sizes the corresponding tests will approximately maintain the desired level. Analogous plots for Drees (2023) method can be found in Figure 7 within their Supplementary Material.

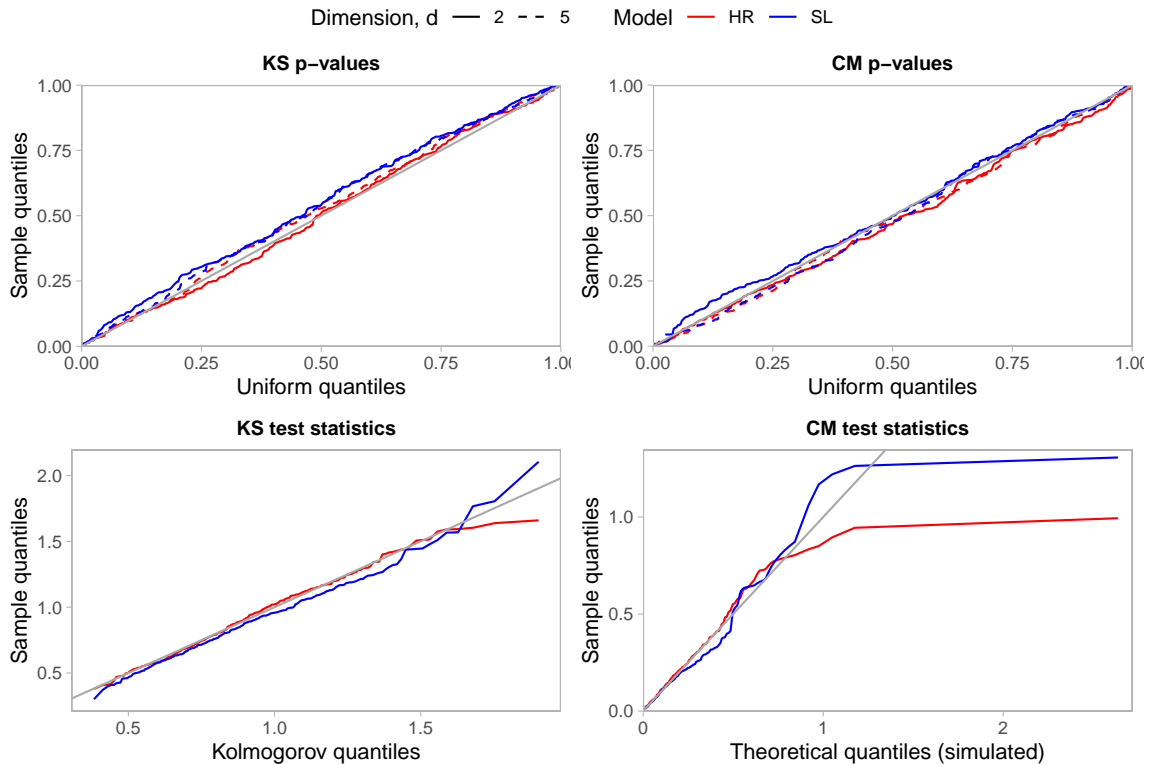


Figure 3.2.: Large sample Q-Q plots for the p-values (top) and test statistics (bottom) associated with the KS test (left) and CM test (right). Based on 350 simulations from the SL- and HR-constant models with  $n = 10^6$ ,  $b = 2000$  and  $k = 50$ .

Next, we check that our procedure detects dependence changes with high probability when the number of samples is large. The experimental procedure is unchanged, except that data are now generated from the SL-jump model with  $\vartheta_0 = 2$  and  $\vartheta_1 = 2.5$ . These values bring about relatively subtle shifts in the dependence strength, with  $\sigma_{ij}(t) = 0.85$  for  $t < 0.5$  and  $\sigma_{ij}(t) = 0.91$  for  $t \geq 0.5$ . All p-values are less than  $10^{-15}$ , meaning our method

consistently and overwhelmingly identifies the dependence change. To fully explore the asymptotic properties of the proposed methods, in the next sections we investigate how they perform for more moderate sample sizes.

### 3.6.3. Small sample performance

In finite sample settings, the empirical size of an asymptotic test will generally differ from its nominal size. The only guarantee is that the correct level is attained as  $n \rightarrow \infty$ . The hope is that convergence occurs with sufficient rapidity so that the difference between the prescribed and actual Type I error rates is acceptably small. To test this, we run simulations using the SL-constant ( $\vartheta_0 = 2$ ) and HR-constant ( $\vartheta_0 = 1$ ) models in dimensions  $d \in \{2, 5, 10, 25\}$  with sample sizes  $n \in \{2.5 \times 10^3, 5 \times 10^3, 10^4\}$ . For each data set, we apply our method at the 5% level. The number of blocks is  $n/b \in \{25, 50\}$  and the proportion of extreme observations within each block is  $k/b \in \{0.05, 0.10, 0.15\}$ . Table 3.2 reports the empirical Type I error rates of these tests. Blank cells indicate that the corresponding combination of tuning parameters was excluded because they violate the rank condition (3.20) or because  $k \leq d$ . Each value in the table is based on  $N$  repeated simulations, where  $N = 10^3$  if  $d \leq 5$  and  $N = 300$  otherwise. Results from the large sample experiments in dimensions  $d \in \{2, 5\}$  are included (bottom row) for completeness.

First we review the results for  $d = 2$ . Under our method and Drees' method, the rejection rate of the CM-based test is consistently around 5% for almost any choice of  $b$  and  $k$ , even when  $n = 2,500$ . The KS-based tests are universally more conservative than the CM-based tests, particularly for larger block sizes. Drees (2023) attribute this to the fact that a coarsely discretised path may only attain its supremum at a small number of time points (integer multiples of  $2h$ ), whereas the corresponding critical values arise from suprema of continuous processes. However, for any value of  $n$ , there exists a pair of tuning parameters such that the discrepancy between the empirical and nominal size is at most 0.7%.

Now consider the columns for  $d \geq 5$ . It is not possible to include Drees (2023) as a comparator here because, by their own admission, the necessary computations become prohibitively expensive. We find that the KS-test remains rather conservative, so we shall focus on the CM-test instead. When  $d = 5$ , our procedure works well for both models, even when  $n$  is small. For  $d = 10$  and  $d = 25$ , the rank conditions on  $\hat{V}$  and  $\hat{\Sigma}(t)$  take effect,

Table 3.2.: Empirical Type I error rates (%). All tests have nominal size 5%.

(a) SL-constant.

$n$	$n/b$	$k/b$	$d = 2$				$d = 5$				$d = 10$		$d = 25$	
			Drees		Pawley		Pawley		Pawley		Pawley		Pawley	
			CM	KS	CM	KS	CM	KS	CM	KS	CM	KS	CM	KS
2,500	25	0.050	3.2	2.4	5.5	2.9								
		0.100	3.9	2.2	5.0	2.7	4.5	1.2						
		0.150	3.6	2.1	5.6	3.7	6.1	3.0	2.9	0.6				
	50	0.100	3.6	2.6	6.4	3.5								
		0.150	2.9	2.1	5.8	3.9	3.8	2.2						
5,000	25	0.050	3.7	1.0	4.7	2.9	4.5	1.4						
		0.100	3.5	2.2	4.9	2.5	4.5	1.5	3.1	1.7				
		0.150	3.5	2.0	5.4	2.7	5.1	2.3	3.7	0.9	4.0	0.3		
	50	0.050	4.1	3.1	5.5	3.7								
		0.100	3.7	3.2	5.5	3.5	4.2	2.6						
		0.150	3.9	2.5	5.8	3.4	5.9	2.9	4.0	0.9				
10,000	25	0.050	4.6	3.0	4.5	2.1	4.5	2.0	4.0	0.9				
		0.100	4.5	2.5	4.4	2.5	4.3	2.3	3.4	1.1	1.7	0.6		
		0.150	3.6	2.1	4.5	2.2	4.0	1.9	5.7	2.3	3.4	0.6		
	50	0.050	3.6	2.5	4.1	2.7	5.5	3.2						
		0.100	4.5	2.9	5.9	2.8	5.1	2.4	5.4	1.7				
		0.150	3.9	2.4	5.1	2.8	6.0	3.0	3.1	0.9	5.4	2.6		
1,000,000	500	0.025	2.9	3.1	4.3	3.4	5.1	4.6						

(b) HR-constant.

$n$	$n/b$	$k/b$	$d = 2$				$d = 5$				$d = 10$		$d = 25$	
			Drees		Pawley		Pawley		Pawley		Pawley		Pawley	
			CM	KS	CM	KS	CM	KS	CM	KS	CM	KS	CM	KS
2,500	25	0.050	3.7	2.0	5.5	3.6								
		0.100	4.7	2.9	6.9	4.2	4.8	1.5						
		0.150	3.8	2.4	6.5	3.8	4.9	1.9	4.6	1.7				
	50	0.100	3.4	2.6	6.6	4.5								
		0.150	4.6	2.9	7.4	5.4	4.6	2.5						
5,000	25	0.050	3.6	1.8	5.6	3.8	4.5	2.9						
		0.100	4.0	2.5	8.3	4.9	5.0	2.4	1.7	0.0				
		0.150	4.4	2.6	6.4	3.3	4.5	2.1	4.3	2.6	1.4	0.3		
	50	0.050	4.1	2.7	7.5	5.3								
		0.100	5.3	3.8	8.2	5.3	4.2	2.2						
		0.150	4.7	3.8	6.1	4.8	5.2	2.5	2.6	1.4				
10,000	25	0.050	4.4	2.6	6.6	4.2	4.5	1.8	4.0	0.6				
		0.100	5.8	2.8	5.6	3.0	5.2	2.5	3.7	2.0	0.9	0.0		
		0.150	5.1	3.4	6.9	3.6	5.3	1.9	6.3	2.6	2.0	1.1		
	50	0.050	4.4	3.2	6.9	5.1	5.1	2.4						
		0.100	3.8	2.8	5.8	3.5	5.7	3.0	4.9	2.6				
		0.150	4.6	2.9	5.4	3.5	4.9	3.5	6.0	4.6	2.0	0.6		
1,000,000	500	0.025	6.0	4.9	5.4	4.9	6.6	4.6						

drastically reducing the set of admissible tuning parameters when  $n \leq 5,000$ . Nevertheless, even in these high-dimensional settings, the test produces reasonable results, especially for symmetric logistic data. Performance deteriorates under the 25-dimensional Hüsler-Reiss model, suggesting there may be insufficient data for the asymptotic approximations to hold.

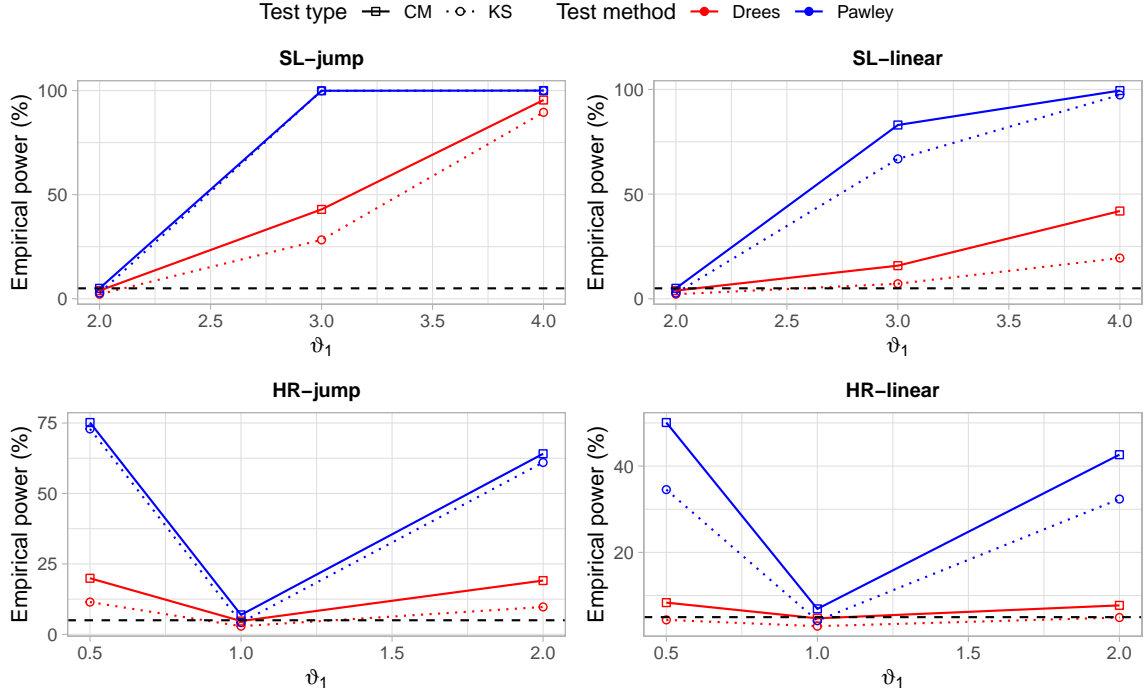


Figure 3.3.: Empirical power (%) as a function of the dependence parameter  $\vartheta_1$ . Based on 1000 simulations with  $n = 2,500$  and  $d = 2$ . For the SL and HR models,  $\vartheta_0 = 2$  and  $\vartheta_0 = 1$ , respectively. Tests are conducted at the 5% level (black dashed line).

Our next experiment assesses the empirical power under alternatives. For this, we generate data from the SL-jump ( $\vartheta_0 = 2$ ), SL-linear ( $\vartheta_0 = 2$ ), HR-jump ( $\vartheta_0 = 1$ ) and HR-linear ( $\vartheta_0 = 1$ ) models. The parameter  $\vartheta_1$  at time 1 is allowed to vary, permitting an examination of the relationship between the power and the magnitude of the dependence change. For each model and value of  $\vartheta_1$ , we simulate 1,000 data sets with  $d = 2$  and  $n = 2,500$ . All tests are conducted at the 5% level.

Figure 3.3 displays the results for  $n/b = 25$  and  $k/b = 0.1$ ; Figure B.1 in Section B.2 confirms that the conclusions are not overly sensitive to this choice. The plots show that our test achieves superior power compared to Drees (2023) in all scenarios. When the null is true,  $\vartheta_1 = \vartheta_0$ , the power of the test reverts to 5%. All tests easily detect the largest SL-jump

change, achieving near full power in this case. On the other hand, Drees' test is virtually powerless under the more challenging HR-linear scenario, while our procedure maintains a respectable level of performance. Here, the effect of focusing on bivariate summaries rather than the full angular measure becomes evident. Imposing additional structure/assumptions – namely that the TPDM provides an adequate summary of dependence – improves the signal-to-noise ratio, so that subtle dependence changes may be detected. In the case of both the symmetric logistic and Hüsler-Reiss models, this assumption is valid (and therefore helpful) due to the one-to-one correspondence between the model parameter and the TPDM. An example where this is not the case is given in Section 3.7. When dependence changes abruptly (SL-jump and HR-jump), the CM- and KS-based test perform equally well. Upon further investigation, we find that the path  $\{\hat{Z}_{12}(t) : t \in [0, 1]\}$  is a  $\wedge$ -shaped curve attaining its maximum at  $t = 0.5$  (when the changepoint occurs). Thus  $T^{KS} \approx \hat{Z}_{12}(0.5)$  and, upon approximating  $\{|\hat{Z}_{12}(t)|^2 : t \in [0, 1]\}$  by a triangle,  $T^{CM} \approx \hat{Z}_{12}^2(0.5)/2$ . Both test statistics are determined by  $\hat{Z}_{12}(t)$ , so they invariably reach the same outcome. For gradual changes the CM-based test is superior, cf. Figures 1 and 2 in Drees (2023).

Figure 3.4 shows how the power of the KS test evolves as more data is acquired. The experimental procedure is the same as above, except the sample size is allowed to vary. The Q-Q plots depict the distribution of the p-values across 1,000 repeated tests for the HR-jump (left) and HR-linear (right) models based on different values of  $\vartheta_1$  (line type) and  $n$  (line colour). If a test is highly-powered, then the associated curve will lie below the diagonal. In both scenarios, the power improves as  $n$  increases. The effect is more pronounced for the linear dependence change. Intuitively, for an instantaneous change the test only needs to learn the dependence strength before the change-point and after the change-point. This does not require a large amount of information. Detecting gradual changes places more emphasis on accurate local estimation, especially near the end-points of the time interval, so acquiring additional data has a greater effect.

### 3.6.4. Computation time

A key advantage of our approach is that the computations are considerably less intensive than those required by Drees (2023). As explained earlier, this permits its application in moderate to high-dimensional settings. Another benefit is reduced run times, which

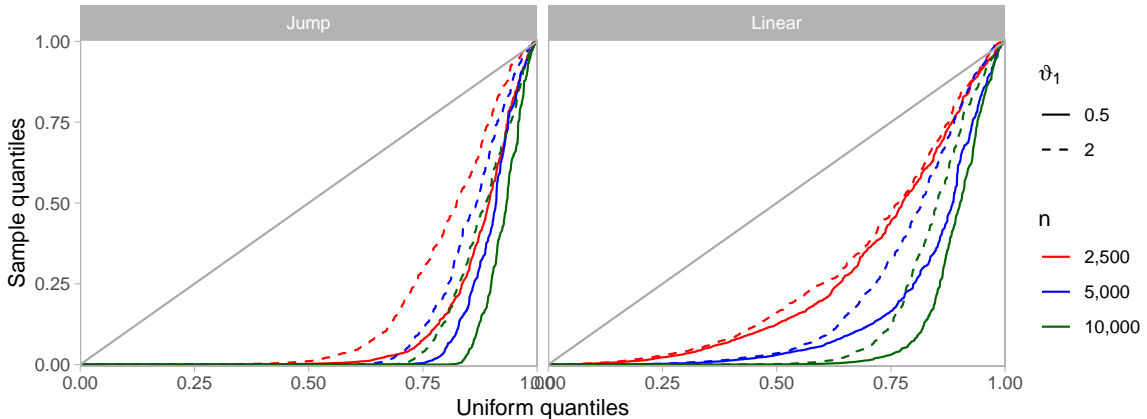


Figure 3.4.: QQ-plots for the KS p-values with varying sample size. Based on 1,000 simulations from the HR-jump (left) and HR-linear (right) models with tuning parameters  $n/b = 25$  and  $k/b = 0.1$ .

may be an important consideration if the test is to be performed repeatedly (e.g. see the data application in Section 3.8). This prompts us to analyse the computation times for the simulation experiments in Section 3.6.3. The left-hand plot in Figure 3.5 shows the distribution of the total elapsed time (in seconds) against  $n$ . The number of blocks is  $n/b = 50$ ; the number of extremes per block is indicated by the bar colour. Our procedure is faster than Drees', though the difference is only a few hundredths of a second. The test remains fast even when  $n = 10^4$ . This isn't particularly surprising, since discarding the non-extreme observations means the effective sample size is never actually very large. The right-hand plot shows average computation time to run the test as a function of  $k_{\text{total}}$  for different dimensions  $d$ . Dimension is clearly the key determinant of computation time. This is predominantly due to the inversion of the  $\mathcal{D} \times \mathcal{D}$  matrix  $\hat{V}$ , which has  $\mathcal{O}(\mathcal{D}^3) = \mathcal{O}(d^6)$  complexity.

### 3.7. Loss of power under TPDM-invariant dependence changes

Our test affords several advantages compared to Drees (2023), most notably the ability to conduct tests in high dimensions. However, the correspondence between dependence structures and TPDMs is many-to-one, so we forgo the ability to detect certain dependence changes where the TPDM is invariant. For this class of alternatives our test is inherently predisposed to commit Type II errors. In contrast, Drees' test is consistent under general

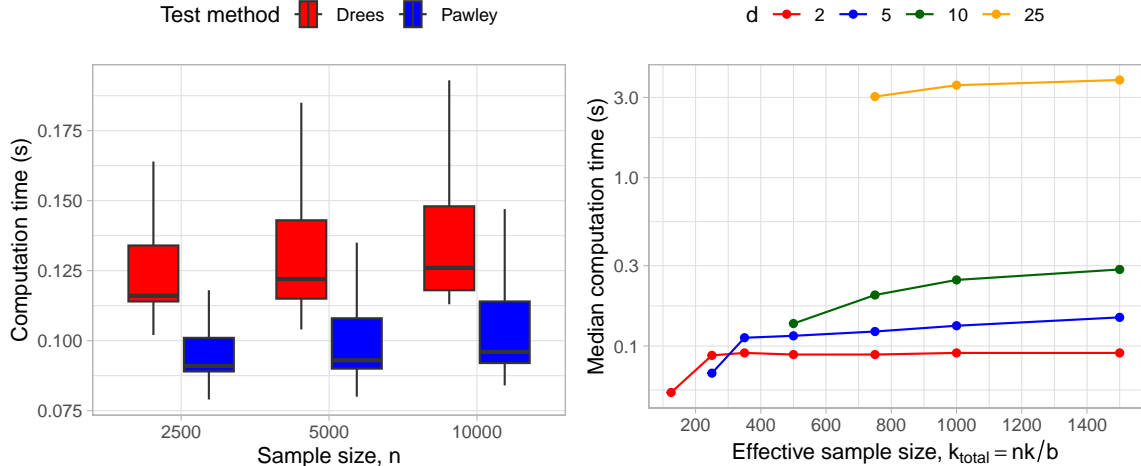


Figure 3.5.: Analysis of computation times across the numerical experiments described in Section 3.6.3. Left: empirical distribution of run times when  $d = 2$ ,  $n/b = 50$ ,  $k/b = 0.1$ . Right: median computation time for the test as a function of the total number of threshold exceedances.

alternatives (Drees 2023, Corollary 3.2(ii)). We exemplify this using a time-dependent generalisation of the max-linear model.

Suppose  $\{\mathbf{X}(t) : t \in [0, 1]\}$  is a  $d$ -dimensional stochastic process defined by

$$\mathbf{X}(t) = A(t) \times_{\max} \mathbf{Z}(t), \quad A(t) = A_0 \mathbf{1}\{t < 0.5\} + A_1 \mathbf{1}\{t \geq 0.5\}. \quad (3.22)$$

The stochastic innovations process  $\{\mathbf{Z}(t) = (Z_1(t), \dots, Z_q(t)) : t \in [0, 1]\}$  is a collection of independent random vectors such that, for any  $t \in [0, 1]$ , the  $q \geq 1$  components of  $\mathbf{Z}(t)$  are independent 2-Fréchet random variables. The dependence structure of  $\mathbf{X}(t)$  is characterised by the parameter matrix  $A(t) = (a_{ij}(t)) \in \mathbb{R}_+^{d \times q}$ . Under the model (3.22),  $A(t)$  undergoes a jump-change from  $A_0 \in \mathbb{R}_+^{d \times q}$  to  $A_1 \in \mathbb{R}_+^{d \times q}$  at time  $\tau = 0.5$ . More complicated models can easily be conceived, whereby  $A(t)$  evolves smoothly, perhaps even with a varying number of factors  $q = q(t)$ . The local angular measure associated with (3.22) can be expressed in terms of the columns  $\mathbf{a}_1(t), \dots, \mathbf{a}_q(t) \in \mathbb{R}_+^d$  of  $A(t)$  as

$$H(\cdot ; t) = \sum_{j=1}^q \|\mathbf{a}_j(t)\|_2^2 \delta_{\mathbf{a}_j(t)/\|\mathbf{a}_j(t)\|_2}(\cdot).$$

By Example 2.7, the local TPDM is given by  $\Sigma(t) = A(t)A(t)^T$ . A formula for the asymptotic asymptotic covariance  $V(t)$  matrix is derived in Section A.1.4.

Suppose  $A_0$  and  $A_1$ , with  $A_0 \neq A_1$  including up to permutations of their columns, are such that  $\Sigma(0) = \Sigma(1)$  and  $V(0) = V(1)$ . Then the alternative hypothesis (3.3) is true but the asymptotic distributions of  $T^{(KS)}$  and  $T^{(CM)}$  are the null distributions in (3.18). Clearly this presents an issue for our test.

To illustrate this problem empirically, we seek a pair of matrices  $A_0, A_1$  with a common TPDM and asymptotic covariance. Constructing a non-trivial (i.e.  $q > 2$ ) pair by hand would be extremely laborious. Instead, we generate a large set of valid candidate matrices  $A \in \mathbb{R}_+^{d \times q}$  with  $d = 2$  and  $q = 20$  and search for a suitable pair among these. This process yields the matrices shown in Figure 3.6. To emphasise that they parametrise different extreme value distributions, the matrices' columns are reordered so that  $a_{11} < a_{12} < \dots < a_{1q}$ . Substituting these into (3.22) gives  $\sigma_{12}(t) = 0.100$  and  $\nu_{12}^2(t) = 0.060$  for all  $t \in [0, 1]$ .

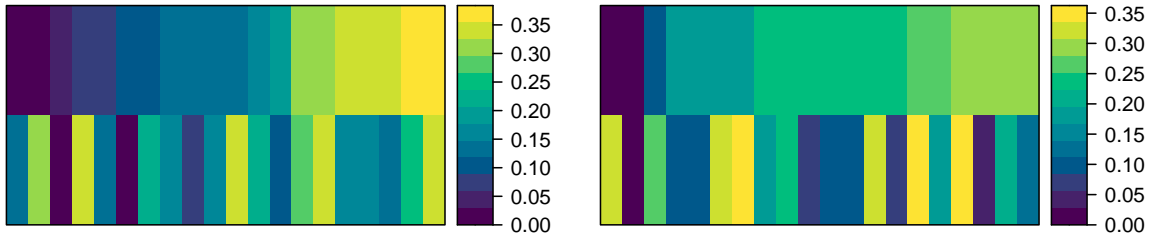


Figure 3.6.: A pair of max-linear parameter matrices  $A_0$  (left) and  $A_1$  (right) such that the process (3.22) satisfies  $\sigma_{12}(t) = 0.100$  and  $\nu_{12}^2(t) = 0.060$  for all  $t \in [0, 1]$ .

We generate 1,000 realisations of (3.22) with  $n = 10,000$  and test for changing dependence using 25 blocks of size  $b = 400$  and  $k = 40$  extremes per block. The diagnostic plots in Figure 3.7 provide insight into what happens for one of these tests. The top-left plot shows that  $\hat{\sigma}(t) \approx 0.8$  for all  $t \in [0, 1]$ , up to some random variation. Using (2.58) one can show that  $\mathbb{P}(\hat{\sigma}_{12}(t) \in (0.724, 0.876)) \approx 0.95$ . Indeed, the empirical coverage of this interval is 93.56%, based on all  $1,000 \times 25 = 25,000$  estimates of  $\sigma_{12}(t)$ . The empirical integrated TPDM  $\{\hat{\psi}_{12}(t) : t \in [0, 1]\}$  (top-right) is approximately a straight line and the test process  $\{\hat{Z}_{12}(t) : t \in [0, 1]\}$  (bottom-left) resembles a typical Brownian bridge sample path. The bottom-right plot depicts  $\int_0^t |\hat{Z}_{12}(s)|^2 ds$  (upper sub-panel) and  $\sup_{0 \leq s \leq t} |\hat{Z}_{12}(s)|$  (lower sub-panel) as functions of  $t$ . The maxima of these processes are the CM and KS test statistics. Neither exceed the associated critical values at the 5% level, marked by the dashed lines. We conclude there is insufficient evidence to reject the null and commit a Type II error. The empirical Type II error rates across 1,000 repetitions of the experiment

are 94.5% (CM) and 96.5% (KS). In other words, the rejection rate approximately equals the nominal size of the test, meaning the test has no power.

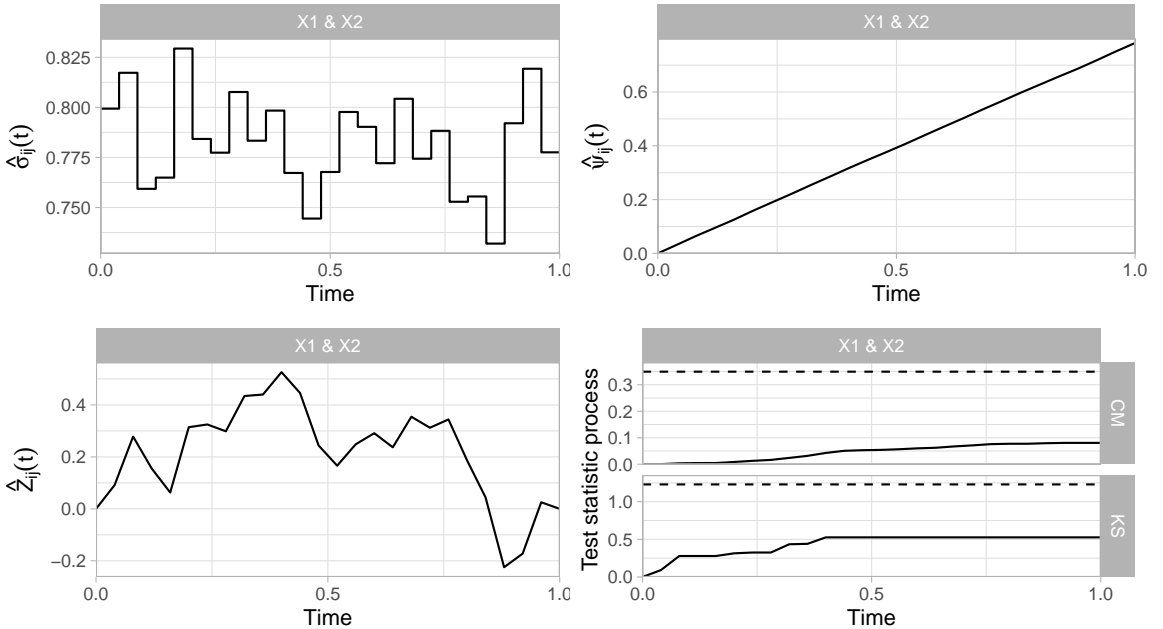


Figure 3.7.: Diagnostic plots for our testing procedure based on one realisation of (3.22) with  $A_0$  and  $A_1$  as shown in Figure 3.6 and  $n = 10,000$ . The tuning parameters are  $b = 400$  and  $k = 40$ . Top-left: the empirical local TPDM  $\{\hat{\sigma}_{12}(t) : t \in [0, 1]\}$ . Top-right: the empirical integrated TPDM  $\{\hat{\psi}_{12}(t) : t \in [0, 1]\}$ . Bottom-left: the test process  $\{\hat{Z}_{12}(t) : t \in [0, 1]\}$ . Bottom-right:  $\int_0^t |\hat{Z}_{12}(s)|^2 ds$  (upper sub-panel) and  $\sup_{0 \leq s \leq t} |\hat{Z}_{12}(s)|$  (lower sub-panel) as functions of  $t$  along with the CM and KS critical values at the 5% level (dashed line).

Figure 3.8 presents analogous plots based on Drees' testing method applied to the same data. The left-hand plot shows the normalised empirical integrated angular measure  $d^{-1}\hat{IH}(A_y; t)$  as a function of  $t$ . Each curve corresponds to a particular set  $A_y \in \mathcal{A}$  defined in (3.21) with darker colours indicating larger values of  $y$ . Close inspection of these curves reveals that some of them are slightly kinked at  $t = 0.5$ . The middle panel visualises the processes

$$\hat{Z}_y(t) := \sqrt{\frac{k}{2h}}(\widehat{\text{IH}}(A_y; t) - t\widehat{\text{IH}}(A_y; 1)), \quad (A_y \in \mathcal{A}). \quad (3.23)$$

These perform the same role as  $\{\hat{Z}_{ij}(t) : t \in [0, 1]\}$  but are less straightforward to interpret due to the presence of cross-correlation. The maxima (taken over all  $A_y \in \mathcal{A}$ ) of the processes  $\int_0^t |\hat{Z}_y(s)|^2 ds$  (right, upper sub-panel) and  $\sup_{0 \leq s \leq t} |\hat{Z}_y(s)|$  (right, bottom sub-panel) are the CM and KS test statistics. These exceed the dashed lines marking the critical values (Drees 2023, Table 1). According to either test we (correctly) reject the null

hypothesis at the 5% level. The empirical power based on 1,000 repeats is 100% (CM) and 99.8% (KS). Clearly the dependence change is easily detectable with the available data, emphasising that the deficiency of our test is purely methodological and not due to, say, a lack of data.

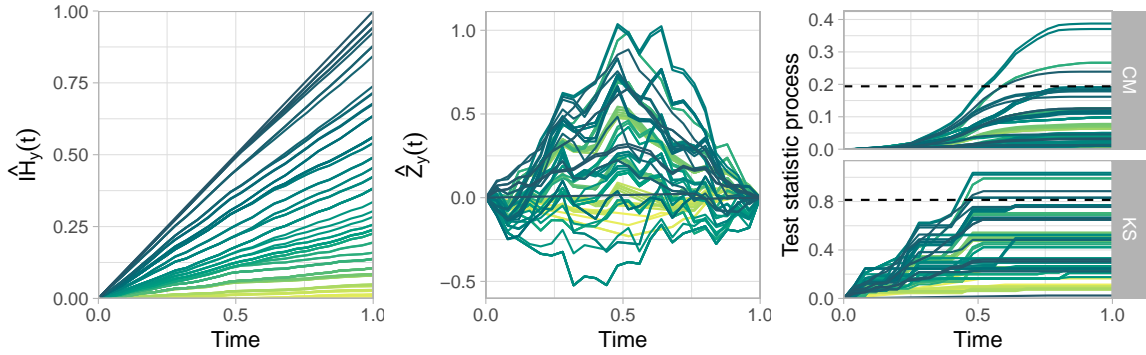


Figure 3.8.: Diagnostic plots for Drees' testing procedure based on one realisation of (3.22) with  $A_0$  and  $A_1$  as shown in Figure 3.6 and  $n = 10,000$ . The tuning parameters are  $b = 400$  and  $k = 40$ . Each curve represents a set  $A_y$  with darker colours indicating larger values of  $y$ . Left: the empirical integrated angular measure  $\{\widehat{IH}_{12}(A_y; t) : t \in [0, 1]\}$ . Middle: the test process  $\{\widehat{Z}_y(t) : t \in [0, 1]\}$ . Right:  $\int_0^t |\widehat{Z}_y(s)|^2 ds$  (upper sub-panel) and  $\sup_{0 \leq s \leq t} |\widehat{Z}_y(s)|$  (lower sub-panel) as functions of  $t$  along with the CM and KS critical values at the 5% level (dashed line).

### 3.8. Application: Extreme Red Sea surface temperatures

We now apply our methodology to test for changing dependence in extreme Red Sea surface temperature anomalies. The dataset has been widely studied in the extremes community (Castro-Camilo et al. 2021; Rohrbeck et al. 2021; Simpson and Wadsworth 2021) having been the subject of the EVA (2019) Data Challenge (Huser 2021). Further details about the data set and pre-processing can be found in Huser (2021). Non-stationarity in the marginal distributions was handled using the approach in Castro-Camilo et al. (2021). (The pre-processed data were obtained directly from the authors of the paper; we did not implement their approach ourselves.)

Detecting changes in extremal dependence in the Red Sea is of significant practical importance. Increased spatial dependence could lead to prolonged periods of elevated sea temperatures, exacerbating ecological issues such as coral bleaching and reducing the re-

silence of marine biodiversity. Red Sea surface temperatures are influenced by broader climate drivers, including the El Niño–Southern Oscillation (ENSO) (Karnauskas and Jones 2018). In a study of extreme precipitation, Jiang et al. (2020) found evidence for a positive temporal trend in the coefficients associated to principal eigenvectors related with ENSO. Moreover, Figure 3 in Kakampakou et al. (2024) shows increases in the tail dependence coefficient  $\chi$  between pairs of sites based on data from the periods 1985-1989 and 2011-2015, especially in the north. These findings point towards the possibility of non-stationary tail dependence.

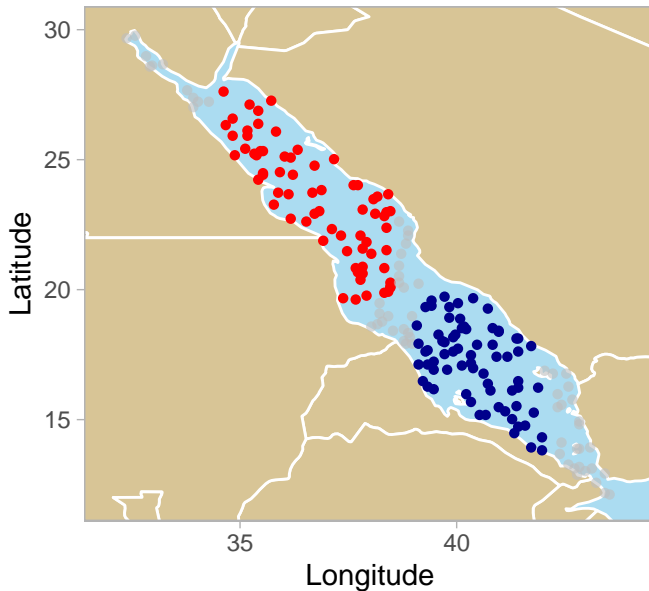


Figure 3.9.: Locations of the 70 sites in each of the two sub-regions in the Red Sea.

From the original gridded data set, we select 200 sites at random before dividing the spatial domain into northerly and southerly sub-regions, each comprising 70 sites as shown in Figure 3.9. Simpson and Wadsworth (2021) advise treating these areas separately because surface temperature extremes exhibit differing behaviour in the north and south. Additionally, they show that, at any particular location, high temperatures may persist across several days resulting in (temporal) clusters of extremes of daily maxima. To eliminate serial dependence we instead work with weekly maxima, yielding  $n = 1605$  samples spanning approximately 31 years. Let  $X_i^{(\text{north})}(t)$  and  $X_i^{(\text{south})}(t)$  denote the surface temperature anomaly (on stationary 2-Fréchet margins) at site  $i \in \{1, \dots, 70\}$  and time  $t \in [0, 1]$  in the two sub-regions. Our goal is to determine whether it is reasonable to assume stationary

dependence for either/both of

$$\begin{aligned}\mathbf{X}^{(\text{north})}(t) &= \{X_i^{(\text{north})}(t) : i = 1, \dots, 70\}, \\ \mathbf{X}^{(\text{south})}(t) &= \{X_i^{(\text{south})}(t) : i = 1, \dots, 70\}.\end{aligned}$$

To this end, we run the test using 15 blocks of size  $b = 107$  and  $k = 20$ , yielding  $k_{\text{total}} = 15 \times 20 = 300$ . The rank condition (3.20) restricts us to testing up to 17 sites at a time, but even this seems excessive with only 20 extremes per block. Our strategy will be to repeatedly re-sample  $2 \leq d \leq 17$  sites from each region and apply the test to these lower-dimensional data sets. The distribution of p-values across 1,000 repeats with  $d \in \{2, 5, 10\}$  are shown in Figure 3.10. The columns correspond to different numbers of re-sampled sites. The rows indicate the sub-region and the test type. The value printed at the top of each panel is the proportion of tests that are rejected at the 5% level. If dependence is constant (resp. time-varying) across the sub-region, then the distribution of p-values is expected to be approximately uniform (resp. positively skewed). The evidence for non-stationarity is fairly strong in the north (average rejection rate of 48.6%) and comparatively weaker in the south (20.1%). This aligns with the findings in Kakampakou et al. (2024). The CM test rejects the null much more frequently than the KS test. Our simulation studies suggested that CM tends to be superior when the dependence change is gradual, as is likely to be the case here. For all tests and regions, the rejection rate is highest when  $d = 5$ , and drops off when  $d$  is reduced or increased. We believe this reflects the trade-off between two factors. On the one hand, taking a large pool of sites increases the chance that among them there exists at least one pair with time-varying dependence. On the other hand, the local TPDM estimates become noisier, potentially masking any temporal trends. Figure B.2 in Section B.2 provides some diagnostic plots for one run of our test in the north and south when  $d = 5$ .

### 3.9. Conclusion and outlook

In this chapter, we presented a new test for detecting changes in the extremal dependence structure over time. Compared to the test of Drees (2023), our method is less intensive computationally, applicable in higher dimensions, and is more powerful provided the de-

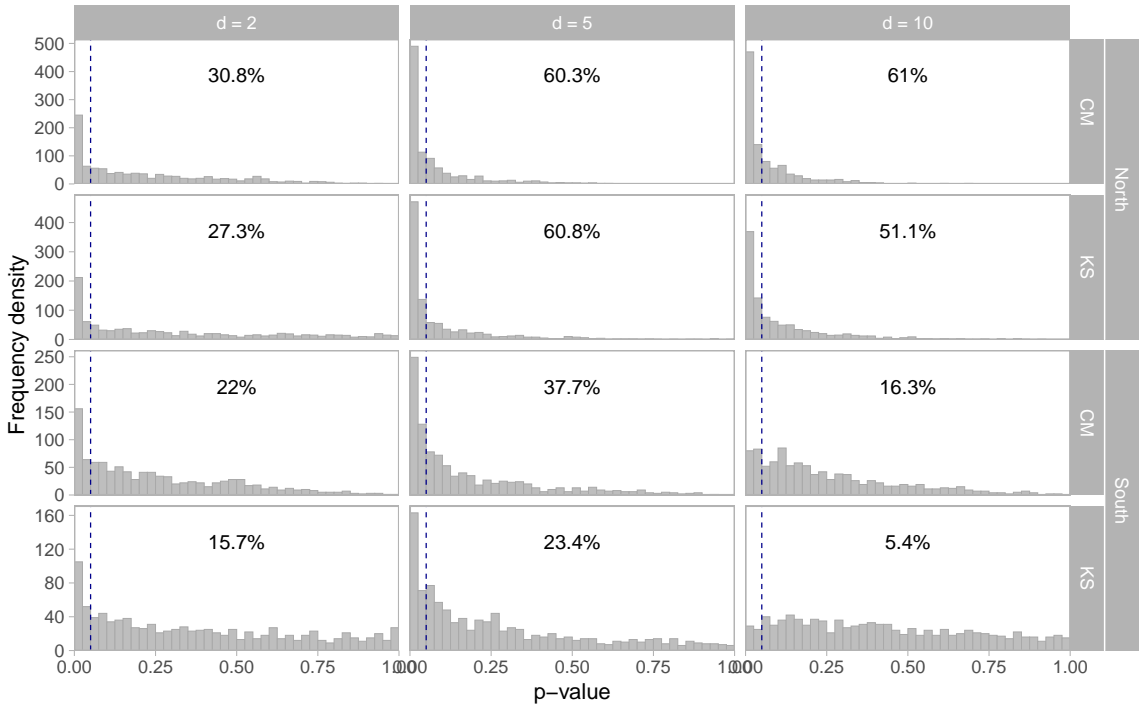


Figure 3.10.: Empirical distributions of the p-values based on tests for changing dependence in the north and south regions of the Red Sea. The columns correspond to the number of re-sampled sites; the rows indicate the sub-region and the test type. The rejection rate at the 5% level is printed at the top of each panel.

pendence change manifests as a change in the entries of TPDM. We anticipate that our test will be of use to applied statisticians seeking to validate key model assumptions and practitioners hoping to explore how climate change or regulatory changes have affected the stochastic behaviour of joint extremes over time.

At present, there are several minor drawbacks to our proposed approach. In terms of computational complexity, the main bottleneck is inversion of the asymptotic covariance matrix  $V$ . To apply our test in very high dimensions it will be necessary to speed up this step, perhaps by making some additional assumptions (e.g. sparsity) about the structure of  $V$ . Secondly, the performance of our test is constrained by the performance of the TPDM estimator it is founded on. In situations where the empirical TPDM performs poorly, our test's performance may suffer accordingly. This is evidenced by the results of some preliminary simulation experiments – see Section B.3. The development of improved estimators, such as those in Chapter 6, should ameliorate this issue.

The theory underpinning our procedure holds for the general class of dependence measures

of the form  $\mathbb{E}_H[f(\Theta)]$ , provided  $f$  is continuous (Theorem 2.3). Thus, one is not necessarily wedded to the TPDM. It is conceivable that particular choices for  $f$  are better-suited to detecting certain kinds of dependence changes. An exploration into this is beyond the scope of our present investigation.

An obvious extension to our framework is to consider *when* a change occurs, i.e. change point detection. This research direction is being actively pursued – see Section 7.2.1 for further details.

## 4. A compositional perspective on multivariate extremes

### 4.1. Motivation

In multivariate extreme value statistics, the analysis of angular distributions is central to understanding the tail dependence structure. The angular measure describes the direction of large observations, focussing on the relative proportions of variables at extreme levels rather than their absolute values. Compositional data analysis (CoDA) provides tools to handle data that carry only relative information, enabling a more robust inference by accounting for the constraints imposed by their simplex structure (Aitchison 1986). EVA and CoDA have been connected on several occasions: Coles and Tawn (1991) remark on the similarity between parametric models for CoDA and models for the angular measure; De Carvalho (2016) sketches a possible approach to extremal PCA that involves applying “PCA for compositional data to the pseudo-angles” to “disentangle dependence into components of practical interest”; Serrano (2022) constructs bivariate extreme value copulas using compositional splines. Apart from these sporadic cases, the connection between these two disciplines remains unexplored in the current literature. This chapter aims to demonstrate this untapped potential.

First, we will review the core CoDA principles and concepts and draw high-level connections to MEV analysis. Then, we provide some tangible examples that illustrate our point more concretely. Specifically, we apply a CoDA lens to two statistical learning problems within multivariate extremes: tail dimension reduction via principal components analysis (Clémençon et al. 2024; Cooley and Thibaud 2019; Drees and Sabourin 2021) and binary classification in extreme regions (Jalalzai et al. 2018). We demonstrate that off-the-shelf

CoDA methods are readily applicable to these problems and are competitive against the current state-of-the-art.

## 4.2. Compositional data analysis

### 4.2.1. Compositions and the Aitchison geometry

Compositional data analysis is a relatively modern statistical discipline that has been adopted across various fields including economics, geology, biology, political science, and many others (Alenazi 2023). Its widespread applicability stems from the ubiquity of compositional data, i.e. data whose components represent parts of a whole and convey only relative information. For example, a geologist analysing the chemical composition of rock samples is interested in the relative abundances of its constituent elements rather than the absolute amounts (which ultimately depend on the size of the rock sample). Two vectors  $\mathbf{x}, \mathbf{y} \in \mathbb{R}_+^d := (0, \infty)^d$  are compositionally equivalent, denoted  $\mathbf{x} \sim \mathbf{y}$ , if there exists  $c > 0$  such that  $\mathbf{y} = c\mathbf{x}$ . The equivalence relation  $\sim$  defines equivalence classes on  $\mathbb{R}_+^d$ . For  $\mathbf{x} \in \mathbb{R}_+^d$ , the compositional class  $[\mathbf{x}] := \{c\mathbf{x} : c > 0\}$  may be represented by a closed composition on the  $d$ -part unitary simplex,

$$\mathcal{C}\mathbf{x} := \frac{\mathbf{x}}{\|\mathbf{x}\|_1} \in \mathbb{S}_{+(1)}^{d-1}.$$

Thus the natural sample space of compositional random vectors is the  $L_1$ -simplex  $\mathbb{S}_{+(1)}^{d-1}$ . In his seminal paper, Aitchison (1982) contends that standard multivariate analysis techniques are inappropriate for modelling compositions because they are intended for unconstrained data. Neglecting the compositional constraint causes an array of difficulties, including detecting spurious correlations (Pearson 1897; Aitchison 1982), difficulties representing the structure of the data (Aitchison 1983), and contradictory conclusions between analyses (Aitchison 1986). The consensus solution is to work in a statistical framework that satisfies the core CoDA principles laid out by Aitchison (1986):

1. **(Scale invariance)** Analyses based on the raw observations  $\mathbf{x}_1, \dots, \mathbf{x}_n \in \mathbb{R}_+^d$  and on the closed compositions  $\mathcal{C}\mathbf{x}_1, \dots, \mathcal{C}\mathbf{x}_n \in \mathbb{S}_{+(1)}^{d-1}$  should yield the same results. In other words, the magnitudes of  $\mathbf{x}_1, \dots, \mathbf{x}_n$  are not relevant for inference.

2. **(Subcompositional coherence)** Analyses based on the full composition and any subcomposition should yield consistent conclusions.
3. **(Permutation invariance)** Analyses should yield equivalent results when parts in the composition are permuted.

Adherence to the foundational CoDA principles is achieved by discarding Euclidean geometry and instead working in the so-called Aitchison geometry (Aitchison 1986). Formally, this involves constructing a Hilbert space structure on the interior of  $\mathbb{S}_{+(1)}^{d-1}$  (Pawlowsky-Glahn and Egozcue 2001). Suppose  $\mathbf{x}, \mathbf{y} \in \mathbb{S}_{+(1)}^{d-1} \setminus \partial\mathbb{S}_{+(1)}^{d-1}$ , where

$$\partial\mathbb{S}_{+(1)}^{d-1} := \{\mathbf{x} \in \mathbb{S}_{+(1)}^{d-1} : x_i = 0 \text{ for at least one } i\}$$

is the simplex boundary. For  $\alpha \in \mathbb{R}$ , the perturbation and power operations are defined by

$$\mathbf{x} \oplus \mathbf{y} = \mathcal{C}(x_1 y_1, \dots, x_d y_d), \quad \alpha \odot \mathbf{x} = \mathcal{C}(x_1^\alpha, \dots, x_d^\alpha).$$

The real vector space  $(\mathbb{S}_{+(1)}^{d-1}, \odot, \oplus)$  has additive identity  $\mathbf{e}_a := \mathcal{C}(1, \dots, 1)$  and inverse elements  $\ominus\mathbf{x} := \mathcal{C}(x_1^{-1}, \dots, x_d^{-1})$ . Central to the Aitchison geometry is the centred log-ratio (CLR) transformation

$$\text{clr} : \mathbb{S}_{+(1)}^{d-1} \rightarrow \mathbb{R}^d, \quad \mathbf{x} \mapsto \log\left(\frac{\mathbf{x}}{\bar{g}(\mathbf{x})}\right),$$

where  $\bar{g}(\mathbf{x}) := (\prod_{i=1}^d x_i)^{1/d}$  denotes the geometric mean of the components of  $\mathbf{x}$ . The inverse transformation is  $\text{clr}^{-1}(\mathbf{v}) = \mathcal{C} \exp(\mathbf{v})$ . With this transformation, the inner product may be defined in terms of  $\langle \cdot, \cdot \rangle_e$ , the Euclidean inner product in  $\mathbb{R}^d$ , as

$$\langle \mathbf{x}, \mathbf{y} \rangle_a := \langle \text{clr}(\mathbf{x}), \text{clr}(\mathbf{y}) \rangle_e,$$

The Aitchison norm and distance are the metric elements induced by  $\langle \cdot, \cdot \rangle_a$ , given by

$$\|\mathbf{x}\|_a := \langle \mathbf{x}, \mathbf{x} \rangle_a^{1/2} = \|\text{clr}(\mathbf{x})\|_2, \quad d_a(\mathbf{x}, \mathbf{y}) := \|\mathbf{x} \ominus \mathbf{y}\|_a = \|\text{clr}(\mathbf{x}) - \text{clr}(\mathbf{y})\|_2. \quad (4.1)$$

The CLR transformation is an isometry between the Aitchison simplex and the Euclidean hyperplane

$$\mathcal{T}^{d-1} := \{\mathbf{y} \in \mathbb{R}^d : y_1 + \dots + y_d = 0\} \subset \mathbb{R}^d$$

passing through the origin and parallel to the simplex in  $\mathbb{R}^d$ . Therefore CoDA methods can be formulated in two equivalent ways: in terms of compositions in the Aitchison geometry (the in-the-simplex approach) or based on the CLR-transformed vectors in the Euclidean geometry (the out-of-the-simplex approach). If one chooses the in-the-simplex route, statistical and probabilistic concepts must be appropriately generalised. For example, Pawlowsky-Glahn and Egozcue (2001) define measures of central tendency and total variability for compositions as

$$\begin{aligned}\text{cen}_a(\mathbf{X}) &:= \arg \min_{\mathbf{y} \in \mathbb{S}_+^{d-1}} \mathbb{E}[d_a^2(\mathbf{X}, \mathbf{y})] = \mathcal{C}(\exp(\mathbb{E}[\log(\mathbf{X})])), \\ \text{totVar}_a(\mathbf{X}) &:= \mathbb{E}[d_a^2(\mathbf{X}, \text{cen}_a(\mathbf{X}))] = \sum_{j=1}^d \text{Var}([\text{clr}(\mathbf{X})]_j).\end{aligned}$$

#### 4.2.2. Connections between CoDA and multivariate extremes

Suppose  $\mathbf{X} \in \mathcal{RV}_+^d(\alpha)$  and let  $\mathbf{X}_1, \dots, \mathbf{X}_n$  be independent copies of  $\mathbf{X}$ . Inference for  $H$  is typically based on the extremal angles  $\Theta_{(1)}, \dots, \Theta_{(k)}$  associated with radial threshold exceedances. This process is rigorously justified by the MRV property. Extreme events may be represented by their angles with zero loss of information since the radii  $R_{(1)}, \dots, R_{(k)}$  are uninformative for  $H$ , except insofar as they must exceed a high threshold. Extremal dependence modelling therefore proceeds under an assumption of scale invariance, the first axiom of CoDA. Moreover, choosing the  $L_1$ -norm implies that  $H$  is a distribution on  $\mathbb{S}_{+(1)}^{d-1}$  and  $\Theta_{(1)}, \dots, \Theta_{(k)}$  are random compositions in  $\mathbb{S}_{+(1)}^{d-1} \setminus \partial\mathbb{S}_{+(1)}^{d-1}$  almost surely. Thus CoDA techniques are readily applicable to the kind of data that arise in such analyses.

#### 4.2.3. Comparison of the Euclidean and Aitchison distances

The Aitchison distance is a simplicial metric (i.e. satisfies the CoDA axioms) and is therefore an appropriate measure of distance between compositions (Aitchison 1992). In general, the Aitchison dissimilarity  $\|\mathbf{x} \ominus \mathbf{y}\|_a$  between two compositions  $\mathbf{x}, \mathbf{y} \in \mathbb{S}_{+(1)}^{d-1} \setminus \partial\mathbb{S}_{+(1)}^{d-1}$  behaves very differently to  $\|\mathbf{x} - \mathbf{y}\|_2$ . Figure 4.1 provides further insight into this. Each ternary plot graphs the distance between  $d_\bullet(\mathbf{x}, \mathbf{y})$  as a function of  $\mathbf{y}$  with respect to some fixed point  $\mathbf{x}$ , where  $\bullet \in \{a, e\}$ . The fixed points are  $\mathbf{x} = (1/3, 1/3, 1/3)$  (top row) and

$\mathbf{x} = (0.1, 0.45, 0.45)$  (bottom row). The left- and right-hand plots correspond to Euclidean and Aitchison distances, respectively. Consider the plots in the top row. The Euclidean distance is bounded by  $\sqrt{2/3} \approx 0.82$ , the distance between the centroid and any vertex, since the simplex is a bounded subspace of  $\mathbb{R}^d$ . In contrast, the Aitchison distance  $d_a(\mathbf{x}, \mathbf{y})$  is unbounded. CLR transforms are based on log-ratios and  $\log y$  diverges to  $\pm\infty$  as  $y \rightarrow 0$  or  $y \rightarrow \infty$ . Thus, points close to the boundary should be regarded as being close to infinity (Park et al. 2022). In the top-left plot, distance decays in a concentric fashion. Consequently, the point labelled A, which may be interpreted as being arbitrarily close to its neighbouring edge, is deemed closer to the centre than point B. On the other hand, the Aitchison contours are decidedly non-concentric and the points C and D are approximately equidistant to the centre. In the bottom plots, the fixed point  $\mathbf{x} = (0.1, 0.45, 0.45)$  is located at the ‘hotspot’ near the right-hand edge. Intuitively, the Euclidean metric (bottom left) says that point E is very close to  $\mathbf{x}$ , while F is much further away. However, in the Aitchison geometry (bottom right) the distance between G and  $\mathbf{x}$  becomes arbitrarily large as G is nudged towards the boundary, so that eventually H is actually closer to  $\mathbf{x}$  than G!

These examples demonstrate that, when analysing data on the simplex, the choice of distance metric is of huge practical importance and should not be dismissed as merely a mathematical technicality.

## 4.3. Compositional PCA for extremes

### 4.3.1. Motivation

Compositional principal component analysis (CoDA-PCA) aims at finding low-dimensional representations of compositional data via projections onto linear subspaces of the Aitchison simplex (Aitchison 1983). It is inadvisable to apply classical PCA to compositions for three reasons. First, spurious correlations arising from the compositional constraint mean it is unreliable as an exploratory tool for analysing the correlation structure between variables (Aitchison 1982). Second, compositional data often exhibit curvature that cannot be captured by traditional linear methods, leading to a loss of efficiency (Aitchison 1983). Third, interpretability is hindered by the fact that low-dimensional projections of the data

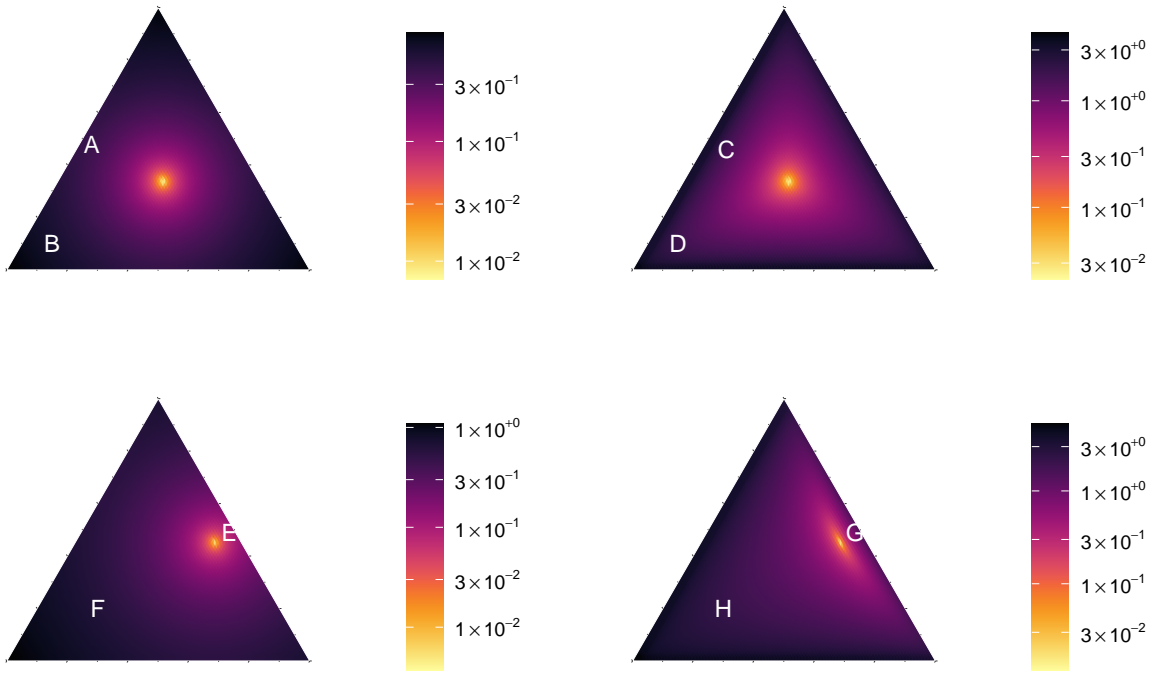


Figure 4.1.: Visualisation of the Euclidean distance (left) and Aitchison distance (right) between points on  $\mathbb{S}_{+(1)}^{d-1}$  and the reference points  $(1/3, 1/3, 1/3)$  (top) and  $(0.1, 0.45, 0.45)$  (bottom). The labelled points A-H are referred to in the body text.

are not guaranteed to lie in the simplex. These problems are solved by performing PCA in the Aitchison Hilbert space.

### 4.3.2. Methodology

Suppose  $\mathbf{X} \in \mathcal{RV}_+^d(\alpha)$  and let  $H$  be the angular measure with respect to the  $L_1$ -norm  $\|\cdot\|_1$ . Let  $\mathbf{X}_1, \dots, \mathbf{X}_n$  be independent random vectors with the same distribution as  $\mathbf{X}$ . Following the spirit of Drees and Sabourin (2021), we seek to minimise the limiting mean-squared reconstruction error associated with the extremal angles  $\Theta_{(1)}, \dots, \Theta_{(k)}$  upon projecting onto a low-dimensional linear subspace. For any Aitchison subspace  $\mathcal{S} \subset \mathbb{S}_{+(1)}^{d-1}$ , let  $\Pi_{\mathcal{S}}$  denote the orthogonal projection (matrix) onto  $\mathcal{S}$  and define the true asymptotic risk

$$R(\mathcal{S}) := \mathbb{E}_H[\|\Theta \ominus \Pi_{\mathcal{S}}\Theta\|_a^2].$$

For some  $1 \leq p \leq d - 1$ , let  $\mathcal{V}_p$  be the class of linear subspaces (in the Aitchison sense) of dimension  $p$  in  $\mathbb{S}_{+(1)}^{d-1}$ . As usual, the minimisers of  $R(\mathcal{S})$  over  $\mathcal{V}_p$  corresponds to the

principal eigenspace of a covariance matrix. The following result explains how the CoDA-PCA procedure outlined by Aitchison (1982) applies to our setting.

**Proposition 4.1.** *Let  $\tilde{\Theta} \sim d^{-1}H$  be a random composition. Assume  $\tilde{\Theta}$  is centred (without loss of generality) and has finite total variance. Let  $\Gamma = \text{Cov}(\text{clr}(\tilde{\Theta}))$  be the CLR-covariance matrix of  $\tilde{\Theta}$  and  $\Gamma = \Omega D \Omega^T$  its eigendecomposition, where  $D$  is a diagonal matrix of eigenvalues  $\lambda_1 \geq \lambda_2 \geq \dots \geq \lambda_{d-1} \geq \lambda_d = 0$  and  $\Omega$  is an orthonormal  $d \times d$  matrix whose columns are the eigenvectors  $\omega_1, \dots, \omega_{d-1} \in \mathcal{T}^{d-1}$  and  $\omega_d \propto \mathbf{1}_d$ . The back-transformed eigenvectors  $\{\mathbf{u}_1, \dots, \mathbf{u}_{d-1}\} := \{\text{clr}^{-1}(\omega_1), \dots, \text{clr}^{-1}(\omega_{d-1})\}$  form an orthonormal basis of  $\mathbb{S}_{+(1)}^{d-1}$  and for any  $1 \leq p \leq d-1$ ,*

$$\mathcal{S}_p^* := \text{span}\{\mathbf{u}_1, \dots, \mathbf{u}_p\} = \left\{ \bigoplus_{j=1}^p (\tau_j \odot \mathbf{u}_j) : \tau_1, \dots, \tau_p \in \mathbb{R} \right\}$$

minimises  $R$  over  $\mathcal{V}_p$ .

*Proof.* Let  $\tilde{\mathbf{Y}} := \text{clr}(\tilde{\Theta})$ . The assumptions give that  $\tilde{\mathbf{Y}}$  has zero mean and finite second order moments, since

$$\mathbb{E}[\tilde{\mathbf{Y}}] = \arg \min_{\mu} \mathbb{E}[d_e^2(\tilde{\mathbf{Y}}, \mu)] = \arg \min_{\mu} \mathbb{E}[d_a^2(\tilde{\Theta}, \text{clr}^{-1}(\mu))] = \text{clr}(\mathbf{e}_a) = \mathbf{0}$$

and

$$\text{Var}(\tilde{Y}_j) = \text{Var}([\text{clr}(\tilde{\Theta})]_j) < \infty.$$

Using well-known results from classical PCA – e.g. Theorem 5.3 in Seber (1984) – we have that

$$\{\omega_1, \dots, \omega_p\} = \arg \min_{v_1, \dots, v_p \in \mathbb{R}^d} \mathbb{E} \left[ \|\tilde{\mathbf{Y}} - \Pi_{\text{span}\{v_1, \dots, v_p\}} \tilde{\mathbf{Y}}\|_2^2 \right].$$

Observe that for any scalar  $a \in \mathbb{R}$  and compositional vectors  $\mathbf{x}, \mathbf{y} \in \mathbb{S}_{+(1)}^{d-1}$ ,

$$\text{clr}((a \odot \mathbf{x}) \oplus \mathbf{y}) = a \text{clr}(\mathbf{x}) + \text{clr}(\mathbf{y})$$

and therefore

$$\begin{aligned}
\{\omega_1, \dots, \omega_p\} &= \arg \min_{v_1, \dots, v_p \in \mathbb{R}^d} \mathbb{E} \left[ \|\tilde{\mathbf{Y}} - \Pi_{\text{span}\{v_1, \dots, v_p\}} \tilde{\mathbf{Y}}\|_2^2 \right] \\
&= \arg \min_{v_1, \dots, v_p \in \mathbb{R}^d} \mathbb{E}[d_e^2(\tilde{\mathbf{Y}}, \Pi_{\text{span}\{v_1, \dots, v_p\}} \tilde{\mathbf{Y}})] \\
&= \arg \min_{v_1, \dots, v_p \in \mathbb{R}^d} \mathbb{E}[d_a^2(\tilde{\Theta}, \text{clr}^{-1}(\Pi_{\text{span}\{v_1, \dots, v_p\}} \tilde{\mathbf{Y}}))] \\
&= \arg \min_{v_1, \dots, v_p \in \mathbb{R}^d} \mathbb{E} \left[ d_a^2 \left( \tilde{\Theta}, \text{clr}^{-1} \left( \sum_{j=1}^p \langle \tilde{\mathbf{Y}}, v_j \rangle v_j \right) \right) \right] \\
&= \arg \min_{v_1, \dots, v_p \in \mathbb{R}^d} \mathbb{E} \left[ d_a^2 \left( \tilde{\Theta}, \bigoplus_{j=1}^p \langle \tilde{\Theta}, \text{clr}^{-1}(v_j) \rangle_a \odot \text{clr}^{-1}(v_j) \right) \right].
\end{aligned}$$

This optimisation depends on each vector  $v_j$  only through  $\text{clr}^{-1}(v_j)$ , so we can map the problem to the simplex, yielding

$$\begin{aligned}
\{\text{clr}^{-1}(\omega_1), \dots, \text{clr}^{-1}(\omega_p)\} &= \arg \min_{v_1, \dots, v_p \in \mathbb{S}_{+(1)}^{d-1}} \mathbb{E} \left[ d_a^2 \left( \tilde{\Theta}, \bigoplus_{j=1}^p \langle \tilde{\Theta}, v_j \rangle_a \odot v_j \right) \right] \\
&= \arg \min_{v_1, \dots, v_p \in \mathbb{S}_{+(1)}^{d-1}} R(\text{span}\{v_1, \dots, v_p\})
\end{aligned}$$

Since  $\mathcal{S}_p^\star = \text{span}\{\text{clr}^{-1}(\omega_1), \dots, \text{clr}^{-1}(\omega_p)\}$ , this completes the proof.  $\square$

The finite total variance condition prohibits the angular measure from placing mass on the simplex boundary and restricts how much mass may be concentrated near the boundary. A sufficient condition is  $\text{Var}_H(\log(\Theta_i/\Theta_j)) < \infty$  for all  $i \neq j$ . No such condition is required by Drees and Sabourin (2021) because finite variances are guaranteed by boundedness of the simplex in  $\mathbb{R}^d$ . The assumption that  $\tilde{\Theta}$  is centred at the simplex barycentre is not equivalent to the moment constraint (2.13) on  $H$ . Informally, the moment constraints dictate the arithmetic mean of  $H$ , whereas the compositional centre represents the geometric mean. Finally, we point out that  $\text{rank}(\Gamma) = d - 1$  in accordance with the dimensions of  $\mathbb{S}_{+(1)}^{d-1}$  and  $\mathcal{T}^{d-1}$ . For compositional PCA we need only consider reconstructions up to rank  $d - 1$ , whereas Drees and Sabourin (2021) and Cooley and Thibaud (2019) require all  $d$  components to be retained to guarantee perfect reconstruction (in general).

In practice  $H$  is unknown, so we must resort to minimising an empirical risk based on the

$k$  most extreme data points. The empirical risk is defined by

$$\hat{R}(\mathcal{S}) := \hat{\mathbb{E}}_H[\|\boldsymbol{\Theta} - \Pi_{\mathcal{S}}\boldsymbol{\Theta}\|_a^2] = \frac{d}{k} \sum_{i=1}^k \|\boldsymbol{\Theta}_{(i)} - \Pi_{\mathcal{S}}\boldsymbol{\Theta}_{(i)}\|_a^2.$$

By replacing  $H$  with  $\hat{H}$  in Proposition 4.1, one can show that the minimiser of  $\hat{R}$  in  $\mathcal{V}_p$  is simply the principal subspace

$$\hat{S}_p = \text{span}\{\hat{\mathbf{u}}_1, \dots, \hat{\mathbf{u}}_p\},$$

where  $\hat{\mathbf{u}}_1, \dots, \hat{\mathbf{u}}_{d-1} \in \mathbb{S}_{+(1)}^{d-1}$  are the back-transformed principal eigenvectors of the empirical CLR-covariance matrix (Egozcue and Pawlowsky-Glahn 2018)

$$\hat{\Gamma} = \frac{1}{k-1} \sum_{i=1}^k \text{clr}(\boldsymbol{\Theta}_{(i)} \ominus \bar{\boldsymbol{\Theta}}) \text{clr}(\boldsymbol{\Theta}_{(i)} \ominus \bar{\boldsymbol{\Theta}})^T, \quad \bar{\boldsymbol{\Theta}} = \frac{1}{k} \bigoplus_{i=1}^k \boldsymbol{\Theta}_{(i)}.$$

Our setup is identical to Drees and Sabourin (2021), except that all algebraic-geometric concepts (linear, projection, orthogonal, etc.) are interpreted in the Aitchison sense. This subtle change fundamentally alters the problem in two different ways. While we still optimise over the class of linear subspaces, we refer to a different notion of linearity to Drees and Sabourin (2021). Linear trends are now represented by compositional straight lines  $\{\mathbf{a} \oplus (\tau \odot \mathbf{b}) : \tau \in \mathbb{R}\} \subset \mathbb{S}_{+(1)}^{d-1}$  for some  $\mathbf{a}, \mathbf{b} \in \mathbb{S}_{+(1)}^{d-1}$ . From a Euclidean perspective these ‘lines’ are curved, so compositional PCA is able to capture features of the data that appear non-linear – see Figure 1b in Aitchison (1983) for an illustration of this phenomenon. The second crucial difference is that our objective criterion perceives reconstruction errors in the Aitchison rather than Euclidean metric. Section 4.2.3 showed that these two measures can produce wildly different assessments of how close two points are; in fact, for any  $\epsilon > 0$  and  $\varepsilon > 0$ , there exists  $\mathbf{x}, \mathbf{y} \in \mathbb{S}_{+(1)}^{d-1}$  such that  $d_e(\mathbf{x}, \mathbf{y}) < \epsilon$  and  $d_a(\mathbf{x}, \mathbf{y}) > \epsilon$ . The Aitchison loss is especially sensitive to reconstruction errors near the boundary, steering the optimiser to target these regions more closely.

### 4.3.3. Simulation experiments

We now compare the performance of our proposed procedure against Drees and Sabourin (2021), Herein referred to as CoDA-PCA and DS-PCA, respectively. Let  $\mathbf{X} \in \mathcal{RV}_+^d(1)$  be on 1-Fréchet margins with angular measure  $H$ . We generate independent realisations  $\mathbf{x}_1, \dots, \mathbf{x}_n$  of  $\mathbf{X}$  and, for a fixed level  $k$ , compute the optimal linear subspaces  $\hat{\mathcal{S}}_1, \dots, \hat{\mathcal{S}}_{p-1}$  using CoDA-PCA and DS-PCA.

#### 4.3.3.1. Performance metrics

We assess performance in two ways: mean-squared reconstruction error (MSRE) and tail event probability estimation. To quantify reconstruction error we use the asymptotic risk of  $\mathcal{S}$  under the Aitchison and Euclidean metrics, i.e.

$$\mathcal{L}_a(\mathcal{S}) = \mathbb{E}_H[\|\Theta \ominus \Pi_{\mathcal{S}}\Theta\|_a^2 \mathbf{1}\{\Pi_{\mathcal{S}}\Theta \in (0, \infty)^d\}], \quad (4.2)$$

$$\mathcal{L}_e(\mathcal{S}) = \mathbb{E}_H[\|\Theta - \Pi_{\mathcal{S}}\Theta\|_2^2]. \quad (4.3)$$

These quantities can be computed to arbitrary precision using Monte Carlo estimation. To sample from the true angular measure we employ the `rmevspec` function in the `mev` package. The inclusion of  $\mathbf{1}\{\Pi_{\mathcal{S}}\Theta \in (0, \infty)^d\}$  ensures that  $\mathcal{L}_a$  is well-defined in cases where DS-PCA yields reconstructed vectors that lie outside of the positive orthant. In such cases, the Aitchison distance is undefined. Naively, one might consider projecting invalid reconstructions on to the positive orthant, but this does not really resolve the core issue. Naturally such points should be sent somewhere near the coordinate axes, but by adjusting *how close* you place the point, the Aitchison loss can be made arbitrarily large. Instead, we simply ignore such points. Arguably this choice favours DS-PCA, since we do not penalise its failure to produce valid reconstructions.

Measuring reconstruction error gives a high-level summary of how closely the low-dimensional approximation of  $H$  resembles the true measure over its entire support. The second class of performance metrics focusses on assessing performance in specific regions of the simplex that are relevant for estimating tail event probabilities. Consider the

estimands

$$p_{\min} := \lim_{u \rightarrow \infty} \mathbb{P}(\min \mathbf{X} > u \mid \|\mathbf{X}\|_1 > u) = \mathbb{E}_H \left[ \min_{j=1,\dots,d} \Theta_j \right], \quad (4.4)$$

$$p_{\max} := \lim_{u \rightarrow \infty} \mathbb{P}(\max \mathbf{X} > u \mid \|\mathbf{X}\|_1 > u) = \mathbb{E}_H \left[ \max_{j=1,\dots,d} \Theta_j \right]. \quad (4.5)$$

These probabilities specify the minimum and maximum contributions of each variable to the norm. The true probabilities may be computed via Monte Carlo simulation or analytically. To assess a principal subspace  $\hat{\mathcal{S}}_p$ , we compute estimates of  $p_{\min}$  and  $p_{\max}$  using the empirical angular measure *after* projecting the data onto  $\hat{\mathcal{S}}_p$ . Specifically, for any subspace  $\mathcal{S}$  we define

$$\hat{H}_{\mathcal{S}}(\cdot) := \frac{d}{\sum_{i=1}^k \mathbf{1}\{\Pi_{\mathcal{S}}\Theta_{(i)} \in (0, \infty)^d\}} \sum_{i=1}^k \delta_{\Pi_{\mathcal{S}}\Theta_{(i)}}(\cdot) \mathbf{1}\{\Pi_{\mathcal{S}}\Theta_{(i)} \in (0, \infty)^d\}$$

and compute

$$\hat{p}_{\min}(\mathcal{S}) := \mathbb{E}_{\hat{H}_{\mathcal{S}}} \left[ \min_{j=1,\dots,d} \Theta_j \right], \quad \hat{p}_{\max}(\mathcal{S}) := \mathbb{E}_{\hat{H}_{\mathcal{S}}} \left[ \max_{j=1,\dots,d} \Theta_j \right]. \quad (4.6)$$

The performance of each dimension reduction method is assessed by examining the sequence of estimates  $\hat{p}_{\bullet}(\hat{\mathcal{S}}_1), \dots, \hat{p}_{\bullet}(\hat{\mathcal{S}}_{p-1})$  and comparing against the true probability  $p_{\bullet}$  and the (uncompressed) empirical estimate  $\hat{p}_{\bullet}(\mathbb{S}_{+(1)}^{d-1})$ , for  $\bullet \in \{\min, \max\}$ .

#### 4.3.3.2. Max-linear model with compositionally colinear factors

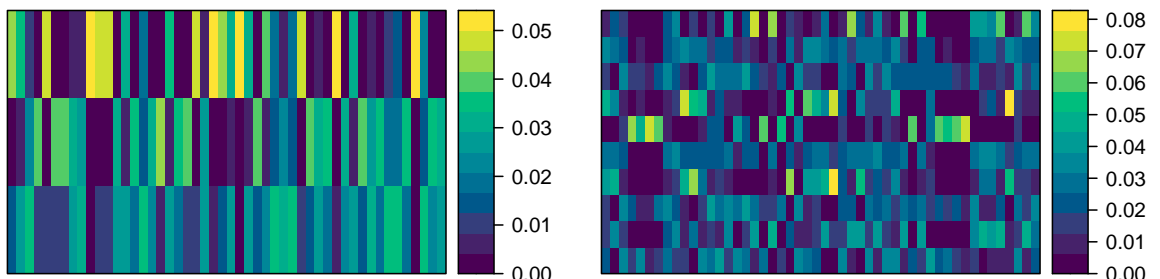


Figure 4.2.: Max-linear parameter matrices  $A \in \mathbb{R}_+^{d \times q}$  whose columns are spanned by  $s$  compositional vectors  $\mathbf{v}_1, \dots, \mathbf{v}_s$ . Left:  $d = 3, q = 50, s = 1, \mathbf{v}_1 = (0.12, 0.58, 0.3)$ . Right:  $d = 10, q = 50, s = 2$ .

Our first experiment involves max-linear random vectors. The parameter matrix  $A$  will be constructed in a particular way so as to nicely illustrate the benefits of our proposed

approach. We stock the factor matrix  $A \in \mathbb{R}_+^{d \times q}$  with power-perturbation combinations of linearly independent compositions  $\mathbf{v}_1, \dots, \mathbf{v}_s \in \mathbb{S}_{+(1)}^{d-1}$ , that is  $A = (\mathbf{a}_1, \dots, \mathbf{a}_q)$  and for each  $j = 1, \dots, q$ ,

$$\mathcal{C}\mathbf{a}_j = \bigoplus_{l=1}^s (\beta_{jl} \odot \mathbf{v}_l)$$

for some scalars  $\beta_{j1}, \dots, \beta_{js} \in \mathbb{R}$ . Then the angular measure of the associated max-linear random vector  $\mathbf{X} \in \mathcal{RV}_+^d(1)$  is

$$H(\cdot) = \sum_{j=1}^q \|\mathbf{a}_j\|_1 \delta_{\bigoplus_{l=1}^s (\beta_{jl} \odot \mathbf{v}_l)}(\cdot)$$

The support of  $H$  is spanned (in the Aitchison geometry) by  $\mathbf{v}_1, \dots, \mathbf{v}_s$ . If  $s < d - 1$ , then the angular measure may be represented by a low-dimensional object with no information loss incurred.

We start with a low-dimensional example to facilitate visualisation. Let  $d = 3$ ,  $s = 1$ ,  $q = 50$  and  $\mathbf{v}_1 = (0.12, 0.58, 0.3)$ . The values  $\beta_{11}, \dots, \beta_{q1}$  are sampled uniformly between -4 and 4. The resulting matrix is shown in Figure 4.3 (left). Since the angular measure is discrete, the true probabilities (4.4) and (4.5) can be computed analytically as  $p_{\min} \approx 0.068$  and  $p_{\max} \approx 0.636$  to three decimal places. Realisations of  $\mathbf{X}$  are generated using the max-stable (MS) construction  $\mathbf{X} = A \times_{\max} \mathbf{Z}$  and the transformed-linear (TL) construction  $\mathbf{X} = A \otimes \mathbf{Z}$  defined in (2.20) and (2.21). For both processes, we generate 50 datasets of size  $n = 5 \times 10^3$  and run the PCA methods with  $k/n = 0.01$ .

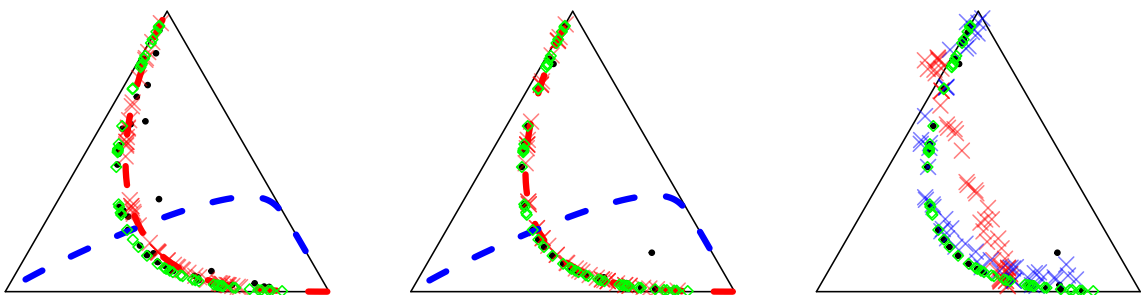


Figure 4.3.: CoDA-PCA (left and middle) and DS-PCA (right) applied to max-linear data from the TL process (left) and MS process (middle and right). The green diamonds represent the support of the true angular measure. The black points are the angular components associated with the  $k = 50$  largest observations among  $n = 5,000$  samples. The red and blue dashed lines represent the first and second principal axes, respectively. The red and blue crosses represent the projections onto the first and second principal subspaces, respectively.

The exploratory plots in Figure 4.3 provides some insight into the data structure and the mechanics of the two procedures. In each plot, the support of the angular measure (i.e. the points  $\mathcal{Ca}_1, \dots, \mathcal{Ca}_{50}$ ) is represented by the green diamonds. By construction, these points exhibit a one-dimensional structure and lie on the compositional straight line  $\{\tau \odot (0.12, 0.58, 0.3) : \tau \in \mathbb{R}\}$ . The black points are the extremal angles  $\theta_{(1)}, \dots, \theta_{(k)}$  taken from one set of realisations from the TL max-linear random vector (left) and the MS max-linear random vector (middle and left). The TL data are noisier in the sense that the extremal angles do not tend to lie exactly on the green points, whereas the MS angles converge to the limiting distribution very quickly. The left and middle plots show the results of CoDA-PCA. The red and blue dashed lines represents the first and second (sample) principal axes, respectively. The method correctly identifies the true low-dimensional structure, though there is some estimation error visible in the TL case (left). The red crosses represent the rank-one reconstructions obtained by projecting the black points onto the red line. The rank-two projections always reconstruct the data perfectly since  $\mathbb{S}_{+(1)}^2$  is a two-dimensional space. The right-hand plot depicts the results of DS-PCA for the same MS dataset. Now we add blue crosses showing the rank-two reconstructions. Clearly, there are several issues to discuss. The one-dimensional projections lie along a straight line (the process of visualising the line on a ternary plot distorts it slightly) and do a poor job of describing the data. Some points lie outside of the triangle; this means the projected vector had a negative component. The rank-two reconstructions do a much better job, but are still imperfect because DS-PCA treats the data as points in  $\mathbb{R}^3$ .

The full results are shown in Figure 4.4. The four sub-plots show the distributions of the four performance measures: the Aitchison MSRE  $\mathcal{L}_a$  (top left), the Euclidean MSRE (top right), estimates  $\hat{p}_{\min}$  (bottom left), and estimates  $\hat{p}_{\max}$  (bottom right). Within each subplot, the two sub-panels are based on the two data generating processes. The horizontal axis indicates which PCA method is being used and the number of retained principal components,  $p$ . As expected from Figure 4.3, CoDA-PCA produces excellent reconstructions when  $p = 1$  under *both* the Aitchison and Euclidean loss. The picture for DS-PCA is more mixed. According to  $\mathcal{L}_e$ , adding a second component improves the reconstructions considerably. The Aitchison loss  $\mathcal{L}_a$  disagrees, suggesting that the two-dimensional projections are poor approximations of points near the simplex boundary. This can be observed in Figure 4.3 (right) near the upper and right-hand vertices. In terms of reconstruction error,

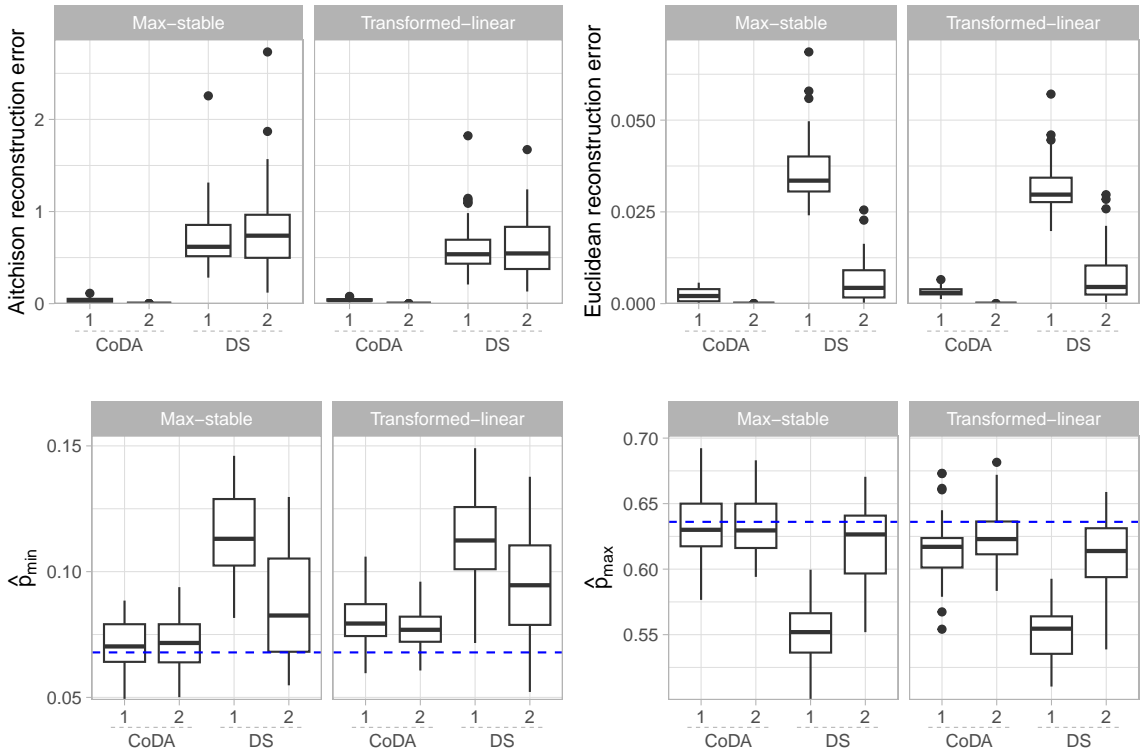


Figure 4.4.: Performance of CoDA-PCA and DS-PCA for the trivariate max-linear data. Results are based on 50 repeated simulations from the MS and TL processes with  $n = 5,000$  and  $k/n = 0.01$ . Top row: the Aitchison reconstruction error (4.2) and Euclidean reconstruction error (4.3) against the number of retained components. Reconstruction errors are obtained from 10,000 samples from the true angular measure. Bottom row: estimates of  $p_{\min}$  (left) and  $p_{\max}$  (left) based on (4.6) against  $p$ , the rank of the principal subspace.

there is not any noticeable difference between the MS and TL results. Now consider the tail probability estimates in the bottom row. The boxplots are the estimates  $\hat{p}_{\bullet}(\hat{\mathcal{S}}_p)$  and the blue dashed line marks the true probability  $p_{\bullet}$ . CoDA-PCA with  $p = 1$  yields very good estimates in the sense of (i) being close to the true value and (ii) being as good as the  $p = 2$  estimate resulting from the uncompressed empirical angular measure. The estimates are slightly biased for the TL data, suggesting that the extremal angles converge to their limiting distribution in such a way that biases the principal eigenvector of the empirical CLR-covariance matrix. For DS-PCA,  $\hat{p}_{\min}(\hat{\mathcal{S}}_1)$  and  $\hat{p}_{\max}(\hat{\mathcal{S}}_1)$  show a large positive and negative bias, respectively. Adding a second component reduces the bias considerably but the uncertainty is quite large. Euclidean loss treats all errors equally irrespective of where they occur in the simplex, so the PCA solution finds a compromise between good fit near the centre and near the boundary. In contrast, the Aitchison loss prioritises good recon-

struction of points near the boundary, resulting in more stable PCA solutions. Analogous plots based on samples of size  $n = 50,000$  are shown in Figure C.1 in Appendix C. The results are virtually identical, confirming that errors are due to methodological deficiencies, not a lack of data. Even with infinite samples DS-PCA will fit a straight line to curved data!

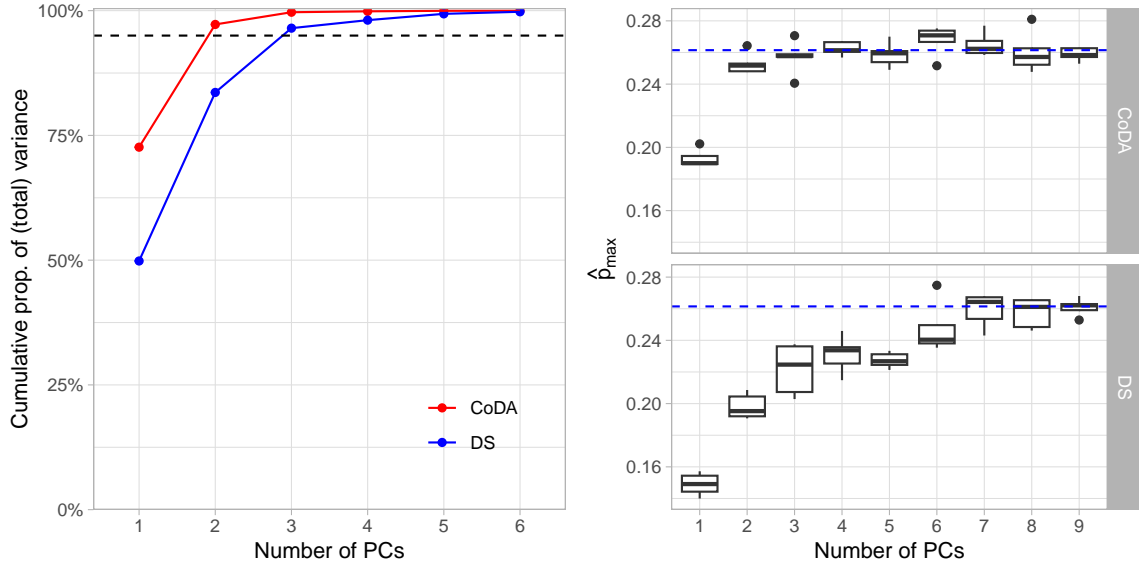


Figure 4.5.: Performance of CoDA-PCA and DS-PCA for the 10-dimensional max-linear data. Results are based on 50 repeated simulations from the MS and TL processes with  $n = 10,000$  and  $k/n = 0.02$ . Left: the median proportion of total variability explained by the leading  $p$  components as a function of  $p$ , computed using the eigenvalues of the TPDM (DS) and CLR-covariance matrix (CoDA). Right: estimates of  $\hat{p}_{\max}$  based on (4.6) against  $p$ , the rank of the principal subspace.

The three-dimensional example is instructive but limited in terms of comparing dimension reducing capabilities. Our next experiment is based on the same construction with  $d = 10$ ,  $q = 50$  and  $s = 2$ . The vectors  $\mathbf{v}_1, \mathbf{v}_2 \in \mathbb{S}_{+(1)}^9$  and scalars  $\{\beta_{jl} : j = 1, \dots, 50, l = 1, 2\}$  are generated randomly producing the matrix in Figure 4.2 (right). The results in Figure 4.5 are based on 25 repeated simulations from the MS construction with  $n = 10^4$  and  $k/n = 0.02$ . The left-hand plot shows the average cumulative proportion of the total variance as a function of the number of retained components. These are computed as  $\sum_{j \leq p} \hat{\lambda}_j / \sum_{j=1}^d \hat{\lambda}_j$ , where  $\{\hat{\lambda}_j : j = 1, \dots, 10\}$  are the sample eigenvalues of the TPDM or CLR-covariance matrix. Note that for CoDA-PCA it is the total variance  $\text{totVar}_a(\Pi_{\hat{S}_p} \Theta)$  being measured. The dashed line represents the 95% threshold. In PCA a common rule-of-thumb is to

retain as many components as necessary to explain 95% of the variance. Based on this criterion, CoDA-PCA correctly identifies that two components are sufficient, whereas DS-PCA requires one additional dimension. However, this only means that three components are adequate for capturing *Euclidean* variability in the angles. Hopefully the reader is by now persuaded that this is not sufficient for a good description of extremal dependence. The right-hand plot confirms our hypothesis. Here we see estimates  $\hat{p}_{\max}(\hat{\mathcal{S}}_p)$  against  $p$  for each PCA algorithm. CoDA-PCA estimates  $p_{\max}$  very accurately with  $p = 2$ . DS-PCA requires at least six or seven components. This stark contrast emphasises our point that diagnosing PCA performance using the Euclidean notions of reconstruction error or proportion of variance can be rather misleading.

#### 4.3.3.3. Hüsler-Reiss

Now we consider more realistic examples where the data are generated from four different Hüsler-Reiss models. For  $i = 1, \dots, 4$ , suppose  $\mathbf{X}_i \in \mathcal{RV}_+^d(1)$  follows a Hüsler-Reiss distribution parametrised by  $\Lambda_i \in \mathbb{R}_+^{d \times d}$ . For the first three examples we set  $d = 3$  and

$$\Lambda_1 = \begin{pmatrix} 0 & 0.025 & 0.311 \\ 0.025 & 0 & 0.168 \\ 0.311 & 0.168 & 0 \end{pmatrix}, \quad \Lambda_2 = \begin{pmatrix} 0 & 0.034 & 0.009 \\ 0.034 & 0 & 0.024 \\ 0.009 & 0.024 & 0 \end{pmatrix}, \quad \Lambda_3 = \begin{pmatrix} 0 & 0.001 & 0.322 \\ 0.001 & 0 & 0.309 \\ 0.322 & 0.309 & 0 \end{pmatrix}$$

The fourth example is 10-dimensional with  $\Lambda_4 \in \mathbb{R}_+^{10 \times 10}$  constructed in such a way that there are three clusters of asymptotically dependent variables – see the corresponding tail dependence matrix (TDM)  $\chi_{ij}$  in Figure 4.6 (left). The entries of  $\Lambda_1, \dots, \Lambda_4$  were randomly generated following the steps in Appendix B1 in Fomichov and Ivanovs (2023).

The exploratory plots in Figure 4.7 show that  $\Lambda_1, \Lambda_2, \Lambda_3$  induce qualitatively different dependence structures. The plots' interpretation is the same as in Figure 4.3. Each ternary plot displays  $k = 250$  extremal angles extracted from  $n = 10^4$  samples of  $\mathbf{X}$  under the three models. For  $\Lambda_1$  (left) and  $\Lambda_3$  (right) the data variability is approximately one-dimensional with differing degrees of curvature. Under  $\Lambda_2$  (middle) the data cloud is two-dimensional. The dependence structure corresponding pairwise tail dependence coefficients  $\chi_{ij}$  is shown in Figure 4.6 (left). There are three clusters of asymptotically dependent variables. The pairwise dependencies are strong in clusters 1 and 3 and more variable in cluster 2. This

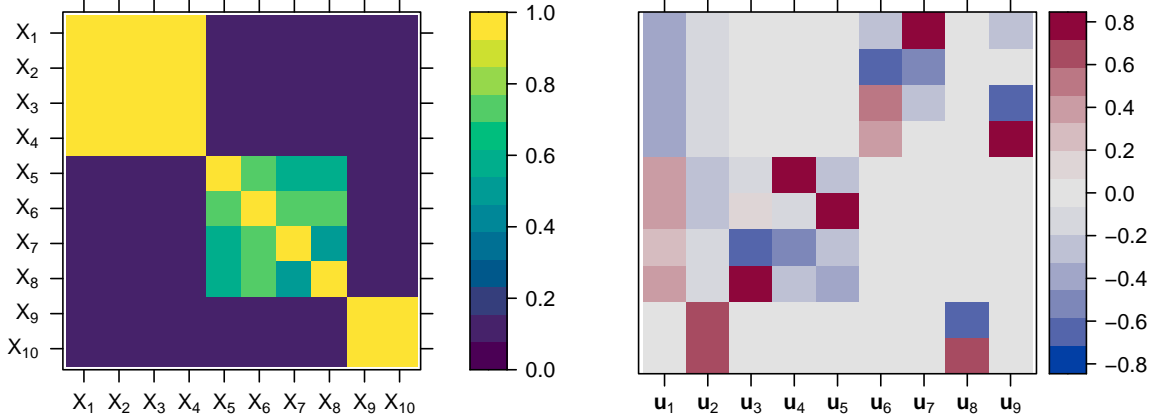


Figure 4.6.: Representations of the extremal dependence structure of the 10-dimensional Hüsler-Reiss distribution parametrised by  $\Lambda_4$ . Left: the TDM, i.e. the matrix of tail dependence coefficients  $\chi_{ij}$ . Right: eigenvectors of the true CLR-covariance matrix.

structure can also be seen via the CLR-covariance matrix eigenvectors (Figure 4.6, right). The leading eigenvectors  $u_1$  and  $u_2$  separate out the three clusters. The localised behaviour of cluster 2 is captured by eigenvectors  $u_3$ ,  $u_4$  and  $u_5$ . The remaining four (non-zero) eigenvectors relate to fine-scale behaviour in clusters 1 and 3.

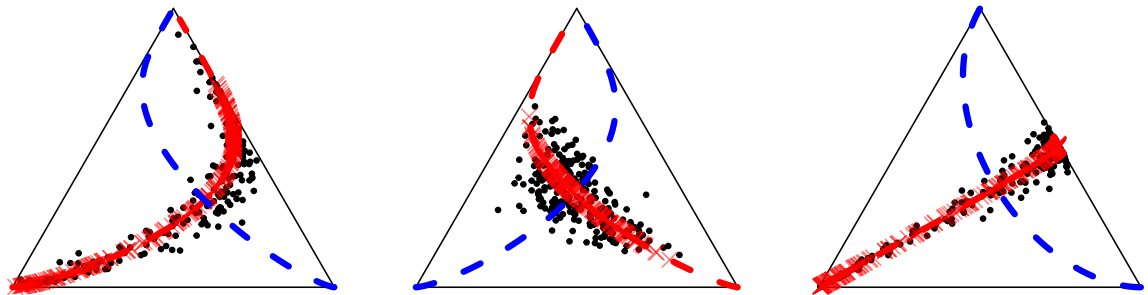


Figure 4.7.: CoDA-PCA applied to data from Hüsler-Reiss models parametrised by  $\Lambda_1$  (left)  $\Lambda_2$  (middle) and  $\Lambda_3$  (right). The black points are the extremal angles ( $k = 250$ ,  $n = 10^4$ ). The red and blue dashed lines represent the first and second principal axes, respectively. The red crosses represent the projections onto the first principal subspace.

Similar to before, we repeatedly generate  $n$  samples of each random vector  $\mathbf{X}_i$ ,  $i = 1, \dots, 4$ , and perform PCA based on the  $k$  largest observations in norm. We choose  $n = 5,000$  and  $k = 50$  when  $d = 3$  and  $n = 10^4$  and  $k = 200$  when  $d = 10$ . The true probabilities  $p_{\min}$  and  $p_{\max}$  are computed empirically from  $n = 10^6$  samples based on  $u = 100$ . To three decimal places, the true values of  $p_{\min}$  (resp.  $p_{\max}$ ) under the four sub-models are found to be 0.089, 0.228, 0.081 and 0.000 (resp. 0.603, 0.456, 0.586 and 0.385). Results are based

on 50 repeats of the experiment.

Figure 4.8 illustrates the Aitchison loss  $\mathcal{L}_a$  for the first three models. As expected, models 1 and 3 permit an accurate one-dimensional representation, whereas model 2 requires both CoDA components. Under model 2, extremal dependence is strong and the angular measure is concentrated near the barycentre of the simplex, where the Euclidean and Aitchison geometries are most similar. Therefore both methods produce comparable outcomes. On the other hand, the extremal angles of  $\mathbf{X}_1$  and  $\mathbf{X}_3$  lie near the simplex boundary, so we expect the methods to diverge. It is obvious from Figure 4.7 (left) that DS-PCA with  $p = 1$  will fail for model 1; this is borne out in the results. Interestingly, it also performs poorly for model 3, despite the apparently linear structure of the data. This is because lines that are visually straight in a ternary diagram do not generally correspond to Euclidean straight lines. (Line segments that are visually straight and near the simplex centre may be well-approximated by a Euclidean line segment.)

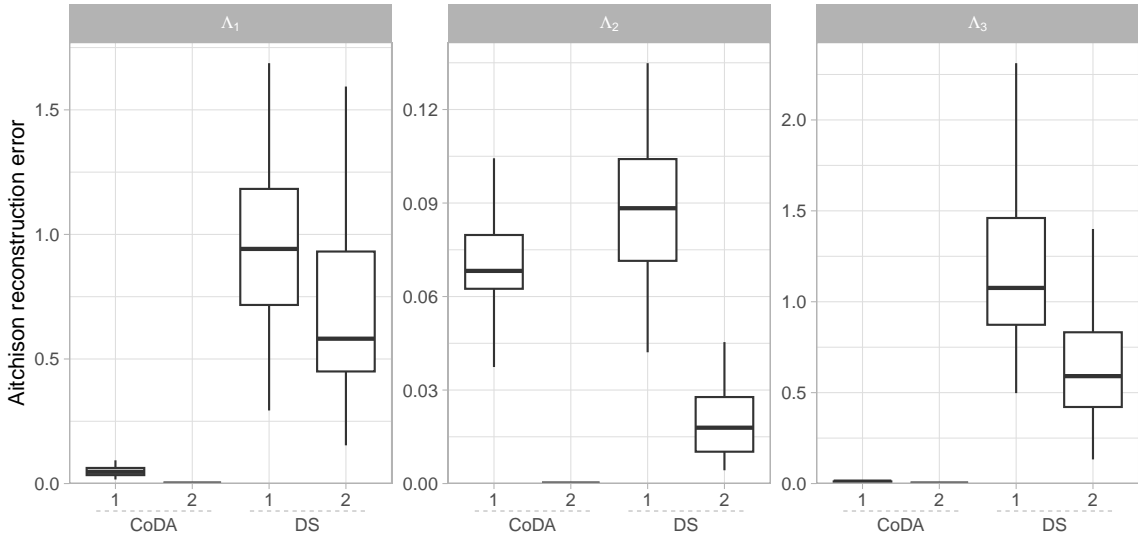


Figure 4.8.: Reconstruction errors associated with CoDA-PCA and DS-PCA for the three trivariate Hüsler-Reiss models. Results are based on 50 repeated simulations. For each rank, the Aitchison reconstruction error (4.2) is estimated from 10,000 samples from the true angular measures.

Finally, we analyse the quality of the dimension reduction in terms of the tail event probabilities. The box plots in Figure 4.9 represent the empirical distributions of  $\hat{p}_{\min}$  across the four generative models. The true probabilities are indicated by the blue dashed lines. For models 1-3, the results follow the same pattern as for the Aitchison loss: for models 1 and 3 one component is sufficient for CoDA but not for DS; for model 2 the PCA methods

perform similarly. Recall that  $p_{\min} \approx 0$  under model 4, owing to the fact that there are three clusters which act (almost) independently. DS-PCA is founded on the empirical TPDM, which tends to overestimate weak dependence – recall the bias issue described in Section 2.6 – inducing a positive bias in the estimates of  $p_{\min}$ . The CoDA-based estimates do not suffer the same issue, suggesting the CLR-covariance matrix is more robust in such settings. Angles corresponding to events occurring in different clusters are mapped to very distant points in CLR-space. This creates large separation between clusters, enabling accurate detection of weakly dependent variables. Analogous plots corresponding to  $p_{\max}$  are provided in Figure C.2 in Appendix C, where the conclusions are broadly the same. For model 4, we point out that our CoDA estimates have lower variance and are therefore superior in terms of mean squared error.

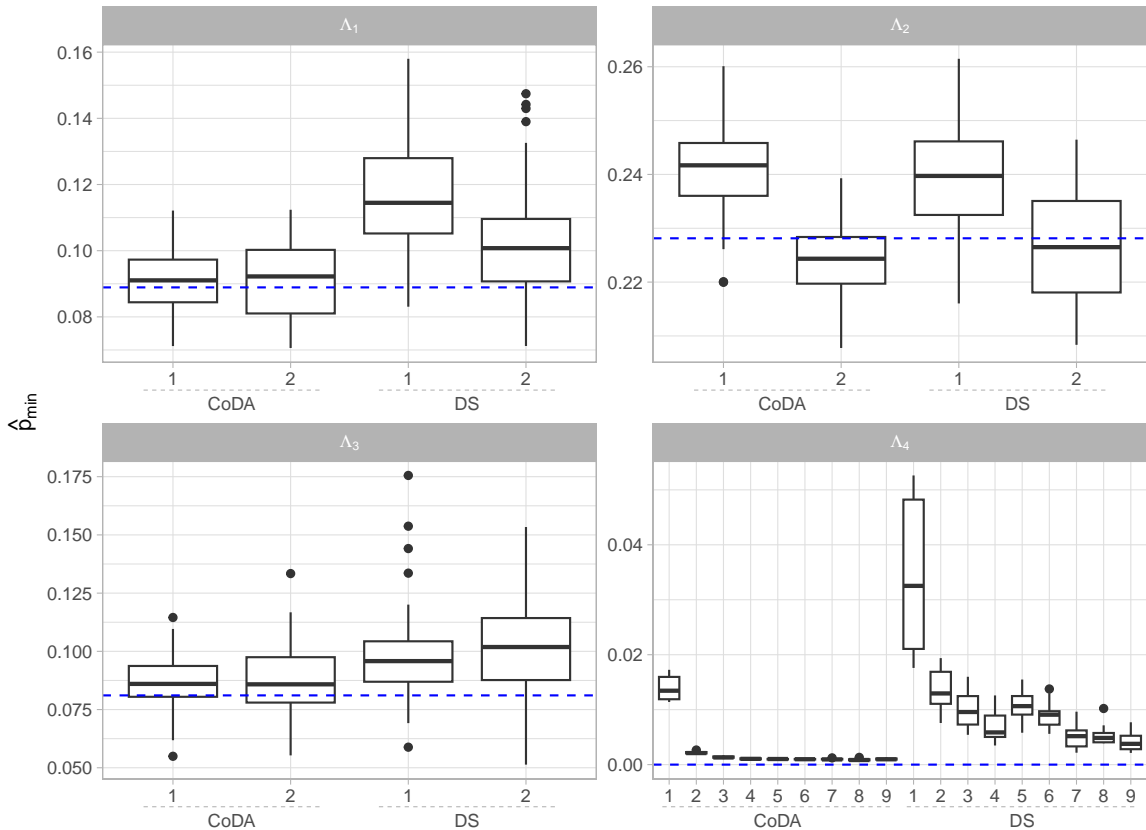


Figure 4.9.: Estimates of  $p_{\min}$  against the rank of the CoDA- or DS-PCA reconstruction for the four Hüsler-Reiss models. Results are based on 50 repeated simulations.

## 4.4. Compositional classification for extremes

### 4.4.1. Motivation and framework

To lay out the framework for this section, we formulate the problem of binary classification in extreme regions as set out in Jalalzai et al. (2018). Let  $(\mathbf{X}, Y)$  be a random pair with unknown joint distribution  $F_{(\mathbf{X}, Y)}$ , where  $Y \in \{-1, +1\}$  is a binary class label and  $\mathbf{X} = (X_1, \dots, X_d)$  is an  $\mathbb{R}_+^d$ -valued random vector containing covariate information that is presumed to be useful for predicting  $Y$ . For  $\sigma \in \{-, +\}$ , assume  $\mathbf{X} | Y = \sigma 1$  is multivariate regularly varying with tail index  $\alpha = 1$  and angular measure  $H_\sigma$  with respect to  $\|\cdot\|_1$ . Suppose  $(\mathbf{X}_1, Y_1), \dots, (\mathbf{X}_n, Y_n)$  is a labelled training set comprising independent copies of  $(\mathbf{X}, Y)$ . In general classification settings, the goal is to learn a classifier  $g : \mathbb{R}^d \rightarrow \{-1, +1\}$  that minimises the expected classification error rate

$$\mathcal{L}(g) := \mathbb{P}(Y \neq g(\mathbf{X})).$$

By the law of total probability, this decomposes as

$$\mathcal{L}(g) = \mathbb{P}(Y \neq g(\mathbf{X}) | \|\mathbf{X}\| \leq t)\mathbb{P}(\|\mathbf{X}\| \leq t) + \mathbb{P}(Y \neq g(\mathbf{X}) | \|\mathbf{X}\| > t)\mathbb{P}(\|\mathbf{X}\| > t)$$

for some large  $t > 0$ . Jalalzai et al. (2018) point out that the optimal classifier need not perform well in extreme regions of the predictor space  $\{\|\mathbf{X}\| > t\}$ , since such regions exert a negligible influence over the global prediction error. They propose building a classifier that minimises the asymptotic risk in the extremes, defined as

$$\mathcal{L}_\infty(g) := \lim_{t \rightarrow \infty} \mathbb{P}(Y \neq g(\mathbf{X}) | \|\mathbf{X}\| > t).$$

They prove that, under certain assumptions and over a certain family of classifiers  $\mathcal{G}$ , the optimal tail classifier  $g^* := \arg \min_{g \in \mathcal{G}} \mathcal{L}_\infty(g)$  is of the form  $g^*(\mathbf{x}) = g^*(\mathbf{x}/\|\mathbf{x}\|)$  (Jalalzai et al. 2018, Theorem 1). That is, the optimal classifier depends on  $\mathbf{x}$  only through its angular component. In practice, they suggest estimating  $g^*$  by minimising the empirical risk

$$\hat{\mathcal{L}}_t(g) = \frac{1}{k} \sum_{i=1}^k \mathbf{1}\{g(\Theta_{(i)}) \neq Y_{(i)}\}, \quad (4.7)$$

where  $Y_{(i)}$  is the class label associated with  $\mathbf{X}_{(i)}$ . The remainder of their paper is devoted to providing theoretical guarantees for this learning principle. They leave aside the practical issue of designing algorithms for solving (4.7), instead resorting to general-purpose classifiers such as  $k$ -NN and random forests.

Being familiar with CoDA, we may recognise (4.7) as simply a compositional binary classification problem. The CoDA community has developed bespoke algorithms for classifying compositional data in a way that accounts for their unique geometry (Joo and Lee 2021; Martín-Fernández et al. 1998; Tsagris et al. 2016). The contribution of this section is to showcase the use of off-the-shelf CoDA methods for extremal classification and demonstrate their superiority over traditional classifiers intended for unconstrained data.

#### 4.4.2. Compositional classifiers and the $\alpha$ -metric

Classifiers are intrinsically linked to the geometry of the sample space. Suppose we observe training samples  $(\mathbf{x}_1, y_1), \dots, (\mathbf{x}_n, y_n)$  of  $(\mathbf{X}, Y)$  and wish to classify a new, unseen data point  $\mathbf{x}^*$ . Consider three popular classifiers:  $k$ -nearest neighbours ( $k$ -NN), support vector machines (SVM) and random forest (RF). We assume basic familiarity with these algorithms and refer the reader to Hastie et al. (2009) for more details. The  $k$ -NN algorithm allocates  $\mathbf{x}^*$  to the majority class among its  $k$  nearest neighbours. The notion of neighbours implicitly assumes an underlying distance metric. An SVM finds the optimal hyperplane that maximally separates data into different classes. The definition of a hyperplane is inherently dependent on the ambient space and speaking of maximal separation assumes a distance metric. Random forests are less dependent on the geometry, but it still influences the model in terms of how points are distributed over the feature space. If  $\mathbf{X}$  is a compositional random vector, then the CoDA philosophy dictates that each algorithm should be tailored to the geometry of the simplex. The Aitchison Hilbert space is an obvious choice. Under this approach, the data undergo a CLR-transformation before being classified in the usual way. However, Greenacre (2024) argues that for supervised problems where an objective performance criterion (e.g. out-of-sample classification error rate) is available, we should not be wedded to the Aitchison geometry and might consider alternatives such as the  $\alpha$ -metric proposed by Tsagris et al. (2016). The  $\alpha$ -metric is similar

to the Aitchison matrix, except the CLR-transformation is substituted with a Box-Cox type transformation.

**Definition 4.1.** For  $\alpha \geq 0$ , the  $\alpha$ -transformation is defined by

$$\mathbf{z}_\alpha : \mathbb{S}_{+(1)}^{d-1} \rightarrow \mathbb{R}^d, \quad \mathbf{x} \mapsto H \cdot \left( \frac{d(\alpha \odot \mathbf{x}) - \mathbf{1}_d}{\alpha} \right),$$

where  $H$  is any  $(d-1) \times d$  real matrix with orthonormal rows and the  $\alpha = 0$  case is interpreted as  $\mathbf{z}_0(\mathbf{x}) := \lim_{\alpha \downarrow 0} \mathbf{z}_\alpha(\mathbf{x})$ .

Typically  $H$  is chosen as the Helmert matrix with its first row removed, but the classification algorithms we consider are invariant to this choice. Note that  $\alpha$  is completely unrelated to the tail index of  $\mathbf{X}$ , also denoted by  $\alpha$ , which we have fixed equal to 1 throughout this section.

**Definition 4.2.** Let  $\mathbf{x}, \mathbf{y} \in \mathbb{S}_{+(1)}^{d-1}$  be closed compositions. For  $\alpha \in \mathbb{R}$ , the  $\alpha$ -metric is defined as

$$d_\alpha(\mathbf{x}, \mathbf{y}) := \|\mathbf{z}_\alpha(\mathbf{x}) - \mathbf{z}_\alpha(\mathbf{y})\|_e$$

The special cases  $\alpha = 0$  and  $\alpha = 1$  are equivalent to the Aitchison and Euclidean distances, respectively. For any Euclidean classifier  $g_e : \mathbb{R}^d \rightarrow \{-1, 1\}$  and  $\alpha \geq 0$ , the  $\alpha$ -transformed compositional classifier is simply

$$g_\alpha : \mathbb{S}_{+(1)}^{d-1} \rightarrow \{-1, 1\}, \quad \boldsymbol{\theta} \mapsto g_e(\mathbf{z}_\alpha(\boldsymbol{\theta})).$$

Adapting  $k$ -NN, SVM and RF in this way, Tsagris et al. (2016) define three families of compositional classification algorithms, which we denote by  $k$ -NN( $\alpha$ ), SVM( $\alpha$ ) and RF( $\alpha$ ). Each family encompasses a Euclidean- and Aitchison-based classifier corresponding to  $g_0$  and  $g_1$ , respectively. The hyperparameter  $\alpha$  may be selected by standard tuning procedures such as cross-validation and provides a way of comparing prediction error across different geometries. Crucially, if the classification error rate is lower for  $\alpha = 0$  than for  $\alpha = 1$ , then it confirms that switching to a simplicial geometry is beneficial for performance.

### 4.4.3. Simulation experiments

For our simulation experiments, we generate realisations of  $\mathbf{X} \mid Y = y$  in  $d = 3$  dimensions on 1-Fréchet margins from one of three MEV models: symmetric logistic (SL), negative symmetric logistic (NL), and bilogistic (BL). The classes are balanced globally and asymptotically, meaning

$$p = \mathbb{P}(Y = +1) = 0.5, \quad p_\infty := \lim_{t \rightarrow \infty} \mathbb{P}(Y = +1 \mid \|\mathbf{X}\|_1 > t) = 0.5.$$

The negative ( $y = -1$ ) and positive ( $y = +1$ ) class instances are generated using different (scalar) dependence parameters, denoted  $\vartheta_{-1}$  and  $\vartheta_1$ , respectively. For the SL and NL models,  $\vartheta_\sigma$  corresponds to the parameter  $1/\gamma$  as in Definition 2.1. The BL model sets all of its parameters equal to  $\vartheta_\sigma \in [0, 1]$  – see the documentation of the `mev` package for more details.

From each model, we simulate  $n = 5 \times 10^3$  training samples  $(\mathbf{x}_1, y_1), \dots, (\mathbf{x}_n, y_n)$  and use  $\{(\boldsymbol{\theta}_{(i)}, y_{(i)}) : i = 1, \dots, k\}$  with  $k = 500$  to train each tail classifier. The set of classifiers we consider is  $k$ -NN( $\alpha$ ) and RF( $\alpha$ ) for  $\alpha \in \{0, 0.1, \dots, 0.9, 1\}$  and SVM( $\alpha$ ) for  $\alpha \in \{0, 0.2, \dots, 0.8, 1\}$ . Implementations of these algorithms are readily available in the `Compositional` and `CompositionalML` R packages. The hyperparameters (e.g. the number of neighbours in  $k$ -NN( $\alpha$ )) are chosen by minimising the estimated out-of-sample classification error through 10-fold cross-validation. The use of cross-validation for estimating asymptotic classification risk is studied in more detail in Aghbalou et al. (2024). The cross-validated empirical risk is used as a measure of the training error of the optimal classifier. To assess its out-of-sample, asymptotic performance, we compute an approximation of the asymptotic risk  $\mathcal{L}_\infty$  by measuring the error rate across  $10^5$  realisations from the true limit model, i.e. angles sampled from  $H_-$  and  $H_+$  generated via the `rmevspec` function from the `mev` package. All reported results are based on 100 repeated simulations.

Figure 4.10 illustrates one realisation of the extremal angles in the training set for each model and different combinations of  $\vartheta_{-1}, \vartheta_1$ . In the top row,  $\vartheta_1/\vartheta_{-1} = 1.5$  and the classes' dependence structures are very similar, making prediction very challenging. For the bottom row, the ratio becomes  $\vartheta_1/\vartheta_{-1} = 3$  and the class separation becomes much greater. In general classification settings the classes may concentrate in different sub-regions of the

feature space. Our setting is complicated by the fact that the angular measures  $H_+$  and  $H_-$  are subject to the constraints (2.13). It is impossible to encounter a scenario where, say, the red points are all near the bottom edge and the blue points are all near the opposing vertex. Instead, any class separation that occurs tends to relate to whether the points are close to the centre or near the boundary, as shown in the bottom middle and bottom right plots. For the other sub-models, the plots suggest that predictive performance will vary across the features space. For example, under the BL model with  $\vartheta_1/\vartheta_{-1} = 1.5$  (top left), points near the right-most edge can be classified as  $Y = 1$  with a reasonable degree of confidence, but points near the centre are near-impossible to classify.

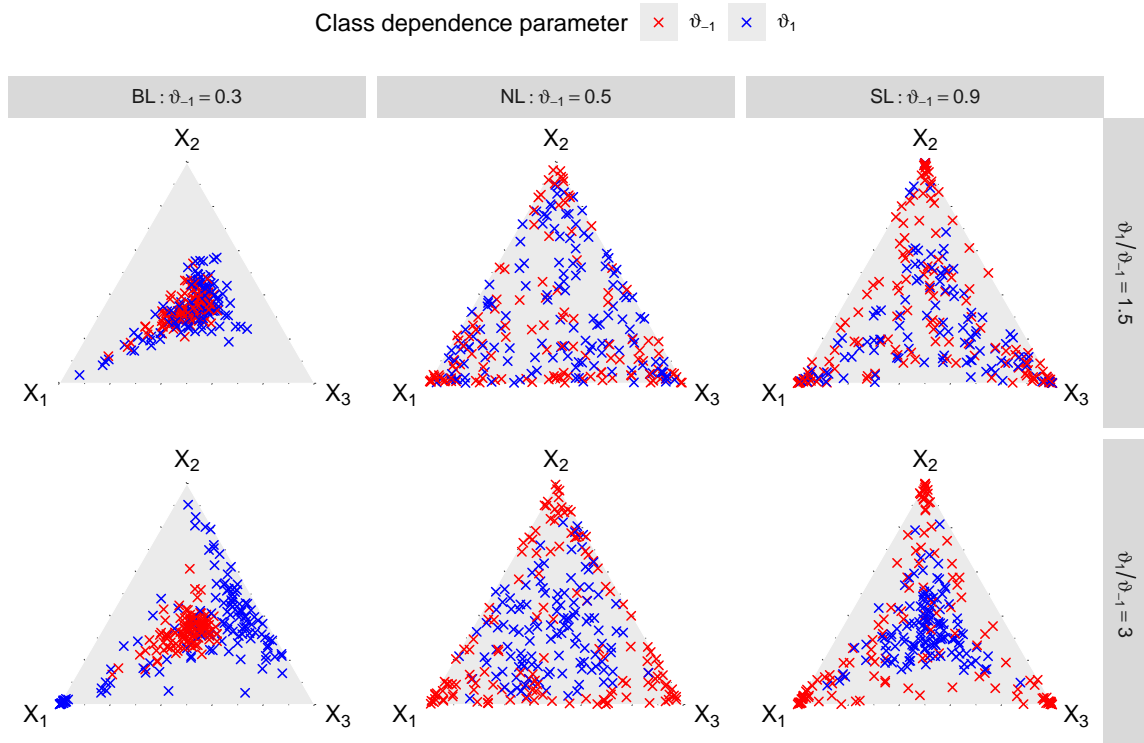


Figure 4.10.: Examples of the  $k = 500$  extremal angles simulated from the bilogistic (left), negative logistic (middle) and symmetric logistic (right) models for different combinations of  $\vartheta_{-1}, \vartheta_1$ . The red and blue crosses correspond to realisations from the negative and positive classes, respectively.

Figure 4.11 plots the asymptotic risk as a function of  $\alpha$  for each algorithm and generative process. The coloured lines are the median risk across the 100 simulations while the shaded regions demarcate the interquartile range. As expected, the ratio between the dependence parameters dictates the difficulty level of the learning task: the error rates are between 30-40% when  $\vartheta_1/\vartheta_0 = 1.5$  and between 2-16% when  $\vartheta_1/\vartheta_0 = 3$ . Universally,

the classifiers perform worst when  $\alpha = 1$ , i.e. in the Euclidean geometry. This supports our main argument that traditional multivariate techniques are ill-suited to tasks of this nature. For the BL and SL data, the asymptotic risk is minimised by taking  $\alpha = 0$ . For the NL data, the optimum occurs at some intermediate value, say  $0.2 \leq \alpha \leq 0.4$ . Thus the optimal classifiers fall somewhere under the CoDA umbrella and are significantly different from the naive Euclidean classifiers. The choice of classifier is obviously a key determinant of performance, with  $k\text{-NN}(\alpha)$  typically being the worst-performing and  $\alpha\text{-SVM}$  the best. A full comparison of the relative merits of each classifier is beyond the scope of our investigation. However, it should be pointed out that for each  $\vartheta_1/\vartheta_0 = 3$  sub-case (bottom row), the worst-performing Aitchison classifier is as good as the best-performing Euclidean classifier. Switching to a more appropriate geometry reaps similar performance benefits to utilising more sophisticated classifiers.

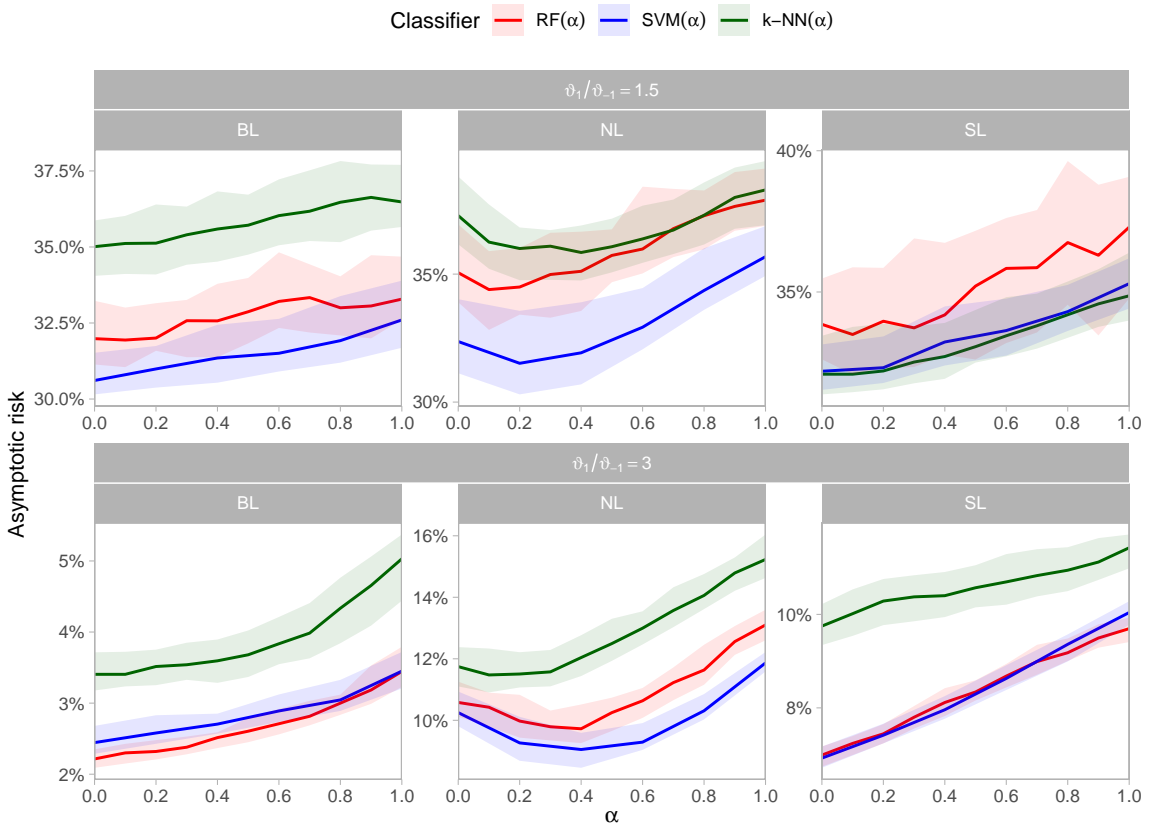


Figure 4.11.: The asymptotic risk  $\mathcal{L}_\infty$  of the estimated classifiers as a function of the transformation parameter  $\alpha$ . The solid lines and shaded regions represent the median risk and the interquartile range over 100 simulations.

In practice, we cannot choose  $\alpha$  by examining the asymptotic risk. Instead,  $\alpha$  becomes an

additional hyperparameter to be selected by minimising the cross-validation training error along with the other tuning parameters. Let  $\hat{\alpha}$  denote the selected value of  $\alpha$  (i.e. the  $\alpha$  that attains the lowest training error) and  $\alpha^*$  the true optimum with respect to the asymptotic risk. Figure 4.12 depicts kernel density estimates of the distribution of  $\hat{\alpha}$  across the 100 data sets. In accordance with Figure 4.11, the mode of  $\hat{\alpha}$  is close to  $\alpha^* = 0$  for SL and BL and  $\alpha^* \approx 0.3$  for the NL model. However, there is significant variation and even  $\hat{\alpha} = 1$  is selected in some instances. The profile of  $\hat{\alpha}$  indicates the degree to which the difficulty of the classification task varies across geometries. For example, consider the BL model with  $\vartheta_1/\vartheta_0 = 3$  (top left). Here, the large variation in  $\hat{\alpha}$  can be attributed to the minimal separation between the classes (see Figure 4.10, top left). Adjusting the geometry does little to improve this predicament, so the error rate will be quite insensitive to the choice of  $\alpha$ . Noisy estimates of  $\alpha^*$  are the result. Another example can be seen in the SL data with  $\vartheta_1/\vartheta_0 = 3$ . In this case, classification is relatively easy (Figure 4.10, bottom right). However, the classes are so well separated that Euclidean nearest-neighbours are the same as Aitchison nearest-neighbours, so the performance of  $k$ -NN( $\alpha$ ) does not change dramatically between  $\alpha = 0$  and  $\alpha = 1$ . For SVM( $\alpha$ ) and RF( $\alpha$ ), adjusting the geometry affects the way they partition the feature space, so classification performance is sensitive to this choice and  $\hat{\alpha}$  concentrates near  $\alpha^*$ .

## 4.5. Discussion and outlook

In this chapter, our primary contribution was to establish a link between the disciplines of multivariate EVT and CoDA. Under MRV, they are connected by virtue of the fact that all relevant information provided by a given data point is contained in the relative rather than absolute magnitudes of its constituent parts and, as such, they boil down to modelling a distribution on the simplex. When applied to the extremal angles associated with radial threshold exceedances, compositional principal components analysis may yield more efficient dimension reduction than existing methods. It is able to capture seemingly non-linear associations and demonstrates greater robustness near the simplex boundary. The performance benefits extend beyond the (perhaps slightly esoteric) realm of reconstruction errors; we showed empirically that compressing the angular measure via a CoDA approach leads to substantially better estimates of extreme event probabilities. These findings are

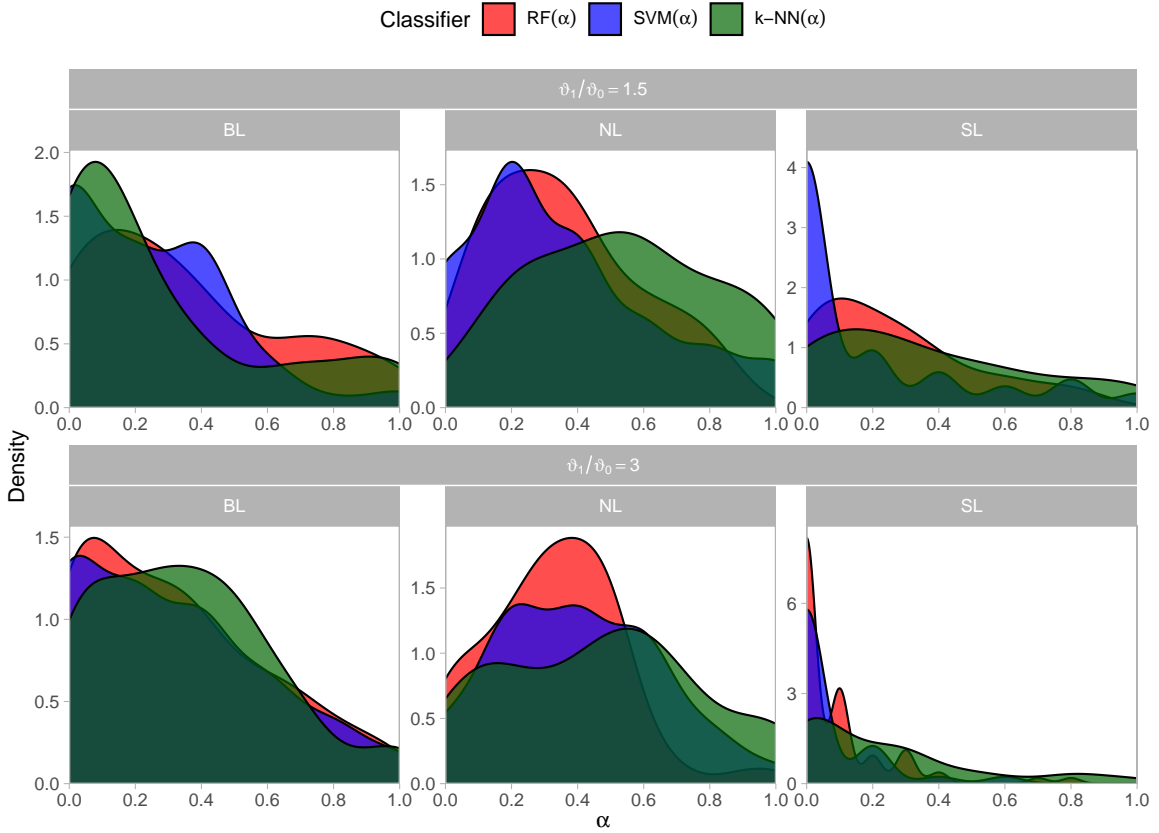


Figure 4.12.: Kernel density estimates of the sampling distribution of  $\hat{\alpha}$ , the transformation parameter that minimises the empirical tail classification risk, across 100 simulations.

echoed in our second application, classification of tail events, where the asymptotic prediction accuracy of various well-known classifiers was shown to improve when the simplex structure of the extremal angles is respected.

The exploratory nature of this chapter means there are several avenues left unexplored. First, it would be desirable to provide some theoretical statistical guarantees for our CoDA-PCA approach, e.g. uniform risk bounds akin to those in Section 3 of Drees and Sabourin (2021). Here, the main hurdle to overcome is the fact that the Aitchison risk can be arbitrarily large, whereas the Euclidean risk is necessarily bounded. Second, our PCA results suggest the CLR-covariance matrix as a potential alternative to the TPDM for summarising the correlation structure of the extremal angles. A more detailed comparison could be useful, to better understand the relative merits and drawbacks of the two. Third, an obvious next step is to apply a CoDA perspective to other problems in multivariate EVT. Clustering seems an obvious initial choice, but the CoDA methods and sub-disciplines

described in Alenazi (2023) might provide some alternative ideas, such as regression.

# 5. EVA (2023) Data Challenge

## 5.1. Preliminaries

The subsequent sections in this chapter contain our paper, published in *Extremes*, based on our submission to the EVA (2023) Data Challenge. In this section, we aim to provide some background information about the competition and the context in which the research was produced. For a more comprehensive overview of the competition format, refer to Rohrbeck et al. (2023). The corresponding data have been made publicly available by Rohrbeck et al. (2024). Readers who are familiar with the EVA (2023) Data Challenge may skip to Section 5.2.

Entrants were tasked with completing four problems, herein referred to as Challenges 1 to 4, and scoring points according to their ranking for each challenge. The tasks entailed estimating quantiles/probabilities associated with extreme events, and were designed to reflect scenarios that might be encountered by applied statisticians analysing environmental extremes data. Specifically, the data were simulated from a fictional country, Utopia. Although the data represent an environmental variable recorded at various locations across Utopia, we are told that spatial information or knowledge about environmental processes is irrelevant. The generative processes used to produce the data were revealed in Rohrbeck et al. (2023) after the competition concluded.

Challenge 1 is a univariate task concerning the conditional distribution of  $Y | \mathbf{X}$ , where  $Y$  represents the environmental variable at a fixed location and  $\mathbf{X}$  is a vector of covariates (e.g. season and wind speed/direction). Teams were asked to submit point estimates and 50% confidence intervals for the 99.99% quantile of  $Y | \mathbf{X} = \mathbf{x}$  for 100 given covariate combinations. Performance was assessed in terms of the intervals' coverage (with 50% being optimal, of course). Challenge 2 involves estimating the 200-year return level of

Table 5.1.: EVA (2023) Data Challenge sub-challenge rankings and overall points.

Team	C1	C2	C3	C4	Points
Yalla	2	2	2	1	42
SHSmultiscale	1	6	7	2	31
genEVA	5	1	4	5	31
Yahabe	3	3	6	4	28
Uniofbathtopia	7	4	1	6	28
Lancopula University	6	5	5	3	25
Wee-Extremes	4	7	3	7	23

$Y$ . Accounting for the altered time-scales of Utopia, this corresponds to the quantile  $q$  such that  $\mathbb{P}(Y > q) = 1/(6 \times 10^4)$ . The performance metric  $L(q, \hat{q})$  in (5.6) quantifies the discrepancy between  $q$  and the submitted estimate  $\hat{q}$  in such a way that under-estimation is penalised more harshly than over-estimation.

Challenge 3 was a three-dimensional, multivariate problem. We consider random variables  $Y_1, Y_2, Y_3$  representing the environmental variable at three sites in Utopia. The challenge requires estimating two probabilities corresponding to extreme events involving some/all of these variables. In particular,  $p_1$  is the probability that all three variables exceed a given high threshold, while  $p_2$  is the probability that  $Y_1$  and  $Y_2$  exceed a high threshold while  $Y_3$  is below a low threshold. The accuracy of teams' estimates was quantified by a probability-based scoring rule. Challenge 4 is similar to Challenge 3, except now there are fifty random variables,  $Y_1, \dots, Y_{50}$ , corresponding to spatial sites located in two administrative zones, 25 in U1 and 25 in U2. The estimands  $p_1$  and  $p_2$  represent the probabilities of joint threshold exceedance events at all fifty sites under two scenarios, depending on whether the protective infrastructure in each zone are subject to the same design standards or not. The same scoring rule as Challenge 3 was used to assess the predictions.

The team affiliated with the University of Bath, ‘Uniofbathtopia’, comprised myself and Henry Elsom (PhD student). Considering our respective research interests, H. Elsom worked on the univariate challenges and I worked on the multivariate ones. The remaining sections of our co-authored paper were researched and written jointly. Our overall performance is summarised in Table 5.1. The remainder of this chapter is reproduced from our published paper.

**Appendix 6B****QA7****Appendix B: Statement of Authorship**(For help with copyright and permissions contact [openaccess@bath.ac.uk](mailto:openaccess@bath.ac.uk)).

<b>This declaration concerns the article entitled:</b>					
Extreme value statistics for analysing simulated environmental extremes					
<b>Publication status (tick one)</b>					
Draft manuscript	<input type="checkbox"/>	Submitted	<input type="checkbox"/>	In review	<input type="checkbox"/>
Accepted	<input type="checkbox"/>	Published	<input checked="" type="checkbox"/> X		
<b>Publication details (reference)</b>	Elsom, H., Pawley, M. Extreme value statistics for analysing simulated environmental extremes. Extremes (2024). <a href="https://doi.org/10.1007/s10687-024-00502-3">https://doi.org/10.1007/s10687-024-00502-3</a>				
<b>Copyright status (tick the appropriate statement)</b>					
The material has been published with a CC-BY license			X	The publisher has granted permission to replicate the material included here	
<b>Candidate's contribution to the paper (provide details, and also indicate as a percentage)</b>	The candidate contributed to / considerably contributed to / predominantly executed the...				
	Formulation of ideas:				
	<ul style="list-style-type: none"> <li>• Section 5.4 (Univariate Challenges): 0% — all ideas formulated and researched by HE.</li> <li>• Section 5.5 (Multivariate Challenges): 100% — all ideas formulated and researched by MP.</li> <li>• Section 5.6 (Conclusion): 50% — ideas relating to multivariate challenges are by MP.</li> </ul>				
	Design of methodology:				
	<ul style="list-style-type: none"> <li>• Section 5.4 (Univariate Challenges): 0% — methodology designed by HE.</li> <li>• Section 5.5 (Multivariate Challenges): 100% — methodology designed by MP.</li> </ul>				
	Experimental work:				
<ul style="list-style-type: none"> <li>• Section 5.4 (Univariate Challenges): 0% — analysis conducted by HE.</li> <li>• Section 5.5 (Multivariate Challenges): 100% — analysis conducted by MP.</li> </ul>					
Presentation of data in journal format:					
<ul style="list-style-type: none"> <li>• Section 5.2 + 5.3 (Abstract + Introduction): 50% — written jointly with HE.</li> <li>• Section 5.4 (Univariate Challenges): 0% — written by HE.</li> <li>• Section 5.5 (Multivariate Challenges): 100% — written by MP.</li> <li>• Section 5.6 (Conclusion): 50% — discussion of univariate challenges is written by HE; discussion of multivariate challenges is written by MP.</li> <li>• Formatting in journal format: 50% — equal contribution with HE.</li> </ul>					
<b>Statement from Candidate</b>	This paper reports on original research I conducted during the period of my Doctoral Degree candidature.				
<b>Signed (typed signature)</b>	Matthew Pawley	Date	08/12/2024		

## 5.2. Abstract

We present the methods employed by team ‘Uniofbathtopia’ as part of a competition organised for the 13th International Conference on Extreme Value Analysis (EVA2023), including our winning entry for the third sub-challenge. Our approaches unite ideas from extreme value theory, which provides a statistical framework for the estimation of probabilities/return levels associated with rare events, with techniques from unsupervised statistical learning, such as clustering and support identification. The methods are demonstrated on the data provided for the EVA (2023) Conference Data Challenge – environmental data sampled from the fantasy country of ‘Utopia’ – but the underlying assumptions and frameworks should apply in more general settings and applications.

## 5.3. Introduction

In recent decades, the field of environmental sciences has experienced significant advancements, particularly through the utilisation of sophisticated modelling techniques to better understand extreme events. Extreme value analysis is the branch of statistical modelling that focuses on quantifying the frequency and severity of very rare events. Notably, the Peaks over Threshold (PoT) approach (Davison and Smith 1990; Pickands III 1975), has played a pivotal role in enhancing our comprehension of extreme environmental phenomena. Within climate science, significant strides have been made in the modelling of a broad spectrum of variables, including temperature (Clarkson et al. 2023), precipitation (Katz 1999), wind speeds (Fawcett and Walshaw 2006; Kunz et al. 2010), as well as other broader environmental topics including hydrology (Katz et al. 2002; Towler et al. 2010) and air pollution (Gouldsborough et al. 2022).

In this paper, we outline the techniques utilised by the team ‘Uniofbathtopia’ for the data challenge organised for the 13<sup>th</sup> International Conference on Extreme Value Analysis (EVA2023). A full description of the tasks can be found in the editorial (Rohrbeck et al. 2023). We outline our methodologies for each of the four sub-challenges, in which we complement traditional methods from extreme value statistics with other statistical modelling techniques according to the requirements of each task. The challenges involve the

estimation of extreme marginal quantiles, marginal exceedance probabilities and joint tail probabilities within the context of an environmental application, designed on the fictitious country of ‘Utopia’. The organisers of the competition simulated the data using known parameters, so that teams’ models could be validated and compared, and in such a way as to mimic the rich, complex behaviour exhibited by real-world processes. Therefore, we expect that the performance of our proposed methods should extend to general settings and applications.

In the univariate tasks we utilise the generalised Pareto distribution (GPD) and use model-based clustering methods including hierarchical models (Hastie et al. 2009) and mixture models (Fraley and Raftery 2002), as well as Markov chain Monte Carlo (MCMC) for parameter estimation (Coles and Powell 1996). We also use bootstrapping methods for confidence interval estimation (Gilleland 2020). For the multivariate problems our approaches are heavily based on the parametric family of max-linear combinations of regularly varying random variables (Fougères et al. 2013). We introduce novel methods for performing inference for these models, advancing existing approaches (Cooley and Thibaud 2019; Kiriliouk and Zhou 2022) using modern statistical learning techniques including sparsity-inducing projections and clustering. The novel aspects of our work are: exploring MCMC parameter estimation bias for systems with large uncertainty in tail behaviour, and proposing a new estimator for the noise coefficient matrix of a max-linear model based on sparse projections onto the simplex.

The format of the paper is as follows: Section 5.4 describes our solutions for the univariate challenges with each challenge split into methodology and results sections. Section 5.5 introduces the requisite background theory from multivariate extremes before outlining the methodological frameworks and the results attained for Challenges 3 and 4. We conclude with some final discussion of our performance in Section 5.6.

## 5.4. Univariate Challenges

The first two challenges both involve estimating univariate extreme marginal quantiles, so we initially describe some of the theory that will be used across both tasks. Suppose that a generalised Pareto distribution with scale and shape parameters,  $\sigma$  and  $\xi$  respectively, is

a suitable model for exceedances of a high threshold  $u$  by a variable  $Y$ . Then, for  $y > u$ ,

$$\mathbb{P}(Y > y \mid Y > u) = \begin{cases} \left(1 + \xi \left(\frac{y-u}{\sigma}\right)\right)_+^{-1/\xi}, & \xi \neq 0, \\ \exp\left(-\frac{y-u}{\sigma}\right), & \xi = 0, \end{cases}$$

where  $\xi, u \in \mathbb{R}$ ,  $\sigma \in \mathbb{R}^+$  and  $(\cdot)_+ = \max(\cdot, 0)$ . Given the probability  $\zeta_u = \mathbb{P}(Y > u)$ , the probability of  $Y > y$  can be expressed as

$$\mathbb{P}(Y > y) = \zeta_u \mathbb{P}(Y > y \mid Y > u). \quad (5.1)$$

We can find the  $p$ th percentile of the distribution of  $Y$  by rearranging the distribution function to form the quantile function,

$$q(p) = \begin{cases} u + \frac{\sigma}{\xi} \left( \left( \frac{\zeta_u}{1-p} \right)^\xi - 1 \right), & \xi \neq 0, \\ u + \sigma \log \left( \frac{\zeta_u}{1-p} \right), & \xi = 0, \end{cases}$$

where  $p > 1 - \zeta_u$  to ensure that  $q(p) > u$ . However, we can also write down this expression for a return level, that is, the level  $y_T$  that is exceeded on average once every  $T$  years,

$$y_T = \begin{cases} u + \frac{\sigma}{\xi} ((Tn_{\text{yr}}\zeta_u)^\xi - 1), & \xi \neq 0, \\ u + \sigma \log(Tn_{\text{yr}}\zeta_u), & \xi = 0. \end{cases} \quad (5.2)$$

where  $n_{\text{yr}}$  is the number of observations per year. For the purposes of the second challenge,  $n_{\text{yr}} = 300$  as we are given that a year in Utopia consists of 12 months and 25 days per month, and there is one observation per day.

These expressions imply that, having chosen an appropriate threshold  $u$ , we can estimate quantiles and return levels once we obtain estimates of  $\sigma$  and  $\xi$ . The method of obtaining these values is different for different tasks and will be described, for the univariate challenges, in Section 5.4.2 and Section 5.4.2. We also require an estimate of  $\zeta_u$ , the probability of an individual observation exceeding the threshold  $u$ . We can achieve this by using the empirical probability of  $Y$  exceeding  $u$ ,

$$\hat{\zeta}_u = \sum_{i=1}^n \mathbf{1}\{y_i > u\}/n, \quad (5.3)$$

that is, the proportion of the total number of observations that exceed the threshold for observations  $y_1, \dots, y_n$ , where for the univariate challenges  $n = 21,000$ , and where  $\mathbf{1}\{y_i > u\}$  is the indicator function,

$$\mathbf{1}\{y_i > u\} = \begin{cases} 1 & \text{if } y_i > u, \\ 0 & \text{otherwise.} \end{cases}$$

### 5.4.1. Data

We are interested in the extreme values of the environmental variable  $Y$  which, for the two univariate tasks, we denote  $Y_i$  for day  $i$ . For each day, we also have a vector of covariates  $\mathbf{X}_i = (V_{1,i}, \dots, V_{8,i})$  with variables  $(V_1, \dots, V_4)$  representing unnamed covariates and  $(V_5, V_6, V_7, V_8)$  representing season, wind speed, wind direction and atmosphere respectively. Season is a factor variable, where  $V_5 \in \{1, 2\}$ , and each season covers half of the year. We perform our methodology for this challenge on each season individually. Given the covariates  $\mathbf{X}_1, \dots, \mathbf{X}_n$ ,  $Y_1, \dots, Y_n$  are independent (Rohrbeck et al. 2023). For the first challenge, the data is divided into a training set comprising 70 years' worth of daily environmental data and a test set featuring 100 days of environmental data, showcasing diverse combinations of the covariates. We denote the test data points by  $\tilde{\mathbf{x}}_1, \dots, \tilde{\mathbf{x}}_{100}$ . A comprehensive description of the dataset for this challenge is available in the competition editorial (Rohrbeck et al. 2023).

### 5.4.2. Challenge 1

#### 5.4.2.1. Methodology

In the first task, we are required to provide point estimates and central 50% confidence intervals for extreme quantiles. As such, we need a model for the distribution of  $Y | \mathbf{X}$  in order to estimate the conditional quantiles,  $q_1, \dots, q_{100}$ , where

$$\mathbb{P}(Y \leq q_k) | \mathbf{X} = \tilde{\mathbf{x}}_k = 0.9999.$$

We approach this problem with a two step strategy. We first partition the covariate space into clusters and then analyse the extremes of each cluster individually. In each resulting

cluster, it is assumed that the extreme values can be adequately modelled using a GPD, characterised by common scale and shape parameters, along with a common threshold and exceedance probability. To implement this, we propose partitioning the observations into groups by fitting a Gaussian mixture model to the environmental covariates. The dataset contained some missing values. We assumed that the missing observations were missing completely at random and removed them from the analysis, which was a valid assumption based on the editorial Rohrbeck et al. (2023).

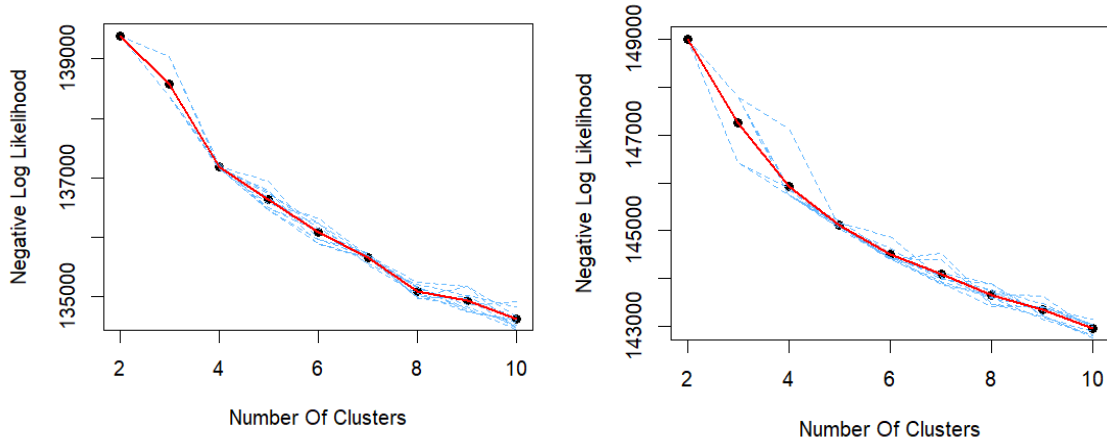


Figure 5.1.: An elbow plot to determine an optimum number of clusters for season 1 (top) and season 2 (bottom). The figure displays the negative log-likelihood for different simulations (blue) as well as the average (red).

We perform the clustering of the covariates for each season individually by using the method in Fraley and Raftery (2003). Let  $\mathbf{x}_1^{(s)}, \dots, \mathbf{x}_N^{(s)}$ , where  $N = n/2$ , denote the observations for season  $s \in \{1, 2\}$ . We then assume that the covariates are sampled from a mixture of multivariate normal distributions. More formally, we want to estimate a  $d$ -dimensional Gaussian mixture model (where  $d = 7$  in this challenge) with  $J^{(s)}$  components, mean vectors  $\boldsymbol{\mu}_1^{(s)}, \dots, \boldsymbol{\mu}_{J^{(s)}}^{(s)} \in \mathbb{R}^d$ , mixture probabilities  $\boldsymbol{\alpha}^{(s)} = \{\alpha_1^{(s)}, \dots, \alpha_{J^{(s)}}^{(s)}\}$ , where  $\alpha_j^{(s)} > 0$  and  $\sum_{j=1}^{J^{(s)}} \alpha_j^{(s)} = 1$ , and covariance matrices  $\boldsymbol{\Sigma}_1^{(s)}, \dots, \boldsymbol{\Sigma}_{J^{(s)}}^{(s)} \in \mathbb{R}^{d \times d}$ , which are symmetric and positive definite. In the remainder of the subsection, we drop the season index  $s$  for brevity. The probability density function of the observation  $\mathbf{x}_i$  can then be written as

$$p(\mathbf{x}_i | \boldsymbol{\Psi}) = \sum_{j=1}^J \alpha_j \phi(\mathbf{x}_i; \boldsymbol{\mu}_j, \boldsymbol{\Sigma}_j) \quad (5.4)$$

where  $\boldsymbol{\Psi} = \{\boldsymbol{\alpha}, \boldsymbol{\mu}, \boldsymbol{\Sigma}\}$  are the parameters of the mixture model and we use  $\phi(\cdot; \boldsymbol{\mu}_j, \boldsymbol{\Sigma}_j)$  to

denote the probability density function of the Gaussian distribution with mean vector  $\boldsymbol{\mu}_j$  and covariance matrix  $\boldsymbol{\Sigma}_j$ . Assuming that an appropriate fixed  $J$  has been found for each season, the mixture model parameters  $\boldsymbol{\Psi}$  are unknown and to be found. In order to achieve this, we use the expectation maximisation (EM) algorithm to perform maximum likelihood estimation (McLachlan and Peel 2000), which is executed using the `mclust` package in R (Fraley and Raftery 2003). The optimum number of clusters is then found by using the elbow method; we derive the negative log-likelihood for each choice of  $J$ , and identify the point at which this value begins to plateau.

In addition to the cluster parameters, the EM algorithm gives a cluster allocation for the observations. We use this allocation to split the observations of  $Y$ , and we denote by  $\mathcal{Y}^{(j)}$  the data points in the  $j$ th cluster ( $j = 1, \dots, J$ ). We are then able to perform extreme value analysis on each set of points  $\mathcal{Y}^{(j)}$  separately, by fitting a GPD, with parameters  $\hat{\sigma}_j$  and  $\hat{\xi}_j$ , to the extremal data, using maximum likelihood estimation, as outlined at the start of Section 5.4. We make the assumption that the effects of the covariates on  $Y$  are entirely captured by the cluster assignments. The threshold,  $\hat{u}_j$ , is chosen by interpreting mean residual life plots and parameter stability plots (Coles 2001).

The cluster estimates are then used to estimate  $q_k$ . We introduce a latent variable  $Z_k$ , where  $Z_k = j$  refers to  $\tilde{\mathbf{x}}_k$  being allocated to the  $j$ th cluster. Using the law of total probability, we then write  $\mathbb{P}(Y > q_k | \mathbf{X} = \tilde{\mathbf{x}}_k)$  as

$$\mathbb{P}(Y > q_k | \mathbf{X} = \tilde{\mathbf{x}}_k) = \sum_{j=1}^J \mathbb{P}(Z_k = j | \mathbf{X} = \tilde{\mathbf{x}}_k) \mathbb{P}(Y > q_k | \mathbf{X} = \tilde{\mathbf{x}}_k, Z_k = j). \quad (5.5)$$

We can write the first probability in this expression using (5.4),

$$\mathbb{P}(Z_k = j | \mathbf{X} = \tilde{\mathbf{x}}_k) = \frac{\alpha_j \phi(\tilde{\mathbf{x}}_k; \boldsymbol{\mu}_j, \boldsymbol{\Sigma}_j)}{p(\tilde{\mathbf{x}}_k | \boldsymbol{\Psi})},$$

and using (5.1), it is possible to express the second probability as

$$\mathbb{P}(Y > q_k | Z_k = j, \mathbf{X} = \tilde{\mathbf{x}}_k) = \mathbb{P}(Y > q_k | Y > \hat{u}_j, Z_k = j) \mathbb{P}(Y > \hat{u}_j | Z_k = j).$$

The exceedance probability,  $\mathbb{P}(Y > \hat{u}_j | Z_k = j)$  is calculated empirically using (5.3), and the other probability in the expression is found by fitting a GPD to the clusters. We then

have all the components in (5.5) to find  $q_k$  that satisfies  $\mathbb{P}(Y > q_k \mid \mathbf{X} = \tilde{\mathbf{x}}_k) = 0.0001$ .

The challenge also requires central 50% confidence intervals for the estimates of these extreme conditional quantiles. For each set of points in a cluster,  $\mathcal{Y}^{(j)}$ , we are able to find an estimate of the quantile by performing a jackknife resampling (Efron and Stein 1981) of the extremal data and use this to fit the GPD. In the jackknife resampling method, sets of samples are created by leaving out one observation at a time and calculating the quantile point estimate based on the remaining observations. For each observation  $i$  in the extremal dataset  $\mathcal{Y}^{(j)} \mid \mathcal{Y}^{(j)} > \hat{u}_j$ , we create a new dataset  $\mathcal{Y}_{(-i)}^{(j)} \mid \mathcal{Y}^{(j)} > \hat{u}_j$  by excluding the  $i$ th observation. We then fit a new GPD to this data and, using these parameter estimates, calculate the quantile point estimate in (5.2). Once we have undertaken this process for every observation in the dataset, we calculate the empirical 25th and 75th percentiles for the jackknife samples.

#### 5.4.2.2. Results

As mentioned above, we perform clustering separately for each of the two seasons - Season 1 and Season 2. Elbow plots are used to determine suitable number of clusters; these results are displayed in Figure 5.1. It is clear from these figures that the negative log-likelihood does not obviously level off for up to 10 clusters. After balancing the trade-off between maximising the number of covariate clusters, and maximising the number of data points within each cluster, the number of covariate clusters was determined to be  $J = 5$  for each season. By choosing  $J = 5$ , the average number of observations in each cluster was 2,580 (with a standard deviation of 535).

The performance of this method was disappointing (see editorial Rohrbeck et al. (2023)), and there are a few reasons why this could have been the case. Firstly, there were no clearly defined clusters. This points to the fact that the fitted Gaussian mixture distribution may have been unable to fully capture the non-Gaussian distribution of the covariate values. In Figure 5.1, the point at which the negative log-likelihood plateaus is not clear, illustrating this argument. The second reason could be that covariates were not used when fitting the GPDs to the extreme data in each cluster, only for cluster assignment. A GPD with covariate models for each cluster may have resulted in better quantile estimates. A further

development could be to explore generalised Pareto regression trees, as they are able to perform clustering using trends in the covariates (Farkas et al. 2021).

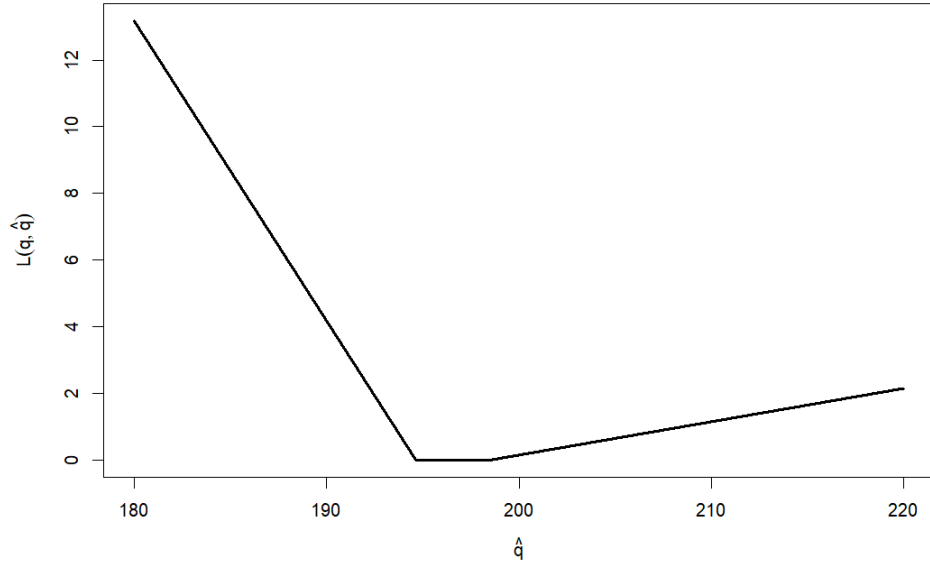


Figure 5.2.: A diagram of the loss function using the true quantile value  $q = 196.6$ .

### 5.4.3. Challenge 2

In the second challenge, we are required to estimate the marginal quantile  $q \in \mathbb{R}$  such that

$$\mathbb{P}(Y > q) = \frac{1}{300T},$$

where  $T = 200$ , that is, an estimate of the 200 year return level for Amaurot. This challenge was assessed using a loss function that penalises under-estimating the quantile more than over-estimating it. Formally, for a given estimate  $\hat{q}$  and the true marginal quantile  $q$ , the loss is calculated as,

$$L(q, \hat{q}) = \begin{cases} 0.9(0.99q - \hat{q}) & \text{if } 0.99q > \hat{q}, \\ 0, & \text{if } |q - \hat{q}| \leq 0.01q, \\ 0.1(\hat{q} - 1.01q), & \text{if } 1.01q < \hat{q}. \end{cases} \quad (5.6)$$

This replicates real-world scenarios. For example, in a hydrology context, over-estimating flood defences leads to increased costs, while under-estimating them results in severe consequences, such as fatalities. After completing the challenge, we were given the correct quantile  $q = 196.6$  and so we can substitute this value into the loss function, as displayed in Figure 5.2.

For this analysis, we make the underlying assumption that the extreme values of  $Y$  are independent and identically distributed (IID), that is, we ignore any dependence on  $\mathbf{X}$ . This assumption is made to simplify the modelling process. We then assume that the exceedances of  $Y$  above a high threshold  $u$  follow a GPD,

$$Y - u \mid Y > u \sim \text{GPD}(\sigma, \xi).$$

Using (5.2), the 200-year return level is then

$$y_{200} = \hat{u} + \frac{\hat{\sigma}}{\hat{\xi}}((200 \times 300\hat{\zeta}_u)^{\hat{\xi}} - 1),$$

where we have substituted  $T = 200$  and  $n_y = 300$  as we have 300 daily observations a year.

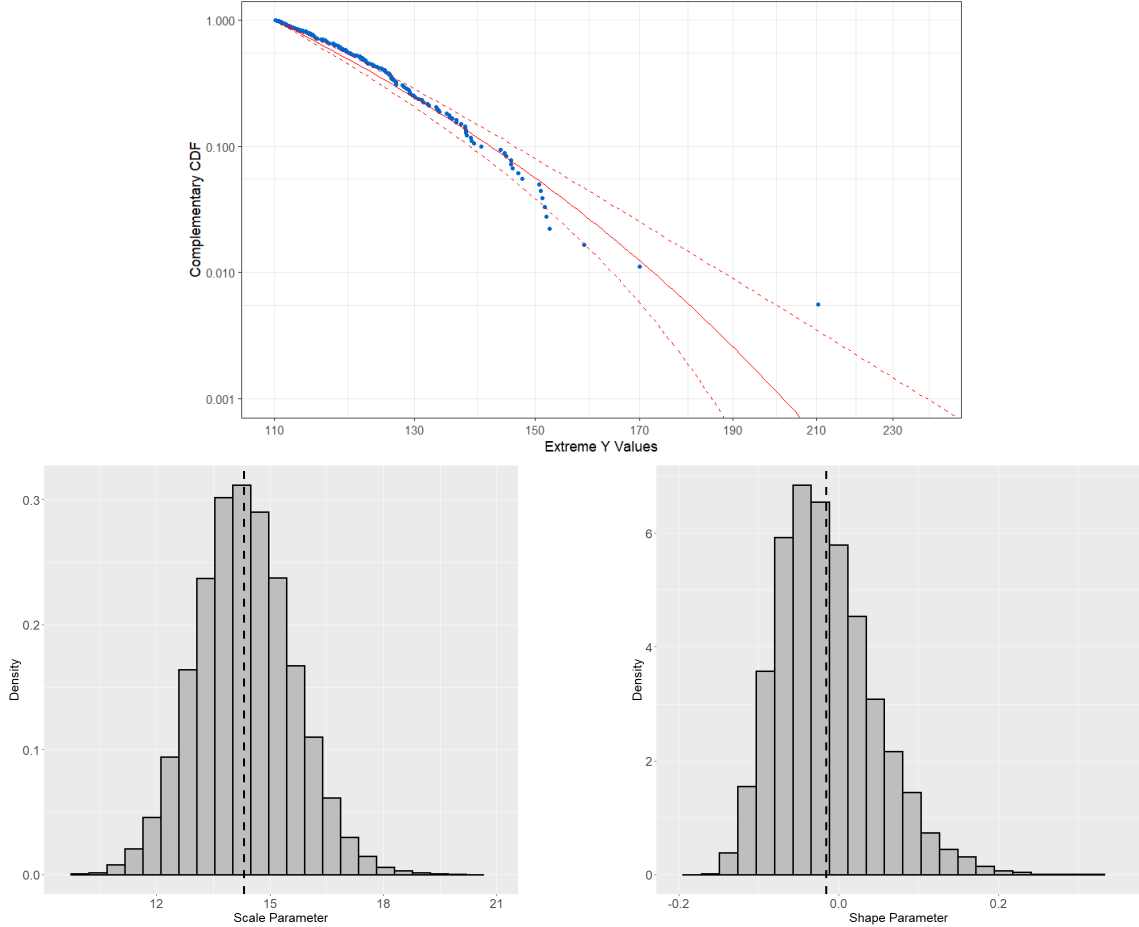


Figure 5.3.: A GPD fitted to extreme  $Y$  values above threshold 110, with a survival curve (top) fitted using the mean of the posterior parameter values, with a 90% confidence interval as dashed lines, and the respective posterior distributions of sampled scale (bottom left) and shape (bottom right) parameters, with the mean values as dashed lines.

To define a Bayesian framework, we choose prior distributions for  $\sigma$  and  $\xi$ ,  $\sigma \sim \text{Gamma}(4, 1)$ ,  $\xi \sim N(0, 1)$ . These prior distributions are selected to reflect minimal prior knowledge about the exact parameter values (whilst ensuring that  $\sigma$  remain positive). Subsequent analysis demonstrated that the parameter estimates were robust and largely unaffected by the specific choice of priors, which indicated that the data provided sufficient information to primarily determine the posterior distributions.

We use Markov chain Monte Carlo methods (Coles and Powell 1996; Gelfand and Smith 1990) to sample from the resulting posterior distribution of  $(\sigma, \xi)$ . This method was preferred over maximum likelihood estimation as we wanted a full distribution of the param-

eters, allowing for more insight into the uncertainty of the estimates.

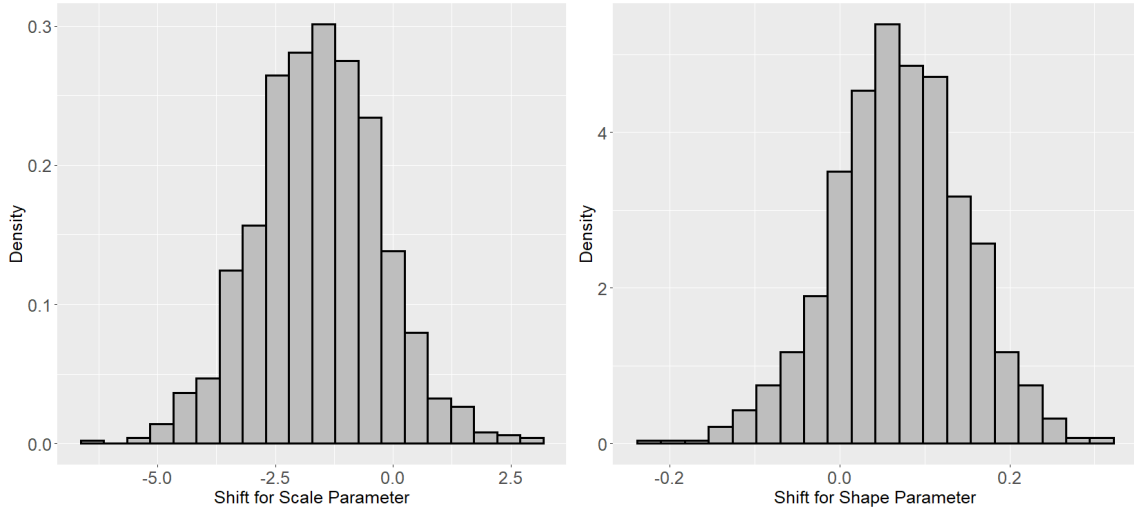


Figure 5.4.: A histogram of residuals of predicted and simulated scale (left) and shape (right) parameters. These residuals are then used as a bias correction for the return level estimate.

To assess how well our approach recovers the true parameter values, we generate sets of simulated data from GPDs with parameters that were representative of the ones sampled via our MCMC algorithm. Formally, for each simulated dataset, we sample values  $\tilde{\sigma}$  and  $\tilde{\xi}$ , and then generate data points  $\tilde{w}_1, \tilde{w}_2, \dots, \tilde{w}_m$  from a  $\text{GPD}(\tilde{\sigma}, \tilde{\xi})$ , where  $m$  is equal to the number of exceedances of  $Y$  above  $u$ . We considered two approaches to sample  $\tilde{\sigma}$  and  $\tilde{\xi}$ , and we generated 1000 datasets for each. The first approach is to sample these parameters from the posterior distribution. The other approach is to sample the parameters from uniform distributions,  $\tilde{\sigma} \sim U(11, 18)$  and  $\tilde{\xi} \sim \text{Unif}(-0.15, 0.20)$ ; these limits were selected based on the posterior samples. For each generated dataset, we again run our MCMC algorithm and store the posterior mean estimate for  $\tilde{\sigma}$  and  $\tilde{\xi}$ . Finally, we apply the mean corrections to the initial GPD parameter estimates to calculate an adjusted return level.

#### 5.4.3.1. Results

We determine a threshold of  $\hat{u} = 110$  by using mean excess plots, resulting in  $m = 180$ . We can then use this to calculate the empirical estimate for the exceedance probability  $\hat{\zeta}_u = 180/21000 \approx 0.0086$ . Figure 5.3 shows the posterior samples of the shape and scale distributions for the initial GPD fit. The range of these distributions are then used to

inform the sampling boundaries for the simulated datasets as described in Section 5.4.3. We also plot a survival function to assess the model fit (Figure 5.3), where the dashed red lines reflect a 90% credible interval for the fit. We find that the posterior distribution of the shape parameter spanned both negative and positive values, indicating uncertainty in the tail behaviour of the underlying distribution. It was also clear from inspecting smaller values of the extremes in the survival curve, that the GPD fit could be improved.

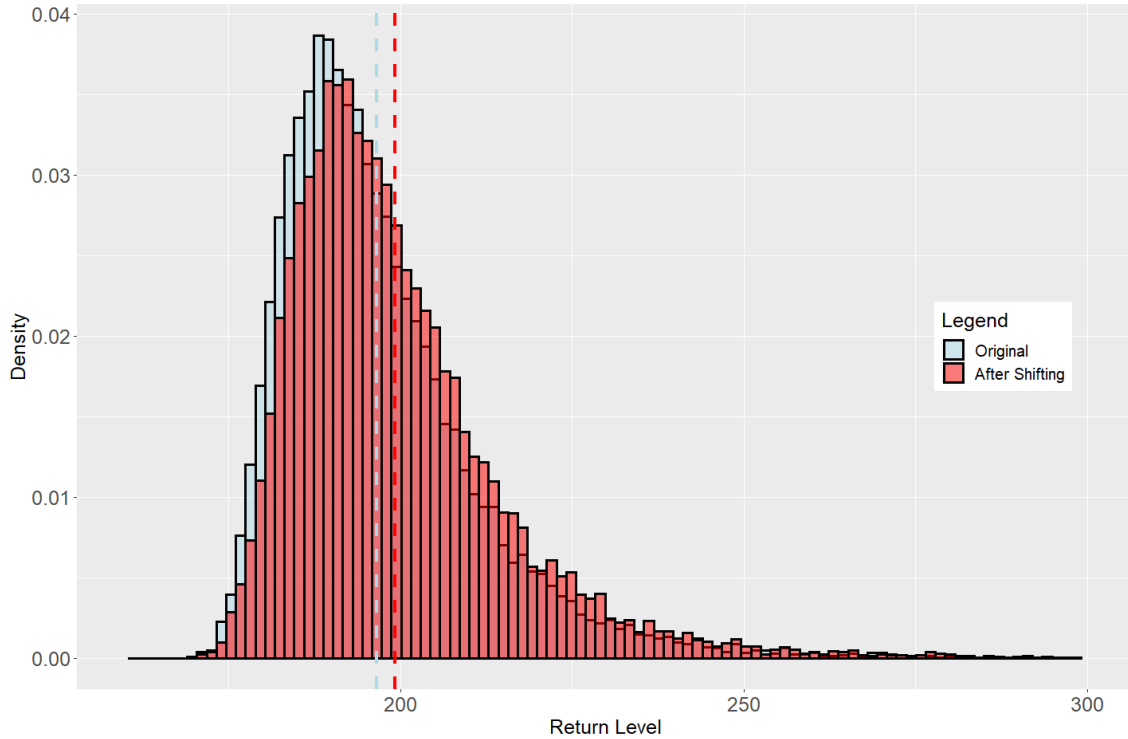


Figure 5.5.: The return level samples before shifting (blue) and after shifting (red). The dashed lines denote the mean of the samples.

We opted for our second approach to create the simulated datasets, that is, we sampled the parameters from uniform distributions to make the corrections for our final results. We choose this approach as, by employing uniform coverage of the parameter space, we return a more risk-averse return level with respect to the challenge loss function. The distributions of the residuals of the mean predicted parameters and the true (simulated) parameters are displayed in Figure 5.4. There are significant negative residuals for the scale parameter and significant positive residuals for the shape parameter. We wanted to use these residual distributions to make a correction to the initial parameter estimates. We apply the mean corrections to the initial posterior parameter values and compared the

mean return levels. These are shown in Figure 5.5. This non-standard approach was used for simplicity, however, some further work could be to more carefully incorporate these results into the initial posterior parameter distributions. This gives an overall increase in the average return level from 196.4 to 199.4.

The correct quantile value was  $q = 196.6$ . We were interested to find that the initial GPD fit to the data gave a return level of 196.4, which led to a loss of  $L(196.6, 196.4) = 0$ . It is possible that small effects of the covariates are compensated for by other factors, giving a correct return level under the misspecified model assumption. Although our final answer, with the correction, increased our return level, it also increased the loss from  $L(196.6, 196.4) = 0$  to  $L(196.6, 199.4) = 0.0834$  (using (5.6)). Before the correct quantile value was announced, we were encouraged that the method resulted in an increase in the return level, as an over-estimate was preferable to an under-estimate in the context of the competition. It is worth noting that if we had opted to sample the parameters of the simulated data from the posterior distributions, we would have got an average return level of 198.7, which would have given a smaller loss,  $L(196.6, 198.7) = 0.0134$ . The simplicity of the model, given the underlying assumption about the data, creates ambiguity regarding whether the large residuals in the parameter estimates are caused by bias or by model misspecification. For future work, it would be appropriate to incorporate a more sophisticated model of the covariates to reduce model misspecification and to investigate whether any residuals in parameter estimates are due to bias.

## 5.5. Multivariate Challenges

In Challenges 3 and 4 we are presented with a  $d$ -dimensional random vector  $\mathbf{X} = (X_1, \dots, X_d) \sim F_{\mathbf{X}}$ , representing the value of an environmental variable at  $d$  sites in Utopia, where  $F_{\mathbf{X}}$  is an unknown joint distribution function. Our goal is to estimate the probability that  $\mathbf{X}$  lies in a given extreme ‘failure region’ based on a sample of independent observations of  $\mathbf{X}$ . The failure regions of interest are such that certain components of  $\mathbf{X}$  are simultaneously large while all remaining components (if any) are of lower order. The inherent difficulty of the task stems from the fact that the events’ return periods are of similar order or even significantly longer than the observation period over

which the data are collected; empirical methods based solely on the relative frequency of event occurrences are fruitless. Instead, we use the observed data to infer an estimate for the probabilistic structure of the joint tail of  $\mathbf{X}$  and subsequently compute tail event probabilities under this model. This encapsulates the philosophy of multivariate extreme value statistics.

In the absence of prior knowledge about the physical processes driving the environment of Utopia, we are compelled to recourse to data-driven, statistical learning methods for multivariate extremes. The particular tools we choose will depend on the nature and difficulties of the task at hand. In Challenge 3, the failure regions are defined by different subsets of variables being large, thereby placing emphasis on accurately modelling the so-called extremal directions of  $\mathbf{X}$ . The salient characteristic of Challenge 4 is its high dimensionality, which calls for the utilisation of dimension reduction techniques, such as clustering, in order to overcome the curse of dimensionality inherent to tail dependence estimation.

## 5.5.1. Background

### 5.5.1.1. Multivariate regular variation and the angular measure

Let  $\mathbf{X}$  denote a random vector that takes values in the positive orthant  $\mathbb{R}_+^d := [0, \infty)^d$ . As is commonly done in multivariate extremes, we work in the framework of multivariate regular variation (MRV).

### 5.5.1.2. Multivariate regular variation and the angular measure

Let  $\mathbf{X}$  denote a random vector that takes values in the positive orthant  $\mathbb{R}_+^d := [0, \infty)^d$ . As is commonly done in multivariate extremes, we work in the framework of multivariate regular variation (MRV).

**Definition 5.1.** We say that  $\mathbf{X}$  is *multivariate regularly varying* with index  $\alpha > 0$ , denoted  $\mathbf{X} \in \text{RV}_+^d(\alpha)$ , if it satisfies the following (equivalent) definitions (Resnick 2007, Theorem 6.1):

1. There exists a sequence  $b_n \rightarrow \infty$  and a non-negative Radon measure  $\nu_{\mathbf{X}}$  on  $\mathbb{E}_0 := [0, \infty]^d \setminus \{\mathbf{0}\}$  such that

$$n\mathbb{P}(b_n^{-1}\mathbf{X} \in \cdot) \xrightarrow{\text{v}} \nu_{\mathbf{X}}(\cdot), \quad (n \rightarrow \infty), \quad (5.7)$$

where  $\xrightarrow{\text{v}}$  denotes vague convergence in the space of non-negative Radon measures on  $\mathbb{E}_0$ . The *exponent measure*  $\nu_{\mathbf{X}}$  is homogeneous of order  $-\alpha$ , i.e.  $\nu_{\mathbf{X}}(s \cdot) = s^{-\alpha} \nu_{\mathbf{X}}(\cdot)$  for any  $s > 0$ .

2. For any norm  $\|\cdot\|$  on  $\mathbb{R}^d$ , there exists a sequence  $b_n \rightarrow \infty$  and a finite *angular measure*  $H_{\mathbf{X}}$  on  $\mathbb{S}_+^{d-1} := \{\mathbf{x} \in \mathbb{R}_+^d : \|\mathbf{x}\| = 1\}$  such that for  $(R, \Theta) := (\|\mathbf{X}\|, \mathbf{X}/\|\mathbf{X}\|)$ ,

$$n\mathbb{P}((b_n^{-1}R, \Theta) \in \cdot) \xrightarrow{\text{v}} \nu_{\alpha} \times H_{\mathbf{X}}(\cdot), \quad (n \rightarrow \infty), \quad (5.8)$$

in the space of non-negative Radon measures on  $(0, \infty] \times \mathbb{S}_+^{d-1}$ , where  $\nu_{\alpha}((x, \infty)) = x^{-\alpha}$  for any  $x > 0$ .

The limit measures  $\nu_{\mathbf{X}}$  and  $H_{\mathbf{X}}$  are related via

$$\begin{aligned} \nu_{\mathbf{X}}(\{\mathbf{x} \in \mathbb{E}_0 : \|\mathbf{x}\| > s, \mathbf{x}/\|\mathbf{x}\| \in \cdot\}) &= s^{-\alpha} H_{\mathbf{X}}(\cdot), \\ \nu_{\mathbf{X}}(dr \times d\Theta) &= \alpha r^{-\alpha-1} dr dH_{\mathbf{X}}(\Theta). \end{aligned}$$

The probabilistic tail of  $\mathbf{X}$  decomposes into a univariate  $\alpha$ -regularly varying radial component (Resnick 2007, Theorem 3.6), that is asymptotically independent of the angular component. The angular measure represents the limiting distribution of the angular component and encodes all information about the tail dependence structure.

The MRV property implies that the margins of  $\mathbf{X}$  are heavy-tailed with a common tail index. Henceforth, assume that the components of  $\mathbf{X} \in \text{RV}_+^d(\alpha)$  are Fréchet distributed with shape parameter  $\alpha$ , that is  $\mathbb{P}(X_i < x) = \Psi_{\alpha}(x) := \exp(-x^{-\alpha})$  for  $x > 0$  and  $i = 1, \dots, d$ . (The data for Challenges 3 and 4 are on Gumbel margins but can be accommodated into our framework following a suitable transformation.) Moreover, we choose  $\|\cdot\| = \|\cdot\|_{\alpha}$ , the  $L_{\alpha}$ -norm on  $\mathbb{R}^d$ , and specify that the normalising sequence in (5.8) is  $b_n = n^{1/\alpha}$ . With these particular choices the marginal variables have unit scale (Klüppelberg and Krali 2021, Definition 4) and  $H_{\mathbf{X}}(\mathbb{S}_+^{d-1}) = d$ .

The problem of modelling the angular measure has attracted considerable attention in recent years – a survey of the related literature can be found in Engelke and Ivanovs (2021). One research avenue concerns learning which sets of variables may be concurrently extreme; this can be posed as a support detection problem (Goix et al. 2017; Simpson et al. 2020). Consider the index set  $\mathbb{V}(d) := \{1, \dots, d\}$  and denote by  $\mathcal{P}_d^* = \mathcal{P}(\mathbb{V}(d)) \setminus \emptyset$  its power set excluding the empty set. A set  $\beta \in \mathcal{P}_d^*$  is termed an extremal direction of  $\mathbf{X}$  if  $H_{\mathbf{X}}$  places mass on the subspace

$$C_{\beta} = \{\mathbf{w} \in \mathbb{S}_+^{d-1} : w_i > 0 \iff i \in \beta\} \subseteq \mathbb{S}_+^{d-1}.$$

Another branch of research aims at developing dimension reduction techniques for analysing the angular measure in high dimensions. To this end, one often considers a summary of the full dependence structure encoded in a matrix of pairwise extremal dependence metrics. One such matrix, originally proposed in Larsson and Resnick (2012) and later popularised by Cooley and Thibaud (2019), is the tail pairwise dependence matrix (TPDM). The TPDM of  $\mathbf{X} \in \text{RV}_+^d(2)$  is the  $d \times d$  matrix  $\Sigma = (\sigma_{ij})$  with entries

$$\sigma_{ij} = \int_{\mathbb{S}_+^{d-1}} \theta_i \theta_j \, dH_{\mathbf{X}}(\boldsymbol{\theta}), \quad (i, j = 1, \dots, d). \quad (5.9)$$

The diagonal entries are the squared marginal scales, i.e.  $\sigma_{ii} = 1$  for  $i = 1, \dots, d$ . The off-diagonal entries measure extremal dependence between the associated pairs of variables. In particular,  $\sigma_{ij} = 0$  if and only if  $X_i$  and  $X_j$  are asymptotically independent. For asymptotically dependent variables the magnitude of  $\sigma_{ij}$  represents the dependence strength. An important property of the TPDM is its complete positivity (Cooley and Thibaud 2019, Proposition 5).

**Definition 5.2.** A matrix  $S$  is *completely positive* if there exists a matrix  $A$  with non-negative entries such that  $S = AA^T$ . We call  $A$  (resp.  $AA^T$ ) a *CP-factor* (resp. *CP-decomposition*) of  $S$ .

This property connects the TPDM to the model class introduced in the following section.

### 5.5.1.3. The max-linear model for multivariate extremes

Our proposed methods for Challenges 3 and 4 employ the max-linear model, a parametric model based on the class of random vectors constructed by max-linear combinations of independent Fréchet random variables (Fougères et al. 2013). This model is appealing for several reasons. First, it is flexible, in the sense that any regularly varying random vector can be arbitrarily well-approximated by a max-linear model with sufficiently many parameters (Fougères et al. 2013). Since neither Challenge 3 nor Challenge 4 provide any prior information about the underlying data-generating processes, it is preferable to avoid imposing overly restrictive assumptions on the tail dependence structure. Secondly, although the number of parameters grows rapidly – at least  $\mathcal{O}(d)$  but often even  $\mathcal{O}(d^2)$  – efficient inference procedures are available even in high dimensions. Scalability is critical for Challenge 4. Finally, extremal directions and failure probabilities can be straightforwardly identified and computed directly from the model parameters (Kiriliouk and Zhou 2022).

**Definition 5.3.** For some  $q \geq 1$  and  $\alpha > 0$ , let  $\mathbf{Z} = (Z_1, \dots, Z_q)$  be a random vector with independent components  $Z_1, \dots, Z_q \sim \Psi_\alpha$  and let  $A = (a_{ij}) \in \mathbb{R}_+^{d \times q}$  be a deterministic matrix. If

$$X_i := \bigvee_{j=1}^q a_{ij} Z_j, \quad (i = 1, \dots, d),$$

then  $\mathbf{X} = (X_1, \dots, X_d)$  is said to be *max-linear* with *noise coefficient matrix*  $A$ , denoted  $\mathbf{X} \sim \text{MaxLinear}(A; \alpha)$ , and we write  $\mathbf{X} = A \circ \mathbf{Z}$ .

Cooley and Thibaud (2019) show that  $\mathbf{X} = A \circ \mathbf{Z} \in \text{RV}_+^d(\alpha)$  and

$$H_{\mathbf{X}}(\cdot) = \sum_{j=1}^q \|\mathbf{a}_j\|_\alpha^\alpha \delta_{\mathbf{a}_j/\|\mathbf{a}_j\|_\alpha}(\cdot), \quad (5.10)$$

where  $\delta_{\mathbf{x}}(A) := \mathbf{1}\{\mathbf{x} \in A\}$  is the Dirac mass function. The angles along which extremes can occur are (in the limit) precisely the  $q$  self-normalised columns of  $A$ . Therefore  $\beta \in \mathcal{P}_d^*$  is an extremal direction of  $\mathbf{X}$  if and only if there exists  $j \in \{1, \dots, q\}$  such that  $\mathbf{a}_j/\|\mathbf{a}_j\|_\alpha \in C_\beta$ . When it comes to model fitting, the testing procedure of Kiriliouk (2020) can provide guidance for choosing  $q$ ; for our purposes, it either represents a tuning parameter (Challenge 3) or takes a fixed value owing to computational/algorithmic restrictions (Challenge 4).

Substituting (5.10) into (5.9), we observe that  $\mathbf{X} \sim \text{MaxLinear}(A, 2)$  has TPDM  $\Sigma_{\mathbf{X}} = AA^T$ . In other words, the noise coefficient matrix is a CP-factor of the model TPDM. Conversely, given an arbitrary random vector  $\mathbf{X} \in \text{RV}_+^d(2)$  with TPDM  $\Sigma$ , any CP-factor  $A$  of  $\Sigma$  parametrises a max-linear model with identical pairwise tail dependence metrics to  $\mathbf{X}$ .

Kiriliouk and Zhou (2022) give examples of classes of tail events  $\mathcal{R} \subset \mathbb{E}_0$  for which  $\mathbb{P}(\mathbf{X} \in \mathcal{R})$  can be well-approximated by a function of the parameter matrix  $A$ . With a view to Challenges 3 and 4, we focus on tail events where  $\mathbf{X}$  is large in the  $s \leq d$  components indexed by  $\beta = \{\beta_1, \dots, \beta_s\} \in \mathcal{P}_d^\star$ , while all  $d - s$  remaining components are of lower order. Formally, for  $\mathbf{u} = (u_1, \dots, u_s) \in \mathbb{R}_+^s$  a vector of high thresholds and  $\mathbf{l} \in \mathbb{R}_+^{d-s}$  a vector of comparatively low thresholds, we consider

$$\mathcal{C}_{\beta, \mathbf{u}, \mathbf{l}} := \{\mathbf{x} \in \mathbb{E}_0 : \mathbf{x}_\beta > \mathbf{u}, \mathbf{x}_{-\beta} < \mathbf{l}\}, \quad \mathbb{P}(\mathbf{X} \in \mathcal{C}_{\beta, \mathbf{u}, \mathbf{l}}) = \mathbb{P}(\mathbf{X}_\beta > \mathbf{u}, \mathbf{X}_{-\beta} < \mathbf{l}).$$

When  $\beta = \mathbb{V}(d)$  the threshold vector  $\mathbf{l}$  is superfluous and is omitted. Kiriliouk and Zhou (2022) specify an approximate formula for  $\mathbb{P}(A \circ \mathbf{Z} \in \mathcal{C}_{\mathbb{V}(d), \mathbf{u}})$  in terms of  $A$ . We derive an analogous formula for  $\mathbb{P}(A \circ \mathbf{Z} \in \mathcal{C}_{\beta, \mathbf{u}, \mathbf{l}})$  for general  $\beta \in \mathcal{P}_d^\star$  stated as follows: if  $\mathbf{X} \sim \text{MaxLinear}(A; \alpha)$ , then

$$\mathbb{P}(\mathbf{X} \in \mathcal{C}_{\beta, \mathbf{u}, \mathbf{l}}) \approx \hat{\mathbb{P}}(\mathbf{X} \in \mathcal{C}_{\beta, \mathbf{u}, \mathbf{l}}) := \sum_{j: \frac{\mathbf{a}_j}{\|\mathbf{a}_j\|^\alpha} \in C_\beta} \min_{i=1, \dots, s} \left( \frac{a_{\beta_i, j}}{u_i} \right)^\alpha. \quad (5.11)$$

The approximation should be understood as being valid as  $u_1, \dots, u_s \rightarrow \infty$  while  $\mathbf{l}$  remains fixed. Note that the entries of  $\mathbf{l}$  do not appear in the right-hand side of (5.11). This reflects the fact that, asymptotically, the magnitude of the probability of the event  $\{\mathbf{X}_\beta > \mathbf{u}\} \cap \{\mathbf{X}_{-\beta} < \mathbf{l}\}$  is predominantly determined by the threshold exceedance event  $\{\mathbf{X}_\beta > \mathbf{u}\}$  while the relative contribution of the threshold non-exceedance event  $\{\mathbf{X}_{-\beta} < \mathbf{l}\}$  vanishes. Henceforth, the threshold  $\mathbf{l}$  may at times be suppressed for notational convenience. From (5.7) we have that, provided  $u_1, \dots, u_s$  are sufficiently large,

$$\mathbb{P}(\mathbf{X} \in \mathcal{C}_{\beta, \mathbf{u}, \mathbf{l}}) = \frac{1}{n} \left[ n \mathbb{P} \left( \frac{\mathbf{X}}{n^{1/\alpha}} \in \frac{\mathcal{C}_{\beta, \mathbf{u}, \mathbf{l}}}{n^{1/\alpha}} \right) \right] \approx \frac{1}{n} \nu_{\mathbf{X}} \left( \frac{\mathcal{C}_{\beta, \mathbf{u}, \mathbf{l}}}{n^{1/\alpha}} \right) = \nu_{\mathbf{X}}(\mathcal{C}_{\beta, \mathbf{u}, \mathbf{l}}),$$

where the last step exploits homogeneity of the exponent measure. Transforming to pseudo-

polar coordinates this becomes

$$\nu_{\mathbf{X}}(\mathcal{C}_{\beta, \mathbf{u}, \mathbf{l}}) = \int_{\{(r, \mathbf{w}) : r\mathbf{w}_\beta > \mathbf{u}, r\mathbf{w}_{-\beta} < \mathbf{l}\}} \alpha r^{-\alpha-1} dr dH_{\mathbf{X}}(\mathbf{w}).$$

Based on (5.10), there are only  $q$  possible angles along which extremes can occur, but only those with  $\mathbf{a}_j/\|\mathbf{a}_j\|_\alpha \in C_\beta$  will contribute to the integral. To see this, consider  $\mathbf{w} = \mathbf{a}/\|\mathbf{a}\|_\alpha \in C_\gamma$ , where  $\mathbf{a}$  denotes an arbitrary column of  $A$  and  $\gamma \in \mathcal{P}_d^*$ . First, suppose  $\gamma \subset \beta$  (strictly) so that there exists  $i \in \beta$  such that  $i \notin \gamma$ . Then, for all  $r > 0$ , we have  $r\mathbf{w}_\beta \not> \mathbf{u}$ , since  $r\mathbf{w}_i = 0$ . Similarly, suppose  $\gamma \supset \beta$ , in which case there exists  $i \in \gamma$  with  $i \notin \beta$ . Let  $\ell$  denote the entry of  $\mathbf{l}$  corresponding to component  $i$ . An extreme event along  $\mathbf{w}$  requires  $r\mathbf{w}_i < \ell$  and  $r\mathbf{w}_\beta > \mathbf{u}$ , but for  $\mathbf{u}$  sufficiently large these inequalities have no solution  $r > 0$ . On the other hand, if  $\beta = \gamma$ , then  $\mathbf{w}_{-\beta} = \mathbf{0} \in \mathbb{R}^{d-s}$  and so

$$r\mathbf{w}_\beta > \mathbf{u}, r\mathbf{w}_{-\beta} < \mathbf{l} \iff r\mathbf{w}_\beta > \mathbf{u} \iff r > \max_{i=1,\dots,s} \left( \frac{\|\mathbf{a}\|_\alpha u_i}{a_{\beta_i}} \right).$$

This yields the final result

$$\nu_{\mathbf{X}}(\mathcal{C}_{\beta, \mathbf{u}, \mathbf{l}}) = \sum_{j: \frac{\mathbf{a}_j}{\|\mathbf{a}_j\|_\alpha} \in C_\beta} \|\mathbf{a}_j\|_\alpha^\alpha \int_{\max_i \left( \frac{\|\mathbf{a}_j\|_\alpha u_i}{a_{\beta_i, j}} \right)}^\infty \alpha r^{-\alpha-1} dr = \sum_{j: \frac{\mathbf{a}_j}{\|\mathbf{a}_j\|_\alpha} \in C_\beta} \min_{i=1,\dots,s} \left( \frac{a_{\beta_i, j}}{u_i} \right)^\alpha.$$

For  $\alpha = 1$  we can establish the upper bound  $\hat{\mathbb{P}}(\mathbf{X} \in \mathcal{C}_{\beta, \mathbf{u}, \mathbf{l}}) \leq H_{\mathbf{X}}(C_\beta)/(su)$  with equality attained if and only if the angular measure places all of its mass on  $C_\beta$  at the centroid  $\mathbf{e}(\beta)/|\beta|$ , where  $\mathbf{e}(\beta) := (\mathbf{1}\{i \in \beta\} : i = 1, \dots, d) \in \{0, 1\}^d$ . The form of this bound offers an intuitive interpretation as the limiting probability of the angular component lying in the required subspace multiplied by the survivor function of a Pareto( $\alpha = 1$ ) random variable evaluated at the effective radial threshold  $\|\mathbf{u}\mathbf{1}_s\|_1 = su$ .

#### 5.5.1.4. Existing approaches to inference for max-linear models

Suppose  $\mathbf{X} \sim \text{MaxLinear}(A, \alpha)$ , where  $\alpha$  is known and  $A$  must be estimated from a sample  $\{\mathbf{x}_t = (r_t, \boldsymbol{\theta}_t) : t = 1, \dots, n\}$  of  $\mathbf{X} = (R, \Theta)$ . For  $j \in \{1, \dots, n\}$ , let  $r_{(j)}$  denote the  $j$ th upper order statistic of  $\{r_1, \dots, r_n\}$  and let  $\mathbf{x}_{(j)}, \boldsymbol{\theta}_{(j)}$  denote the corresponding observation and angular component, respectively.

One estimate of  $A$  is motivated by (5.10), which says its normalised columns represent the set of realisable extremal angles (Cooley and Thibaud 2019)

**Definition 5.4.** The empirical estimate of  $A$  based on  $\mathbf{x}_1, \dots, \mathbf{x}_n$  is  $\hat{A} = (\hat{\mathbf{a}}_1, \dots, \hat{\mathbf{a}}_k) \in \mathbb{R}_+^{d \times k}$ , where  $1 \leq k \leq n$  and  $\hat{\mathbf{a}}_j = (d/k)^{1/\alpha} \boldsymbol{\theta}_{(j)}$  for  $j = 1, \dots, k$ .

The quantity  $k$  is the customary tuning parameter that represents the number of ‘extreme’ observations with norm not less than the implied radial threshold  $r_{(k)}$ . The associated angular measure (for any  $\alpha$ ) and TPDM (for  $\alpha = 2$ ) are given by

$$\hat{H}_{\mathbf{X}}(\cdot) := H_{\hat{A} \times_{\max} \mathbf{Z}}(\cdot) = \frac{d}{k} \sum_{t=1}^n \mathbf{1}\{\boldsymbol{\theta}_t \in \cdot, r_t \geq r_{(k)}\} \quad (5.12)$$

$$\hat{\sigma}_{\mathbf{X}_{ij}} := \sigma_{\hat{A} \times_{\max} \mathbf{Z}, ij} = \frac{d}{k} \sum_{t=1}^n \theta_{ti} \theta_{tj} \mathbf{1}\{r_t \geq r_{(k)}\} = [\hat{A} \hat{A}^T]_{ij}. \quad (5.13)$$

These are the empirical angular measure (Einmahl and Segers 2009) and empirical TPDM (Cooley and Thibaud 2019), respectively. In view of (5.13), alternative estimates of  $A$  can be obtained by CP decomposition of the empirical TPDM.

**Definition 5.5.** CP-factors of  $\hat{\Sigma}_{\mathbf{X}} = (\hat{\sigma}_{\mathbf{X}_{ij}})$  are called CP-estimates of  $A$ , denoted  $\tilde{A}$ .

An estimate  $\tilde{A}$  induces a different angular measure  $\tilde{H}_{\mathbf{X}} := H_{\tilde{A} \times_{\max} \mathbf{Z}}$  but, by construction, the empirical and CP models share identical tail pairwise dependencies, since  $\tilde{\Sigma}_{\mathbf{X}} := \Sigma_{\tilde{A} \times_{\max} \mathbf{Z}} = \tilde{A} \tilde{A}^T = \hat{\Sigma}_{\mathbf{X}}$ . Note that  $\tilde{A}$  implicitly depends on the same tuning parameter  $k$  as  $\hat{A}$  via the empirical TPDM. All CP-estimates in this paper are obtained using the decomposition algorithm of Kiriliouk and Zhou (2022), which efficiently factorises moderate-to high-dimensional TPDMs. Their algorithm takes as input a strictly positive TPDM and a permutation  $(i_1, \dots, i_d)$  of  $\mathbb{V}_d$  and (for some permutations) returns a square CP-factor  $\tilde{A} \in \mathbb{R}_+^{d \times d}$  whose columns satisfy  $\tilde{\mathbf{a}}_j / \|\tilde{\mathbf{a}}_j\|_2 \in C_{\mathbb{V}_d \setminus \{i_l : l < j\}}$  for  $j = 1, \dots, d$ .

### 5.5.1.5. Inference for max-linear models based on sparse projections

A limitation of  $\hat{A}$  and  $\tilde{A}$  is that they fail to capture the true extremal directions of  $\mathbf{X}$ . In the case of  $\hat{A}$  this is because the angles  $\boldsymbol{\Theta} = \mathbf{X} / \|\mathbf{X}\|$  lie in the simplex interior almost surely, meaning  $\hat{\mathbf{a}}_1, \dots, \hat{\mathbf{a}}_k \in \mathbb{V}_d$  and  $\hat{\mathbb{P}}(\hat{A} \times_{\max} \mathbf{Z} \in \mathcal{C}_{\beta, \mathbf{u}}) = 0$  for any  $\beta \neq \mathbb{V}_d$ . The  $d$  extremal

directions of  $\tilde{A} \times_{\max} \mathbf{Z}$  are fully determined by the input path  $(i_1, \dots, i_d)$  and need not bear any resemblance to the extremal directions suggested by the data. To address this gap, we propose augmenting the empirical estimate with an alternative notion of angle based on Euclidean projections onto the  $L_1$ -simplex (Meyer and Wintenberger 2023).

**Definition 5.6.** The Euclidean projection onto the  $L_1$ -simplex is defined by

$$\pi : \mathbb{R}_+^d \rightarrow \mathbb{S}_+^{d-1}, \quad \pi(\mathbf{v}) = \arg \min_{\mathbf{w} \in \mathbb{S}_+^{d-1}} \|\mathbf{w} - \mathbf{v}\|_2^2.$$

This projection is useful because  $\pi(\mathbf{v})$  may lie on a boundary of the simplex even if  $\mathbf{v}/\|\mathbf{v}\|_1$  lies in its interior. Assume now that  $\alpha = 1$ .

**Definition 5.7.** The *sparse empirical estimate* of  $A$  based on  $\mathbf{x}_1, \dots, \mathbf{x}_n$  is  $\hat{A}^\star = (\hat{\mathbf{a}}_1^\star, \dots, \hat{\mathbf{a}}_k^\star) \in \mathbb{R}_+^{d \times k}$ , where  $1 \leq k < n$  and  $\hat{\mathbf{a}}_j^\star = (d/k)\pi(\mathbf{x}_{(j)}/r_{(k+1)})$  for  $j = 1, \dots, k$ .

The corresponding angular measure

$$\hat{H}_{\mathbf{X}}^\star(\cdot) := H_{\hat{A}^\star \times_{\max} \mathbf{Z}}(\cdot) = \frac{d}{k} \sum_{j=1}^k \mathbf{1}\{\pi(\mathbf{x}_{(j)}/r_{(k+1)}) \in \cdot\}$$

spreads mass across the subspaces  $C_\beta \subseteq \mathbb{S}_+^{d-1}$  on which the projected data lie and  $\hat{\mathbb{P}}(\hat{A}^\star \times_{\max} \mathbf{Z} \in \mathcal{C}_{\beta,u}) \neq 0$  for all corresponding  $\beta$ . A full study of the theoretical properties of  $\hat{A}^\star$  has not been conducted. Having introduced our estimator and all the requisite theory, we are ready to present our methods for the multivariate challenges.

### 5.5.2. Challenge 3

#### 5.5.2.1. Data

Challenge 3 considers a trivariate random vector  $\mathbf{Y} = (Y_1, Y_2, Y_3)$  on standard Gumbel margins, i.e.  $\mathbb{P}(Y_i < y) = G(y) := \exp(-\exp(-y))$  for  $y \in \mathbb{R}$  and  $i = 1, 2, 3$ . It entails estimating

$$p_1 := \mathbb{P}(Y_1 > 6, Y_2 > 6, Y_3 > 6), \quad p_2 := \mathbb{P}(Y_1 > 7, Y_2 > 7, Y_3 < -\log(\log(2))).$$

The data comprise  $n = 21,000$  independent observations  $\{\mathbf{y}_t = (y_{t1}, y_{t2}, y_{t3}) : t = 1, \dots, n\}$  of  $\mathbf{Y}$ . The available covariate information is not leveraged by our method.

### 5.5.2.2. Methodology

Let  $\mathbf{X} = (X_1, X_2, X_3)$  denote the random vector obtained by transforming  $\mathbf{Y}$  to Fréchet margins with shape parameter 1, i.e.  $X_i = \Psi_1^{-1}(G(Y_i)) = \exp(Y_i) \sim \Psi_1$  for  $i = 1, 2, 3$ . The above probabilities can be expressed as

$$p_1 = \mathbb{P}(X_1 > e^6, X_2 > e^6, X_3 > e^6), \quad p_2 = \mathbb{P}\left(X_1 > e^7, X_2 > e^7, X_3 < \frac{1}{\log 2}\right). \quad (5.14)$$

The thresholds  $e^6$ ,  $e^7$ , and  $1/\log(2)$  correspond approximately to the 99.8%, 99.9% and 50% quantiles of  $\Psi_1$ , respectively. Our solution models  $\mathbf{X}$  as max-linear, infers  $A$  using the sparse empirical estimator (for some hyperparameter  $k$ ) and computes estimates for  $p_1$  and  $p_2$  via (5.11), that is

$$\hat{p}_1 = \hat{\mathbb{P}}(\hat{A}^\star \circ \mathbf{Z} \in \mathcal{C}_{V(3), e^6}), \quad \hat{p}_2 = \hat{\mathbb{P}}(\hat{A}^\star \circ \mathbf{Z} \in \mathcal{C}_{\{1,2\}, e^7, 1/\log(2)}). \quad (5.15)$$

Inference is based on the transformed data  $\{\mathbf{x}_t = (x_{t1}, x_{t2}, x_{t3}) : t = 1, \dots, n\}$ , where  $x_{ti} := \exp(y_{ti})$  for  $t = 1, \dots, n$  and  $i = 1, 2, 3$ .

### 5.5.2.3. Results

The results presented are based on  $k = 500 \approx 2.5\% \times n$ . This value was used for our competition submission and the results' sensitivity to this choice will be examined later.

The ternary plots in Figure 5.6 depict the angular components associated with the  $k$  largest observations in norm, i.e. exceeding the radial threshold  $r_{(k+1)} \approx 138.77$ . The left-hand plot represents the self-normalised vectors  $\boldsymbol{\theta}_{(1)}, \dots, \boldsymbol{\theta}_{(k)}$ . We find points lying near the centre of the triangle and in the neighbourhood of all its edges and vertices. This suggests that the angular measure spreads mass across all seven faces of  $\mathbb{S}_+^2$ . However, we reiterate that no points lie *exactly* on the boundary. In contrast, the sparse angles  $\{\pi(\mathbf{x}_t/r_{(k+1)}) : r_t > r_{(k+1)}\}$  in the right-hand plot lie in the interior (black, 40 points), along the edges (red, 139 points), and on the vertices (blue, 321 points) of the closed

simplex. Only the 40 vectors in  $C_{\mathbb{V}(3)}$  and 23 vectors in  $C_{\{1,2\}}$  will enter into the estimates of (5.14).

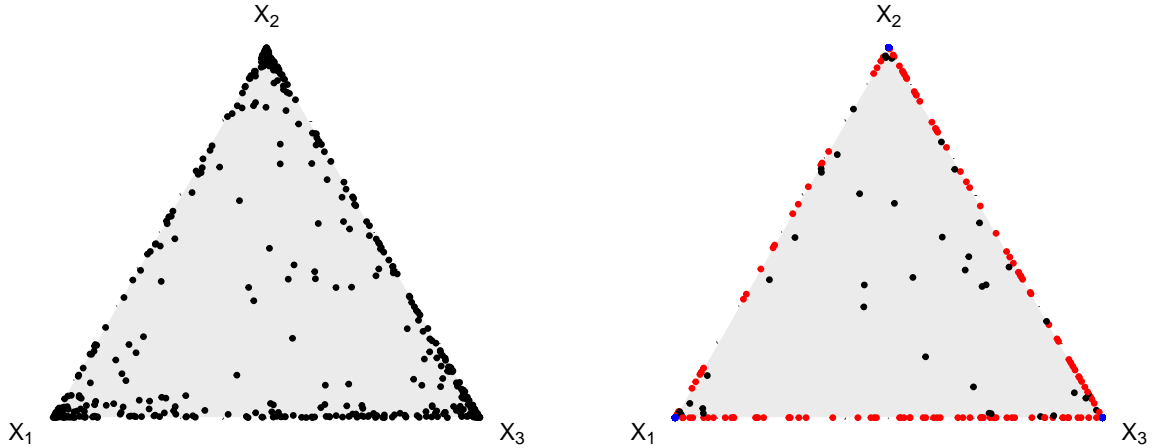


Figure 5.6.: The angles  $\mathbf{x}_{(j)} / \|\mathbf{x}_{(j)}\|_1 \in \mathbb{S}_+^2$  (left) and Euclidean projections  $\pi(\mathbf{x}_{(j)} / r_{(k+1)}) \in \mathbb{S}_+^2$  (right) for the 500 largest observations in Challenge 3. Points are coloured according to whether they lie in the interior (black), on an edge (red) or on a vertex (blue).

The projected vectors are collated to form the  $3 \times 500$  matrix  $\hat{A}^*$ . The first 100 columns of the matrices  $\hat{A}$  and  $\hat{A}^*$  are represented visually in Figure 5.7. As expected,  $\hat{A}$  is dense, albeit populated with small values, while  $\hat{A}^*$  exhibits a high degree of sparsity, in the sense that most of its columns satisfy  $\|\hat{a}_j^*\|_0 < \|\hat{a}_j\|_0 = 3$ . Duplicated columns in  $\hat{A}^*$  could be merged and re-weighted to produce a compressed estimate  $\hat{A}_{\text{comp}}^*$  with  $q_{\text{comp}} = 40 + 139 + 3 = 182$  unique columns, but ultimately they parametrise identical models since  $H_{\hat{A}^* \circ \mathbf{Z}} = H_{\hat{A}_{\text{comp}}^* \circ \mathbf{Z}}$ .

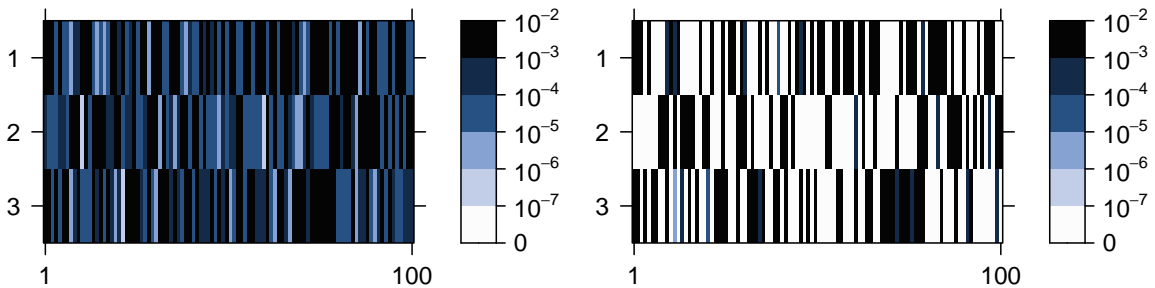


Figure 5.7.: The first 100 columns of  $\hat{A}$  (left) and  $\hat{A}^*$  (right) for Challenge 3. The colour intensity of each cell represents the magnitude of the corresponding matrix entry.

Substituting  $\hat{A}^*$  into (5.15) yields the final point estimates  $\hat{p}_1 = 3.36 \times 10^{-5}$  and  $\hat{p}_2 = 2.76 \times 10^{-5}$ , to three significant figures. We are pleased to find that our estimates are very

close to the true values given in Rohrbeck et al. (2023). Furthermore, Figure 5.8 shows that our estimates of  $p_2$  are fairly stable across a range of ‘reasonable’ choices of  $k$ , say,  $1\% \leq k/n \leq 5\%$ . When  $k$  is smaller than this, the estimates become highly variable due to the limited effective sample size. If  $k$  is too large, we risk introducing bias by including observations that do not reflect the true tail dependence structure. The estimates of  $p_1$  exhibit greater sensitivity to the choice of threshold. The development of theoretically justified diagnostics/procedures for selecting the threshold represents an avenue for future work.

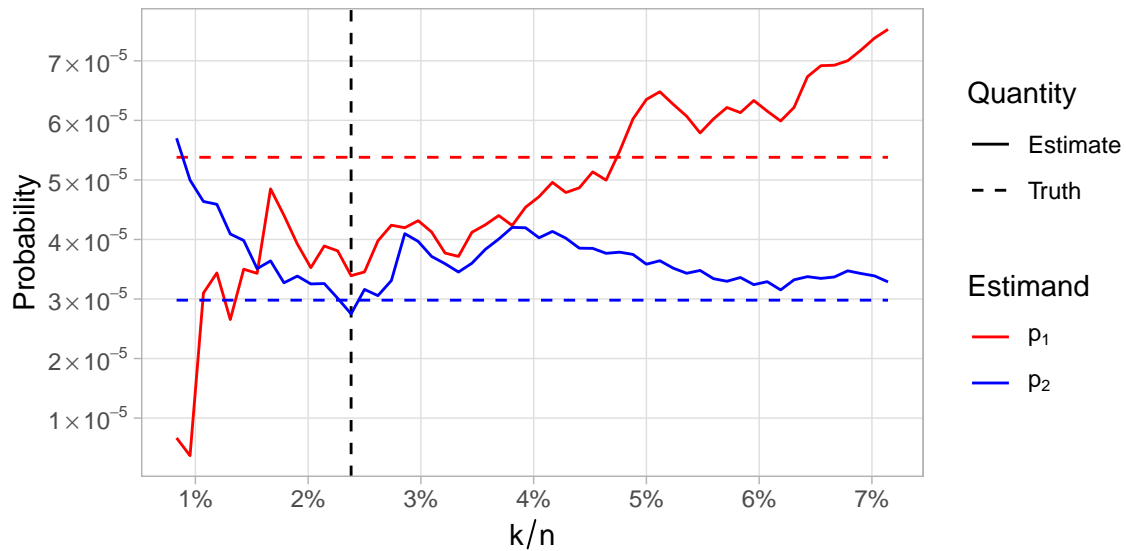


Figure 5.8.: Challenge 3 results for different choices for the tuning parameter,  $k$ . The horizontal dashed lines indicate the estimands’ true values. Our submitted solution was based on  $k = 500$  (vertical dashed line).

### 5.5.3. Challenge 4

#### 5.5.3.1. Data

Challenge 4 regards a  $d = 50$  dimensional random vector  $\mathbf{Y}$  on standard Gumbel margins. The components of  $\mathbf{Y}$  are random variables  $Y_{i,j}$  for  $i = 1, \dots, 25$  and  $j = 1, 2$ , representing the value of an environmental variable at the  $i$ th site in the administrative area of

government area  $j$ . The joint exceedance probabilities

$$\begin{aligned} p_1 &:= \mathbb{P}(Y_{i,j} > G^{-1}(1 - \phi_j) : i = 1, \dots, 25, j = 1, 2), \\ p_2 &:= \mathbb{P}(Y_{i,j} > G^{-1}(1 - \phi_1) : i = 1, \dots, 25, j = 1, 2), \end{aligned}$$

where  $\phi_1 = 1/300$  and  $\phi_2 = 12/300$ , are to be estimated from  $n = 10,000$  independent observations  $\{\mathbf{y}_t = (y_{t,i,j} : i = 1, \dots, 25, j = 1, 2) : t = 1, \dots, n\}$  of  $\mathbf{Y}$ .

### 5.5.3.2. Methodology

Let  $\mathbf{X} = (X_1, \dots, X_d)$  denote the random vector obtained from  $\mathbf{Y}$  by re-indexing its variables and transforming to Fréchet margins with shape parameter  $\alpha = 2$ , i.e.

$$X_{i+25(j-1)} := \Psi_2^{-1}(G(Y_{i,j})) = \exp(Y_{i,j}/2) \sim \Psi_2, \quad (i = 1, \dots, 25, j = 1, 2).$$

The choice of  $\alpha = 2$  will be justified later. The data are transformed in an identical way yielding  $\{\mathbf{x}_t = (x_{t1}, \dots, x_{td}) : t = 1, \dots, n\}$ , where  $x_{t,i+25(j-1)} := \exp(y_{t,i,j}/2)$  for  $t = 1, \dots, n$ ,  $i = 1, \dots, 25$  and  $j = 1, 2$ . The estimands can now be expressed as

$$\begin{aligned} p_1 &= \mathbb{P}(\mathbf{X} \in \mathcal{C}_{\mathbb{V}(d), \mathbf{u}_1}), \quad [\mathbf{u}_1]_i = \begin{cases} \Psi_2^{-1}(1 - \phi_1), & \text{if } 1 \leq i \leq 25 \\ \Psi_2^{-1}(1 - \phi_2), & \text{if } 26 \leq i \leq 50 \end{cases}, \\ p_2 &= \mathbb{P}(\mathbf{X} \in \mathcal{C}_{\mathbb{V}(d), \mathbf{u}_2}), \quad \mathbf{u}_2 = \Psi_2^{-1}(1 - \phi_1)\mathbf{1}_{50}. \end{aligned}$$

At a high level, our method proceeds in a similar vein to Challenge 3: we will model  $\mathbf{X}$  as max-linear and compute estimates for  $p_1$  and  $p_2$  based on (5.11). However, our exploratory analysis revealed that not all components of  $\mathbf{X}$  are asymptotically dependent, implying that  $H_{\mathbf{X}}(\mathbb{V}(d)) = 0$ . This has important ramifications for how we construct our solution. On the one hand, empirical or CP-estimates of  $A$  will assert that  $C_{\mathbb{V}(d)}$  is an extremal direction, resulting in a misspecified model. On the other hand, a model that correctly identifies  $C_{\mathbb{V}(d)}$  as a  $H_{\mathbf{X}}$ -null set will yield  $\hat{p}_1 = \hat{p}_2 = 0$ , despite the true values being non-zero (Rohrbeck et al. 2023). How do we resolve this difficulty? The key is to identify clusters of asymptotically dependent variables prior to model fitting and estimate the

probability of concurrent joint exceedance events in all clusters. Our working hypothesis – that the marginal variables can be partitioned such that asymptotic independence is present between clusters but not within them – is formalised below.

**Assumption 1.** There exists  $2 \leq K \leq d$  and a partition  $\beta_1, \dots, \beta_K$  of  $\mathbb{V}(d)$  such that the angular measure is supported on the closed subspaces  $\bar{C}_{\beta_1}, \dots, \bar{C}_{\beta_K} \subset \mathbb{S}_+^{d-1}$ , where  $\bar{C}_\beta := \{C_{\beta'} : \beta' \subseteq \beta\}$  for any  $\beta \in \mathcal{P}_d^*$ . That is,  $H_{\mathbf{X}}(\cup_{l=1}^K \bar{C}_{\beta_l}) = H_{\mathbf{X}}(\mathbb{S}_+^{d-1})$ .

This scenario has been considered before, cf. Assumption 1 in Fomichov and Ivanovs (2023). If  $\mathbf{X}$  is max-linear with parameter  $A = (\mathbf{a}_1, \dots, \mathbf{a}_q) \in \mathbb{R}_+^{d \times q}$ , we may restate the assumption as follows.

**Assumption 2.** There exist permutations  $\pi : \mathbb{V}(d) \rightarrow \mathbb{V}(d)$  and  $\phi : \mathbb{V}(q) \rightarrow \mathbb{V}(q)$  such that  $\mathbf{X}_\pi := (X_{\pi(1)}, \dots, X_{\pi(d)}) \sim \text{MaxLinear}(A_\phi; \alpha)$ , where  $A_\phi := (\mathbf{a}_{\phi(1)}, \dots, \mathbf{a}_{\phi(q)}) \in \mathbb{R}_+^{d \times q}$  is block-diagonal with  $2 \leq K \leq d$  blocks. For  $l = 1, \dots, K$ , the  $l$ th block matrix  $A_\phi^{(l)}$  has  $d_l = |\beta_l|$  rows,  $1 \leq q_l < q$  columns, and is such that the  $q_l \times q_l$  matrix  $A_\phi^{(l)}(A_\phi^{(l)})^T$  has strictly positive entries. The blocks' dimensions satisfy  $\sum_{l=1}^K d_l = d$  and  $\sum_{l=1}^K q_l = q$ .

Under Assumption 2,  $\mathbf{X}$  divides into random sub-vectors  $\mathbf{X}^{(1)}, \dots, \mathbf{X}^{(K)}$ , where  $\mathbf{X}^{(l)} := (X_j : j \in \beta_l) \sim \text{MaxLinear}(A_\phi^{(l)}; \alpha)$  for  $l = 1, \dots, K$ . (Henceforth, assume for notational convenience that the columns of  $A$  are already appropriately ordered, so that  $A = A_\phi$ .) While the clustering assumption is simplistic and cannot be expected to hold in general applications, it reflects what we suspect to be the true dependence structure for Challenge 4. Moreover, it is dimension reducing because the original  $d$ -dimensional problem is transformed to a set of  $K$  independent problems with dimensions  $d_1, \dots, d_K < d$ . This ameliorates the curse of dimensionality to some extent.

In general, a joint exceedance event can be decomposed into concurrent joint exceedances in all  $K$  clusters as  $\{\mathbf{X} \in \mathcal{C}_{\mathbb{V}(d), \mathbf{u}}\} = \cap_{l=1}^K \{\mathbf{X} \in \mathcal{C}_{\mathbb{V}(d_l), \mathbf{u}^{(l)}}\}$ , where each threshold sub-vector  $\mathbf{u}^{(l)}$  is defined from  $\mathbf{u}$  analogously to  $\mathbf{X}^{(l)}$ . Since we consider variables in different clusters to be asymptotically independent, we assume that for large, finite thresholds, joint exceedances in each cluster are approximately independent events, so that

$$\mathbb{P}(\mathbf{X} \in \mathcal{C}_{\mathbb{V}(d), \mathbf{u}}) = \mathbb{P}\left(\bigcap_{l=1}^K \{\mathbf{X}^{(l)} \in \mathcal{C}_{\mathbb{V}(d_l), \mathbf{u}^{(l)}}\}\right) \approx \prod_{l=1}^K \mathbb{P}(\mathbf{X}^{(l)} \in \mathcal{C}_{\mathbb{V}(d_l), \mathbf{u}^{(l)}}).$$

Assuming  $\mathbf{X}^{(l)} \sim \text{MaxLinear}(A^{(l)}; \alpha)$  for  $l = 1, \dots, K$ , each term in the product can be estimated using (5.11), so that

$$\mathbb{P}(\mathbf{X} \in \mathcal{C}_{\mathbb{V}(d), \mathbf{u}}) \approx \prod_{l=1}^K \hat{\mathbb{P}}(A^{(l)} \circ \mathbf{Z} \in \mathcal{C}_{\mathbb{V}(d_l), \mathbf{u}^{(l)}}). \quad (5.16)$$

The final step is to replace  $A^{(1)}, \dots, A^{(K)}$  with suitable estimates. We opted to use CP-estimates for two reasons: (i) they are rooted in the TPDM, which is geared towards high-dimensional settings, and (ii) their non-uniqueness enables us to compute numerous parameter/probability estimates, whose variation reflects the model uncertainty that arises from summarising dependence via the TPDM and thereby overlooking higher-order dependencies between components. The use of CP-estimates justifies our choosing  $\alpha = 2$  in the pre-processing step and throughout.

### 5.5.3.3. Results

We now present our results for Challenge 4. First, the variables  $X_1, \dots, X_d$  are partitioned into  $K$  groups based on asymptotic (in)dependence using the clustering algorithm of Bernard et al. (2013). This entails constructing a distance matrix  $\mathcal{D} = (\hat{d}_{ij})$ , where  $\hat{d}_{ij}$  denotes a non-parametric estimate of the F-madogram distance between variables  $X_i$  and  $X_j$ . The distance metric is connected to the strength of extremal dependence between  $X_i$  and  $X_j$ , with  $\hat{d}_{ij} \approx 0$  implying strong asymptotic dependence and  $\hat{d}_{ij} = 1/6$  in the case of asymptotic independence. The partition around medoids (PAM) clustering algorithm (Kaufman and Rousseeuw 1990) returns a partition  $\beta_1, \dots, \beta_K$  of  $\mathbb{V}(d)$  based on  $\mathcal{D}$ . The number of clusters  $K$  is a pre-specified tuning parameter; we identify  $K = 5$  clusters whose sizes are given in Table 5.2. By consulting Rohrbeck et al. (2023), we have verified that our clustering was correct. Defining cluster membership variables  $\mathcal{M}_1, \dots, \mathcal{M}_d \in \{1, \dots, K\}$  by  $\mathcal{M}_i = l \iff i \in \beta_l$  for  $i = 1, \dots, d$ , we find that  $\max\{\hat{d}_{ij} : \mathcal{M}_i = \mathcal{M}_j\} = 0.113 < 1/6$  and  $\min\{\hat{d}_{ij} : \mathcal{M}_i \neq \mathcal{M}_j\} = 0.164 \approx 1/6$ . These summary statistics are consistent with Assumption 1.

Next, we compute the empirical TPDMs of  $\mathbf{X}^{(1)}, \dots, \mathbf{X}^{(K)}$ . For  $l = 1, \dots, K$  and  $t = 1, \dots, n$ , define the observational sub-vector  $\mathbf{x}_t^{(l)} = (x_{ti} : i \in \beta_l)$  and its radial and angular components  $r_t^{(l)} = \|\mathbf{x}_t^{(l)}\|_2$ ,  $\boldsymbol{\theta}_t^{(l)} = \mathbf{x}_t^{(l)} / \|\mathbf{x}_t^{(l)}\|_2$ , respectively. Let  $\mathbf{x}_{(j)}^{(l)}$ ,  $r_{(j)}^{(l)}$  and  $\boldsymbol{\theta}_{(j)}^{(l)}$  denote

Table 5.2.: Summary statistics for the Challenge 4 clusters' empirical TPDMs.

Cluster	Size	U1 sites	U2 sites	$\{\hat{\sigma}_{ij} : i \neq j\}$		
				Min.	Median	Max.
1	9	7	2	0.30	0.33	0.40
2	8	5	3	0.64	0.68	0.74
3	8	3	5	0.62	0.67	0.74
4	12	7	5	0.27	0.33	0.39
5	13	3	10	0.43	0.50	0.58

the vector, radius, and angle associated with the  $j$ th largest observation in norm among  $\mathbf{x}_1^{(l)}, \dots, \mathbf{x}_n^{(l)}$ . Choose a tuning parameter  $1 \leq k_l \leq n$  representing the number of extreme observations that enter into the estimate for cluster  $l$ . Then

$$\hat{A}^{(l)} = \left( \frac{d_l}{k_l} \boldsymbol{\theta}_{(1)}^{(l)}, \dots, \frac{d_l}{k_l} \boldsymbol{\theta}_{(k_l)}^{(l)} \right), \quad \hat{\Sigma}_{\mathbf{X}^{(l)}} = \hat{A}^{(l)} (\hat{A}^{(l)})^T.$$

We set  $k_1 = \dots = k_K =: k = 250$ , corresponding to a sampling fraction of  $k/n = 2.5\%$  for each cluster. The empirical TPDMs for the first two clusters are displayed in Figure 5.9; summary statistics for all clusters' TPDMs are listed in Table 5.2. Asymptotic dependence is strongest in clusters 2 and 3 and weakest in clusters 1 and 4.

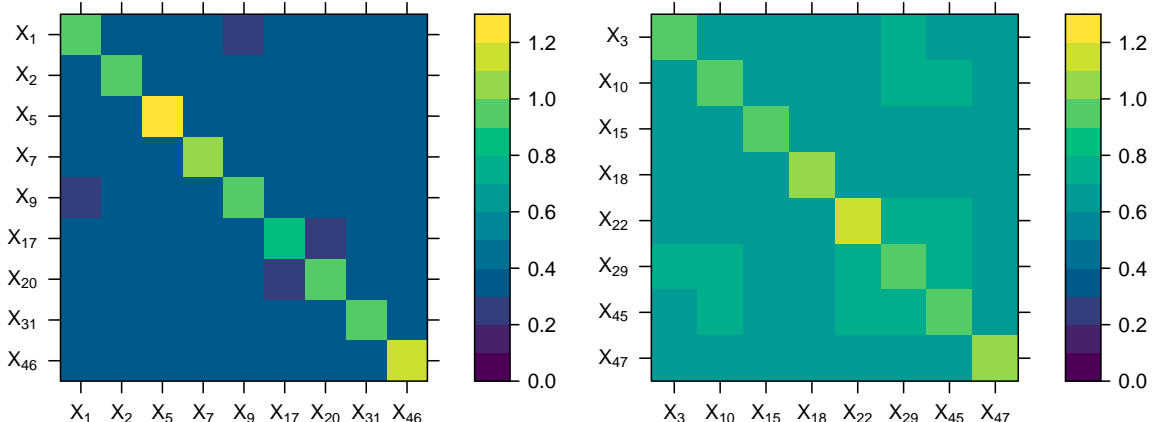


Figure 5.9.: The estimated TPDMs for the first two clusters,  $\hat{\Sigma}_{\mathbf{X}^{(1)}}$  (left) and  $\hat{\Sigma}_{\mathbf{X}^{(2)}}$  (right), based on the  $k = 250$  most extreme observations in norm.

By repeated application of the CP-decomposition algorithm of Kiriliouk and Zhou (2022) with randomly chosen inputs, we obtain  $N_{cp} = 50$  CP-estimates of each matrix  $A^{(l)}$ . The resulting CP-factors are denoted by  $\tilde{A}_1^{(l)}, \dots, \tilde{A}_{N_{cp}}^{(l)}$ . Note that among  $\tilde{A}_1^{(l)}, \dots, \tilde{A}_{N_{cp}}^{(l)}$  there are at most  $d_l$  distinct leading columns, because there are only  $d_l$  unique ways to initialise

the (deterministic) algorithm. But  $\hat{\mathbb{P}}(\tilde{A} \circ \mathbf{Z} \in \mathcal{C}_{\mathbb{V}(d), \mathbf{u}})$  is fully determined by  $\tilde{\mathbf{a}}_1$ , so in fact  $\{\hat{\mathbb{P}}(\tilde{A}_r^{(l)} \circ \mathbf{Z} \in \mathcal{C}_{\mathbb{V}(d_l), \mathbf{u}^{(l)}}) : r = 1, \dots, N_{\text{cp}}\}$  contains at most  $d_l$  distinct values. These values are represented by black points in the left-hand plot in Figure 5.10. Clusters 2 and 3 are deemed most likely to experience a joint extreme event, because they contain a small number ( $d_2 = d_3 = 8$ ) of highly dependent variables. The effect of changing the threshold from  $\mathbf{u}_1$  to  $\mathbf{u}_2$  is most pronounced in cluster 5, since it is primarily composed of sites in area U2.

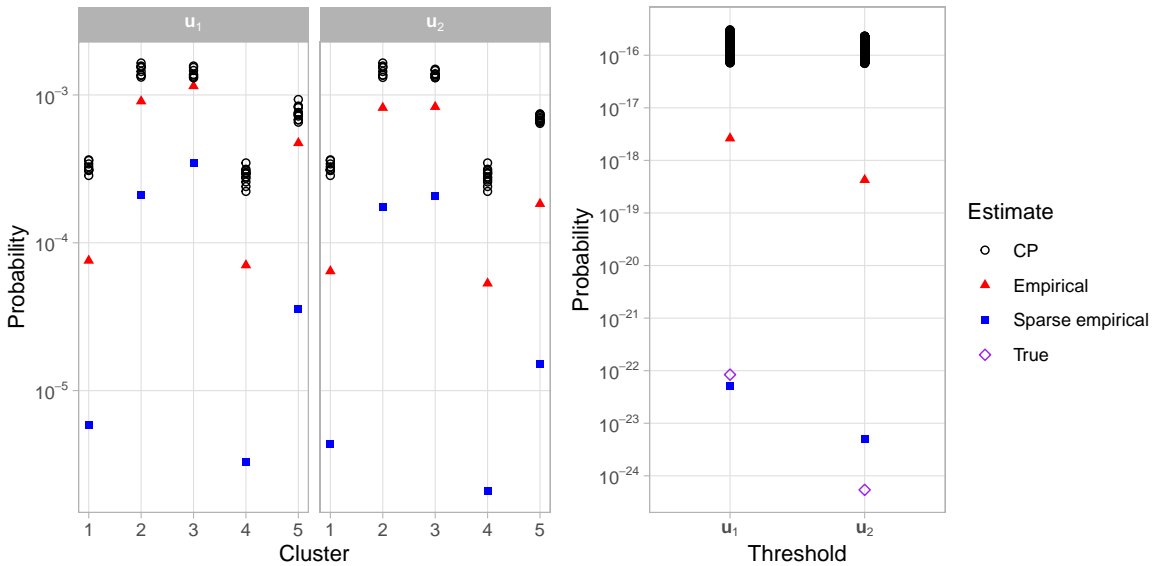


Figure 5.10.: Joint exceedance probability estimates for each cluster sub-vector (left) and the full vector (right) based on different estimators for the parameters  $A^{(1)}, \dots, A^{(5)}$ .

Substituting each CP-estimate into (5.16) and enumerating over all possible combinations, we produce sets of estimates of  $p_i$ , for  $i = 1, 2$ , given by

$$\tilde{P}_i := \{\hat{\mathbb{P}}(\tilde{A}_{r_1}^{(1)} \circ \mathbf{Z} \in \mathcal{C}_{\mathbb{V}(d_1), \mathbf{u}_i^{(1)}}) \times \dots \times \hat{\mathbb{P}}(\tilde{A}_{r_K}^{(K)} \circ \mathbf{Z} \in \mathcal{C}_{\mathbb{V}(d_K), \mathbf{u}_i^{(K)}}) : r_1, \dots, r_K = 1, \dots, N_{\text{cp}}\}.$$

Each set has size  $N_{\text{cp}}^K \approx 3 \times 10^8$  (including repeated values) and contains  $\prod_{l=1}^K d_l = 89,856$  distinct values. The distributions of the estimates are represented by the black points in the right-hand panel of Figure 5.10. Our final point estimates are taken as the median values  $\tilde{p}_1 := \text{median}(\tilde{P}_1) = 1.4 \times 10^{-16}$  and  $\tilde{p}_2 := \text{median}(\tilde{P}_2) = 1.3 \times 10^{-16}$ , respectively, to two significant figures.

#### 5.5.3.4. Improving performance using sparse empirical estimates

Unfortunately, it transpires that our method dramatically over-estimated the true probabilities. In hindsight, this could have been anticipated in view of the simulation study in Section 5.1 in Kiriliouk and Zhou (2022), where the authors remark that failure regions of the type  $\mathcal{C}_{V(d),u}$  are poorly summarised by the TPDM. This prompts us to investigate whether using empirical or sparse empirical estimates instead of a CP-based approach would have improved our performance. For the former, this simply involves replacing  $A^{(l)}$  with the precomputed matrix  $\hat{A}^{(l)}$  in (5.16). The approach based on sparse empirical estimates proceeds analogously except that we must revert to the  $\alpha = 1$  setting and transform the data and thresholds accordingly. The resulting estimates for the joint exceedance probabilities are represented by the red and blue points in Figure 5.10. The values are smaller (better) in all clusters and consequently the final estimates are closer to the true event probabilities (purple). In fact, using sparse empirical estimates yields  $\hat{p}_1^* = 5.1 \times 10^{-23}$  and  $\hat{p}_2^* = 5.0 \times 10^{-24}$ , which are remarkably close to the correct solutions  $p_1 = 8.4 \times 10^{-23}$  and  $p_2 = 5.4 \times 10^{-25}$ . Submitting these values would have significantly improved our ranking for this sub-challenge.

## 5.6. Conclusion

We propose four different methods in order to solve the EVA (2023) Conference Data Challenge. These methods allow for the estimation of extreme quantiles and probabilities. In the univariate cases, we estimate the conditional quantile by attempting to cluster the covariates to categorise the extremes. Once clustered, bootstrapping was used in order to estimate central 50% confidence intervals of the extreme quantiles. In practice however, we found no clearly defined clusters and that the Gaussian mixture distribution was not able to capture the non-Gaussian distribution of the covariates. This could also be extended by using GPDs with covariate models for each cluster, to try to improve quantile estimates. In the second challenge, we were able to assess the GPD fit of a misspecified model and apply a correction to an initial fit where there was large uncertainty in the tail behaviour. This resulted in a change in the return level from an under-estimate to a potentially less-severe over-estimate. By using a more sophisticated model for the covariates, further work can

be done to articulate the extent to which the correction was due to a bias in the model fit.

Our performance in the multivariate challenges demonstrates that the max-linear model provides a good framework for estimating tail event probabilities. By connecting this model with sparse simplex projections, one can achieve exceptional performance on both Challenges 3 and 4. Given these results, further research on the theoretical properties of the sparse empirical estimator  $\hat{A}^*$  is warranted. An obvious shortcoming of our Challenge 3 methodology is that it ignores the available covariate information. Incorporating covariates into the max-linear/TPDM framework remains an unexplored area. The upwards bias in our Challenge 4 probability estimates is partly caused by over-estimating the dependence strength between certain groups of variables. The empirical TPDM has a known tendency to over-estimate weak/moderate dependence (Fix et al. 2021), as is the case in clusters 1, 3, and 5. A better TPDM estimator that takes this issue into account would likely improve our final results. In Challenges 3 and 4 we switch between  $\alpha = 1$  and  $\alpha = 2$  in a way that is somewhat unsatisfactory (mathematically and presentationally). In hindsight, employing a generalised version of the TPDM (Kiriliouk and Zhou 2022, Equation 4) would have allowed us to fix  $\alpha = 1$  throughout. Finally, uncertainty quantification is a crucial aspect of risk assessment in practice, especially when dealing with the exceedingly rare events encountered in Challenge 4. Fix et al. (2021) utilise a bootstrapping procedure in the context of TPDM-based inference for extremes and their approach would transfer to our methods very naturally.

## 5.7. Data availability

The data for the EVA (2023) Conference Data Challenge has been made publicly available by Rohrbeck et al. (2024). The code used for Challenges 3 and 4 is available at <https://github.com/pawleymatthew/eva-2023-data-challenge>.

## 5.8. Acknowledgements

The authors are thankful to Christian Rohrbeck, Emma Simpson and Jonathan Tawn of the University of Bath, University College London, and Lancaster University, respectively, for organising the challenges that inspired this work.

## 5.9. Funding

Matthew Pawley is supported by a scholarship from the EPSRC Centre for Doctoral Training in Statistical Applied Mathematics at Bath (SAMBa), under the project EP/S022945/1. Henry Elsom is supported by the University Research Studentship Award (URSA) from the University of Bath.

# 6. Bias-corrected estimation of the TPDM

## 6.1. Introduction and motivation

Section 2.6 demonstrated a deficiency of the empirical TPDM estimator, which we termed the bias issue. Specifically, the empirical TPDM  $\hat{\Sigma}$  has a tendency to overestimate weak pairwise dependence – see (2.64). The bias issue has arisen at several subsequent points throughout the thesis: our test for time-varying dependence becomes less powerful when dependence is weak (Figure B.3); projections onto principal eigenspaces of  $\hat{\Sigma}$  result in poor reconstructions near the simplex boundary (e.g. see bottom right plot in Figure 4.9); tail probability estimates based on completely positive factorisations of  $\hat{\Sigma}$  are biased (Figure 5.10).

This chapter addresses the problem of reducing bias in the empirical TPDM. Bias reduction requires grappling with two interconnected problems. First, what *form* should a bias-corrected estimator take? The procedure proposed in Fix et al. (2021) (see Section 2.5.2) shrinks all entries of  $\hat{\Sigma}$  equally. We contend that this is not ideal, given that the bias is greatest for pairs of variables where dependence is weak. Inspired by Rothman et al. (2009), a flexible extension based on the adaptive lasso is proposed. This permits control over whether shrinkage is applied equally to all entries or targeted towards smaller entries, at the cost of introducing an additional parameter. The second problem concerns *how much* bias correction should be applied. Fix et al. (2021) solve this by assuming that dependence strength is a decreasing function of spatial distance and is approximately zero for the most distant pair(s) of sites in the study region. However, these assumptions are only meaningful (let alone satisfied) in spatial settings, precluding its use in general applications. While we were unable to find a general solution to this research problem, we made progress in a special case where bias-reduction is achieved via linear shrinkage

techniques (Ledoit and Wolf 2003). For this class, we are able to devise a theoretically justified, data-driven procedure for selecting the magnitude of the shrinkage.

## 6.2. Regularised TPDM estimators

In high-dimensional settings, where the number of variables is comparable to the number of observations, the empirical covariance matrix may be noisy and poorly conditioned. Regularisation may be applied to obtain more stable and accurate estimates. In particular, thresholding is used to enforce sparsity by shrinking small values towards zero, enhancing stability and interpretability in cases where many variables are weakly correlated (Rothman et al. 2009). On the other hand, shrinkage methods move the empirical estimate towards a biased but highly structured pre-specified target matrix (Ledoit and Wolf 2003). In both cases, more accurate estimates are obtained by reducing the entries of the empirical estimator in some way. Thus, we may consider applying these techniques to the empirical TPDM to achieve bias-reduction. This may have the additional benefit of improving stability in cases where  $d$  is comparable to the number of extremes  $k$ , but this aspect will not be explored.

### 6.2.1. Thresholded TPDM estimators

The core idea of thresholded estimation is to apply a thresholding operator to the raw, empirical estimate (in our case  $\hat{\Sigma}$ ). The thresholding operator controls the nature of the regularisation and must satisfy certain properties.

**Definition 6.1.** Let  $\lambda \geq 0$  be a fixed threshold. A function  $s_\lambda : \mathbb{R}_+ \rightarrow \mathbb{R}_+$  is called a thresholding operator if, for all  $x \in \mathbb{R}_+$ ,

$$s_\lambda(x) \leq x, \tag{6.1}$$

$$x \leq \lambda \implies s_\lambda(x) = 0, \tag{6.2}$$

$$|s_\lambda(x) - x| \leq \lambda. \tag{6.3}$$

The tuning parameter  $\lambda$  controls the strength of the regularisation. In the two extreme cases, we have  $s_0(x) = x$  (no regularisation) and  $s_\infty(x) = 0$  for all  $x \in \mathbb{R}_+$  (full shrinkage). Condition (6.1) states that  $s_\lambda$  should push  $x$  towards zero. Condition (6.2) enforces a threshold below which values are mapped to zero, potentially inducing sparsity in the output. Condition (6.3) limits the amount of shrinkage. For simplicity, we assume the threshold in (6.2) and the maximal shrinkage in (6.3) are identical. This could be relaxed by introducing separate parameters  $\lambda_1$  and  $\lambda_2$  if desired (Antoniadis and Fan 2001). Thresholding operators may be equivalently formulated as solutions to regularised optimisation problems of the form

$$s_\lambda(x) = \arg \min_{y \in \mathbb{R}_+} \left[ \frac{1}{2}(y - x)^2 + p_\lambda(y; x) \right] \quad (6.4)$$

for some penalty function  $p_\lambda$ . While we do not explicitly make use of this formulation, the penalty function is useful for providing insight into an operator's behaviour.

We will consider three popular thresholding operators: hard-thresholding, soft-thresholding, and adaptive lasso. For reference, the corresponding functions  $x \mapsto s_{0.1}(x)$  are shown in Figure 6.1. The hard-thresholding rule

$$s_\lambda^H(x) = x \mathbf{1}\{x > \lambda\} \quad (6.5)$$

applies no shrinkage to values above  $\lambda$ . The jump discontinuity in  $s_\lambda^H(x)$  at  $\lambda = x$  can be observed in Figure 6.1. In the space of thresholding operators, it is diametrically opposed to the soft-thresholding operator

$$s_\lambda^S(x) = (x - \lambda)_+, \quad (6.6)$$

which induces the maximal amount of shrinkage permitted by (6.3). Soft-thresholding corresponds to solving (6.4) with lasso penalty function  $p_\lambda(y; x) = \lambda y$ . Note that  $p_\lambda(y; x)$  does not depend on  $x$ , reflecting the fact that equal shrinkage is applied to large and small values (exceeding  $\lambda$ ) alike. Other thresholding operators offer some kind of compromise between these two cases. The adaptive lasso penalty function  $p_\lambda(y; x) = \lambda^{\eta+1} y x^{-\eta}$  down-weights larger values, leading to the thresholding rule

$$s_{\lambda, \eta}^{AL}(x) = (x - \lambda^{\eta+1} x^{-\eta})_+, \quad (\eta \geq 0). \quad (6.7)$$

The degree of down-weighting is controlled by the tuning parameter  $\eta \geq 0$ . Setting  $\eta = 0$  results in no down-weighting, yielding the soft-thresholding operator  $s_{\lambda,0}^{AL}(x) = s_\lambda^S(x)$ . On the other hand,  $s_{\lambda,\eta}^{AL}(x) \rightarrow s_\lambda^H(x)$  as  $\eta \rightarrow \infty$ . Thus, soft- and hard-thresholding are special (limiting) cases of adaptive lasso. The clipped  $L_1$ -penalty and the smoothly clipped absolute deviations (SCAD) penalty behave in a similar fashion (Antoniadis and Fan 2001).

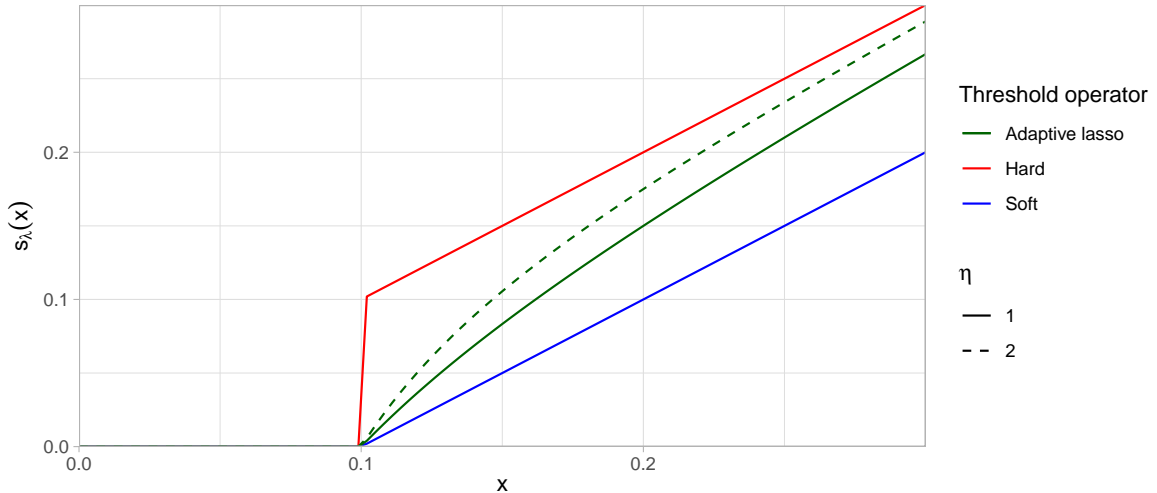


Figure 6.1.: Popular thresholding operators  $s_\lambda(x)$  with  $\lambda = 0.1$ .

We now proceed to apply thresholding to the empirical TPDM to define our first class of bias-reduced estimators. Let  $A = (a_{ij}) \in \mathbb{R}_+^{m \times n}$  be a non-negative matrix and  $s_\lambda : \mathbb{R}_+ \rightarrow \mathbb{R}_+$  a thresholding operator. The thresholded matrix  $s_\lambda(A) := (s_\lambda(a_{ij}))$  is defined by element-wise application of  $s_\lambda$  to  $A$ . Clearly this is very simple and fast to compute.

**Definition 6.2.** Let  $s_\lambda$  be a thresholding operator. The thresholded TPDM estimator is the  $d \times d$  matrix

$$\tilde{\Sigma}(\lambda) = (\tilde{\sigma}_{ij}(\lambda)), \quad \tilde{\sigma}_{ij} = \begin{cases} \hat{\sigma}_{ij}, & i = j, \\ s_\lambda(\hat{\sigma}_{ij}), & i \neq j. \end{cases} \quad (6.8)$$

Note that we do not shrink the diagonal entries, but in any case the performance of estimators will be evaluated using the off-diagonal entries only. The soft-thresholded TPDM  $s_\lambda^S(\hat{\Sigma})$  coincides with estimator proposed by Fix et al. (2021). However, Definition 6.2 includes a much broader class of estimators with more flexible behaviours. In particular, the adaptive lasso TPDM  $s_{\lambda,\eta}^{AL}(\hat{\Sigma})$  allows us to concentrate shrinkage towards small entries in  $\hat{\Sigma}$ , where the bias is presumed to be greater. Figure 6.2 provides a visual comparison

between the three thresholding methods using the Red Sea surface temperature data from Section 3.8. Each matrix represents a regularised TPDM  $\tilde{\Sigma}$  of the random vector  $\mathbf{X}$ , where  $X_i$  corresponds to the  $i$ th site in Figure 3.9 (ordered by longitude and then by latitude) for  $i = 1, \dots, 200$ . The figure shows how the hard-thresholded, soft-thresholded and adaptive lasso ( $\eta = 2$ ) estimates vary with the regularisation parameter  $\lambda \in \{0, 0.1, \dots, 0.5\}$ . The empirical TPDM is estimated from the proportion  $k/n = 0.15$  of largest observations; this matrix is shown in the sub-panels where  $\lambda = 0$ . Since the components of  $\mathbf{X}$  are ordered according to the spatial locations,  $\hat{\Sigma}$  generally exhibits stronger dependencies among variable pairs closer to the diagonal and weaker dependencies for those farther away. Hard-thresholding (top left) has no effect when  $\lambda < \min\{\hat{\sigma}_{ij} : i \neq j\} \approx 0.249$ . Increasing the threshold introduces abrupt shifts, resulting in a non-smooth sequence of solutions. In contrast, soft-thresholding yields smoother solutions because all off-diagonal entries receive some shrinkage when  $\lambda > 0$ . However, the regularisation acts indiscriminately by applying an equal penalty to all entries. Consequently, as  $\lambda$  increases the dependence strength is close to zero for all pairs of sites, including neighbouring ones. The adaptive lasso (bottom left) combines the advantages of hard- and soft-thresholding, yielding smooth solution paths but prioritising shrinkage of entries that are close to zero.

A drawback of these estimators is that thresholding fails to preserve certain matrix properties, including positive semi-definiteness and complete positivity. Evidence of this is provided in Figure 6.3, which depicts the eigenvalues of the hard-thresholded TPDMs  $\tilde{\Sigma}(\lambda)$  from Figure 6.2. Specifically, the plot shows the absolute value of the eigenvalues, with positive eigenvalues in black and negative eigenvalues in red. As  $\lambda$  increases and the thresholding takes effect, the eigenvalues of  $\tilde{\Sigma}(\lambda)$  get shrunk, occasionally causing them to become negative. Thus,  $\tilde{\Sigma}$  may need to undergo pre-processing before it can be incorporated into existing TPDM-based modelling tools such as PCA. This motivates us to propose an alternative approach to bias-reduction based on linear shrinkage methods. While this class is less flexible than thresholded TPDMs, its simplicity ensures estimates possess nice properties and are more amenable to mathematical analysis.

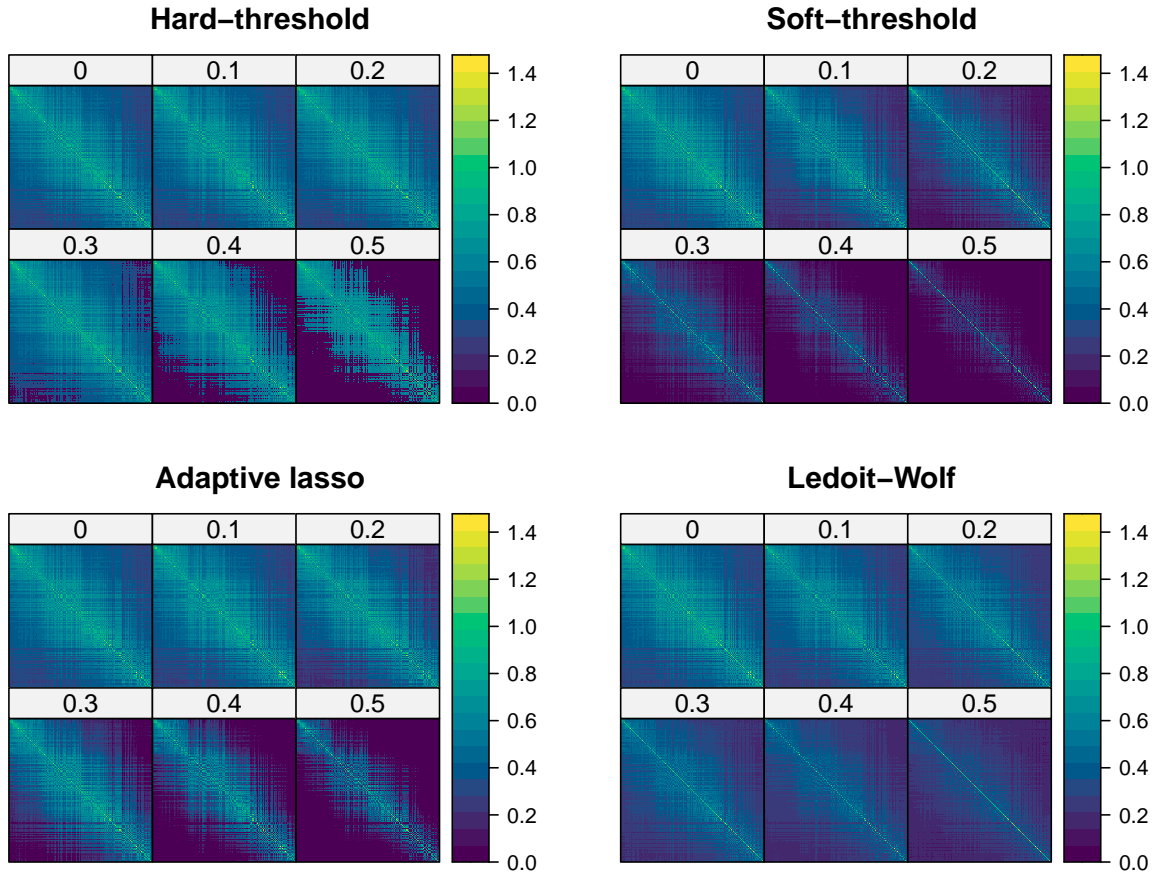


Figure 6.2.: Regularised TPDM estimates  $\tilde{\Sigma}(\lambda)$  based on the Red Sea surface temperature data from Section 3.8. The  $d = 200$  sites in Figure 3.9 are ordered by longitude and then latitude and  $\hat{\Sigma}$  is estimated with  $k/n = 0.15$ . The values at the top of each sub-panel represent the regularisation parameter  $\lambda \in \{0, 0.1, \dots, 0.5\}$ . For the adaptive lasso estimates we take  $\eta = 2$ .

### 6.2.2. The Ledoit-Wolf TPDM estimator

Shrinkage is a regularisation technique dating back to Stein (1956), whereby a sample estimate is shrunk towards some pre-specified target. The simplest shrinkage method is Ledoit-Wolf linear shrinkage (Ledoit and Wolf 2003). Their approach to regularising the sample covariance matrix transfers easily to the TPDM.

**Definition 6.3.** Let  $T$  be a  $d \times d$  target matrix. For  $\lambda \in [0, 1]$ , the Ledoit-Wolf TPDM is the  $d \times d$  matrix

$$\tilde{\Sigma}(\lambda) = \lambda T + (1 - \lambda)\hat{\Sigma}. \quad (6.9)$$

The key idea is to bias the empirical TPDM  $\hat{\Sigma}$  towards a highly structure target  $T$  by

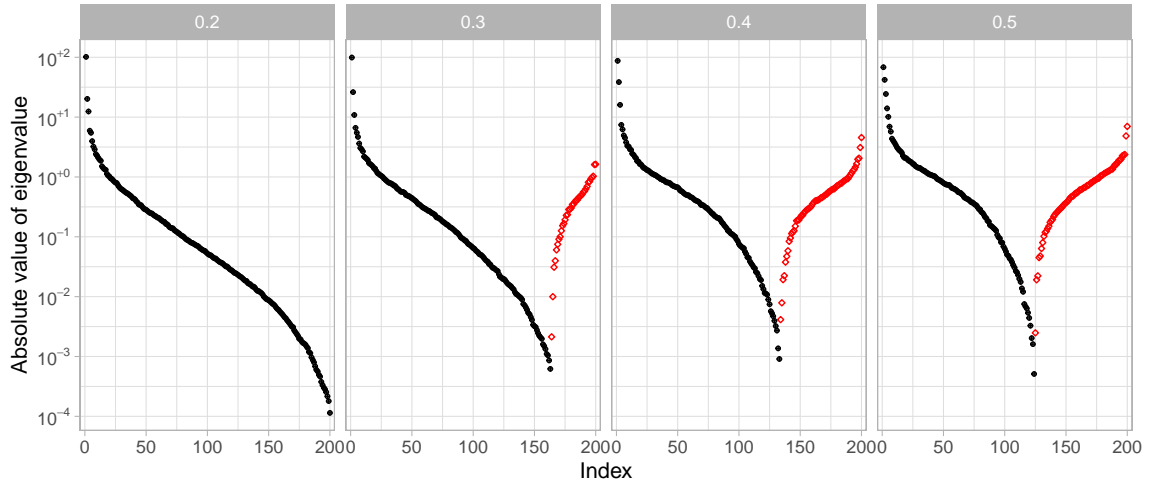


Figure 6.3.: Absolute values of the eigenvalues of the hard-thresholded TPDM estimates  $\tilde{\Sigma}(\lambda)$  from Figure 6.2 (top left) for  $\lambda \in \{0.2, 0.3, 0.4, 0.5\}$ . Positive and negative eigenvalues are coloured black and red, respectively.

forming a convex linear combination between the two. The shrinkage intensity  $\lambda \in [0, 1]$  determines the weight allocated to each matrix. No shrinkage occurs when  $\lambda = 0$ . If  $\lambda = 1$  the estimator returns  $T$ , which is biased but perfectly stable (it has zero variance). The choice of target depends on the context at hand. We will always choose  $T = I_d$ , the  $d \times d$  identity matrix. This means the off-diagonal entries are shrunk towards zero and the diagonal entries are left unaltered. Similar to soft-thresholding, the Ledoit-Wolf TPDM counters the bias by applying equal shrinkage to all entries. A slight difference is that the Ledoit-Wolf shrinkage intensity is applied multiplicatively, i.e.  $\tilde{\sigma}_{ij} = (1 - \lambda)\hat{\sigma}_{ij}$ , whereas thresholding works additively. Figure 6.2 (bottom right) shows the sequence of Ledoit-Wolf TPDMs for the Red Sea data, as described earlier. We observe that linear shrinkage behaves quite differently to any of the thresholding estimators; the general structure of the matrix does not change all that much as  $\lambda$  increases. While this behaviour is not necessarily desirable from a modelling perspective, it explains why the Ledoit-Wolf TPDM retains many of the mathematical properties of the empirical TPDM.

**Proposition 6.1.** *The Ledoit-Wolf TPDM  $\tilde{\Sigma}(\lambda)$  is symmetric, positive semi-definite, and completely positive.*

*Proof.* For brevity, we suppress dependence on  $\lambda$ . Symmetry follows immediately because

for any  $i, j$ ,

$$\tilde{\sigma}_{ij} = \lambda \mathbf{1}\{i = j\} + (1 - \lambda)\hat{\sigma}_{ij} = \lambda \mathbf{1}\{j = i\} + (1 - \lambda)\hat{\sigma}_{ji} = \tilde{\sigma}_{ji}.$$

For positive semi-definiteness, recall that  $\hat{\Sigma}$  is positive semi-definite and so for any  $\mathbf{y} \in \mathbb{R}^d \setminus \{\mathbf{0}\}$ ,

$$\mathbf{y}^T \tilde{\Sigma} \mathbf{y} = \lambda \mathbf{y}^T \mathbf{y} + (1 - \lambda) \mathbf{y}^T \hat{\Sigma} \mathbf{y} = \lambda \|\mathbf{y}\|_2^2 + (1 - \lambda) \mathbf{y}^T \hat{\Sigma} \mathbf{y} \geq 0.$$

The identity matrix is trivially completely positive since  $I_d = I_d I_d^T$  and  $\hat{\Sigma}$  is completely positive by Proposition 2.3. The class of completely positive matrices is a convex cone (Berman and Shaked-Monderer 2003), so complete positivity is preserved under convex combinations.  $\square$

Positive semi-definiteness means the Ledoit-Wolf estimator may replace  $\hat{\Sigma}$  in PCA techniques. Complete positivity implies that there exists a max-linear random vector  $\mathbf{X}_\lambda$  whose TPDM is  $\tilde{\Sigma}(\lambda)$ . Therefore the Ledoit-Wolf TPDM is more straightforward to use in practice compared to the thresholded estimators.

## 6.3. Selecting the regularisation parameter

### 6.3.1. Frobenius risk minimisation

Statistically, the main challenge is to select the regularisation parameter  $\lambda$ . A natural criterion is to choose  $\lambda$  so as to minimise the discrepancy between the true TPDM  $\Sigma$  and the regularised estimate  $\tilde{\Sigma}(\lambda)$ . We are generally only interested in the error in the off-diagonal entries, so we will tend to refer to the upper-half vectorised quantities

$$\boldsymbol{\sigma} = \text{vecu}(\Sigma), \quad \hat{\boldsymbol{\sigma}} = \text{vecu}(\hat{\Sigma}), \quad \tilde{\boldsymbol{\sigma}}(\lambda) = \text{vecu}(\tilde{\Sigma}(\lambda)),$$

where the  $\text{vecu}$  operator was defined in (2.60). For a given class  $\{\tilde{\Sigma}(\lambda) : \lambda \geq 0\}$ , the risk associated with  $\lambda$  is defined as

$$\mathcal{R}(\lambda) := \mathbb{E}[\|\tilde{\boldsymbol{\sigma}}(\lambda) - \boldsymbol{\sigma}\|_2^2] = \mathbb{E} \left[ \sum_{i < j} (\tilde{\sigma}_{ij}(\lambda) - \sigma_{ij})^2 \right]. \quad (6.10)$$

We refer to  $\mathcal{R}(\lambda)$  as the Frobenius risk. The minimiser

$$\lambda^* := \arg \min_{\lambda} \mathcal{R}(\lambda)$$

corresponds to the regularisation parameter which gives the TDPM estimate closest to the true TPDM in terms of the mean-square error. Of course, the true TPDM is always unknown in practice, so the risk  $\mathcal{R}(\lambda)$  cannot be evaluated or minimised directly. We call  $\lambda^*$  the oracle parameter to signify that it is the value that would be chosen by an oracle with knowledge of the underlying true TPDM. Our goal is to devise a statistical procedure for estimating  $\lambda^*$ .

The task of estimating  $\lambda^*$  becomes much simpler if we are privy to additional information about the data-generating process. For example, Fix et al. (2021) infer a reasonable soft-thresholding parameter  $\lambda = \beta_2$  in (2.65) by exploiting prior information about the spatial configuration and the spatial extent of the modelled phenomenon. Similarly, in supervised learning settings where an objective loss function and labelled training data are available, one may resort to standard hyperparameter tuning procedures such as cross validation. We study the problem in its most general, challenging form, where no additional structure/information is available.

For covariance matrices, a standard strategy for selecting the regularisation parameter is to minimise an empirical estimate of  $\mathcal{R}$ , i.e. an approximation of the risk function constructed from the data (Yi and Zou 2013). Unfortunately, this strategy does not transfer easily to the TPDM context. Upon noting that

$$(\tilde{\sigma}_{ij}(\lambda) - \sigma_{ij})^2 = (\tilde{\sigma}_{ij}(\lambda) - \hat{\sigma}_{ij})^2 + 2(\tilde{\sigma}_{ij}(\lambda) - \sigma_{ij})(\hat{\sigma}_{ij}(\lambda) - \sigma_{ij}) - (\hat{\sigma}_{ij} - \sigma_{ij})^2$$

the risk function (6.10) can be equivalently expressed as

$$\mathcal{R}(\lambda) = \mathbb{E}[\|\tilde{\boldsymbol{\sigma}}(\lambda) - \hat{\boldsymbol{\sigma}}\|_2^2] + 2 \sum_{i < j} \mathbb{E}[(\tilde{\sigma}_{ij}(\lambda) - \sigma_{ij})(\hat{\sigma}_{ij} - \sigma_{ij})] - \mathbb{E}[\|\hat{\boldsymbol{\sigma}} - \boldsymbol{\sigma}\|_2^2] \quad (6.11)$$

These three terms are called apparent error, optimism, and constant (Yi and Zou 2013). The apparent error acts as a penalty against departing too far away from the empirical TPDM. This term can be estimated using the unbiased estimator  $\|\tilde{\boldsymbol{\sigma}}(\lambda) - \hat{\boldsymbol{\sigma}}\|_2^2$ . The con-

stant term is irrelevant and can be ignored for the risk minimization as it does not depend on  $\lambda$ . The fundamental issue stems from the optimism term. For covariance matrices, the empirical estimator is unbiased and the summand may be replaced with  $\text{Cov}(\tilde{\sigma}_{ij}(\lambda), \hat{\sigma}_{ij})$ , which may be estimated via bootstrapping (Fang et al. 2016). This approach cannot be replicated for TPDMs, because the empirical estimator is biased. This impediment prevented us from finding a solution to the general problem of tuning arbitrary regularised TPDMs. However, we were able to devise a procedure for optimising Ledoit-Wolf estimators by taking a completely different approach to the one sketched above.

### 6.3.2. The optimal Ledoit-Wolf shrinkage intensity

Ledoit and Wolf (2003) provide a formula for the asymptotically optimal Ledoit-Wolf shrinkage intensity for covariance matrices. Inspired by their approach, we are able to obtain an analogous result for TPDMs. Suppose  $\mathbf{X}_1, \mathbf{X}_2, \dots$  is a sequence of independent copies of  $\mathbf{X}$  and let  $\tilde{\Sigma}(\lambda)$  denote a Ledoit-Wolf estimator of the TPDM. For any  $\lambda \in [0, 1]$ , the associated Frobenius risk is

$$\begin{aligned}\mathcal{R}(\lambda) &= \mathbb{E}[\|(1-\lambda)\hat{\boldsymbol{\sigma}} - \boldsymbol{\sigma}\|_2^2] \\ &= \sum_{i < j} \mathbb{E}[((1-\lambda)\hat{\sigma}_{ij} - \sigma_{ij})^2] \\ &= \sum_{i < j} \left\{ (1-\lambda)^2 \mathbb{E}[\hat{\sigma}_{ij}^2] - 2(1-\lambda)\sigma_{ij}\mathbb{E}[\hat{\sigma}_{ij}] + \sigma_{ij}^2 \right\}.\end{aligned}$$

The first-order optimality condition gives

$$\mathcal{R}'(\lambda) = 0 \implies \sum_{i < j} 2(\lambda-1)\mathbb{E}[\hat{\sigma}_{ij}^2] + 2\sigma_{ij}\mathbb{E}[\hat{\sigma}_{ij}] = 0 \implies \lambda^* := \frac{\sum_{i < j} \left\{ \mathbb{E}[\hat{\sigma}_{ij}^2] - \sigma_{ij}\mathbb{E}[\hat{\sigma}_{ij}] \right\}}{\mathbb{E}[\|\hat{\boldsymbol{\sigma}}\|_2^2]}.$$

It is simple to check that  $\mathcal{R}''(\lambda) = \sum_{i < j} 2\mathbb{E}[\hat{\sigma}_{ij}^2] > 0$ , confirming that  $\lambda^*$  is indeed the risk minimiser. The formula for  $\lambda^*$  still depends on the true TPDM, so this is not helpful by itself. However, we may recognise the numerator of  $\lambda^*$  as being related to the variance of  $\hat{\sigma}_{ij}$  and recall from Proposition 2.5 that the asymptotic variance of  $\sqrt{k}\hat{\sigma}_{ij}$  is  $\nu_{ij}^2$ . For clarity, we now include dependence on the sample size  $n$  explicitly. Assume the conditions

of Proposition 2.5 hold and also that for all  $i \neq j$  there exists a constant  $C_{ij}$  such that

$$\mathbb{E}[\hat{\sigma}_{ij}(n)] - \sigma_{ij} = \frac{C_{ij}}{k(n)} + \mathcal{O}(k(n)^{-2}), \quad (6.12)$$

so that  $k(n)(\mathbb{E}[\hat{\sigma}_{ij}(n)] - \sigma_{ij}) \rightarrow C_{ij}$  as  $n \rightarrow \infty$ . The condition (6.12) ensures the rate of convergence of  $\hat{\sigma}_{ij}$  to  $\sigma_{ij}$  is sufficiently rapid. Then we have that

$$\begin{aligned} & \lim_{n \rightarrow \infty} k(n)\mathbb{E}[\|\hat{\boldsymbol{\sigma}}(n)\|_2^2]\lambda^*(n) \\ &= \lim_{n \rightarrow \infty} \sum_{i < j} k(n) \left\{ \mathbb{E}[\hat{\sigma}_{ij}(n)^2] - \sigma_{ij}\mathbb{E}[\hat{\sigma}_{ij}(n)] \right\} \\ &= \lim_{n \rightarrow \infty} \sum_{i < j} k(n) \left\{ \mathbb{E}[\hat{\sigma}_{ij}(n)^2] - \mathbb{E}[\hat{\sigma}_{ij}(n)]^2 \right\} + \lim_{n \rightarrow \infty} \sum_{i < j} k(n) \left\{ \mathbb{E}[\hat{\sigma}_{ij}(n)]^2 - \sigma_{ij}\mathbb{E}[\hat{\sigma}_{ij}(n)] \right\} \\ &= \lim_{n \rightarrow \infty} \sum_{i < j} k(n)\text{Var}(\hat{\sigma}_{ij}(n)) + \lim_{n \rightarrow \infty} \sum_{i < j} \mathbb{E}[\hat{\sigma}_{ij}(n)]k(n) \{ \mathbb{E}[\hat{\sigma}_{ij}(n)] - \sigma_{ij} \} \\ &= \sum_{i < j} (\nu_{ij}^2 + \sigma_{ij}C_{ij}). \end{aligned}$$

Assuming (as we are) that the bias of the TPDM is non-negative, then  $C_{ij} \geq 0$ . Then, noting that  $\|\hat{\boldsymbol{\sigma}}(n)\|_2^2 > 0$  almost surely, it follows that  $\lambda^*(n) > 0$  for sufficiently large  $n$ . The above result gives that, asymptotically, the optimal shrinkage behaves as a constant divided by  $k(n)\mathbb{E}[\|\hat{\boldsymbol{\sigma}}(n)\|_2^2]$ . As the asymptotic constant is unknown, we eliminate it by taking ratios at different values of  $n$ . Given a fixed proportion  $\kappa \in (0, 1)$ , it is easy to see that

$$\lim_{n \rightarrow \infty} k(n)\mathbb{E}[\|\hat{\boldsymbol{\sigma}}(n)\|_2^2]\lambda^*(n) = \sum_{i < j} (\nu_{ij}^2 + c_{ij}) = \lim_{n \rightarrow \infty} k(\lfloor \kappa n \rfloor)\mathbb{E}[\|\hat{\boldsymbol{\sigma}}(\lfloor \kappa n \rfloor)\|_2^2]\lambda^*(\lfloor \kappa n \rfloor).$$

and the algebra of limits then yields

$$\lim_{n \rightarrow \infty} \frac{k(n)\mathbb{E}[\|\hat{\boldsymbol{\sigma}}(n)\|_2^2]\lambda^*(n)}{k(\lfloor \kappa n \rfloor)\mathbb{E}[\|\hat{\boldsymbol{\sigma}}(\lfloor \kappa n \rfloor)\|_2^2]\lambda^*(\lfloor \kappa n \rfloor)} = 1.$$

For sufficiently large  $n$  all quantities in the denominator are non-zero, so the limit is well-defined. Moreover it holds that

$$\frac{\lambda^*(\lfloor \kappa n \rfloor)}{\lambda^*(n)} \approx \frac{k(n)\mathbb{E}[\|\hat{\boldsymbol{\sigma}}(n)\|_2^2]}{k(\lfloor \kappa n \rfloor)\mathbb{E}[\|\hat{\boldsymbol{\sigma}}(\lfloor \kappa n \rfloor)\|_2^2]} =: \zeta(n; \kappa).$$

In other words, the optimal shrinkage intensities at sample sizes  $n$  and  $\lfloor \kappa n \rfloor$  are  $\lambda^*(n)$  and  $\zeta(n; \kappa) \lambda^*(n)$ , respectively. The ratio  $\zeta(n; \kappa)$  describes the rate of decay of the optimal shrinkage as more data becomes available. It is easy to see that  $\zeta(n, \kappa) \rightarrow 1$  when  $\kappa \rightarrow 1$ . Additionally  $\zeta(n; \kappa) \rightarrow k(n)/k(\lfloor \kappa n \rfloor)$  as  $n \rightarrow \infty$  due to consistency of  $\hat{\boldsymbol{\sigma}}$ . This limit will usually be some function of  $\kappa$ , e.g. choosing  $k(n) \propto \sqrt{n}$  gives  $\zeta(n; \kappa) \rightarrow \kappa^{-1/2}$  as  $n \rightarrow \infty$ . Crucially,  $\zeta(n; \kappa)$  is defined in terms of quantities that are known or may be estimated without bias. Let  $\hat{\zeta} = \hat{\zeta}(n; \kappa)$  be an estimate of  $\zeta = \zeta(n; \kappa)$  to be defined later.

Knowing its asymptotic rate of decay is not sufficient to deduce  $\lambda^*(n)$ . The missing piece of information is its magnitude. Consider the empirical TPDMs  $\hat{\Sigma}(n)$  and  $\hat{\Sigma}(\lfloor \kappa n \rfloor)$  based on samples of sizes  $n$  and  $\lfloor \kappa n \rfloor$ , respectively. If these matrices are very similar (resp. different), then intuitively the absolute difference between  $\lambda^*(n)$  and  $\lambda^*(\lfloor \kappa n \rfloor)$  should be small (resp. large). Now, our large sample theory tells us that our best estimates of  $\boldsymbol{\sigma}$  are of the form  $(1 - \lambda^*(n))\hat{\boldsymbol{\sigma}}(n)$  and  $(1 - \hat{\zeta}\lambda^*(n))\hat{\boldsymbol{\sigma}}(\lfloor \kappa n \rfloor)$ . This hints at estimating  $\lambda^*(n)$  by minimising the discrepancy between these two estimates:

$$\hat{\lambda}(n) := \arg \min_{\lambda \in [0, \min(1, \zeta^{-1})]} \left\| (1 - \lambda)\hat{\boldsymbol{\sigma}}(n) - (1 - \hat{\zeta}\lambda)\hat{\boldsymbol{\sigma}}(\lfloor \kappa n \rfloor) \right\|_2^2. \quad (6.13)$$

### 6.3.3. Practical and statistical considerations

Having outlined the general approach, we fill in some missing details regarding inference. First we address estimation of  $\zeta$ . To estimate  $\mathbb{E}[\|\hat{\boldsymbol{\sigma}}(n)\|_2^2]$  and  $\mathbb{E}[\|\hat{\boldsymbol{\sigma}}(\lfloor \kappa n \rfloor)\|_2^2]$ , we produce a collection of bootstrapped samples  $\mathcal{X}_n^{(b)} = \{\mathbf{X}_1^{(b)}, \dots, \mathbf{X}_n^{(b)}\}$  and  $\mathcal{X}_{\lfloor \kappa n \rfloor}^{(b)} = \{\mathbf{X}_1^{(b)}, \dots, \mathbf{X}_{\lfloor \kappa n \rfloor}^{(b)}\}$  from  $\mathbf{X}_1, \dots, \mathbf{X}_n$ , for  $b = 1, \dots, B$ . Next, we compute empirical TPDMs  $\hat{\Sigma}^{(1)}(n), \dots, \hat{\Sigma}^{(B)}(n)$  and  $\hat{\Sigma}^{(1)}(\lfloor \kappa n \rfloor), \dots, \hat{\Sigma}^{(B)}(\lfloor \kappa n \rfloor)$  using the  $k(n)$  and  $k(\lfloor \kappa n \rfloor)$  largest observations from  $\mathcal{X}_n^{(1)}, \dots, \mathcal{X}_n^{(B)}$  and  $\mathcal{X}_{\lfloor \kappa n \rfloor}^{(1)}, \dots, \mathcal{X}_{\lfloor \kappa n \rfloor}^{(B)}$ , respectively. An estimate of  $\zeta$  is then given by

$$\hat{\zeta}(n; \kappa) := \frac{k(n) \sum_{b=1}^B \|\hat{\boldsymbol{\sigma}}^{(b)}(n)\|_2^2}{k(\lfloor \kappa n \rfloor) \sum_{b=1}^B \|\hat{\boldsymbol{\sigma}}^{(b)}(\lfloor \kappa n \rfloor)\|_2^2}. \quad (6.14)$$

The bootstrapped empirical TPDMs can be reused in the final step, so that instead of (6.13), we actually set

$$\hat{\lambda}(n) := \arg \min_{\lambda \in [0, \zeta^{-1}]} \left\| \frac{1}{B} \sum_{b=1}^B \left[ (1 - \lambda)\hat{\boldsymbol{\sigma}}^{(b)}(n) - (1 - \hat{\zeta}\lambda)\hat{\boldsymbol{\sigma}}^{(b)}(\lfloor \kappa n \rfloor) \right] \right\|_2^2. \quad (6.15)$$

Bootstrapping is intended to reduce noise in the estimation of  $\zeta$  and  $\lambda^*$ , but it is not fundamental to our procedure. The only place where sub-sampling is mandatory is to obtain an empirical TPDM based on  $\lfloor \kappa n \rfloor$  observations.

For fixed  $n$ , selection of  $\kappa$  is subject to the familiar bias-variance trade-off. If  $\kappa$  is small, then  $\lfloor \kappa n \rfloor$  may be too small for the underlying asymptotic approximation to be valid. If  $\kappa$  is very close to one, then the estimate  $\hat{\lambda}$  will be quite sensitive to small changes in  $\hat{\zeta}$ . This is borne out in our simulation experiments. A formal analysis of how to select  $\kappa$  is beyond the scope of our investigation.

## 6.4. Simulation experiments

### 6.4.1. Symmetric logistic

We start by testing our regularised TPDM estimators in the simplest setting, where the data are generated from the symmetric logistic model. Suppose  $\mathbf{X} = (X_1, \dots, X_d) \in \text{RV}_+^d(2)$  follows a symmetric logistic model with dependence parameter  $\gamma \in (0, 1]$ . Then the true TPDM is of the form

$$\sigma_{ij} = \begin{cases} 1, & i = j, \\ \sigma, & i \neq j, \end{cases}$$

where  $\sigma = \sigma(\gamma)$  is some constant – see Example 2.5. Recall from Figure 2.5 that the empirical TPDM overestimates  $\sigma$  when  $\gamma \approx 1$ . Since all off-diagonal entries of the TPDM are equal, the symmetric logistic model is one of the rare cases where penalising all entries equally is actually desirable. Assume for simplicity that  $\hat{\boldsymbol{\sigma}}(n) = \hat{\sigma}(n)\mathbf{1}_{\binom{d}{2}}$  for some scalar  $\hat{\sigma}(n) > \sigma$ . It is straightforward to show that the optimal Ledoit-Wolf shrinkage intensity is  $\lambda_{\text{LW}(n)}^* = 1 - \sigma/\hat{\sigma}(n)$ , since then

$$\tilde{\boldsymbol{\sigma}}(\lambda_{\text{LW}}^*(n)) = [1 - (1 - \lambda_{\text{LW}}^*(n))] \hat{\boldsymbol{\sigma}} = \frac{\sigma}{\hat{\sigma}(n)} \hat{\sigma}(n) \mathbf{1}_{\binom{d}{2}} = \boldsymbol{\sigma}.$$

Similarly, the optimal thresholds under soft-thresholding and adaptive lasso are

$$\begin{aligned}\lambda_S^*(n) &= \hat{\sigma}(n) - \sigma = \hat{\sigma}(n)\lambda_{\text{LW}}^*, \\ \lambda_{\text{AL}}^*(n) &= [\hat{\sigma}(n)^\eta(\hat{\sigma}(n) - \sigma)]^{1/(\eta+1)} = \hat{\sigma}(n)[\lambda_{\text{LW}}^*(n)]^{1/(\eta+1)},\end{aligned}$$

respectively. Note that  $\lambda_S^*$  and  $\lambda_{\text{AL}}^*$  are expressed in terms of  $\lambda_{\text{LW}}^*$ . Thus, finding a good estimate for the Ledoit-Wolf shrinkage is sufficient to obtain reasonable estimates for the other regularisation parameters. On this basis, we allow ourselves to focus exclusively on testing the Ledoit-Wolf estimator.

The setup for our experiment is as follows. We generate  $n$  independent observations of  $\mathbf{X} \in \text{RV}_+^3(2)$  from a symmetric logistic model with dependence parameter  $\gamma$ . The intermediate sequence is set as  $k(n) = \lfloor 4\sqrt{n} \rfloor$ . This satisfies the rate conditions (2.42) and gives a reasonable number of threshold exceedances in practice. The ratio  $\zeta(n; \kappa)$  is estimated using (6.14) with  $B = 10$  and  $\hat{\lambda}$  computed via (6.15) using the `optim()` function in R. Finally, we also compute the optimal shrinkage that minimises the Frobenius loss between the bootstrapped empirical TPDMs and the true TPDM; when averaged over many simulations these provide a good approximation to  $\lambda^*$ . This experimental procedure is repeated for a sequence of sample sizes  $5 \times 10^3 \leq n \leq 2 \times 10^5$ , proportions  $\kappa \in \{0.5, 0.75, 0.9\}$ , and true dependence parameters  $\gamma \in \{0.5, 0.8, 0.9\}$ . The corresponding dependence strengths are  $\sigma(0.5) = 0.85$  (strong dependence),  $\sigma(0.8) = 0.48$  (moderately weak dependence) and  $\sigma(0.9) = 0.27$  (weak dependence). Results are based on 100 repetitions for each combination of parameters.

The left plot in Figure 6.4 shows the average Frobenius loss  $\mathcal{R}(0) = \|\boldsymbol{\sigma} - \hat{\boldsymbol{\sigma}}(n)\|_2^2$  as a function of  $n$  for each value of  $\gamma$ . This summarises the magnitude of the bias of the empirical TPDM; an error  $\mathcal{R}(0) = \epsilon$  is equivalent to overestimating each entry of  $\boldsymbol{\sigma}$  by  $\epsilon/\sqrt{3}$ . As expected, the magnitude of the bias is decreasing in  $n$  and increasing in  $\gamma$ . However, we note that even at  $n = 200,000$  there is non-negligible bias present, showing that bias-corrected estimation has a role to play even when  $n$  is large. This is an important point, considering that our procedure relies on large sample approximations. The right-hand plot shows the mean of  $k(n)\mathbb{E}[\|\hat{\boldsymbol{\sigma}}(n)\|_2^2]\lambda^*(n)$  against  $n$ . Our tuning procedure requires that this quantity is approximately constant beyond  $\lfloor \kappa n \rfloor$ . For  $\gamma = 0.5$ , the convergence is rapid, so we expect our procedure will perform well even when  $n$  is small. When  $\gamma = 0.8$ , the

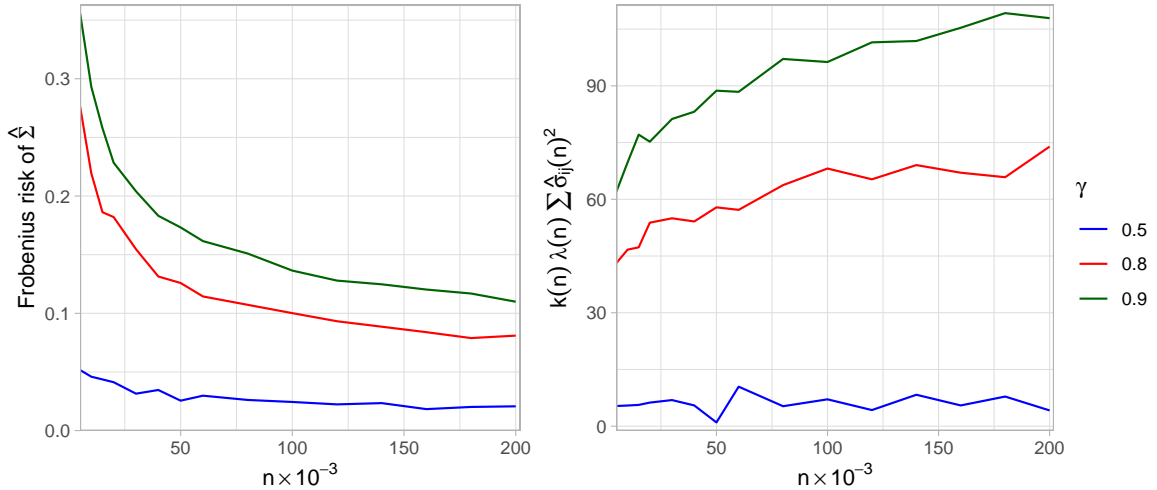


Figure 6.4.: Exploratory plots for understanding the performance of the Ledoit-Wolf TPDM in the symmetric logistic experiment. Left: the Frobenius risk  $\mathcal{R}(0)$  associated with the empirical TPDM  $\hat{\Sigma}$  as a function of  $n$ . Right:  $k(n)\lambda(n)\sum\hat{\delta}_{ij}(n)^2$  as a function of  $n$ .

quantity approximately levels off at approximately  $n = 100,000$ , while for  $\gamma = 0.9$  it is still increasing at  $n = 200,000$ .

Figure 6.5 compares the mean estimates  $\hat{\lambda}(n)$  for different values of  $\kappa$  (dashed/dotted lines) against the oracle value  $\lambda^*(n)$  (solid line). The solid lines represent the true values of the optimal shrinkage parameter  $\lambda(n)$ . For  $\gamma = 0.5$ , the optimal shrinkage is close to zero and the estimates  $\hat{\lambda}(n)$  reflect this, even when  $n$  is small. As predicted, the selection procedure performs well when  $\gamma = 0.8$  provided the sample size is sufficiently large. In particular, we obtain good estimates when  $n \geq 150,000$  (i.e.  $\lfloor \kappa n \rfloor \geq 75,000$ ), which aligns reasonably closely with our earlier comments concerning the convergence in Figure 6.4. Our tuning procedure does not work particularly well in the weakest dependence scenario ( $\gamma = 0.9$ ). While the intensities are sub-optimal, conservative estimates that err towards the empirical TPDM are probably preferable to over-shrinking. Our theoretical analysis provides assurance that these estimates would improve eventually as  $n$  increases. The plot also shows the influence of the tuning parameter  $\kappa$ . When  $\kappa$  is close to one the estimates  $\hat{\lambda}(n)$  have high uncertainty, while conservative choices of  $\kappa$  yield more stable but (negatively) biased estimates.

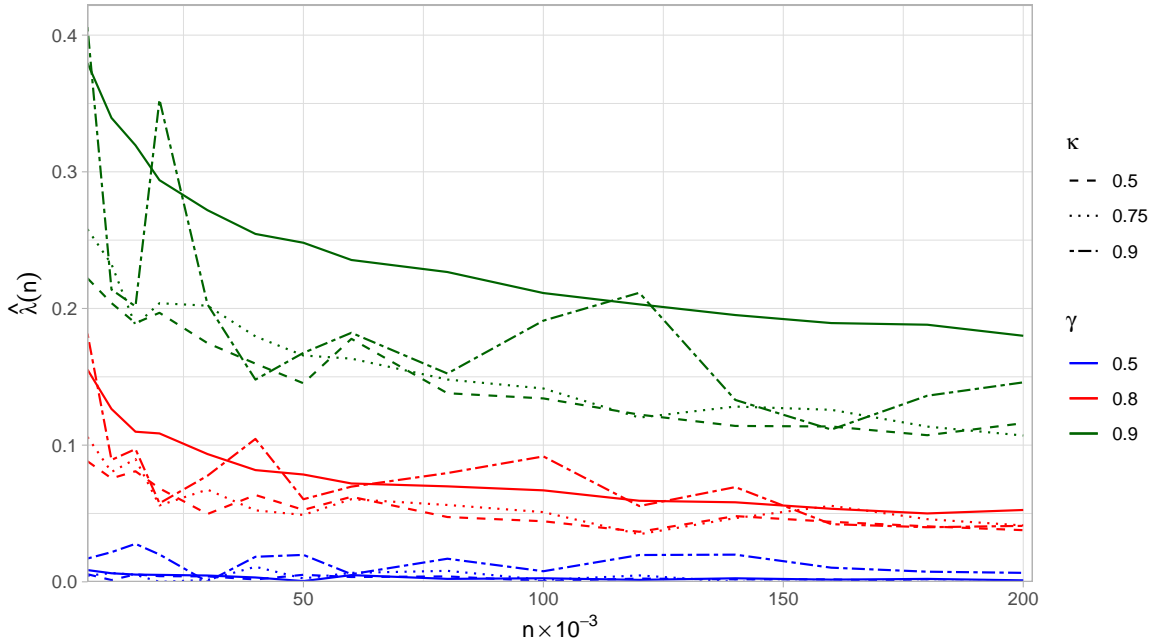


Figure 6.5.: The optimal Ledoit-Wolf shrinkage intensity  $\lambda^*(n)$  (solid lines) and the mean estimates  $\hat{\lambda}(n)$  obtained from our tuning procedure (dashed/dotted lines) as a function of  $n$  for various values of  $\gamma$  and  $\kappa$ .

#### 6.4.2. EVA (2023) Data Challenge 4

Recall from Chapter 5 that our submission to Challenge 4 in the EVA (2023) Data Challenge utilised completely positive (CP) decompositions of the empirical TPDMs corresponding to five separate clusters. It transpired that our approach overestimated the true event probabilities of interest. Subsequent investigation revealed that we overestimated dependence. This was especially true in the first, fourth and fifth clusters, where dependence is weak (Rohrbeck et al. 2023), leading us to suspect that the bias issue might be the root cause. In our post-hoc analysis (Section 5.5.3.4), we proposed a remedy using sparse simplex projections. The intention and effect of this was to spread the mass of the empirical angular measure towards/onto the simplex boundary, thereby artificially ‘weakening’ the dependence. This approach showed great promise, but required wholesale changes to our overall methodology. Armed with the Ledoit-Wolf TPDM estimator, we are now in a position to propose yet another strategy. The new approach follows our original methodology exactly, except we replace the empirical TPDM with the Ledoit-Wolf counterpart. The substitution is seamless due to complete positivity of  $\tilde{\Sigma}$  (Proposition 6.1).

Visual representations of the five clusters' empirical TPDMs are provided in Figure 6.6

(left). From Table 5.2 in Chapter 5 we know that the median values of  $\{\hat{\sigma}_{ij} : i \neq j\}$  in each cluster are 0.33, 0.68, 0.67, 0.33, and 0.50. Crucially, within each cluster the range of  $\{\hat{\sigma}_{ij} : i \neq j\}$  is at most 0.15, implying that the within-cluster pairwise dependence strengths are relatively equal. In such cases, the Ledoit-Wolf estimator is adequate. If this were not the case, more flexible regularisers such as adaptive lasso would be required. Let  $\hat{\Sigma}^{(1)}, \dots, \hat{\Sigma}^{(5)}$  denote the clusters' empirical TPDMs based on the  $k$  largest observations among the  $n = 10^4$  samples provided. We estimate shrinkage parameters  $\hat{\lambda}^{(1)}, \dots, \hat{\lambda}^{(5)}$  for each cluster using our selection procedure with  $k(n) = \lfloor k\sqrt{n}/100 \rfloor$ ,  $\kappa = 0.75$  and  $B = 10$ . The remaining steps follow Section 5.5.3.2: we apply the CP-factorisation algorithm of Kiriliouk and Zhou (2022) to each Ledoit-Wolf TPDM and compute probability estimates using the formula (5.11).

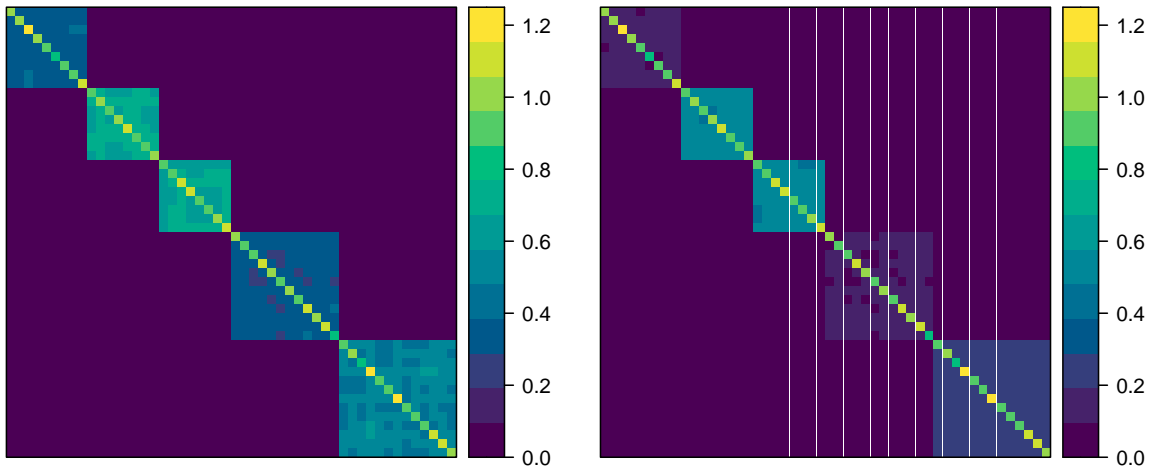


Figure 6.6.: The empirical TPDM  $\hat{\Sigma} = \text{diag}(\hat{\Sigma}^{(1)}, \dots, \hat{\Sigma}^{(5)})$  (left) and the Ledoit-Wolf TPDM  $\tilde{\Sigma} = \text{diag}(\tilde{\Sigma}^{(1)}(\hat{\lambda}_1), \dots, \tilde{\Sigma}^{(5)}(\hat{\lambda}_5))$  for the EVA (2023) Data Challenge based on  $k = 250$ .

Figure 6.7 reveals the amount of each shrinkage for each cluster for  $0.02 \leq k/n \leq 0.07$ . As expected, clusters 1 and 4 are penalised the most and clusters 2 and 3 the least. The shrinkage intensities are sensitive to the choice of  $k$ . Counterintuitively the parameters  $\hat{\lambda}^{(1)}, \dots, \hat{\lambda}^{(5)}$  seem to increase as  $k$  decreases, despite the fact that the bias in the TPDM is usually smaller at higher thresholds (Fix et al. 2021). This warrants further investigation in future. For the present study, we focus on the case where  $k = 250$ , since this is the number of threshold exceedances used in our competition entry. The corresponding Ledoit-Wolf TPDM estimate is shown in Figure 6.6 (right). Comparing against the empirical TPDM on the left, there is a dramatic reduction in the entries in clusters 1 and 4. Consequently, this

matrix is presumably closer to the (unknown) true TPDM than the raw estimate. The final probability estimates in Figure 6.8 support this conclusion. In each panel, the horizontal dashed line shows the true value of the probabilities  $p_1$  (left) and  $p_2$  (right). The grey line corresponds to our original method based on CP-decompositions of the empirical TPDM. It drastically overestimates the event probabilities. The green and blue lines result from fitting a max-linear model using the  $k$  largest angles defined via self-normalisation and Euclidean projections, respectively; these methods were described in detail in Section 5.5. The red line is derived from our new procedure based on CP-decompositions of Ledoit-Wolf TPDMs. At  $k = 250$ , it gives a near-perfect estimate of  $p_1$  and a very good estimate of  $p_2$ . When  $k$  is large the probability estimates are too large because the shrinkage intensities are too small, especially in the first, fourth and fifth clusters (see Figure 6.7).

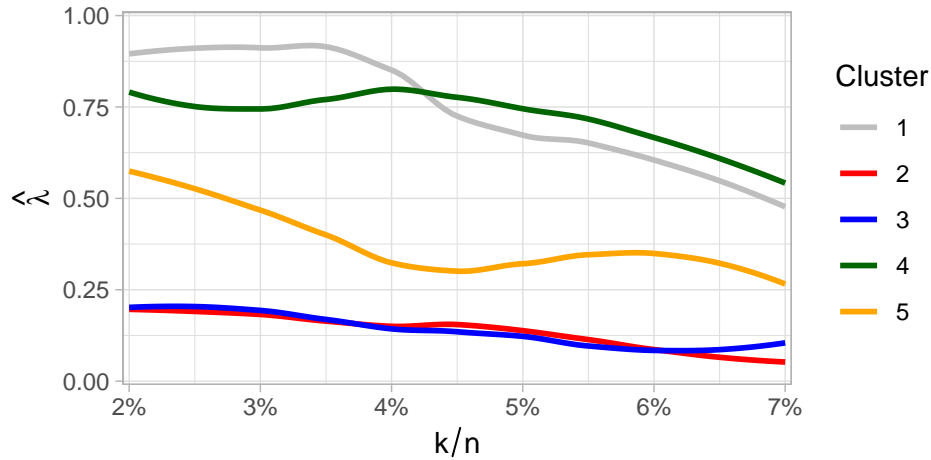


Figure 6.7.: Estimated shrinkage intensities  $\hat{\lambda}^{(1)}, \dots, \hat{\lambda}^{(5)}$  associated with the clusters' empirical TPDMs  $\hat{\Sigma}^{(1)}, \dots, \hat{\Sigma}^{(5)}$  for the EVA (2023) Data Challenge.

#### 6.4.3. Extremal SAR model

Our final experiment emulates the simulation study in Fix et al. (2021). The goal is to estimate the dependence parameter  $\rho$  of the extremal SAR model (Section 2.5.2), a sub-case of the max-linear model used for spatial extremes. This experiment will reinforce the effectiveness of our tuning procedure, while also highlighting the limitations of Ledoit-Wolf shrinkage compared to the more flexible thresholding estimators. Suppose  $\mathbf{X}$  is as described in Section 2.5.2, with (known) neighbourhood matrix  $W$  and (unknown) dependence parameter  $\rho$ . Following Fix et al. (2021),  $\rho$  is to be estimated by minimising the

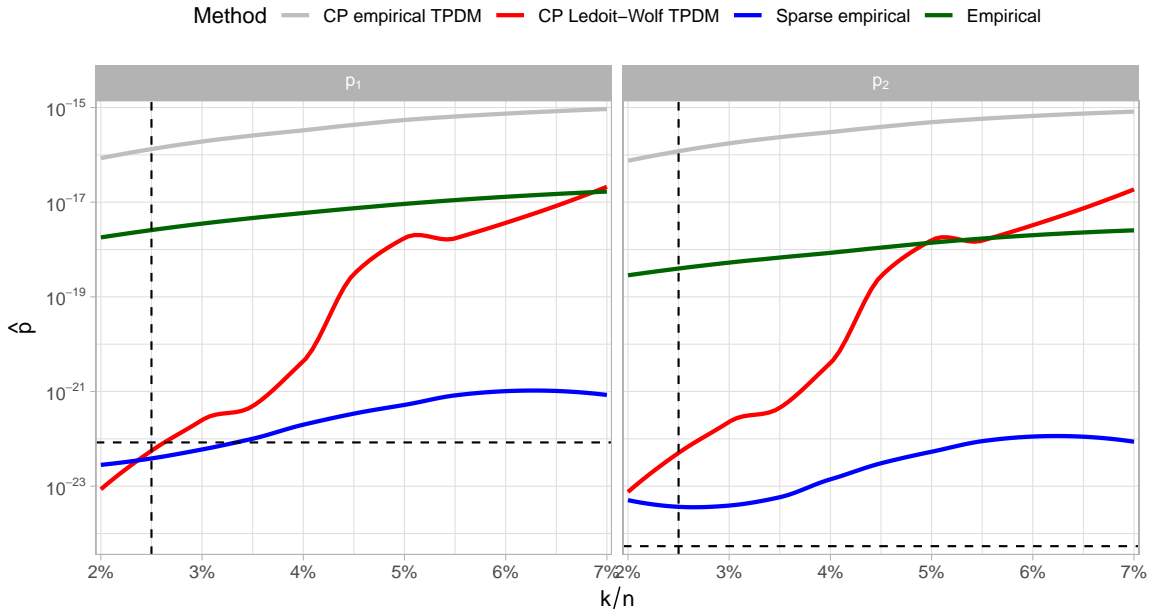


Figure 6.8.: Probability estimates for the EVA (2023) Data Challenge from all four proposed methods. The true probabilities  $p_1$  (left) and  $p_2$  (right) are indicated by the horizontal dashed lines. The methodologies associated with the grey, blue and green lines are described in Chapter 5. The red line shows the results based on CP decompositions of the Ledoit-Wolf estimates. The vertical dashed line is at  $k = 250$ , the number of threshold exceedances used in our competition entry.

Frobenius difference between the model TPDM (viewed as a function of  $\rho$ ) and a bias-corrected estimate of the TPDM. This can be posed as a hierarchical/bilevel optimisation problem, whereby the upper-level objective function (estimating  $\rho$ ) depends on the solution to a lower-level problem (estimating  $\Sigma$ ). Specifically, we define

$$\hat{\rho} := \arg \min_{\varrho} \hat{\mathcal{L}}(\varrho), \quad \hat{\mathcal{L}}(\varrho) := \|\boldsymbol{\sigma}(\varrho) - \tilde{\boldsymbol{\sigma}}(\hat{\lambda})\|_2^2. \quad (6.16)$$

The loss function  $\mathcal{L}(\varrho)$  depends on the estimate  $\tilde{\boldsymbol{\sigma}}(\hat{\lambda})$  of  $\boldsymbol{\sigma}$ , so accurate estimation of the TPDM is critical. If  $\tilde{\boldsymbol{\sigma}}(\hat{\lambda})$  is not representative of  $\boldsymbol{\sigma}$ , then the loss may not be informative for  $\rho$ . In Fix et al. (2021),  $\tilde{\boldsymbol{\sigma}}$  represents the soft-thresholded estimator and  $\hat{\lambda}$  is obtained by fitting a non-linear model relating the pairwise dependence strengths and inter-site distances. The soft-thresholded estimator achieves a reasonable fit – see Figure 3 (right) in Fix et al. (2021).

Our simulation setup follows Section 4.2.1 in Fix et al. (2021) with some minor adjustments. We consider  $d = 36$  sites arranged in an  $6 \times 6$  grid and generate  $n$  independent realisations

of a  $6 \times 6$  spatial field from an extremal SAR model with dependence parameter  $\rho = 0.15$ . With this parameter choice, dependence vanishes at a distance of approximately 4 units. The empirical TPDM  $\hat{\Sigma}$  is computed using the  $k(n) = \lfloor 4\sqrt{n} \rfloor$  largest observations. Next, we use the true TPDM (Example 2.7) to compute  $\lambda^*$  for the soft-threshold, Ledoit-Wolf, and adaptive lasso ( $\eta = 2$ ) TPDMs. From each oracle TPDM  $\tilde{\sigma}(\lambda^*)$ , we compute an estimate of  $\rho$  by solving (6.16). These values represent the estimates of  $\rho$  that would be found by an oracle who is constrained to a particular type of regularisation. Finally, we repeat the same steps using regularisation parameters selected using our data-driven procedure (for Ledoit-Wolf with  $\kappa = 0.75$  and  $B = 5$ ) or the spatial method of Fix et al. (2021) (for soft-threshold). Currently there are no available methods for tuning  $\lambda$  and/or  $\eta$  for the adaptive lasso. The procedure is repeated 100 times at a sequence of sample sizes varying between  $10^4 \leq n \leq 2 \times 10^5$ .

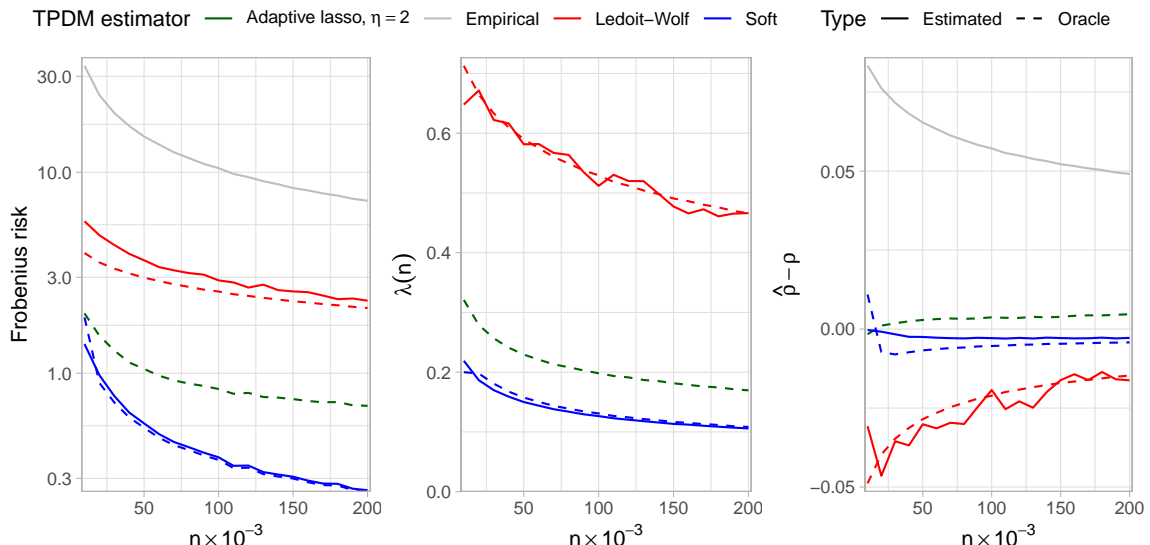


Figure 6.9.: Results for our experiments based on the extremal SAR model. Left: the mean Frobenius error of the oracle and estimated TPDMs. Middle: the values of the regularisation parameter selected by the oracle or tuning procedure. Right: the empirical bias of the estimates of  $\rho$  computed by solving (6.16).

The left-hand plot in Figure 6.9 shows how the Frobenius loss (on a log scale) varies with  $n$  for each oracle/estimated TPDM. The colours correspond to the regularisation method used; the line type indicates whether the regularisation parameter is estimated or an oracle based on knowledge of the true TPDM. By definition, the risk attained by the oracle losses provides a lower bound on the risk that can be attained for a given estimator class. If the solid line lies close to the oracle loss, then  $\lambda$  has been well selected. In this respect,

the blue lines show that the soft-threshold tuning procedure of Fix et al. (2021) performs very well, with the usual caveat that it makes use of extra information to do so. Moreover, the soft-thresholded estimates are very close to the true TPDM in Frobenius norm. For Ledoit-Wolf (red) our data-driven procedure gives reasonably good results provided  $n$  is large. The Ledoit-Wolf estimates are worse than the soft-threshold or adaptive lasso, but are still far superior to the empirical estimate. The middle plot provides more insight into the selected values of  $\lambda$ . The soft-threshold parameter is very close to the oracle value. Our shrinkage parameters also track the oracle quite closely, even for small  $n$ , though these small errors seem to translate into non-negligible errors in the overall Frobenius norm. The right-hand plot examines the empirical bias  $\hat{\rho} - \rho$  in the final estimates of the spatial dependence parameter. The empirical TPDM (grey) overestimates dependence and wildly overestimates  $\rho$ . The soft-threshold estimate is interesting, with the estimator of Fix et al. (2021) actually outperforming the oracle. This is not a contradiction: a smaller Frobenius loss does not guarantee a better estimate of  $\rho$ . Fix et al. (2021) found that their estimator exhibited a slight negative bias for  $\rho$ . Our results confirm this and provide additional insight into why this occurs. Since the oracle suffers the same issue, we can infer that the bias is due to misspecification (i.e. being restricted to the soft-thresholded TPDMs) rather than a deficiency of their tuning procedure. As predicted, the Ledoit-Wolf estimator performs comparatively poorly and generally underestimates  $\rho$ , especially when  $n$  is small. However, we reiterate that this is a shortcoming of using a restrictive shrinkage method and not due to our tuning procedure, since the oracle estimates (dashed line) are no better than our estimated (solid line). Adaptive lasso achieves comparable results to soft-thresholding, except the sign of the bias is reversed. There is scope for further improvement by varying the down-weighting hyperparameter  $\eta$ .

## 6.5. Conclusions and outlook

The main contributions of this chapter are to counteract the bias issue of the empirical TPDM by proposing two classes of bias-corrected estimators. The first class, based on thresholding, generalises the estimator proposed in Fix et al. (2021) and includes more flexible regularisers, such as the adaptive lasso. The second class employs linear shrinkage to reduce the bias. While the restrictive form of this estimator limits its applicability, a key

advantage is that it possesses nice mathematical properties that enable it to be used immediately in existing TPDM-based modelling frameworks. Moreover, we constructed a data-driven statistical procedure for selecting the associated hyperparameter. The procedure is underpinned by asymptotic approximations, but our simulation experiments demonstrate reasonable performance with finite sample sizes in a wide range of settings.

There is ample opportunity to develop these methods further. Establishing a general solution to the problem of data-driven tuning for regularised estimators would be a significant breakthrough. Until this achieved, one might consider ways of enhancing the flexibility of the Ledoit-Wolf estimator, e.g. is it possible to apply different levels of shrinkage to groups of similarly sized entries in  $\hat{\Sigma}$ ? Finally, one might take a broader perspective and consider alternative loss functions instead of the Frobenius risk. For example, if one is interested in applying the TPDM as part of a principal components analysis, a more appropriate criterion might be some measure of agreement between the principal eigenspaces of  $\Sigma$  and  $\tilde{\Sigma}(\lambda)$ , such as the  $K_p$  coefficient (Krzanowski 1979).

# 7. Conclusion

## 7.1. Summary

This thesis explored how the TPDM can be used to enhance our understanding and prediction of extreme events. Such events are of interest across a broad range of domains, such as climatology and finance. Accordingly, we worked in a general framework so that our methods are widely applicable. Our work reiterates the fact that the TPDM is a powerful and versatile tool in multivariate EVT. Specifically, our contributions include: a hypothesis test for detecting changing dependence in high dimensions; an exploration of the link between multivariate EVT and compositional data analysis and concrete examples where leveraging this connection reaps performance benefits; data-driven strategies for predicting extreme events using sparse projections and matrix factorisations; flexible TPDM estimators with reduced bias and a strategy for tuning them. Using our methods will enable practitioners to work in higher dimensions, enjoy reduced computation times, validate their assumptions, and obtain more accurate measures of risk. Cutting-edge performance was evidenced via simulation studies providing direct comparisons against current state-of-the-art as well as achieving a first-placed ranking in the third sub-challenge of the EVA (2023) Data Challenge. The contributions of each chapter are outlined in more detail below.

Chapter 3 introduced a test for the premise that extremal dependence is constant over time. This is a key assumption across multivariate EVT that may be violated due to climate change or new financial regulations. Previously, the only existing method for validating it has been the test of Drees (2023), which is limited to low dimensions for computational and theoretical reasons. Our main contribution was to develop an alternative procedure that is viable in high dimensions. To achieve this, we defined time-dependent extensions to the

TPDM: the local TPDM and integrated TPDM. By studying the asymptotic behaviour of their empirical estimators, we derived the asymptotic null distributions of two test statistics. These are fast to compute and critical values are readily available. Simulation studies examined our test's performance with realistic sample sizes under a range of dependence scenarios. Under the null, our test approximately attained its nominal Type I error rate; under alternatives, it was more powerful than Drees (2023), except in the very specific case described in Section 3.7. An application to Red Sea temperature extremes (Section 3.8) illustrated how our method can be used as an exploratory tool for understanding the effects of climate change and as a preliminary step to determine whether stationary methods are adequate.

Inference in multivariate EVT is generally based on the  $k$  largest pseudo-angles, points lying on the simplex whose (limiting) distribution characterises extremal dependence. Chapter 4 explored ways in which tools from compositional data analysis (CoDA), which is specifically designed for data on the simplex, can be utilised in this context. We drew general connections between the two fields (Section 4.2.2), before applying CoDA tools to two problems in multivariate EVT: principal components analysis (Section 4.3) and extreme event classification (Section 4.4). Our experiments revealed that working in the Aitchison geometry often yields more efficient dimension reduction – both in terms of Euclidean reconstruction error and tail event prediction – and reduces the asymptotic classification error of extreme events. While these improvements to existing methods represent novel contributions in themselves, we hope our research sparks further consideration of how CoDA might be applied in other areas of multivariate EVT.

Chapter 5 contained our submission to the EVA (2023) Data Challenge. For Challenge 3 (Section 5.5.2), the key difficulty was modelling the extremal directions of a low-dimensional random vector. Our main contribution was to show how the sparse simplex projections of Meyer and Wintenberger (2021) can be used to estimate a max-linear model whose angular measure is supported on sub-faces of the simplex. The benefits of our approach are evident from the accuracy of the resulting probability estimates and our first-placed ranking in this task. Our Challenge 4 (Section 5.5.3) methodology extended the framework of Kiriliouk and Zhou (2022), e.g. by incorporating clustering. We identified deficiencies with the procedure, namely the tendency of the empirical TPDM to overestimate weak dependencies,

and showed how these can be addressed by again turning to sparse projections. Thus, a key contribution is to illustrate the practical utility of incorporating Euclidean simplex projections into the TPDM/max-linear modelling framework. We hope the theoretical aspects of this approach are explored further in future.

Section 2.6 and Chapter 6 collectively entailed an in-depth study of the bias of the empirical TPDM. Our first key contribution was to apply thresholding techniques to construct flexible TPDM estimators that mitigate against the bias. In particular, the adaptive lasso estimator is able to target shrinkage towards small entries, unlike the soft-thresholded TPDM proposed by Fix et al. (2021). Our second contribution is to propose and study the Ledoit-Wolf TPDM. In contrast with alternative estimators proposed elsewhere (Fix et al. 2021; Jiang et al. 2020), it satisfies the key properties of a TPDM. Moreover, we were able to devise a purely data-driven procedure for selecting the regularisation parameter, whereas all previous bias-correction tuning procedures rely on heuristics or additional *a priori* knowledge. Compared to the empirical estimator, our methods: permit accurate estimation of the TPDM of a symmetric logistic random vector (Section 6.4.1); correct for the overestimation that hindered our performance in Challenge 4 of the EVA (2023) Data Challenge (Section 6.4.2); facilitate improved inference a spatial extremes model (Section 6.4.3).

## 7.2. Future research ideas

### 7.2.1. Change-point detection

Chapter 3 detailed a procedure for detecting whether the extremal dependence structure is constant or changing over time. If a change is detected, a natural follow-up question is: when did the change occur? This question belongs to the realm of change-point detection and is the subject of an ongoing project in collaboration with Euan McGonigle (University of Southampton), Jordan Richards (University of Edinburgh) and Christian Rohrbeck (University of Bath). The high-level goal is to devise a change-point algorithm for estimating changes in extremal dependence, by extending the methods in Chapter 3 or otherwise. Existing work on this topic is scarce and restricted to likelihood-ratio tests based on parametric models: Dias and Embrechts (2004) consider the bivariate symmetric

logistic model; Hazra and Bose (2024) detect change-points in the Hüsler-Reiss parameter  $\Lambda$ . By leveraging the TPDM, we are able to operate in high dimensions and avoid restrictive parametric assumptions.

Assume there exists a change-point  $\tau \in [0, 1]$  such that  $\Sigma(t)$  is constant up to the change-point and remains constant thereafter. Given samples  $\{\mathbf{x}_l\}_{l/n \in (0, \tau]}$  and  $\{\mathbf{x}_l\}_{l/n \in (\tau, n]}$  and noting that

$$\begin{aligned}\psi_{ij}(t) - t\psi_{ij}(1) &= \int_0^t \sigma_{ij}(s) ds - t \int_0^1 \sigma_{ij}(s) ds \\ &= t(1-t) \left[ \frac{1}{t} \int_0^t \sigma_{ij}(s) ds - \frac{1}{1-t} \int_t^1 \sigma_{ij}(s) ds \right],\end{aligned}$$

a CUSUM-type estimator for the change-point is given by

$$\hat{\tau} = \arg \max_{t \in [0, 1]} (\hat{\psi}(t) - t\hat{\psi}(1)).$$

Alternatively, one can construct MOSUM-type statistics and look for local maxima of these; the main challenge is deriving the behaviour of such statistics near change-points in order to obtain statistical guarantees on the estimation accuracy of the change-points.

### 7.2.2. Incorporating covariate information

Presently, the TPDM framework does not permit the inclusion of covariates. This limitation was raised by an anonymous reviewer of our EVA (2023) Data Challenge paper (Chapter 5), since we neglected to use the available covariate information for Challenge 3. Incorporating covariate information would allow the dependence structure of extreme events to adapt dynamically based on external factors or conditions. Covariates such as time, climate conditions, or economic indicators might influence how extreme values in one variable relate to another. A covariate-adjusted TPDM can better capture varying relationships in different contexts, leading to more accurate predictions of joint extreme events. We extend the definition of the TPDM to include covariate dependence as follows.

**Definition 7.1.** Suppose  $\mathbf{x} \in \mathbb{R}^m$  is a vector of covariates and  $\mathbf{Y}(\mathbf{x}) \in \mathcal{RV}_+^d(2)$  has angular

measure  $H(\boldsymbol{x})$ . The covariate-adjusted TPDM is the  $d \times d$  matrix

$$\Sigma(\boldsymbol{x}) = (\sigma_{ij}(\boldsymbol{x})), \quad \sigma_{ij}(\boldsymbol{x}) = \int_{\mathbb{S}_{+(2)}^{d-1}} \theta_i \theta_j \, dH(\boldsymbol{\theta}; \boldsymbol{x}) = \mathbb{E}_{H(\boldsymbol{x})}[\Theta_i \Theta_j]. \quad (7.1)$$

The main challenge involved in using a covariate-adjusted TPDM lies in performing inference, due to the scarcity of extreme observations. The semi-parametric spectral density ratio model of De Carvalho and Davison (2014) might provide a useful starting point. They consider a family of angular measures  $\{H_l = H(\boldsymbol{x}_l) : l = 1, \dots, L\}$  associated with  $L$  sub-populations corresponding to covariate vectors  $\boldsymbol{x}_1, \dots, \boldsymbol{x}_L \in \mathbb{R}^m$ . The authors simultaneously estimate  $H_1, \dots, H_L$  by assuming that they are related to a unspecified baseline angular measure  $H_0$  via a weight/link function. This setup allows information to be borrowed across the sub-populations, allowing reliable estimation even for sub-populations whose samples are too small to be individually informative about their tails. From this, one could define sub-population TPDMs  $\Sigma_1, \dots, \Sigma_L$  by substituting  $H_1, \dots, H_L$  into (7.1). The theoretical and computational details outlined in De Carvalho and Davison (2014) should carry over fairly naturally. By comparing  $\Sigma_1, \dots, \Sigma_L$  against each other (or the baseline TPDM  $\Sigma_0$ ), one can ascertain the influence of the covariates on the dependence structure.

Once a covariate-adjusted TPDM has been developed (using the approach described above or otherwise), it can then be incorporated into TPDM-based modelling frameworks. For example, completely positive factorisations  $\Sigma(\boldsymbol{x}) = A(\boldsymbol{x})A(\boldsymbol{x})^T$  may be used to fit covariate-dependent max-linear models, from which tail event probabilities can be estimated under different conditions. Another application involves plugging  $\Sigma(\boldsymbol{x})$  into the generative framework of Rohrbeck and Cooley (2023) in order to construct hazard event sets under different scenarios.

### 7.2.3. TPDM based on sparse simplex projections

In multivariate extremes, an important preliminary step in the model selection process is to determine whether sets of variables are asymptotically dependent or asymptotically independent. While the TPDM is a useful exploratory tool, it is limited for this purpose: pairs of variables that are asymptotically independent are difficult to identify from the empirical

TPDM due to the bias issue; even if  $\sigma_{ij} = 0$  the corresponding entry  $\hat{\sigma}_{ij}$  is typically not very close to zero. The bias-correction procedure in Chapter 6 might solve this problem, but an alternative solution utilises the sparse simplex projections from Chapter 5.

**Definition 7.2.** Suppose  $\mathbf{X} \in \mathcal{RV}_+^d(1)$  and let  $\pi$  denote the Euclidean projection onto the simplex (Definition 5.6). The sparse TPDM of  $\mathbf{X}$  is the  $d \times d$  matrix

$$\Sigma^* = (\sigma_{ij}^*), \quad \sigma_{ij}^* = \lim_{t \rightarrow \infty} \mathbb{E} \left[ [\pi(\mathbf{X}/t)]_i^{1/2} [\pi(\mathbf{X}/t)]_j^{1/2} \mid \|\mathbf{X}\|_1 > t \right]. \quad (7.2)$$

Theorem 2 in Meyer and Wintenberger (2021) states that the limiting distribution of the Euclidean angles only places mass on simplicial subspaces where the angular measure places mass or subspaces containing them. This implies that  $\sigma_{ij}^* \neq \sigma_{ij}$  in general, but  $\sigma_{ij}^* = 0$  if and only if  $\sigma_{ij} = 0$ . This relation becomes useful when we consider finite-sample estimates of  $\Sigma^*$  and  $\Sigma$ . The estimator of the sparse TPDM is defined as follows.

**Definition 7.3.** Suppose  $\mathbf{X} \in \mathcal{RV}_+^d(1)$  and let  $\mathbf{x}_1, \dots, \mathbf{x}_n$  be iid observations of  $\mathbf{X}$ . The empirical sparse TPDM is the  $d \times d$  matrix

$$\hat{\Sigma}^* = (\hat{\sigma}_{ij}^*), \quad \hat{\sigma}_{ij}^* := \hat{E}_{\hat{H}^*} [\Theta_i^{1/2} \Theta_j^{1/2}] = \frac{d}{k} \sum_{l=1}^k [\pi(\mathbf{x}_{(l)} / r_{(k+1)})]_i^{1/2} [\pi(\mathbf{x}_{(l)} / r_{(k+1)})]_j^{1/2},$$

where  $\hat{H}^*$  is defined below Definition 5.7 and  $\pi$  is the Euclidean projection onto the simplex (Definition 5.6).

While the entries of the ordinary empirical TPDM are non-zero almost surely, the Euclidean projection yields projections lying on the simplex boundary. Consequently, the estimate  $\hat{\Sigma}^*$  is a sparse matrix. Due to the theoretical connection between  $\Sigma^*$  and  $\Sigma$ , the zero entries of  $\hat{\Sigma}^*$  can be used to estimate the zero entries of  $\Sigma$ .

From here, the research could proceed in any number of directions (e.g. clustering, graphical modelling, fitting max-linear models). We describe one possible application, whereby  $\hat{\Sigma}^*$  is used to select the regularisation parameter for the thresholded TPDM estimates (Definition 6.2). Recall that the goal is to choose the threshold  $\lambda > 0$  so that the thresholded TPDM  $\tilde{\Sigma}(\lambda) = s_\lambda(\hat{\Sigma})$  is close to the true TPDM. In Chapter 6, we measured closeness

using the Frobenius error (6.10), but one might consider alternative metrics such as

$$\begin{aligned} \text{TPR}(\lambda) &:= \frac{|\{(i, j) : i < j, \tilde{\sigma}_{ij}(\lambda) \neq 0, \sigma_{ij} \neq 0\}|}{|\{(i, j) : i < j, \sigma_{ij} \neq 0\}|}, \\ \text{FPR}(\lambda) &:= \frac{|\{(i, j) : i < j, \tilde{\sigma}_{ij}(\lambda) \neq 0, \sigma_{ij} = 0\}|}{|\{(i, j) : i < j, \sigma_{ij} = 0\}|}. \end{aligned}$$

These criteria assess how accurately the regularised TPDM captures the true sparsity structure of  $\Sigma$ . The threshold  $\lambda$  would typically be selected by inspecting a receiver operating characteristic (ROC) curve and/or maximising the area under the curve (AUC). However,  $\text{TPR}(\lambda)$  and  $\text{FPR}(\lambda)$  depend on the unknown TPDM. To overcome this, one might replace  $\sigma_{ij}$  with  $\hat{\sigma}_{ij}^*$  and compute

$$\begin{aligned} \widehat{\text{TPR}}(\lambda) &:= \frac{|\{(i, j) : i < j, \tilde{\sigma}_{ij}(\lambda) \neq 0, \hat{\sigma}_{ij}^* \neq 0\}|}{|\{(i, j) : i < j, \hat{\sigma}_{ij}^* \neq 0\}|}, \\ \widehat{\text{FPR}}(\lambda) &:= \frac{|\{(i, j) : i < j, \tilde{\sigma}_{ij}(\lambda) \neq 0, \hat{\sigma}_{ij}^* = 0\}|}{|\{(i, j) : i < j, \hat{\sigma}_{ij}^* = 0\}|}. \end{aligned}$$

Through theoretical analysis and simulation experiments, one can ascertain whether the pseudo-ROC curve based on  $\widehat{\text{TPR}}$  and  $\widehat{\text{FPR}}$  resembles the true ROC curve. Provided the conclusion is positive, this yields a data-driven procedure for selecting the threshold  $\lambda$ .

# A. Supplementary Material for Chapter 2

## A.1. Properties of the TPDM

### A.1.1. Equivalence of TPDM definitions

The TPDM was originally defined by Cooley and Thibaud (2019) for multivariate random vectors with tail index  $\alpha = 2$  as in Definition 2.10. This was later generalised by Kiriliouk and Zhou (2022) to permit an arbitrary tail index  $\alpha \geq 1$  (Definition 2.11). Beyond the fact that these definitions coincide when  $\alpha = 2$ , it is not obvious why Definition 2.11 is the natural generalisation to Definition 2.10. In this section, we provide some insight into this matter. In doing so, we show that the TPDM is independent of  $\alpha$ , enabling the tail index to be chosen without loss of generality. For example, in Chapter 4 and Chapter 3 we fix  $\alpha = 1$  and  $\alpha = 2$ , respectively. Moreover, the resulting formulae will be used throughout the thesis to compute the true TPDM under various parametric models.

The following lemma provides a formula for the angular density (for arbitrary  $\alpha$ ) in terms of the angular density when  $\alpha = 1$ . We extend a result in the Supplementary Material of Fix et al. (2021), which outlines how to transform from  $\alpha = 1$  to  $\alpha = 2$ .

**Lemma A.1.** *Suppose  $\mathbf{X} = (X_i, X_j) \in \mathcal{RV}_+^2(\alpha)$  for some  $\alpha \geq 1$ . Let  $H_\alpha$  denote the normalised angular measure with respect to  $\|\cdot\|_\alpha$  and  $h_\alpha : \mathbb{S}_{+(\alpha)} \rightarrow \mathbb{R}_+$  the corresponding angular density (assuming it exists). Moreover, we define the re-parametrised density as*

$$\tilde{h}_\alpha : [0, 1] \rightarrow \mathbb{R}_+, \quad \theta \mapsto h_\alpha \left( \left( \theta, (1 - \theta^\alpha)^{1/\alpha} \right) \right).$$

*Then*

$$\tilde{h}_\alpha(\theta) = \alpha \theta^{\alpha-1} \tilde{h}_1(\theta^\alpha). \tag{A.1}$$

*Proof.* The proof generalises the procedure described in Section 3.2 of the Supplementary Material of Fix et al. (2021). First, we transform from  $L_1$  polar coordinates  $(r, \boldsymbol{\theta})$  to Cartesian coordinates  $\mathbf{z} = (z_i, z_j) = (r\theta_i, r\theta_j)$ . The Jacobian of the transformation is  $\|\mathbf{z}\|_1^{-1}$ . Using (2.29) with  $\alpha = 1$  and  $H_1(d\boldsymbol{\theta}) = h_1(\boldsymbol{\theta})d\boldsymbol{\theta}$ ,

$$\begin{aligned}\nu(d\mathbf{r} \times d\boldsymbol{\theta}) &= r^{-2}h_1(\boldsymbol{\theta})drd\boldsymbol{\theta} \\ &= \|\mathbf{z}\|_1^{-2}h_1(\mathbf{z}/\|\mathbf{z}\|_1)\|\mathbf{z}\|_1^{-1}d\mathbf{z} \\ &= \|\mathbf{z}\|_1^{-3}h_1(\mathbf{z}/\|\mathbf{z}\|_1)d\mathbf{z} \\ &= \nu(d\mathbf{z}).\end{aligned}$$

Next, we transform from tail index  $\alpha = 1$  to arbitrary  $\alpha$ . Let  $\mathbf{y} = (y_i, y_j) = (z_i^{1/\alpha}, z_j^{1/\alpha})$ . The Jacobian of this transformation is  $\alpha^2 y_i^{\alpha-1} y_j^{\alpha-1}$ . Note that  $\|\mathbf{z}\|_1 = y_i^\alpha + y_j^\alpha = \|\mathbf{y}\|_\alpha^\alpha$ .

$$\nu(\mathbf{z}) = [\|\mathbf{y}\|_\alpha^\alpha]^{-3} h_1\left(\frac{y_i^\alpha}{\|\mathbf{y}\|_\alpha^\alpha}, \frac{y_j^\alpha}{\|\mathbf{y}\|_\alpha^\alpha}\right) \alpha^2 y_i^{\alpha-1} y_j^{\alpha-1} d\mathbf{y} = \nu(d\mathbf{y}).$$

Finally, we transform to  $L_\alpha$  polar coordinates  $(s, \boldsymbol{\phi})$  with  $s = \|\mathbf{y}\|_\alpha$  and  $\boldsymbol{\phi} = (\phi_i, \phi_j) = \mathbf{y}/s$ . By Lemma 1.1 in Song and Gupta (1997), the Jacobian is  $s(1 - \phi_i^\alpha)^{(1-\alpha)/\alpha} = s\phi_j^{1-\alpha}$ . We now have

$$\begin{aligned}\nu(d\mathbf{y}) &= [s^\alpha]^{-3} h_1\left(\phi_i^\alpha, \phi_j^\alpha\right) \alpha^2 (s\phi_i)^{\alpha-1} (s\phi_j)^{\alpha-1} s\phi_j^{1-\alpha} ds d\boldsymbol{\phi} \\ &= \alpha s^{-\alpha-1} \alpha \phi_i^{\alpha-1} h_1\left(\phi_i^\alpha, \phi_j^\alpha\right) ds d\boldsymbol{\phi} \\ &= \alpha s^{-\alpha-1} h_\alpha(\boldsymbol{\phi}) ds d\boldsymbol{\phi} \\ &= \nu(ds \times d\boldsymbol{\phi}),\end{aligned}$$

where  $h_\alpha(\boldsymbol{\phi}) := \alpha \phi_i^{\alpha-1} h_1\left(\phi_i^\alpha, \phi_j^\alpha\right)$ . The final step is to compute  $\tilde{h}_\alpha$  by projecting the density  $h_\alpha$ , which lives on  $\mathbb{S}_{+(\alpha)}^1$ , down to  $[0, 1]$ . Writing  $\boldsymbol{\phi}$  as  $(\phi, (1 - \phi^\alpha)^{1/\alpha})$  gives

$$\tilde{h}_\alpha(\phi) = h_\alpha\left(\left(\phi, (1 - \phi^\alpha)^{1/\alpha}\right)\right) = \alpha \phi^{\alpha-1} h_1((\phi^\alpha, 1 - \phi^\alpha)) = \alpha \phi^{\alpha-1} \tilde{h}_1(\phi^\alpha). \quad \square$$

In the trivial case  $\alpha = 1$  the formula reduces to  $\tilde{h}_1(\theta) = \tilde{h}_1(\theta)$ , as one would hope. Setting  $\alpha = 2$  yields  $\tilde{h}_2(\theta) = 2\theta \tilde{h}_1(\theta^2)$ , which matches the formula in Fix et al. (2021). Note that

$\tilde{h}_\alpha$  is well-defined (i.e. is a normalised density), since

$$\int_0^1 \tilde{h}_\alpha(\theta) d\theta = \int_0^1 \alpha \theta^{\alpha-1} \tilde{h}_1(\theta^\alpha) d\theta = \int_0^1 \tilde{h}_1(\phi) d\phi = 1.$$

We now apply the transformation formula to express the TPDM for any  $\alpha \geq 1$  in terms of the angular density  $\tilde{h}_1$ .

**Proposition A.1.** *Using the notation of Lemma A.1, the off-diagonal entry in the TPDM of  $\mathbf{X}$  is*

$$\sigma_{ij} = m \int_0^1 \sqrt{u(1-u)} \tilde{h}_1(u) du. \quad (\text{A.2})$$

*Proof.* The relation between the normalised measure  $H_\alpha$  and the measure  $H$  in Definition 2.11 is  $H_\alpha = m^{-1}H$ , where  $m$  is the mass of  $H$ . Therefore, (2.51) can be equivalently restated as

$$\sigma_{ij} = m \int_{\mathbb{S}_{+(\alpha)}} \theta_i^{\alpha/2} \theta_j^{\alpha/2} dH_\alpha(\boldsymbol{\theta})$$

Rewriting this in terms of the angular density and re-parametrising yields

$$\begin{aligned} \sigma_{ij} &= m \int_{\mathbb{S}_{+(\alpha)}} \theta_i^{\alpha/2} \theta_j^{\alpha/2} h_\alpha(\boldsymbol{\theta}) d\boldsymbol{\theta} \\ &= m \int_{\mathbb{S}_{+(\alpha)}} \theta_i^{\alpha/2} [(1 - \theta_i^\alpha)^{1/\alpha}]^{\alpha/2} h_\alpha(\boldsymbol{\theta}) d\boldsymbol{\theta} \\ &= m \int_0^1 \theta^{\alpha/2} (1 - \theta^\alpha)^{1/2} \tilde{h}_\alpha(\theta) d\theta. \end{aligned}$$

Finally, we apply Lemma A.1 and substitute  $u = \theta^\alpha$  to obtain the final result

$$\sigma_{ij} = m \int_0^1 \theta^{\alpha/2} (1 - \theta^\alpha)^{1/2} \alpha \theta^{\alpha-1} \tilde{h}_1(\theta^\alpha) d\theta = m \int_0^1 \sqrt{u(1-u)} \tilde{h}_1(u) du. \quad \square$$

Substituting the angular density of the bivariate symmetric logistic distribution

$$\tilde{h}_1(\theta; \gamma) = \frac{1-\gamma}{2\gamma} [\theta(1-\theta)]^{\frac{1}{\gamma}-2} [\theta^{1/\gamma} + (1-\theta)^{1/\gamma}]^{\gamma-2}$$

or Hüsler-Reiss distribution

$$\tilde{h}_1(\theta; \lambda) = \frac{\exp(-\lambda/4)}{4\lambda[\theta(1-\theta)]^{3/2}} \phi\left(\frac{1}{2\lambda} \log\left(\frac{\theta}{1-\theta}\right)\right)$$

into (A.2) yields the expressions given in Example 2.5 and Example 2.6.

### A.1.2. Formula for the asymptotic variance $\nu_{ij}^2$

In this section, we derive a formula for the asymptotic variance  $\nu_{ij}^2$  of  $\hat{\sigma}_{ij}$  – see Proposition 2.5 in terms of the angular density  $\tilde{h}_1$  of  $(X_i, X_j)$ . Using the identity  $\text{Var}(Y) = \mathbb{E}[Y^2] - \mathbb{E}[Y]^2$  and Proposition A.1, we have

$$\nu_{ij}^2 = m^2 \int_{\mathbb{S}_{+(\alpha)}^{d-1}} (\theta_i \theta_j)^\alpha dH_\alpha(\boldsymbol{\theta}) - \sigma_{ij}^2 = m^2 \int_0^1 \theta^\alpha (1 - \theta^\alpha) \tilde{h}_\alpha(\theta) d\theta - \sigma_{ij}^2.$$

Substituting  $u = \theta^\alpha$  and using Proposition A.1 gives the final expression

$$\nu_{ij}^2 = m^2 \int_0^1 u(1-u) \tilde{h}_1(u) du - \left[ m \int_0^1 \sqrt{u(1-u)} \tilde{h}_1(u) du \right]^2. \quad (\text{A.3})$$

Again, we note that the result, in this case the asymptotic variance (and therefore distribution) of  $\hat{\sigma}_{ij}$ , does not depend on  $\alpha$ .

### A.1.3. Proof of Proposition 2.6

*Proof.* We follow the proof of Theorem 5.23 in Krali (2018) but adapt it to the general  $\alpha$  case. By the Cramér-Wold device, it is sufficient to show asymptotic normality of  $\sqrt{k}\beta^T(\hat{\boldsymbol{\sigma}} - \boldsymbol{\sigma})$  for all  $\boldsymbol{\beta} \in \mathbb{R}^{\binom{d}{2}}$ . For convenience, the components of  $\boldsymbol{\beta}$  are indexed to match the sub-indices of  $\boldsymbol{\sigma}$ . Then

$$\boldsymbol{\beta}^T \boldsymbol{\sigma} = \sum_{i=1}^d \sum_{j=i}^d \beta_{ij} \sigma_{ij} = \mathbb{E}_H \left[ \sum_{i=1}^d \sum_{j=i}^d \beta_{ij} \Theta_i^{\alpha/2} \Theta_j^{\alpha/2} \right] =: \mathbb{E}_H[g(\boldsymbol{\Theta}; \boldsymbol{\beta})],$$

where

$$g(\boldsymbol{\theta}; \boldsymbol{\beta}) := \sum_{i=1}^d \sum_{j=i}^d \beta_{ij} \theta_i^{\alpha/2} \theta_j^{\alpha/2}$$

The corresponding empirical estimator is

$$\hat{\mathbb{E}}_H[g(\boldsymbol{\Theta}; \boldsymbol{\beta})] = \frac{m}{k} \sum_{l=1}^k \sum_{i=1}^d \sum_{j=i}^d \beta_{ij} \Theta_{(l),i}^{\alpha/2} \Theta_{(l),j}^{\alpha/2} = \sum_{i=1}^d \sum_{j=i}^d \beta_{ij} \left( \frac{m}{k} \sum_{l=1}^k \Theta_{(l),i}^{\alpha/2} \Theta_{(l),j}^{\alpha/2} \right) = \boldsymbol{\beta}^T \hat{\boldsymbol{\sigma}}.$$

Noting that  $g(\cdot; \boldsymbol{\beta})$  is continuous and applying Theorem 2.3, we have

$$\sqrt{k}\boldsymbol{\beta}^T(\hat{\boldsymbol{\sigma}} - \boldsymbol{\sigma}) = \sqrt{k} \left( \hat{\mathbb{E}}_H[g(\boldsymbol{\Theta}; \boldsymbol{\beta})] - \mathbb{E}_H[g(\boldsymbol{\Theta}; \boldsymbol{\beta})] \right) \rightarrow N(0, v(\boldsymbol{\beta})).$$

where  $v(\boldsymbol{\beta}) := \text{Var}_H(g(\boldsymbol{\Theta}; \boldsymbol{\beta}))$ . The asymptotic normality of  $\hat{\boldsymbol{\sigma}}$  follows by the Cramér-Wold device. The diagonal elements of the covariance matrix  $V$  are as in Proposition 2.5. The off-diagonal entries are given by

$$\begin{aligned} 2\text{Cov} \left( \sqrt{k}(\hat{\sigma}_{ij} - \sigma_{ij}), \sqrt{k}(\hat{\sigma}_{lm} - \sigma_{lm}) \right) &= 2k \text{Cov}(\hat{\sigma}_{ij}, \hat{\sigma}_{lm}) \\ &= k [\text{Var}(\hat{\sigma}_{ij} + \hat{\sigma}_{lm}) - \text{Var}(\hat{\sigma}_{ij}) - \text{Var}(\hat{\sigma}_{lm})] \\ &\rightarrow \text{Var}_H(\Theta_i^{\alpha/2} \Theta_j^{\alpha/2} + \Theta_l^{\alpha/2} \Theta_m^{\alpha/2}) - \nu_{ij}^2 - \nu_{lm}^2. \quad \square \end{aligned}$$

#### A.1.4. Derivation of $V$ under the max-linear model

Suppose  $\mathbf{X} = (X_1, \dots, X_d) \in \mathcal{RV}_+^d(\alpha)$  is max-linear with  $q$  factors and parameter matrix  $A \in \mathbb{R}_+^{d \times q}$ . Then, for any  $i, j = 1, \dots, d$ , we have  $\sigma_{ij} = \sum_{l=1}^q a_{il}^{\alpha/2} a_{jl}^{\alpha/2}$  and

$$\nu_{ij}^2 = d \int_{\mathbb{S}_{+(\alpha)}^{d-1}} (\theta_i \theta_j)^\alpha dH(\boldsymbol{\theta}) - \sigma_{ij}^2 = d \sum_{s=1}^q \|\mathbf{a}_s\|_\alpha^\alpha \left( \frac{a_{is} a_{js}}{\|\mathbf{a}_s\|_\alpha^2} \right)^\alpha - \sigma_{ij}^2 = d \sum_{s=1}^q \frac{(a_{is} a_{js})^\alpha}{\|\mathbf{a}_s\|_\alpha^\alpha} - \sigma_{ij}^2.$$

For any pair of upper-triangular index pairs  $(i, j)$  and  $(l, m)$ , we have

$$\begin{aligned} \text{Var}_H(\Theta_i^{\alpha/2} \Theta_j^{\alpha/2} + \Theta_l^{\alpha/2} \Theta_m^{\alpha/2}) &= d \int_{\mathbb{S}_{+(\alpha)}^{d-1}} [(\theta_i \theta_j)^\alpha + 2(\theta_i \theta_j \theta_l \theta_m)^{\alpha/2} + (\theta_l \theta_m)^\alpha] dH(\boldsymbol{\theta}) - [\sigma_{ij} + \sigma_{lm}]^2 \\ &= d \sum_{s=1}^q \frac{(a_{is} a_{js})^\alpha + 2(a_{is} a_{js} a_{ls} a_{ms})^{\alpha/2} + (a_{ls} a_{ms})^\alpha}{\|\mathbf{a}_s\|_\alpha^\alpha} - [\sigma_{ij} + \sigma_{lm}]^2 \\ &= \nu_{ij}^2 + \nu_{lm}^2 + d \sum_{s=1}^q \frac{2(a_{is} a_{js} a_{ls} a_{ms})^{\alpha/2}}{\|\mathbf{a}_s\|_\alpha^\alpha} - 2\sigma_{ij}\sigma_{lm} \end{aligned}$$

and therefore

$$2\rho_{ij,lm} = d \sum_{s=1}^q \frac{2(a_{is} a_{js} a_{ls} a_{ms})^{\alpha/2}}{\|\mathbf{a}_s\|_\alpha^\alpha} - 2\sigma_{ij}\sigma_{lm}.$$

$\mathcal{H}$	$\mathbb{R}^d$	$\mathbb{R}_+^d$	$\mathbb{S}_{+(1)}^{d-1}$
$h : \mathcal{H} \rightarrow \mathbb{R}^d$	$h(\mathbf{x}) = \mathbf{x}$	$h(\mathbf{x}) = \tau^{-1}(\mathbf{x}) = \log[\exp(\mathbf{x}) - 1]$	$h(\mathbf{x}) = \text{clr}(\mathbf{x}) = \log[\mathbf{x}/\bar{g}(\mathbf{x})]$
$h^{-1} : \mathbb{R}^d \rightarrow \mathcal{H}$	$h^{-1}(\mathbf{y}) = \mathbf{y}$	$h^{-1}(\mathbf{y}) = \tau(\mathbf{y}) = \log[1 + \exp(\mathbf{y})]$	$h^{-1}(\mathbf{y}) = \text{clr}^{-1}(\mathbf{y}) = \mathcal{C} \exp(\mathbf{y})$
$\mathbf{x} \oplus \mathbf{y}$	$\mathbf{x} + \mathbf{y}$	$\tau[\tau^{-1}(\mathbf{x}) + \tau^{-1}(\mathbf{y})]$	$\mathcal{C}(x_1 y_1, \dots, x_d y_d)$
$\alpha \odot \mathbf{x}$	$\alpha \mathbf{x}$	$\tau[\alpha \tau^{-1}(\mathbf{x})]$	$\mathcal{C}(x_1^\alpha, \dots, x_d^\alpha)$
$\langle \mathbf{x}, \mathbf{y} \rangle_{\mathcal{H}}$	$\sum_{i=1}^d x_i y_i$	$\sum_{i=1}^d \tau^{-1}(x_i) \tau^{-1}(y_i)$	$\sum_{i=1}^d \log[x_i/\bar{g}(\mathbf{x})] \log[y_i/\bar{g}(\mathbf{x})]$

The expressions for  $\nu_{ij}^2$  and  $\rho_{ij,lm}$  can be summarised as

$$v_{ij,lm} = d \sum_{s=1}^q \frac{(a_{is} a_{js} a_{ls} a_{ms})^{\alpha/2}}{\|a_s\|_\alpha^\alpha} - \sigma_{ij} \sigma_{lm}. \quad (\text{A.4})$$

## A.2. PCA in general finite-dimensional Hilbert spaces

In classical multivariate analysis, principal component analysis (PCA) is the flagship method for reducing the dimension of a random vector. PCA identifies linear subspaces that minimise the distance between the data and its low-dimensional projections. This implicitly assumes an underlying algebraic-geometric structure. Specifically, PCA requires one to work in a Hilbert space  $\mathcal{H}$ . Without this theoretical foundation, it is meaningless to speak of principal components as orthogonal basis vectors or consider low-rank reconstructions as unique projections onto a subspace. A Hilbert space comprises a  $d$ -dimensional vector space with operations  $\oplus$  and  $\odot$  endowed with an inner product  $\langle \cdot, \cdot \rangle_{\mathcal{H}}$ . The induced norm and metric are  $\|\cdot\|_{\mathcal{H}} = \langle \cdot, \cdot \rangle_{\mathcal{H}}^{1/2}$  and  $d_{\mathcal{H}}(\mathbf{x}, \mathbf{y}) = \|\mathbf{x} \ominus \mathbf{y}\|_{\mathcal{H}}$ , respectively. In most applications  $\mathcal{H} = \mathbb{R}^d$  with the usual Euclidean geometry. This thesis will additionally consider PCA in alternative spaces, including  $\mathbb{R}_+^d$  and  $\mathbb{S}_{+(1)}^{d-1}$ . However, in each case, the Hilbert space in question will be isometric to the usual Euclidean space  $(\mathbb{R}^d, \langle \cdot, \cdot \rangle)$ . That is, there exists an isomorphism  $h : \mathcal{H} \rightarrow \mathbb{R}^d$  such that for any  $\mathbf{x}, \mathbf{y} \in \mathcal{H}$ ,

$$\langle \mathbf{x}, \mathbf{y} \rangle_{\mathcal{H}} = \langle h(\mathbf{x}), h(\mathbf{y}) \rangle, \quad \|\mathbf{x} \ominus \mathbf{y}\|_{\mathcal{H}} = \|h(\mathbf{x}) - h(\mathbf{y})\|_2.$$

We present PCA for random vectors in  $\mathbb{R}^d$ , with the understanding that the data may have undergone an isometric transformation in pre-processing and outputs may need to be back-transformed to lie in the original space. This transform/back-transform approach is equivalent to conducting the analysis in the original space with appropriately generalised notions of mean, variance, etc. (Pawlowsky-Glahn and Egozcue 2001).

Suppose  $\mathbf{Y} = (Y_1, \dots, Y_d)$  is a random vector in  $\mathbb{R}^d$  satisfying  $\mathbb{E}[\|\mathbf{Y}\|_2^2] < \infty$ . Let  $\mathbf{Y}_1, \dots, \mathbf{Y}_n$  be independent copies of  $\mathbf{Y}$ . The reconstruction error of a subspace  $\mathcal{S} \subseteq \mathbb{R}^d$  is measured as

$$R(\mathcal{S}) := \mathbb{E}[\|\mathbf{Y} - \Pi_{\mathcal{S}}\mathbf{Y}\|_2^2] \quad (\text{A.5})$$

Fundamental to PCA are the eigenvectors  $\mathbf{u}_1, \dots, \mathbf{u}_d \in \mathbb{R}^d$  and respective eigenvalues  $\lambda_1 \geq \dots \geq \lambda_d \geq 0$  of the positive semi-definite matrix

$$\Sigma = \mathbb{E}[\mathbf{Y}\mathbf{Y}^T].$$

The entries of  $\Sigma$ , herein referred to as the non-centred covariance matrix, are the second-order moments of  $\mathbf{Y}$ . By a change of basis, the random vector  $\mathbf{Y}$  may be equivalently decomposed as

$$\mathbf{Y} = \sum_{j=1}^d \langle \mathbf{Y}, \mathbf{u}_j \rangle \mathbf{u}_j.$$

The scores  $V_j := \langle \mathbf{Y}, \mathbf{u}_j \rangle$  represent the stochastic basis coefficients when  $\mathbf{Y}$  is decomposed into the basis  $\{\mathbf{u}_1, \dots, \mathbf{u}_d\}$ . They satisfy  $\mathbb{E}[V_i V_j] = \lambda_i \mathbf{1}\{i = j\}$ . For  $1 \leq p < d$ , the truncated expansion

$$\hat{\mathbf{Y}}^{[p]} := \sum_{j=1}^p V_j \mathbf{u}_j = \Pi_{\text{span}\{\mathbf{u}_1, \dots, \mathbf{u}_p\}} \mathbf{Y}.$$

produces the optimal  $p$ -dimensional projection of  $\mathbf{Y}$ . In other words, the subspace  $\mathcal{S}_p = \text{span}\{\mathbf{u}_1, \dots, \mathbf{u}_p\}$  minimises the criterion (A.5) over  $\mathcal{V}_p$ , the set of all linear subspaces of dimension  $p$  of  $\mathbb{R}^d$ . It is the unique minimiser provided the multiplicity of  $\lambda_p$  is one. The corresponding risk is determined by the eigenvalues of the discarded components via  $R(\mathcal{S}_p) = \sum_{j>p} \lambda_j$ .

In practice, the covariance matrix is unknown so (A.5) cannot be minimised directly. Instead we resort to an empirical risk minimisation (ERM) approach, whereby the risk is replaced by

$$\hat{R}(\mathcal{S}) := \frac{1}{n} \sum_{i=1}^n \|\mathbf{Y}_i - \Pi_{\mathcal{S}}\mathbf{Y}_i\|_2^2 \quad (\text{A.6})$$

Minimisation of the empirical risk follows analogously based on the empirical non-centred covariance matrix

$$\hat{\Sigma} = \frac{1}{n} \sum_{i=1}^n \mathbf{Y}_i \mathbf{Y}_i^T$$

and its ordered eigenpairs  $(\hat{\lambda}_j, \hat{\mathbf{u}}_j)$  for  $j = 1, \dots, d$ . For  $p = 1, \dots, d$  and  $i = 1, \dots, n$ , the rank- $p$  reconstruction of  $\mathbf{Y}_i$  is given by

$$\hat{\mathbf{Y}}_i^{[p]} := \sum_{j=1}^p \hat{V}_{ij} \hat{\mathbf{u}}_j = \Pi_{\text{span}\{\hat{\mathbf{u}}_1, \dots, \hat{\mathbf{u}}_p\}} \mathbf{Y}_i,$$

where  $\hat{V}_{ij} := \langle \mathbf{Y}_i, \hat{\mathbf{u}}_j \rangle$ . The subspace  $\hat{\mathcal{S}}_p = \text{span}\{\hat{\mathbf{u}}_1, \dots, \hat{\mathbf{u}}_p\}$  minimises (A.6) in  $\mathcal{V}_p$ ; the objective at the minimum is  $\hat{R}(\hat{\mathcal{S}}_p) = \sum_{j>p} \hat{\lambda}_j$ .

Usually the dimension of the target subspace (if it exists) is unknown, so the number of retained components  $p$  must be selected according to some criterion. At the heart of this choice is a trade-off between dimension reduction and approximation error. Selecting  $p = \max\{j : \hat{\lambda}_j > 0\}$  results in perfect reconstructions but the reduction in dimension will be minimal if any. Excessive compression incurs information loss and destroys key features of the data. Several criteria for selecting the number of retained components based on the eigenvalues have been proposed. These include stopping when the reconstruction error  $\sum_{j>p} \hat{\lambda}_j$  is acceptably small, cutting off components with  $\lambda_j < 1$ , or retaining components based on where the ‘scree plot’ forms an elbow.

If  $\mathbf{Y}$  is mean-zero (or the  $n \times d$  data matrix is column-centred in pre-processing), then  $\Sigma$  is the covariance matrix of  $\mathbf{Y}$  and the procedure is termed centred PCA. In this case, PCA can be equivalently reformulated in terms of finding low-dimensional projections that maximally preserve variance. In the non-centred case this interpretation is not valid, the projections merely maximise variability around the origin. A detailed comparison between centred PCA and non-centred PCA is conducted in Cadima and Jolliffe (2009). They obtain relationships between and bounds on the eigenvectors/eigenvalues of the non-centred and standard covariance matrices. Based on their theoretical analysis and a series of example, they conclude that both types of PCA generally produce similar results. In particular, the leading eigenvector (up to sign and scaling) of the non-centred covariance matrix is very often close to the vector of the column means of the data matrix. Thus the first non-centred principal component essentially relates to the centre of the data.

### A.3. Literature review: clustering with the TPDM

While clustering methods are not central to this thesis, only being used once in Section 5.5.3, we consider it worthwhile to describe some TPDM-related clustering algorithms. The two algorithms described in this section are closely connected with other topics discussed in this thesis, such as principal components analysis and support identification. Therefore, reviewing these algorithms can enrich the reader's understanding of these other aspects.

Within multivariate extremes, the umbrella term ‘clustering’ has many meanings. To avoid confusion, we briefly describe these and clarify which type we are referring to.

- **Prototypical events.** Assume that the angular measure concentrates at/near a small number of points in  $\mathbb{S}_+^{d-1}$ . Then one might wish to identify cluster centres  $\mathbf{w}_1, \dots, \mathbf{w}_K$  minimising some objective function of the form

$$\mathbb{E}_H \left[ \min_{l=1, \dots, K} \varrho(\boldsymbol{\Theta}, \mathbf{w}_l) \right], \quad (\text{A.7})$$

where  $\varrho : \mathbb{S}_+^{d-1} \times \mathbb{S}_+^{d-1} \rightarrow [0, 1]$  is some distance/dissimilarity function. The cluster centres can be interpreted as the directions of prototypical extremes events. See Chautru (2015), Janßen and Wan (2020) and **medinaSpectralLearningMultivariate2021** for further details.

- **Identification of concomitant extremes.** Suppose that angular measure is supported on a set of  $K \ll 2^{d-1}$  subspaces (faces) of the simplex  $C_{\beta_1}, \dots, C_{\beta_K}$ , where  $\beta_1, \dots, \beta_K \in \mathcal{P}(\{1, \dots, d\}) \setminus \emptyset$  and

$$C_\beta = \{\boldsymbol{\theta} \in \mathbb{S}_+^{d-1} : \theta_i > 0 \iff i \in \beta\}.$$

Only those groups ('clusters') of components indexed by  $\beta_1, \dots, \beta_K$  may be simultaneously extreme. Identification of the support of the angular measure is notoriously challenging because the extremal angles  $\boldsymbol{\Theta}_{(1)}, \dots, \boldsymbol{\Theta}_{(k)}$  lie (almost surely) in the interior of the simplex. Goix et al. (2017) and Simpson et al. (2020) identify clusters according to whether observations fall within appropriately sized rectangular/conic neighbourhoods of the corresponding axis in  $\mathbb{R}_+^d$ . Meyer and Wintenberger (2021) take a different approach, whereby the angular component is defined with respect

to the Euclidean projection (Liu and Ye 2009) rather than usual projection based on self-normalisation. The geometry of the projection is such that the projected data lie on subfaces of the simplex. The price paid is that the limiting conditional distribution of the angles is related to, but not identical to, the angular measure.

- **Partitioning into AD/AI groups components.** This notion of clustering is related to the previous type. We assume that the variables  $X_1, \dots, X_d$  can be partitioned into  $K$  clusters, such that  $X_i$  and  $X_j$  are asymptotically dependent if and only if they belong to the same cluster. In other words, there exists  $2 \leq K \leq d$  and a partition  $\beta_1, \dots, \beta_K$  of  $\{1, \dots, d\}$  such that the angular measure is supported on  $C_{\beta_1}, \dots, C_{\beta_K}$  or lower-dimensional subspaces thereof, i.e.

$$H \left( \bigcup_{l=1}^K \bigcup_{\beta'_l \subseteq \beta_l} C_{\beta'_l} \right) = m.$$

The task of modelling the dependence structure of  $\mathbf{X}$  can be divided into lower-dimensional sub-problems involving the random sub-vectors  $\mathbf{X}_{\beta_1}, \dots, \mathbf{X}_{\beta_K}$ . If  $K = d$ , then all variables are asymptotically independent. The underlying hypothesis is very strong and unlikely to hold in practice. Nevertheless, it is often a useful simplifying modelling assumption. Bernard et al. (2013) propose grouping components using the  $k$ -medoids algorithm (Kaufman and Rousseeuw 1990) with a dissimilarity matrix populated with pairwise measures of tail dependence, similar to  $\chi_{ij}$  and  $\sigma_{ij}$ . The approaches of Fomichov and Ivanovs (2023) and Richards et al. (2024) involve the TPDM; these are reviewed in greater detail below.

Fomichov and Ivanovs (2023) show that the latter kind of clustering may be performed using the framework of the first kind. They provide a link between the principal eigenvector  $\mathbf{u}_1$  of the TPDM and the minimiser of the objective (A.7) with quadratic cost  $\varrho(\boldsymbol{\theta}, \boldsymbol{\phi}) = \langle \boldsymbol{\theta}, \boldsymbol{\phi} \rangle^2$  and  $K = 1$ :

$$\min_{\boldsymbol{\theta} \in \mathbb{S}_{+(2)}^{d-1}} \mathbb{E}_H [\varrho(\boldsymbol{\Theta}, \boldsymbol{\theta})] = \mathbb{E}_H [\varrho(\boldsymbol{\Theta}, \mathbf{u}_1)].$$

Note that  $\mathbf{u}_1 \in \mathbb{S}_{+(2)}^{d-1}$  is assumed to be suitably normalised with all entries being non-negative; the Perron-Frobenius theorem guarantees this is possible. This result informs an iterative clustering procedure called spherical  $k$ -principal-components. Consider a set of extremal angles  $\boldsymbol{\theta}_{(1)}, \dots, \boldsymbol{\theta}_{(k)} \in \mathbb{S}_{+(2)}^{d-1}$  and current centroids  $\hat{\mathbf{w}}_1, \dots, \hat{\mathbf{w}}_K \in \mathbb{S}_{+(2)}^{d-1}$ . A

single iteration of their procedure yields new centroids  $\hat{\mathbf{w}}_1^*, \dots, \hat{\mathbf{w}}_K^* \in \mathbb{S}_{+(2)}^{d-1}$  given by the respective principal eigenvectors of

$$\hat{\Sigma}^{[i]} = \sum_{l=1}^k \boldsymbol{\theta}_{(l)} \boldsymbol{\theta}_{(l)}^T \mathbf{1} \left\{ \arg \min_{j=1, \dots, K} \varrho(\boldsymbol{\theta}_{(l)}, \mathbf{w}_j) = i \right\}, \quad (i = 1, \dots, K).$$

The matrix  $\hat{\Sigma}^{[i]}$  represents the empirical TPDM (up to some multiplicative constant) based on the nearest neighbours of the  $i$ th centroid. Fomichov and Ivanovs (2023) prove that, under certain conditions, the limiting centroids lie in a neighbourhood of the faces of interest  $C_{\beta_1}, \dots, C_{\beta_K}$ . Thresholding the centroid vectors yields the final partition  $\beta_1, \dots, \beta_K$ .

Richards et al. (2024) apply hierarchical clustering using the empirical TPDM as the underlying similarity matrix. The clustering method constitutes a minor aspect of their submission to the EVA (2023) Data Challenge. Few methodological details are provided, so the following explanation constitutes our interpretation of their method, drawing on Figure 4 in Richards et al. (2024) and the accompanying code made available at <https://github.com/matheusguerrero/yalla>. Define the dissimilarity between  $X_i$  and  $X_j$  as  $\varrho_{ij} = 1 - \sigma_{ij}$ . This satisfies the properties of a dissimilarity measure:

$$\varrho_{ij} \geq 0, \quad \varrho_{ii} = 0, \quad \varrho_{ij} = \varrho_{ji}.$$

The  $d \times d$  dissimilarity matrix  $\mathcal{D} = 1 - \Sigma = (\varrho_{ij})$  can be fed into standard hierarchical clustering algorithms. Agglomerative hierarchical clustering initially assigns each variable belongs to its own cluster, i.e.  $\beta_i = \{i\}$  for  $i = 1, \dots, d$ . The algorithm proceeds iteratively, repeatedly joining together the two closest clusters until some stopping criterion is satisfied. Under complete-linkage clustering, the distance between clusters  $\beta \neq \beta'$  is given by  $\max\{\varrho_{ij} : i \in \beta, j \in \beta'\}$ . The merging process may be stopped when there is a sufficiently small number of clusters or when the clusters are sufficiently separated.

## B. Supplementary Material for Chapter 3

### B.1. Overview of Drees (2023)

This appendix provides a concise overview of Drees (2023). The paper is rather technical, so we aim to provide a high-level summary allowing the reader to better understand the results presented in Chapter 3.

Drees (2023) test the hypotheses (3.2) and (3.3) by detecting changes in the full angular measure, rather than a bivariate summary like the TPDM. Let  $\mathcal{A}$  be a large family of Borel subsets of  $\mathbb{S}_{+(2)}^{d-1}$ . Then, suitably rescaled versions of the stochastic processes

$$\left\{ \int_0^t \hat{H}(A; s) ds - t \int_0^1 \hat{H}(A; s) ds : t \in [0, 1] \right\}, \quad A \in \mathcal{A}, \quad (\text{B.1})$$

converge to a mean-zero Gaussian process whose covariance function depends on  $H$ . KS- and CM-type test statistics are defined analogously to (3.16) and (3.17) in terms of this Gaussian process. However, since the covariance function depends on the true angular measure, critical values must be obtained by simulation each time (except in the bivariate case, provided  $\mathcal{A}$  satisfies certain properties). The null is rejected if any paths in (B.1) deviate from what would typically occur under the null. If  $\mathcal{A}$  is sufficiently rich, then very subtle dependence changes may be revealed. However, as the dimension  $d$  increases the family of sets grows rapidly, typically  $|\mathcal{A}| = \mathcal{O}(2^d)$ . Consequently, computing the critical values become prohibitively intensive and the convergence  $\hat{H}(A; t) \rightarrow H(A; t)$  of the non-parametric estimators is too slow to yield reliable results. Thus, their method is primarily intended for the bivariate setting and is restricted to  $d \leq 5$  in practice. Fundamentally, the issue is that one needs to estimate a high-dimensional measure using a very small number of observations (the subset of extreme observations lying within a small temporal

neighbourhood). Our approach mitigates this issue by concentrating on  $\mathcal{O}(d^2)$  bivariate summaries of tail dependence instead of the full dependence structure.

## B.2. Additional figures

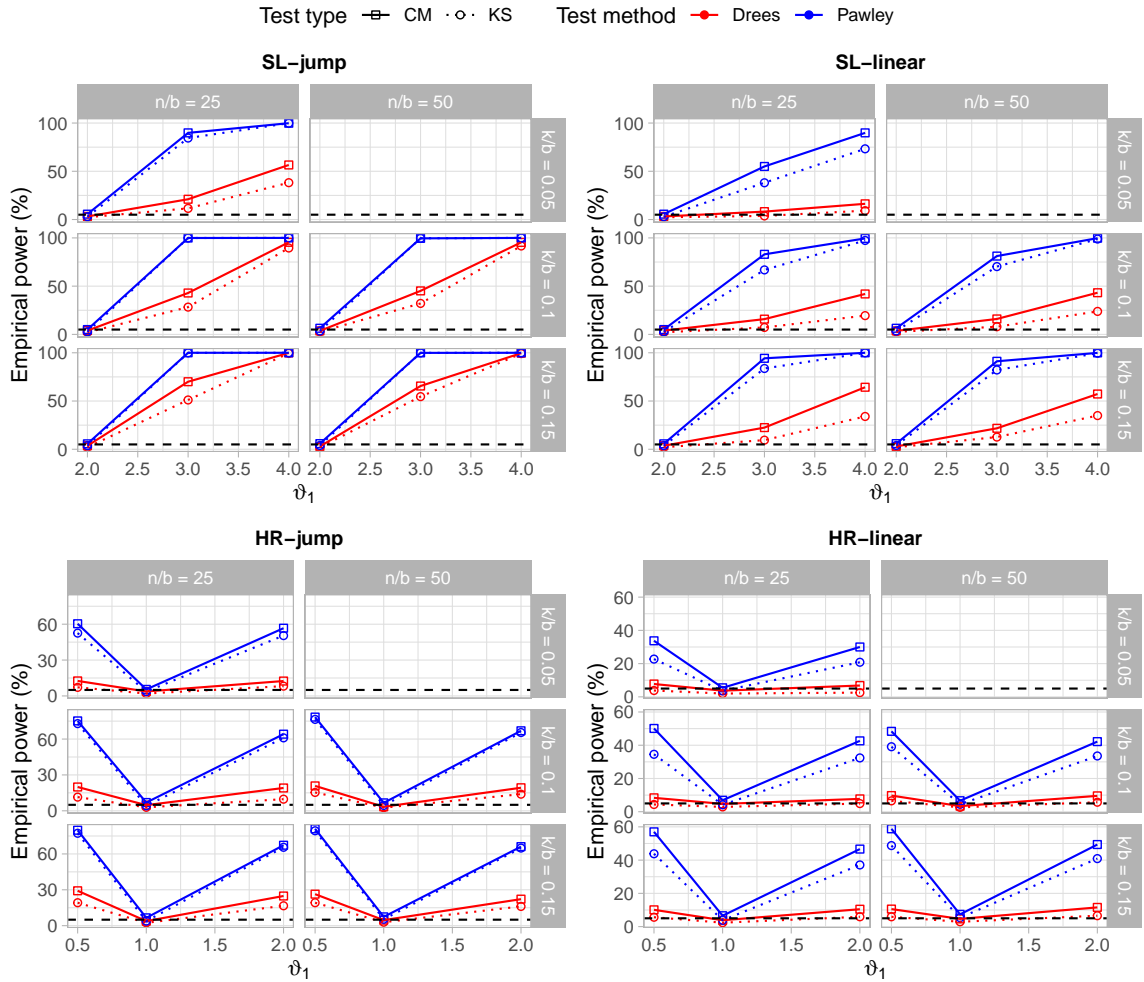


Figure B.1.: Empirical power (%) as a function of the dependence parameter  $\vartheta_1$  for different combinations of tuning parameters  $b$  and  $k$ . Based on 1000 simulations with  $n = 2,500$  and  $d = 2$ . For the SL and HR models,  $\vartheta_0 = 2$  and  $\vartheta_0 = 1$ , respectively. Tests are conducted at the 5% level (black dashed line).

## B.3. Effect of the bias of the empirical TPDM

Since the empirical TPDM struggles to discriminate between differences in dependence strengths at weak levels (Figure 2.5), we find that the power of our test varies according to

the underlying dependence strength. This phenomenon is illustrated in Figure B.3. The plots concern data generated from the SL-linear model with  $d = 3$ . In the top plot, the dependence parameter  $\gamma$  evolves linearly from  $\gamma(0) = 0.06$  (corresponding to  $\sigma_{ij}(0) = 0.998$ ) to  $\gamma(1) = 0.10$  (0.996). In the bottom plot, the corresponding values are  $\gamma(0) = 0.95$  (0.147) to  $\gamma(1) = 0.99$  (0.031). One might assume that the second dependence change is easier to detect, because the change in the TPDM is greater. However, the deficiencies of the empirical TPDM mean this is not the case. Indeed, the bottom-right sub-panels reveal that the null is only rejected for the first test. While we have not conducted a full study of the power, we expect this to replicate over repeated simulations. To address this shortcoming, one might consider employing a TPDM estimator with better finite-sample performance in weak dependence settings. Such an estimator is proposed in Chapter 6. In order to use this estimator in our test, one needs to undertake an asymptotic analysis analogous to Section 3.4.3. We conjecture that the results will follow identically, so in effect the new estimator may simply be plugged in to our testing framework.

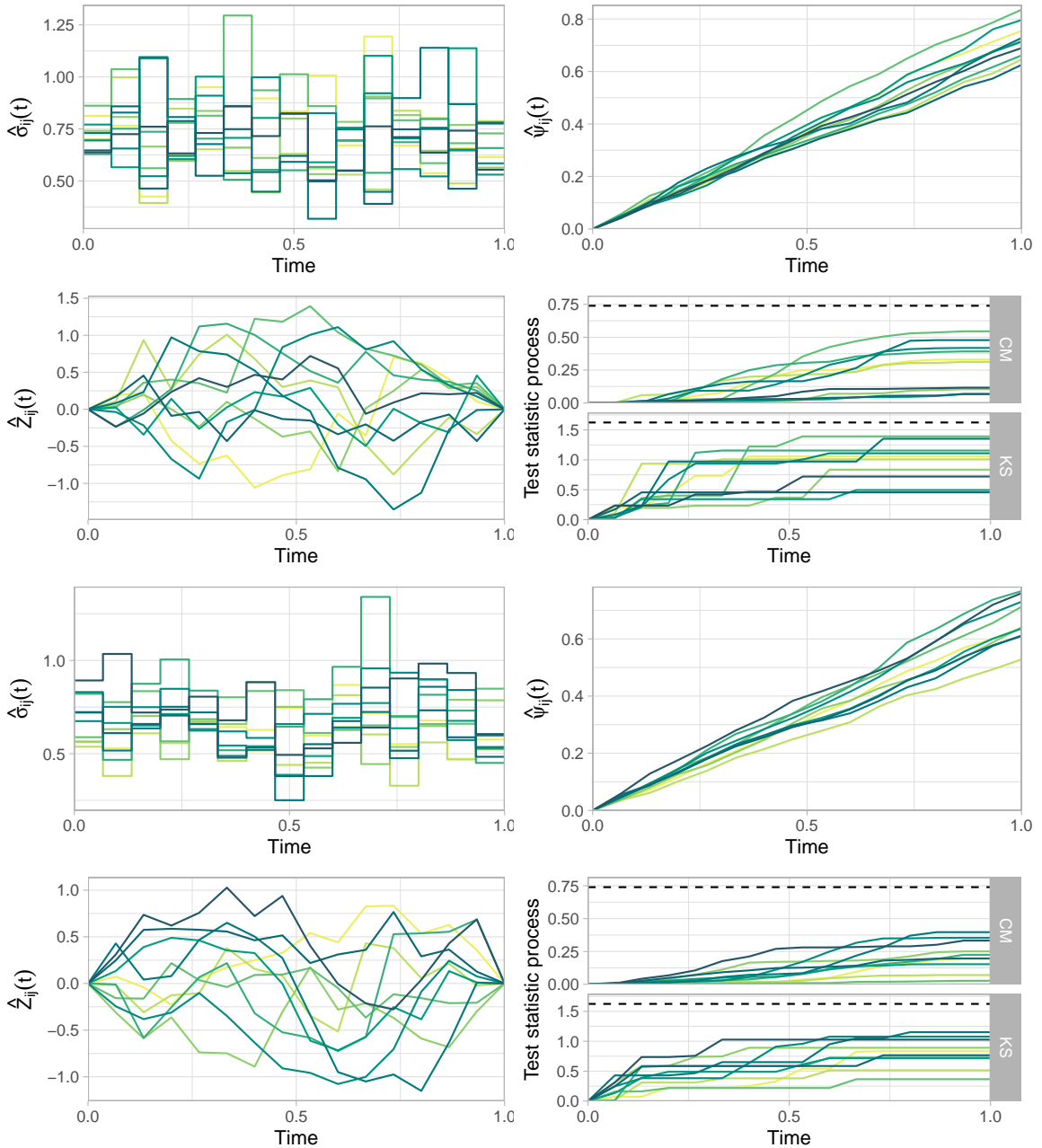


Figure B.2.: Diagnostic plots for our test, based  $b = 107$  and  $k = 20$ , applied to data from  $d = 5$  randomly selected northerly (top two rows) and southerly (bottom two rows) sites in the Red Sea. The interpretation of each plot is the same as in Figure 3.7, except now there are  $\mathcal{D} = 10$  curves, one for each component pair. The variable pairs are coloured light to dark with respect to their lexicographical ordering. For the northerly (resp. southerly) sites there is sufficient (resp. insufficient) evidence to reject the null at the 5% level.

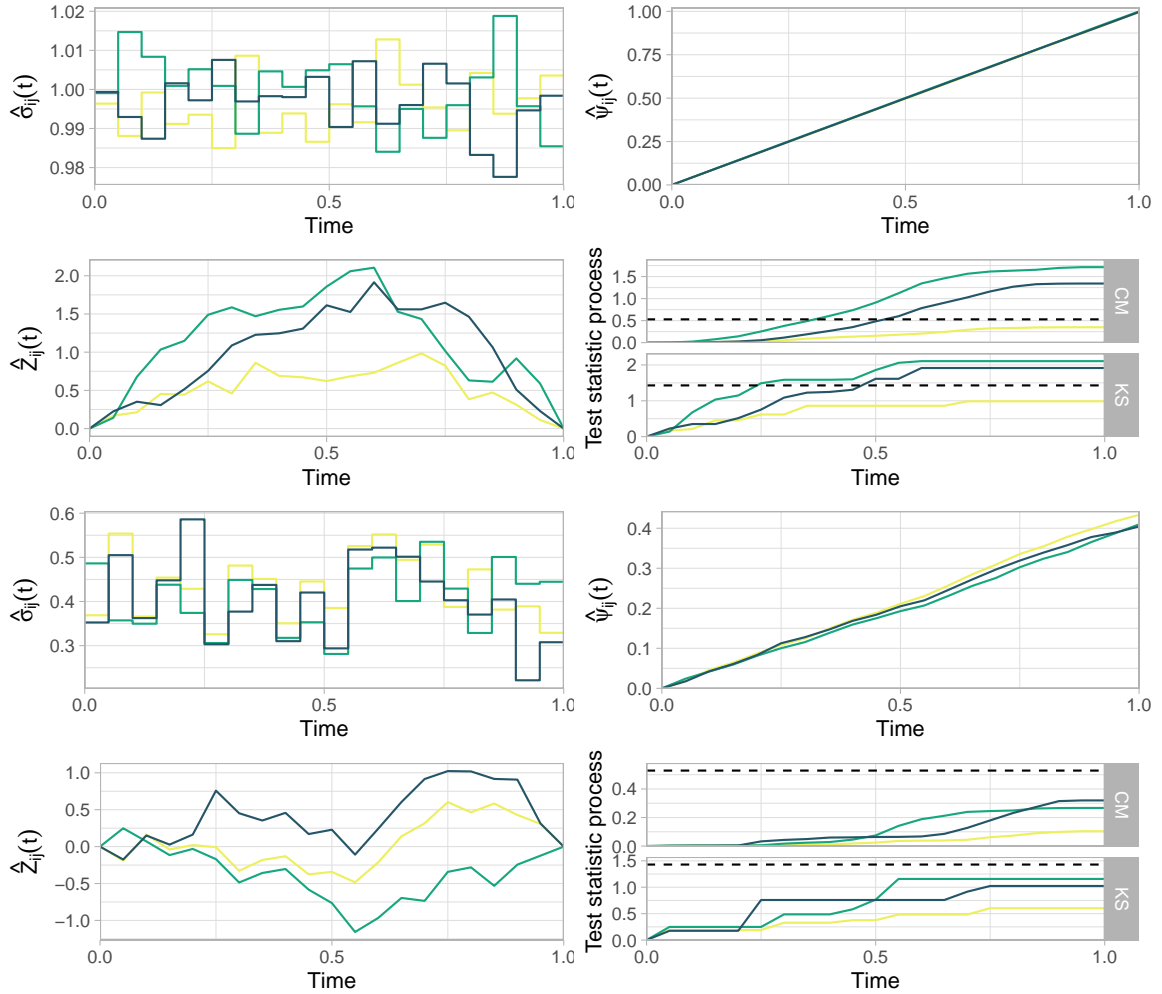


Figure B.3.: Diagnostic plots for our test based on  $n = 5,000$  samples of SL-linear data in  $d = 3$  dimensions. For the interpretation of the plot, see the caption of Figure 3.7. Top: a strong dependence scenario where  $\gamma(0) = 0.06$  and  $\gamma(1) = 0.10$ . Bottom: a weak dependence scenario where  $\gamma(0) = 0.95$  and  $\gamma(1) = 0.99$ .

## C. Supplementary Material for Chapter 4

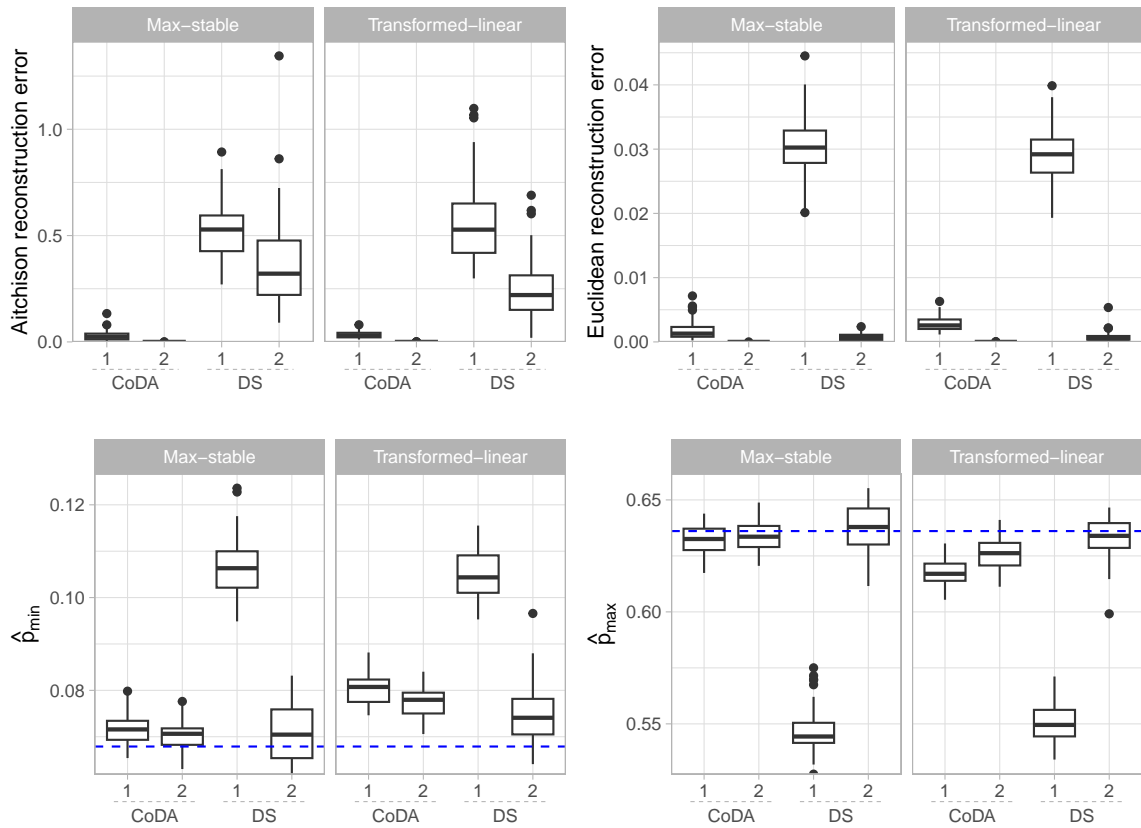


Figure C.1.: Performance of CoDA-PCA and DS-PCA for the trivariate max-linear data. Results are based on 50 repeated simulations from the MS and TL processes with  $n = 50,000$  and  $k/n = 0.01$ . Top row: the Aitchison reconstruction error (4.2) and Euclidean reconstruction error (4.3) against the number of retained components. Reconstruction errors are obtained from 10,000 samples from the true angular measure. Bottom row: estimates of  $p_{\min}$  (left) and  $p_{\max}$  (left) based on (4.6) against  $p$ , the rank of the principal subspace.

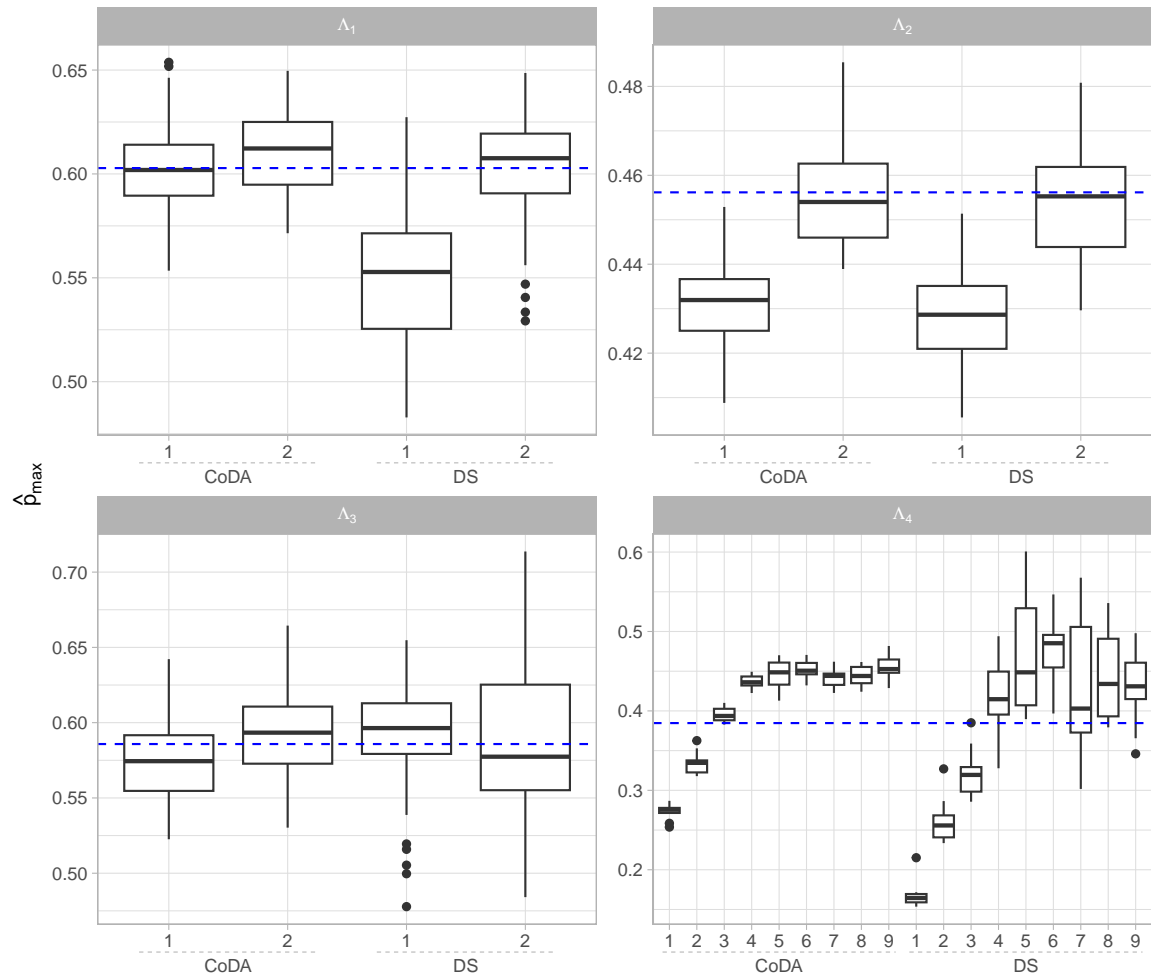


Figure C.2.: Estimates of  $p_{\max}$  against the rank of the CoDA- or DS-PCA reconstruction for the four Hüsler-Reiss models. Results are based on 50 repeated simulations.

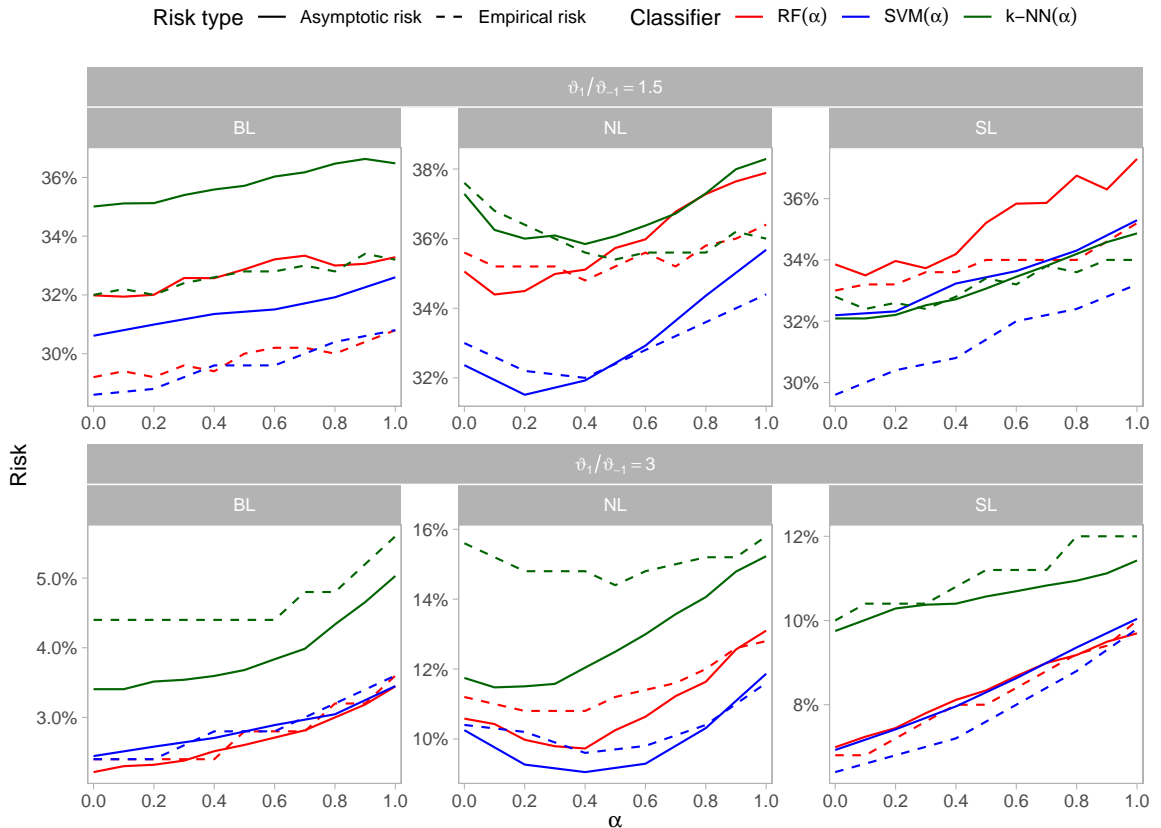


Figure C.3.: Median of the empirical classification risk (based on  $k$  extremal angles) and the true asymptotic classification risk (based on the ‘test’ set of samples from  $H$ ) against the transformation parameter  $\alpha$ . Based on the experiments described in Section 4.4.3.

# References

- Aghbalou, A., P. Bertail, F. Portier, and A. Sabourin (2024). “Cross-validation on extreme regions”. In: *Extremes* 27.4, pp. 505–555.
- Aitchison, J. (1983). “Principal component analysis of compositional data”. In: *Biometrika* 70.1, pp. 57–65.
- Aitchison, J. (1982). “The Statistical Analysis of Compositional Data”. In: *Journal of the Royal Statistical Society: Series B (Methodological)* 44.2, pp. 139–160.
- (1986). *The statistical analysis of compositional data*. Monographs on statistics and applied probability. London: Chapman and Hall.
- (1992). “On criteria for measures of compositional difference”. In: *Mathematical Geology* 24.4, pp. 365–379.
- Alenazi, A. (2023). “A review of compositional data analysis and recent advances”. In: *Communications in Statistics - Theory and Methods* 52.16, pp. 5535–5567.
- Antoniadis, A. and J. Fan (2001). “Regularization of Wavelet Approximations”. In: *Journal of the American Statistical Association* 96.455, pp. 939–967.
- Avella-Medina, M., R. A. Davis, and G. Samorodnitsky (2022). *Kernel PCA for multivariate extremes*. arXiv:2211.13172 [stat].
- (2024). “Spectral learning of multivariate extremes”. In: *Journal of Machine Learning Research* 25, pp. 1–36.
- Berman, A. and N. Shaked-Monderer (2003). *Completely Positive Matrices*. World Scientific.
- Bernard, E., P. Naveau, M. Vrac, and O. Mestre (2013). “Clustering of Maxima: Spatial Dependencies among Heavy Rainfall in France”. In: *Journal of Climate* 26.20, pp. 7929–7937.
- Blanchard, G., O. Bousquet, and L. Zwald (2007). “Statistical properties of kernel principal component analysis”. In: *Machine Learning* 66.2-3, pp. 259–294.

- Boulaguiem, Y., J. Zscheischler, E. Vignotto, K. Van der Wiel, and S. Engelke (2022). “Modeling and simulating spatial extremes by combining extreme value theory with generative adversarial networks”. In: *Environmental Data Science* 1.E5, pp. 1–18.
- Brown, B. M. and S. Resnick (1977). “Extreme Values of Independent Stochastic Processes”. In: *Journal of Applied Probability* 14.4, pp. 732–739.
- Cadima, J. and I. Jolliffe (2009). “On Relationships Between Uncentred and Column-Centred Principal Component Analysis”. In: *Pakistan Journal of Statistics* 25.4, pp. 473–503.
- Calvin, K. et al. (2023). *IPCC, 2023: Climate Change 2023: Synthesis Report. Contribution of Working Groups I, II and III to the Sixth Assessment Report of the Intergovernmental Panel on Climate Change [Core Writing Team, H. Lee and J. Romero (eds.)]*. IPCC, Geneva, Switzerland. Tech. rep. Edition: First. Intergovernmental Panel on Climate Change (IPCC).
- Castro-Camilo, D., M. De Carvalho, and J. Wadsworth (2018). “Time-varying extreme value dependence with application to leading European stock markets”. In: *The Annals of Applied Statistics* 12.1.
- Castro-Camilo, D., L. Mhalla, and T. Opitz (2021). “Bayesian space-time gap filling for inference on extreme hot-spots: an application to Red Sea surface temperatures”. In: *Extremes* 24.1, pp. 105–128.
- Chautru, E. (2015). “Dimension reduction in multivariate extreme value analysis”. In: *Electronic Journal of Statistics* 9.1, pp. 383–418.
- Clarkson, D., E. Eastoe, and A. Leeson (2023). “The importance of context in extreme value analysis with application to extreme temperatures in the U.S. and Greenland”. In: *Journal of the Royal Statistical Society Series C: Applied Statistics* 72.4, pp. 829–843.
- Clémenton, S., N. Huet, and A. Sabourin (2024). “Regular variation in Hilbert spaces and principal component analysis for functional extremes”. In: *Stochastic Processes and their Applications* 174, p. 104375.
- Clémenton, S., H. Jalalzai, S. Lhaut, A. Sabourin, and J. Segers (2023). “Concentration bounds for the empirical angular measure with statistical learning applications”. In: *Bernoulli* 29.4.
- Coles, S. G. (2001). *An Introduction to Statistical Modeling of Extreme Values*. Springer Series in Statistics. London: Springer London.

- Coles, S. G., J. E. Heffernan, and J. A. Tawn (1999). “Dependence Measures for Extreme Value Analyses”. In: *Extremes* 2.4, pp. 339–365.
- Coles, S. G. and E. A. Powell (1996). “Bayesian Methods in Extreme Value Modelling: A Review and New Developments”. In: *International Statistical Review / Revue Internationale de Statistique* 64.1, p. 119.
- Coles, S. G. and J. A. Tawn (1991). “Modelling Extreme Multivariate Events”. In: *Journal of the Royal Statistical Society Series B: Statistical Methodology* 53.2, pp. 377–392.
- (1994). “Statistical Methods for Multivariate Extremes: An Application to Structural Design”. In: *Journal of the Royal Statistical Society: Series C (Applied Statistics)* 43.1, pp. 1–48.
- Cooley, D. and E. Thibaud (2019). “Decompositions of dependence for high-dimensional extremes”. In: *Biometrika* 106.3, pp. 587–604.
- Davison, A. C., S. A. Padoan, and M. Ribatet (2012). “Statistical Modeling of Spatial Extremes”. In: *Statistical Science* 27.2, pp. 161–186.
- Davison, A. C. and R. L. Smith (1990). “Models for Exceedances Over High Thresholds”. In: *Journal of the Royal Statistical Society: Series B (Methodological)* 52.3, pp. 393–425.
- De Carvalho, M. (2016). “Statistics of Extremes: Challenges and Opportunities”. In: *Extreme Events in Finance*. Ed. by F. Longin. 1st ed. Wiley, pp. 195–213.
- De Carvalho, M. and A. C. Davison (2014). “Spectral Density Ratio Models for Multivariate Extremes”. In: *Journal of the American Statistical Association* 109.506, pp. 764–776.
- Dias, A. and P. Embrechts (2004). “Change-point analysis for dependence structures in finance and insurance”. In: *Risk Measures for the 21st Century*. Ed. by G. P. Szegö. reprint. Wiley Finance Series. Chichester: Wiley, pp. 321–335.
- Dickinson, P. J. C. and L. Gijben (2014). “On the computational complexity of membership problems for the completely positive cone and its dual”. In: *Computational Optimization and Applications* 57.2, pp. 403–415.
- Dobrić, J. and F. Schmid (2005). “Nonparametric estimation of the lower tail dependence  $\lambda_L$  in bivariate copulas”. In: *Journal of Applied Statistics* 32.4, pp. 387–407.
- Dombry, C., S. Engelke, and M. Oesting (2016). “Exact simulation of max-stable processes”. In: *Biometrika* 103.2, pp. 303–317.
- Drees, H. (2023). “Statistical inference on a changing extreme value dependence structure”. In: *The Annals of Statistics* 51.4, pp. 1824–1849.

- Drees, H. and A. Sabourin (2021). “Principal component analysis for multivariate extremes”. In: *Electronic Journal of Statistics* 15.1, pp. 908–943.
- Efron, B. and C. M. Stein (1981). “The Jackknife Estimate of Variance”. In: *The Annals of Statistics* 9.3, pp. 586–596.
- Egozcue, J. J. and V. Pawlowsky-Glahn (2018). “Modelling Compositional Data. The Sample Space Approach”. In: *Handbook of Mathematical Geosciences*. Ed. by B. Daya Sagar, Q. Cheng, and F. Agterberg. Cham: Springer International Publishing, pp. 81–103.
- Einmahl, J. H. J., A. Kiriliouk, and J. Segers (2018). “A continuous updating weighted least squares estimator of tail dependence in high dimensions”. In: *Extremes* 21.2, pp. 205–233.
- Einmahl, J. H. J., A. Krajina, and J. Segers (2012). “An M-estimator for tail dependence in arbitrary dimensions”. In: *The Annals of Statistics* 40.3, pp. 1764–1793.
- Einmahl, J. H. J. and J. Segers (2009). “Maximum empirical likelihood estimation of the spectral measure of an extreme-value distribution”. In: *The Annals of Statistics* 37.5B, pp. 2953–2989.
- Einmahl, J. H. J., F. Yang, and C. Zhou (2020). “Testing the Multivariate Regular Variation Model”. In: *Journal of Business & Economic Statistics* 39.4, pp. 1–13.
- Engelke, S. and A. S. Hitz (2019). *Graphical Models for Extremes*. arXiv:1812.01734 [math, stat].
- Engelke, S. and J. Ivanovs (2021). “Sparse Structures for Multivariate Extremes”. In: *Annual Review of Statistics and Its Application* 8.1, pp. 241–270.
- Engelke, S., A. Malinowski, Z. Kabluchko, and M. Schlather (2015). “Estimation of Hüsler-Reiss distributions and Brown-Resnick processes”. In: *Journal of the Royal Statistical Society: Series B (Statistical Methodology)* 77.1, pp. 239–265.
- Fang, Y., B. Wang, and Y. Feng (2016). “Tuning-parameter selection in regularized estimations of large covariance matrices”. In: *Journal of Statistical Computation and Simulation* 86.3, pp. 494–509.
- Farkas, S., O. Lopez, and M. Thomas (2021). “Cyber claim analysis using Generalized Pareto regression trees with applications to insurance”. In: *Insurance: Mathematics and Economics* 98, pp. 92–105.
- Fawcett, L. and D. Walshaw (2006). “A Hierarchical Model for Extreme Wind Speeds”. In: *Journal of the Royal Statistical Society Series C: Applied Statistics* 55.5, pp. 631–646.

- Fix, M. J., D. Cooley, and E. Thibaud (2021). “Simultaneous autoregressive models for spatial extremes”. In: *Environmetrics* 32, e2656.
- Fomichov, V. and J. Ivanovs (2023). “Spherical clustering in detection of groups of concomitant extremes”. In: *Biometrika* 110.1, pp. 135–153.
- Fougères, A.-L., C. Mercadier, and J. P. Nolan (2013). “Dense classes of multivariate extreme value distributions”. In: *Journal of Multivariate Analysis* 116, pp. 109–129.
- Fraley, C. and A. E. Raftery (2002). “Model-Based Clustering, Discriminant Analysis, and Density Estimation”. In: *Journal of the American Statistical Association* 97.458, pp. 611–631.
- (2003). “Enhanced Model-Based Clustering, Density Estimation, and Discriminant Analysis Software: MCLUST”. In: *Journal of Classification* 20.2, pp. 263–286.
- Gadeikis, K. and V. Paulauskas (2005). “On the Estimation of a Changepoint in a Tail Index”. In: *Lithuanian Mathematical Journal* 45.3, pp. 272–283.
- Galambos, J. (1975). “Order Statistics of Samples from Multivariate Distributions”. In: *Journal of the American Statistical Association* 70.351a, pp. 674–680.
- Gelfand, A. E. and A. F. M. Smith (1990). “Sampling-Based Approaches to Calculating Marginal Densities”. In: *Journal of the American Statistical Association* 85.410, pp. 398–409.
- Gilleland, E. (2020). “Bootstrap Methods for Statistical Inference. Part II: Extreme-Value Analysis”. In: *Journal of Atmospheric and Oceanic Technology* 37.11, pp. 2135–2144.
- Gissibl, N. and C. Klüppelberg (2018). “Max-linear models on directed acyclic graphs”. In: *Bernoulli* 24.4A, pp. 2693–2720.
- Gissibl, N., C. Klüppelberg, and S. Lauritzen (2020). “Identifiability and estimation of recursive max-linear models”. In: *Scandinavian Journal of Statistics* 48.1. arXiv: 1901.03556, pp. 188–211.
- Goix, N., A. Sabourin, and S. Clémenton (2017). “Sparse representation of multivariate extremes with applications to anomaly detection”. In: *Journal of Multivariate Analysis* 161, pp. 12–31.
- Gong, Y., P. Zhong, T. Opitz, and R. Huser (2024). “Partial Tail-Correlation Coefficient Applied to Extremal-Network Learning”. In: *Technometrics* 66.3, pp. 331–346.

- Gouldsborough, L., R. Hossaini, E. Eastoe, and P. J. Young (2022). “A temperature dependent extreme value analysis of UK surface ozone, 1980–2019”. In: *Atmospheric Environment* 273. 118975.
- Greenacre, M. (2024). “The chiPower transformation: a valid alternative to logratio transformations in compositional data analysis”. In: *Advances in Data Analysis and Classification* 18, pp. 769–796.
- Gudendorf, G. and J. Segers (2010). “Extreme-Value Copulas”. In: *Copula Theory and Its Applications*. Ed. by P. Jaworski, F. Durante, W. K. Härdle, and T. Rychlik. Vol. 198. Series Title: Lecture Notes in Statistics. Berlin, Heidelberg: Springer Berlin Heidelberg, pp. 127–145.
- Gumbel, E. J. (1960). “Bivariate Exponential Distributions”. In: *Journal of the American Statistical Association* 55.292, pp. 698–707.
- Hastie, T., R. Tibshirani, and J. Friedman (2009). *The Elements of Statistical Learning*. Springer Series in Statistics. New York, NY: Springer New York.
- Haufmann, T. A. (2011). “On Completely Positive Matrices”. MA thesis. Oslo: University of Oslo.
- Hazra, A. and S. Bose (2024). *Estimating Changepoints in Extremal Dependence, Applied to Aviation Stock Prices During COVID-19 Pandemic*. arXiv:2308.13895 [stat].
- Heffernan, J. E. and J. A. Tawn (2004). “A Conditional Approach for Multivariate Extreme Values (with Discussion)”. In: *Journal of the Royal Statistical Society Series B: Statistical Methodology* 66.3, pp. 497–546.
- Henze, N. (2024). *Asymptotic Stochastics: An Introduction with a View towards Statistics*. Vol. 10. Mathematics Study Resources. Berlin, Heidelberg: Springer Berlin Heidelberg.
- Higham, N. J. (2002). “Computing the nearest correlation matrix—a problem from finance”. In: *IMA Journal of Numerical Analysis* 22.3, pp. 329–343.
- Huang, W. K., D. Cooley, I. Ebert-Uphoff, C. Chen, and S. Chatterjee (2019). “New Exploratory Tools for Extremal Dependence:  $\chi$  Networks and Annual Extremal Networks”. In: *Journal of Agricultural, Biological and Environmental Statistics* 24.3, pp. 484–501.
- Huser, R. (2021). “Editorial: EVA 2019 data competition on spatio-temporal prediction of Red Sea surface temperature extremes”. In: *Extremes* 24.1, pp. 91–104.
- Huser, R. and A. C. Davison (2013). “Composite likelihood estimation for the Brown-Resnick process”. In: *Biometrika* 100.2, pp. 511–518.

- Huser, R., A. C. Davison, and M. G. Genton (2016). “Likelihood estimators for multivariate extremes”. In: *Extremes* 19.1, pp. 79–103.
- Hüsler, J. and R.-D. Reiss (1989). “Maxima of normal random vectors: Between independence and complete dependence”. In: *Statistics & Probability Letters* 7.4, pp. 283–286.
- Jalalzai, H., S. Cléménçon, and A. Sabourin (2018). “On Binary Classification in Extreme Regions”. In: *Proceedings of the 32nd International Conference on Neural Information Processing Systems*. NIPS’18, pp. 3096–3104.
- Janßen, A., S. Neblung, and S. Stoev (2023). “Tail-dependence, exceedance sets, and metric embeddings”. In: *Extremes* 26.4, pp. 747–785.
- Janßen, A. and P. Wan (2020). “k-means clustering of extremes”. In: *Electronic Journal of Statistics* 14.1, pp. 1211–1233.
- Jessen, A. H. and T. Mikosch (2006). “Regularly varying functions”. In: *Publications de L’institut Mathématique* 80.94, pp. 171–192.
- Jiang, Y., D. Cooley, and M. F. Wehner (2020). “Principal Component Analysis for Extremes and Application to U.S. Precipitation”. In: *Journal of Climate* 33.15, pp. 6441–6451.
- Joe, H. (1990). “Families of min-stable multivariate exponential and multivariate extreme value distributions”. In: *Statistics & Probability Letters* 9.1, pp. 75–81.
- Jolliffe, I. (2002). *Principal Component Analysis*. 2nd ed. Springer Series in Statistics. New York: Springer-Verlag.
- Joo, J. Y. and S. Lee (2021). “Binary classification on compositional data”. In: *Communications for Statistical Applications and Methods* 28.1, pp. 89–97.
- Kabluchko, Z., M. Schlather, and L. De Haan (2009). “Stationary max-stable fields associated to negative definite functions”. In: *The Annals of Probability* 37.5, pp. 2042–2065.
- Kakampakou, L., E. S. Simpson, and J. L. Wadsworth (2024). *Spatial extremal modelling: A case study on the interplay between margins and dependence*. arXiv:2409.16373 [stat].
- Karnauskas, K. B. and B. H. Jones (2018). “The Interannual Variability of Sea Surface Temperature in the Red Sea From 35 Years of Satellite and In Situ Observations”. In: *Journal of Geophysical Research: Oceans* 123.8, pp. 5824–5841.
- Katz, R. W. (1999). “Extreme value theory for precipitation: sensitivity analysis for climate change”. In: *Advances in Water Resources* 23.2, pp. 133–139.

- Katz, R. W., M. B. Parlange, and P. Naveau (2002). “Statistics of extremes in hydrology”. In: *Advances in Water Resources* 25.8-12, pp. 1287–1304.
- Kaufman, L. and P. J. Rousseeuw (1990). *Finding Groups in Data*. Wiley Series in Probability and Statistics. Hoboken, NJ, USA: John Wiley & Sons, Inc.
- Kiriliouk, A. (2020). “Hypothesis testing for tail dependence parameters on the boundary of the parameter space”. In: *Econometrics and Statistics* 16, pp. 121–135.
- Kiriliouk, A. and P. Naveau (2020). “Climate extreme event attribution using multivariate peaks-over-thresholds modeling and counterfactual theory”. In: *The Annals of Applied Statistics* 14.3, pp. 1342–1358.
- Kiriliouk, A. and C. Zhou (2022). *Estimating probabilities of multivariate failure sets based on pairwise tail dependence coefficients*. arXiv:2210.12618 [stat].
- Klüppelberg, C. and M. Krali (2021). “Estimating an extreme Bayesian network via scalings”. In: *Journal of Multivariate Analysis* 181, 104672.
- Krali, M. (2018). “Causality and Estimation of Multivariate Extremes on Directed Acyclic Graphs”. MA thesis. Munich: Technische Universität München.
- Krzanowski, W. J. (1979). “Between-Groups Comparison of Principal Components”. In: *Journal of the American Statistical Association* 74.367, pp. 703–707.
- Kunz, M., S. Mohr, M. Rauthe, R. Lux, and C. Kottmeier (2010). “Assessment of extreme wind speeds from Regional Climate Models – Part 1: Estimation of return values and their evaluation”. In: *Natural Hazards and Earth System Sciences* 10.4, pp. 907–922.
- Larsson, M. and S. Resnick (2012). “Extremal dependence measure and extremogram: the regularly varying case”. In: *Extremes* 15.2, pp. 231–256.
- Ledoit, O. and M. Wolf (2003). “Improved estimation of the covariance matrix of stock returns with an application to portfolio selection”. In: *Journal of Empirical Finance* 10.5, pp. 603–621.
- Lee, J. and D. Cooley (2023). *Partial Tail Correlation for Extremes*. arXiv:2210.02048 [stat].
- Lehtomaa, J. and S. Resnick (2020). “Asymptotic independence and support detection techniques for heavy-tailed multivariate data”. In: *Insurance: Mathematics and Economics* 93, pp. 262–277.

- Liu, J. and J. Ye (2009). “Efficient Euclidean projections in linear time”. In: *Proceedings of the 26th Annual International Conference on Machine Learning*. Montreal Quebec Canada: ACM, pp. 657–664.
- Martín-Fernández, J.-A., J. Barceló-Vidal, and V. Pawlowsky-Glahn (1998). “A Critical Approach to Non-Parametric Classification of Compositional Data”. In: *Advances in Data Science and Classification*. Ed. by H.-H. Bock, W. Gaul, O. Opitz, M. Schader, A. Rizzi, M. Vichi, and H.-H. Bock. Series Title: Studies in Classification, Data Analysis, and Knowledge Organization. Berlin, Heidelberg: Springer Berlin Heidelberg, pp. 49–56.
- McLachlan, G. and D. Peel (2000). *Finite Mixture Models*. 1st ed. Wiley Series in Probability and Statistics. Wiley.
- Mestre, X. (2008). “Improved Estimation of Eigenvalues and Eigenvectors of Covariance Matrices Using Their Sample Estimates”. In: *IEEE Transactions on Information Theory* 54.11, pp. 5113–5129.
- Meyer, N. and O. Wintenberger (2021). “Sparse regular variation”. In: *Advances in Applied Probability* 53.4, pp. 1115–1148.
- (2023). “Multivariate Sparse Clustering for Extremes”. In: *Journal of the American Statistical Association* 119.547, pp. 1911–1922.
- Mhatre, N. and D. Cooley (2024). “Transformed-Linear Models for Time Series Extremes”. In: *Journal of Time Series Analysis* 45.5, pp. 671–690.
- Mikosch, T. and O. Wintenberger (2024). *Extreme Value Theory for Time Series: Models with Power-Law Tails*. Springer Series in Operations Research and Financial Engineering. Cham: Springer Nature Switzerland.
- Murphy, C., J. A. Tawn, and Z. Varty (2024). “Automated threshold selection and associated inference uncertainty for univariate extremes”. In: *Technometrics*.
- Northrop, P. J., N. Attalides, and P. Jonathan (2017). “Cross-Validatory Extreme Value Threshold Selection and Uncertainty with Application to Ocean Storm Severity”. In: *Journal of the Royal Statistical Society Series C: Applied Statistics* 66.1, pp. 93–120.
- Oesting, M., M. Schlather, and P. Friederichs (2017). “Statistical post-processing of forecasts for extremes using bivariate Brown-Resnick processes with an application to wind gusts”. In: *Extremes* 20.2, pp. 309–332.
- Park, J., C. Yoon, C. Park, and J. Ahn (2022). “Kernel Methods for Radial Transformed Compositional Data with Many Zeros”. In: *Proceedings of the 39th International Con-*

- ference on Machine Learning. Proceedings of Machine Learning Research, pp. 17458–17472.
- Pawlowsky-Glahn, V. and J. J. Egozcue (2001). “Geometric approach to statistical analysis on the simplex”. In: *Stochastic Environmental Research and Risk Assessment* 15.5, pp. 384–398.
- Pearson, K. (1897). “Mathematical contributions to the theory of evolution.—On a form of spurious correlation which may arise when indices are used in the measurement of organs”. In: *Proceedings of the Royal Society of London* 60.359-367, pp. 489–498.
- Pickands III, J. (1975). “Statistical Inference Using Extreme Order Statistics”. In: *Annals of Statistics* 3.1, pp. 119–131.
- Poon, S.-H., M. M. Rockinger, and J. A. Tawn (2003). “Modelling Extreme-Value Dependence in International Stock Markets”. In: *Statistica Sinica* 13.4, pp. 929–953.
- Reiss, R.-D. and M. Thomas (2007). *Statistical Analysis of Extreme Values: with Applications to Insurance, Finance, Hydrology and Other Fields*. Third Edition. SpringerLink Bücher. Basel: Birkhäuser Verlag AG.
- Resnick, S. (2004). “The Extremal Dependence Measure and Asymptotic Independence”. In: *Stochastic Models* 20.2, pp. 205–227.
- (2007). *Heavy-tail phenomena: probabilistic and statistical modeling*. Springer series in operations research and financial engineering. New York, N.Y: Springer.
- Richards, J., N. Alotaibi, D. Cisneros, Y. Gong, M. B. Guerrero, P. V. Redondo, and X. Shao (2024). “Modern extreme value statistics for Utopian extremes. EVA (2023) Conference Data Challenge: Team Yalla”. In: *Extremes*.
- Rohrbeck, C. and D. Cooley (2023). “Simulating flood event sets using extremal principal components”. In: *The Annals of Applied Statistics* 17.2, pp. 1333–1352.
- Rohrbeck, C., E. S. Simpson, and J. A. Tawn (2023). “Editorial: EVA Conference Data Challenge (2023)”. In: *Extremes*.
- (2024). *Dataset for EVA 2023 Data Challenge*. University of Bath Research Data Archive. Bath.
- Rohrbeck, C., E. S. Simpson, and R. P. Towe (2021). “A spatio-temporal model for Red Sea surface temperature anomalies”. In: *Extremes* 24.1, pp. 129–144.

- Rothman, A. J., E. Levina, and J. Zhu (2009). "Generalized Thresholding of Large Covariance Matrices". In: *Journal of the American Statistical Association* 104.485, pp. 177–186.
- Russell, B. T. and P. Hogan (2018). "Analyzing dependence matrices to investigate relationships between National Football League combine event performances". In: *Journal of Quantitative Analysis in Sports* 14.4, pp. 201–212.
- Schellander, H. and T. Hell (2018). "Modeling snow depth extremes in Austria". In: *Natural Hazards* 94.3, pp. 1367–1389.
- Seber, G. A. F. (1984). *Multivariate Observations*. 1st ed. Wiley Series in Probability and Statistics. Wiley.
- Semadeni, C. A. (2020). "Inference on the Angular Distribution of Extremes". Ph.D. Thesis. École Polytechnique Fédérale de Lausanne.
- Serrano, J. F. (2022). *Semiparametric bivariate extreme-value copulas*. arXiv:2109.11307 [math, stat].
- Shaked-Monderer, N. (2021). "On the number of CP factorizations of a completely positive matrix". In: *Linear and Multilinear Algebra* 70.19. arXiv:2009.12290 [math], pp. 3887–3904.
- Shyamalkumar, N. D. and S. Tao (2020). "On tail dependence matrices: The realization problem for parametric families". In: *Extremes* 23.2, pp. 245–285.
- Simpson, E. S. and J. L. Wadsworth (2021). "Conditional modelling of spatio-temporal extremes for Red Sea surface temperatures". In: *Spatial Statistics* 41. 100482.
- Simpson, E. S., J. L. Wadsworth, and J. A. Tawn (2020). "Determining the dependence structure of multivariate extremes". In: *Biometrika* 107.3, pp. 513–532.
- Sklar, A. (1959). "Fonctions de répartition à n dimensions et leurs marges". In: *Publications de l'Institut de Statistique de l'Université de Paris* 8, pp. 229–231.
- Smith, R. L., J. A. Tawn, and H.-K. Yuen (1990). "Statistics of Multivariate Extremes". In: *International Statistical Review* 58.1, pp. 47–58.
- Song, D. and A. K. Gupta (1997). " $L_p$ -norm uniform distribution". In: *Proceedings of the American Mathematical Society* 125.2, pp. 595–601.
- Stein, C. M. (1956). "Inadmissibility of the usual estimator for the mean of a multivariate normal distribution". In: *Contribution to the Theory of Statistics*. University of California Press, pp. 197–206.

- Szemkus, S. and P. Friederichs (2024). “Spatial patterns and indices for heat waves and droughts over Europe using a decomposition of extremal dependency”. In: *Advances in Statistical Climatology, Meteorology and Oceanography* 10.1, pp. 29–49.
- Tawn, J. A. (1990). “Modelling multivariate extreme value distributions”. In: *Biometrika* 77.2, pp. 245–253.
- Towler, E., B. Rajagopalan, E. Gilleland, R. S. Summers, D. Yates, and R. W. Katz (2010). “Modeling hydrologic and water quality extremes in a changing climate: A statistical approach based on extreme value theory”. In: *Water Resources Research* 46.11. W11504.
- Tran, N. M., J. Buck, and C. Klüppelberg (2021). *Causal Discovery of a River Network from its Extremes*.
- Tsagris, M., S. Preston, and A. T. A. Wood (2016). “Improved Classification for Compositional Data Using the -transformation”. In: *Journal of Classification* 33.2, pp. 243–261.
- Vanem, E. (2015). “Non-stationary extreme value models to account for trends and shifts in the extreme wave climate due to climate change”. In: *Applied Ocean Research* 52, pp. 201–211.
- Wadsworth, J. L. (2016). “Exploiting Structure of Maximum Likelihood Estimators for Extreme Value Threshold Selection”. In: *Technometrics* 58.1, pp. 116–126.
- Wixson, T. P. and D. Cooley (2023). “Attribution of Seasonal Wildfire Risk to Changes in Climate: A Statistical Extremes Approach”. In: *Journal of Applied Meteorology and Climatology* 62.11, pp. 1511–1521.
- Yi, F. and H. Zou (2013). “SURE-tuned tapering estimation of large covariance matrices”. In: *Computational Statistics & Data Analysis* 58, pp. 339–351.
- Youngman, B. D. (2019). “Generalized Additive Models for Exceedances of High Thresholds With an Application to Return Level Estimation for U.S. Wind Gusts”. In: *Journal of the American Statistical Association* 114.528, pp. 1865–1879.
- Yuen, R. and S. Stoev (2014a). “CRPS M-estimation for max-stable models”. In: *Extremes* 17.3, pp. 387–410.
- (2014b). “Upper bounds on value-at-risk for the maximum portfolio loss”. In: *Extremes* 17.4, pp. 585–614.
- Zhou, S., B. Yu, and Y. Zhang (2023). “Global concurrent climate extremes exacerbated by anthropogenic climate change”. In: *Science Advances* 9.10. eab01638.